

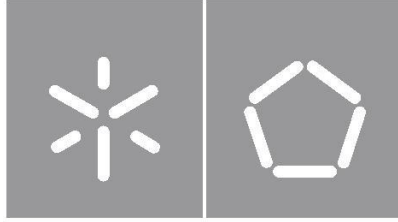


**Design and fabrication of
Silver microelectrodes for
biomedical applications**

Tiago Alexandre da Silva Monteiro

Universidade do Minho
Escola de Engenharia





Universidade do Minho
Escola de Engenharia

Tiago Alexandre da Silva Monteiro

**Design and fabrication of silver
microelectrodes for biomedical applications**

Tese de Doutoramento em
Engenharia Biomédica

Trabalho efetuado sob a orientação dos
Professor Luís Miguel Valente Gonçalves (UMinho)
**Professora Susana Isabel Pinheiro Cardoso de Freitas (INESC-
MN/IST)**

DIREITOS DE AUTOR E CONDIÇÕES DE UTILIZAÇÃO DO TRABALHO POR TERCEIROS

Este é um trabalho académico que pode ser utilizado por terceiros desde que respeitadas as regras e boas práticas internacionalmente aceites, no que concerne aos direitos de autor e direitos conexos.

Assim, o presente trabalho pode ser utilizado nos termos previstos na licença [abaixo](#) indicada.

Caso o utilizador necessite de permissão para poder fazer um uso do trabalho em condições não previstas no licenciamento indicado, deverá contactar o autor, através do RepositóriUM da Universidade do Minho.

Licença concedida aos utilizadores deste trabalho



Atribuição

CC BY

<https://creativecommons.org/licenses/by/4.0/>

ACKNOWLEDGEMENTS

I want to express my gratitude to my supervisor Professor Luís Gonçalves, and to Professor Graça Minas, both from *Universidade of Minho*, whom inspired and challenged me to venture into this project. To all their support during the majority of my Academic years, and for opening new paths for me, I'm truly appreciated. I wouldn't be here presenting this thesis if it weren't for them.

To my co-supervisor Professor Susana Cardoso, from the *Instituto de Engenharia de Sistemas e Computadores – Microsistemas e Nanotecnologias* and *Instituto Superior Técnico*, to whom I devoted an enormous amount of headaches, I can't demonstrate how much I'm grateful for. The opportunities presented to me, to work under the excellent environment of a cleanroom and under the constant demand for excellency, has shaped skills and personality alike in what I am today.

To INESC-MN itself, where more than 90% of the work was performed, I'm deeply appreciated for the opportunity and support. Without it, I doubt I could have achieved so much in this thesis.

To all my close family, my parents and my sister, I cannot state their importance. This thesis is only the final step on a long journey, and undoubtedly could not have been completed if it weren't for all those years of support and encouragement.

To my girlfriend and life partner, I am blessed to have met you before this journey had even begun. To have shared all the emotions, the happiness and the frustration along the way, has been an exciting journey. As this project ends, a new one begins, and as such, I would like to dedicate this thesis to our first child that is on the way.

One last word for all my long lasting friends, and to the new ones that I've made throughout the way. As they fathomed to understand the work every single time I was asked about it, their support was unshaken nonetheless.

This thesis had the support of *Fundação para a Ciência e Tecnologia* under a Doctoral Scholarship - SFRH/BD/90121/2012, to whom I'm honored to have been awarded such grant, and INESC-MN, which has facilitated the use of equipment and resources for this thesis.



PROGRAMAS DE
DOUTORAMENTO
FCT



QR
EN
QUADRO DE REFERÊNCIA
ESTRATÉGICO
NACIONAL
PORTUGAL 2007-2013



UNIAO EUROPEIA
Fundo Europeu
de Desenvolvimento Regional



Microsistemas e
Nanotecnologias

STATEMENT OF INTEGRITY

I hereby declare having conducted this academic work with integrity. I confirm that I have not used plagiarism or any form of undue use of information or falsification of results along the process leading to its elaboration.

I further declare that I have fully acknowledged the Code of Ethical Conduct of the University of Minho.

Design and fabrication of silver microelectrodes for biomedical applications

RESUMO

O cancro é uma das maiores causas de mortalidade e morbidade em países desenvolvidos em todo o mundo. É geralmente precedido por alterações pré-cancerígenas e a sua deteção precoce, especialmente numa fase de displasia, é um dos grandes objetivos da medicina moderna, visto que as probabilidades de tratamento aumentam consideravelmente nesta fase. Estudos *in-vitro* demonstraram que alterações no pH a nível do ambiente intra- e extracelular podem estar correlacionadas com a proliferação de células tumorais em diferentes estados. Contudo, medições *in-situ* das propriedades eletroquímicas das células podem ser desafiantes e requerer equipamento complexo ou dispendioso.

A ambição desta tese consiste no desenvolvimento de ferramentas inovadoras para o diagnóstico celular *in-vitro* e *in-situ*, com base em elétrodos micrométricos “*solid-state*” com capacidade de leitura de pH. Este sistema deverá, preferencialmente, ser compatível e permitir a integração de componentes “*lab-on-chip*” subsequentes, maioritariamente de processos óticos para posterior análise química e biológica.

O protótipo proposto consiste numa matriz de 9600 microelétrodos “*solid-state*” com pontas nanométricas. O processo de fabricação consiste na padronização de um molde negativo para as pontas individuais de cada microelétrodo, seguido de um aumento na altura do perfil (para um maior “*aspect-ratio*” e capacidade de penetração) através da adição de um *Photoresist*, preenchimento do molde com Prata através de um processo inovador de Eletrodeposição “*Through-Silicon*”, e finalmente a transferência do perfil para um substrato de vidro com compatibilidade com processos óticos.

Os resultados finais demonstram a prova de conceito da viabilidade do processo e dos múltiplos desenvolvimentos em engenharia de processos, apesar de estudos e otimizações subsequentes serem necessárias em diversas áreas do projeto de forma a melhor compreender os princípios e mecânicas por detrás de alguns aspetos dos processos inovadores.

Palavras-chave: Microelétrodos de Prata, Micromaquinação de Silício, Eletrodeposição “*Through-Silicon*”, Sensores de pH

Design and fabrication of silver microelectrodes for biomedical applications

ABSTRACT

Cancer is one of the major causes of mortality and morbidity in developed countries worldwide. It is usually preceded by precancerous changes and its early detection, especially at the dysplasia stage, is one of the major goals in modern medicine, as the chances of a successful treatment are increased at this stage. *In-vitro* studies have demonstrated that pH changes in both the intracellular and extracellular environment of a tissue can be correlated with tumor cell proliferation at different stages. However, *in-situ* measurements of the electrochemical properties of cells can be challenging and require complex or costly equipment.

In this thesis, the ambition is to develop a novel tool for *in-vitro* and *in-situ* cell diagnosis, based on solid-state micrometric electrodes with pH sensing capabilities. This system should, optimally, be compatible and allow integration with subsequent lab-on-chip components, mainly optical processes for further biological and chemical analysis.

The proposed prototype consists in an array of 9600 solid-state microelectrodes with nanometric tips. The fabrication process includes the patterning of a negative mold for the individual microelectrode tips, followed by an increase in height (for higher aspect-ratio and deeper penetration capability) through the addition of a Photoresist, filling of the mold with Silver through a novel *Through-Silicon Electrodeposition* process, and finally transferring the pattern to a Glass substrate with optical processing compatibility.

The end results demonstrates a proof-of-concept of the process feasibility and the multiple achievements in process engineering, although further studies and optimization are required in different areas of the project as to better understand the mechanics and principles behind some of the novel aspects of the processes.

Keywords: Silver microelectrodes, Silicon micromachining, Through-Silicon electrodeposition, pH Sensors

INDEX

ACKNOWLEDGEMENTS	ii
RESUMO	iv
ABSTRACT	v
INDEX	vi
ACRONYMS INDEX	viii
FIGURE INDEX	ix
TABLE INDEX	xxi
INTRODUCTION	1
CHAPTER I - THEORETICAL CONCEPTS.....	7
1.1 - pH theory	7
1.2 - pH and human cells	9
1.3- pH sensors	10
1.4- pH sensors for intracellular measurements	13
b.1) Metal-Metal Oxide electrodes.....	14
b.2) Metal Oxide electrodes	14
b.3) Reference electrode	16
CHAPTER II - METHODOLOGIES	19
2.1- Silicon Micromachining.....	19
2.2 - Silicon Wet Etching	22
Etching in the {100} plane	22
Etching in the {111} plane.....	23
Additives to the etchant solution	24
Dispersion methods and etching quality	24
2.3 - Electrodeposition	28
Silver Electrodeposition	31
Through-Silicon Electrodeposition	32
CHAPTER III - MICROFABRICATION PROCESS AND RESULTS	36
3.1 - General Process Description	36
3.2 - Process Definition	37
3.2.1 - Lithographical patterning.....	40

3.2.2 - Silicon wet etching optimization.....	47
3.2.3 - Cell penetration assay.....	64
3.2.4 - Process assessment and redefinition.....	68
3.2.5- Working electrode patterning.....	75
3.2.6 - Profile Definition	80
3.2.7 - Silver plating.....	89
3.2.8 - Contact Patterning.....	115
3.2.9 - Structure release and activation	123
CHAPTER IV - CONCLUSIONS AND FUTURE WORK	146
4.1 - Conclusions.....	146
4.2 - Future work	147
4.3 - Scientific publications	149
BIBLIOGRAPHY	151
ANNEXES	159
Annex 1 - Process Runsheet for the study and optimization of the Silicon Wet Etching process	160
Annex 2 - Cell proliferation protocol.....	165
Annex 3 - Homogeneous Membrane Integrity Assay Protocol	183
Annex 4 - MTS Cell Proliferation Assay Protocol	200
Annex 5 - Process Runsheet for the fabrication of Silver Microneedles.....	213
Annex 6 - Process Diagram for the fabrication of Silver Microneedles	229
Annex 7 - Process Runsheet for the preparation of Silver Electroplating Solutions	249

ACRONYMS INDEX

Materials	Other Acronyms
Ag - Silver	DWL - Direct Writing Lithography
Al - Aluminum	MEMS - Microelectromechanical systems
Ag/Cl - Silver-Chloride	pH - Potential of Hydrogen
BOE - Buffer Oxide Etchant	SEM - Scanning Electron Microscopy
Cl - Chloride	US - Ultrasounds
Cr - Chromium	
IPA - Isopropyl Alcohol	
KOH - Potassium Hydroxide	
PDMS - Polydimethylsiloxane	
PMMA - Polymethyl methacrylate	
+PR - Positive Photoresist	
Si - Silicon	
SiO₂ - Silicon Dioxide	

Measurements
Φ - Flow
μ - Micro
Rpm - Rotations per minute
Sccm - Standard cubic centimeters per minute
Torr - Unit of pressure
W_{dc} - Watts, Direct Current
W_{rf} - Watts, Radio Frequency
wt% - Weight percent

FIGURE INDEX

Figure 1 - Diagram of the microfabricated solid-state micrometric array of Silver electrodes, with Aluminum interconnections for electrical readout. The structure is supported by a flexible elastomer (PDMS) over a glass substrate so to enable further integration with microfluidics and other lab-on-chip components.	4
Figure 2 - Diagram of a standard galvanic electrochemical sensor. Description: E1 - Selective membrane potential; E2 - Asymmetry potential; E3 - Internal potential; E4 - Surface potential at the working electrode; E5 - Surface potential at the reference electrode; E6 - Diffusion potential.	12
Figure 3 - Tridimensional representation of the crystallographic organization of Silicon atoms in a matrix. Grey dots represent inner atoms. Yellow dots represent atoms in plane [81].	19
Figure 4 - RIE-sharpened silicon needle 230 μm tall and with a 200 nm wide tip. Authorized use by [11]	21
Figure 5 - Etching profile obtained by: A) Anisotropic RIE; B) Isotropic RIE or Wet Etching; C) Anisotropic Wet Etching (right).	22
Figure 6 - Schematic diagram representing the chemical structure of the Silicon surface atoms and respective binding of hydroxide ions during a wet etch process for {100} silicon wafers.	23
Figure 7 - Schematic diagram representing the chemical structure of the Silicon surface atoms and respective binding of hydroxide ions during a wet etch process for {111} silicon wafers.	24
Figure 8 - Topology of the etched surface at various etching conditions. Authorized use by [95]	26
Figure 9 - Schematic diagram representing the Wet Etching Process with ultrasonic agitation.	27
Figure 10 - Schematic diagram representing the Electrodeposition process in a two-electrode system.	30
Figure 11 - Schematic diagram representing the effect of photons in the promotion of electroplating in non-desired areas through photon-generated electrons (b).	34
Figure 12 - Schematic diagram representing a general layout of the proposed system: (a) - view of the top layers; and (b) - view of the microelectrodes and contact lines underneath the protective top layer. The individual components consist of: an array of pH sensitive (grey polygons – (a) and (b)); contact lines (green lines – (b)); contact pads (black – (a)); insulating and chemically resistant layer (green – (a)). The image is not to scale to allow for a better visual representation of the desired setup.	36

Figure 13 - Schematic diagram representing the cross-section view of the proposed sensor through Method a), depicting an array of microelectrodes fabricated through the functionalization of a micromachined Silicon surface. 38

Figure 14 - Schematic diagram representing the cross-section view of the proposed sensor through Method b), depicting an array of microelectrodes fabricated through the electroplating (and later functionalization and detachment) of a series of cavities formed by micromachining a Silicon wafer and heightened artificially with a thick resist..... 39

Figure 15 - Schematic diagram representing the microfabrication process of protuberant pyramidal structures through Silicon wet etching (cross-section view). A Chromium layer is used as a mask for the etching process. A sharp pyramidal structure is reached with the release of the mesa mask (optimal etch time). Adapted from [93]..... 41

Figure 16 - Photograph of a 2'' Silicon wafer after Step #03 - Chromium deposition. The darker spots on the wafer are the marks where Kapton tape was used to grab the wafer to the holder. 42

Figure 17 - Microscopic inspection of the patterning profile obtained in Step #04 through Direct Writing Laser. A green filter is used for microscopic inspection without affecting the Photoresist. The dark patterns represent hardened Photoresist, whilst the brighter areas represent the exposed Chromium surface. Mask name: TMpH_array04. The patterns in these arrays are presented in Table 3. (a) 10× amplification; (b) 50× amplification. 43

Figure 18 - AutoCAD™ image representing the profiles patterned through Direct Writing Lithography. Total patterned area of 9 × 9 mm. Complete description of each profile in Table 3. Mask name: TMpH_array04..... 44

Figure 19 - AutoCAD™ image representing the profiles scripted in mask TMpH_array04 in greater detail: (a) Circles; (b) Squares; (c) Rotated Squares; and (d) Honeycomb pattern. 45

Figure 20 - AutoCAD™ image representing the profiles scripted in mask TMpH_array04, detailing the braille inscriptions. In this example it can be read “10 μm QD” on top and “20 μm” on the side, which can be translated to “10 μm squares with a 20 μm relative distance”..... 46

Figure 21 - Photography of a 2'' Silicon wafer after Step #5. In the middle, 9 individual dies contain the exact same profile, allowing for several samples to be fabricated from a single wafer. The bright color represents the exposed Chromium layer, whilst the darker-green color represents the hardened Photoresist. 47

Figure 22 - Microscopic inspection of the patterning profile obtained in Step #07, after Chromium etching and Photoresist cleaning. The bright color represents the exposed Silicon surface, whilst the darker areas represent the patterned Chromium mask. Mask name: TMpH_array04. 48

Figure 23 - Schematic diagram representing the: (a) dissociation of the top mesa mask; and (b) formation of a completed pyramidal structure. Adapted from [93]. 49

Figure 24 - Microscopic inspection of sample processed in Step #08 under an orbital agitator. Some of the Chromium mask profiles can be discerned in the image. The black smudges represent Silicate compounds that were formed as a by-product of Silicon wet etching and have adhered to the surface of the sample, acting as pseudo-masks and affecting the etching profile. Image obtained after 30 min process at room temperature. 50

Figure 25 - Microscopic inspection of sample processed in Step #08 under an ultrasonic agitator. Although some of the profiles were affected and deleted in the process, the overall quality of the etching process increased considerably. Image obtained after 30 min process at room temperature. 51

Figure 26 - Graphical representation of the total initial volume (blue), as a sum of initial KOH volume (20 mL) and IPA volume (ranging from 0 to 5 mL), *versus* the final volume (red) after a total etching time of 120 min. Adapted from [93]. 52

Figure 27 - Evolution of solution volume as a consequence of solvent evaporation. The main chart contains the total volume of the solution (sum of diluted KOH and IPA volume) across time, whilst the inset charts represents only the IPA volume in the solution, during the etch process. Samples 1-4 are represented in Table 5. Adapted from [93]. 54

Figure 28 - Evolution of the base width of $8\ \mu\text{m} \times 8\ \mu\text{m}$ patterned square structures, spaced $16\ \mu\text{m}$ apart, during a Silicon wet etching process under IPA saturated conditions (sample 4 in Table 5). Microscopic inspection demonstrates how the base of each individual profile widens consistently, ending up merging together. These results are a consequence of IPA availability during the entire process time. Adapted from [93]. 55

Figure 29 - Evolution of the base width of $8\ \mu\text{m} \times 8\ \mu\text{m}$ patterned square structures, spaced $40\ \mu\text{m}$ apart, during a Silicon wet etching process under IPA saturated conditions (until minute 80) and under IPA depletion conditions (after minute 80). The results demonstrate that under the influence of IPA, the base width continuously widens under a square shape. Once transposed to a solution of diluted KOH without any IPA, an initial increase of the base width can be observed as a consequence of

crystallographic reorientation towards the (331) plane. Once the reorientation is completed, continuous wet etching will cause the quickly decrease in base width. Adapted from [93].	56
Figure 30 - AutoCAD™ image representing the profiles patterned through Direct Writing Lithography. Total patterned area of 9 × 9 mm. Complete description of each profile in table 6. Mask name: TMpH_array05.	57
Figure 31 - Evolution of the measured pattern angle in different IPA availability conditions, obtained from (a) 200 μm wide rectangular mask (black); (b) 10 μm v-groove from a square mask with a spacing of 20 μm (blue); and (c) 10 μm square mask with a spacing of 20 μm (red). Adapted from [93].	58
Figure 32 - SEM cross-section image of the (331) pyramidal structure obtained from a 10 μm × 10 μm square mask, spaced 20 μm apart (Sample 2 in Table 5). Adapted from [93].	59
Figure 33 - SEM inclined image of (111) pits obtained from 10 μm × 10 μm square inverted masks (holes), spaced 20 μm apart. IPA plays little to no influence in this process (Sample 1 (left) and Sample 3 (right) from Table 5). Adapted from [93].	60
Figure 34 - Microscopic inspection of samples processed under the same conditions as Sample 2 (Table 5), after 20 minutes. Initial profile: (left) 40 μm and (right) 20 μm squares: (a) aligned with the wafer flat; and (b) misaligned 22.5 ° with the wafer flat. Adapted from [93].	61
Figure 35 - Microscopic inspection of samples processed under the same conditions as Sample 4 (Table 5), after 50 minutes. Initial profile: 10 μm squares a) aligned and b) misaligned 22.5 ° with the wafer flat. Adapted from [93].	61
Figure 36 - Microscopic inspection of samples with an initial profile of 40 μm squares aligned with the flat. Conditions are as described in Table 5: (a) Sample 1; (b) Sample 2; (c) Sample 3; and (d) Sample 4. Adapted from [93].	62
Figure 37 - Schematic diagram of the evolution of Silicon wet etched structures, under IPA influence, for a 10 μm square mask and the conditions depicted in Table 5. Adapted from [93].	63
Figure 38 - SEM inclined view of a large array of standing octagonal pyramidal shaped structures, achieved under the conditions of Sample 2 (Table 5).	63
Figure 39 - Schematic diagram representing the setup used for the cell penetration assay using weights of fixed mass to simulate pressure.	65

Figure 40 - Graphical representation of the absorbance results at 490 nm for the experiments described in Table 7..... 67

Figure 41 - Schematic diagram representing the cross-section view of the microfabrication steps for the proposed sensor, depicting the method to form solid-state Silver electrodes through electrodeposition and the release method with the assist of a transparent polymer. (a) Patterning of a mold for the; (b) Fabrication of thick Silver microelectrodes; (c) Vias patterning for contact signal acquisition and encapsulation with a solid substrate and a polymeric buffer; and (d) Structure release and functionalization. 72

Figure 42 - Schematic diagram representing the cross-section view of the microfabrication steps for step #02: deposition of 3000 Å of Silicon Dioxide, through Magnetron Sputtering, on top of a Silicon Wafer with a thickness of 675 μm. 76

Figure 43 - Schematic diagram representing the cross-section view of the microfabrication steps for step #03: deposition of 3000 Å of Chromium, on the backside of the sample, through Magnetron Sputtering. 77

Figure 44 - AutoCAD™ image representing the profile patterned through Direct Writing Lithography for Step #04. Each ¼ of a 6'' Silicon wafer contained 8 identical profiles, representing 8 different dies. All measures and dimensions are represented in micrometers. Mask name: TmpH_backcontact. 78

Figure 45 - Schematic diagram representing the cross-section view of the microfabrication steps for step #04: deposition of a 1.5 μm thick PFR 7790 G +PR, patterning through Direct Writing Laser, and resist development, on the backside of the sample. 78

Figure 46 - Schematic diagram representing the cross-section view of the microfabrication steps for step #05: spin coating of a 1.5 μm thick PFR 7790 G +PR layer, patterning through Direct Writing Laser, and resist development, on the backside of the sample. 79

Figure 47 - Schematic diagram representing the cross-section view of the microfabrication steps for step #06: deposition of 6000 Å thick of Silicon Dioxide, on the backside of the sample, through Magnetron Sputtering. 80

Figure 48 - AutoCAD™ image representing the profile patterned through Direct Writing Lithography for Step #07. Each ¼ of a 6'' Silicon wafer contained 8 identical profiles, representing 8 different dies. (a) Overall profile; (b) detail on the alignment marks that would allow for a secondary lithography later on;

and (c) detail on the matrix profile. All measures and dimensions are represented in micrometers. Mask name: TMpH_holes. 81

Figure 49 - Schematic diagram representing the cross-section view of the microfabrication steps for step #07: spin coating of a 1.5 μm thick PFR 7790 G +PR layer, patterning through Direct Writing Laser, and resist development..... 81

Figure 50 - Schematic diagram representing the cross-section view of the microfabrication steps for step #08: etching of the Silicon Dioxide layer, through Reactive Ion Etching..... 82

Figure 51 - Schematic diagram representing the cross-section view of the microfabrication steps for step #09: wet etching of the Silicon substrate, through a diluted KOH solution. 84

Figure 52 - Microscopic inspection of samples processed through Silicon wet etching (22% wt diluted KOH solution, 40 min at 39 °C with ultrasonic agitation). (a) Focal point at the surface of the Silicon wafer; and (b) at the bottom of the newly created pits. The intercross of the 4 walls at the center of the profiles, in (b), indicates the completion of the process. Slight offset of the intercross towards the profile position is due to optical misalignment of the microscope lenses. 84

Figure 53 - Schematic diagram representing the cross-section view of the microfabrication steps for step #09: wet etching of the Silicon substrate, through a diluted KOH solution. 85

Figure 54 - Schematic diagram representing the cross-section view of the microfabrication steps for step #10: patterning and opening of the Vias through DWL lithography and RIE. 86

Figure 55 - Schematic diagram representing the cross-section view of the patterned structures filled with PDMS, as to ascertain the quality and dimensions of the TMpH_holes mask over the thick ma-P 1275 +PR..... 88

Figure 56 - SEM inspection of a PDMS counter-mold obtained from the patterning of an 8 μm thick ma-P 1275 +PR with the mask TMpH_holes. The base of the PDMS represents the surface of the PR, whilst the top of the PDMS represents the base (or pit) of the PR. The cracks seen in the image can be attributed to damage of the thin gold layer due to striation effects cause by the PDMS flexibility. 88

Figure 57 - Schematic diagram representing the cross-section view of the dummy samples used for the optimization of the Silver plating process..... 89

Figure 58 - Laboratorial apparatus used for the electroless and electroplating deposition of Silver: (a) overall setup composed of a reaction cup, electrodes and heater/agitator equipment; (b) detail of the

reaction cup with electrodes). A PMMA holder was used to assist in the electrodeposition process, whilst a solid Silver slat was used as the counter electrode..... 91

Figure 59 - Schematic diagram representing the cross-section view of the dummy samples used for the optimization of the Silver plating process, connected to the Working Electrode. The Silver layer acts as a seed layer for the electroplating process and as a conductor for the electrical charge applied in the process. 92

Figure 60 - Macroscopic inspection of samples ELP 01 (a) and ELP 06 (b). A white smudge of Silver can be observed in sample ELP 01 due to the adhesion of Silver molecules to the ma-P 1275 +PR surface. In sample ELP 06, Silver depletion had already occurred and no deposition was recorded. ... 94

Figure 61 - A reflective, thin-layer of Silver atoms adhered to the inside wall of the reaction cup during the electroless deposition process..... 94

Figure 62 - Schematic diagram of the electroplating apparatus using a 2-electrode system. 95

Figure 63 - PMMA holder used in the electrodeposition of Silver: (a) schematic diagram; (b) front side; (c) back side. The rectangular slot on the top allows for a metallic tweezer to be connected and transfer the electrical current to the power source. The square slot found in the middle of the front side (a and b) redirects the electroplating towards the desired area. All measures and dimensions are represented in millimeters. 96

Figure 64 - Current source used in the electrodeposition process (Keithley 220 Programmable Current Source) 96

Figure 65 - Microscopic inspection of samples: (a) EP B01; (b) EP B02; (c) EP B03; and (d) EP B04. The red areas consist of ma-P 1275 +PR that survived the prolonged exposure. The black areas consist of oxidized molecules at the surface of the sample. The white areas consist of electroplated silver. The small circles/dots consist of the individual electroplated pits. 98

Figure 66 - Microscopic inspection of samples: (a) EP C01; (b) EP C02; (c) EP C03. The small dots consist of the patterned holes created in the ma-P 1275 +PR. The black areas in the images consist of large aggregates of electroplated Silver that prolong above the sample surface (overplating). In some cases, those aggregates would break, creating cleaved structures with a reflective surface, represented by the white areas. 100

Figure 67 - Microscopic inspection of sample EP C04. The two images represent different areas of the same sample. The small dots represent the patterned holes created in the ma-P 1275 +PR. The black

areas in the images consist of electroplated Silver that prolong above the sample surface (overplating).
..... 101

Figure 68 - Microscopic inspection of sample EP C09. The two images represent different areas of the same sample. The small dots represent the patterned holes created in the ma-P 1275 +PR. The black areas in the images consist of electroplated Silver that prolong above the sample surface (overplating).
..... 101

Figure 69 - Schematic representation of the top-view electroplating gradient observed due to manual positioning errors (tilting). Colors represent the height of each specific area of the sample in relation to the minimum height registered for each sample. Compilation of profilometric measurements of the surface of samples EP C05-C09, averaged into one representation..... 102

Figure 70 - Microscopic inspection of samples: (a) EP C11; and (b) EP C12. The small dots represent the patterned holes created in the ma-P 1275 +PR. The black areas in the images consist of electroplated Silver that prolong above the sample surface (overplating). Cracks and deformations are observable in the images due to prolonged exposure to the electroplating solution at 55 °C..... 104

Figure 71 - Virtual representation of the complete electroplating support system designed in AutoCAD™ and created in a 3D Printer. The printed parts of the system are represented in the colors orange, red, blue and green. The grey color represents the Silver counter electrode. 105

Figure 72 - 3D printed support system (green and blue), with corresponding Silver electrode (grey) and a dummy die (red). On (b), the complete system is assembled and placed inside a glass cup. 105

Figure 73 - Graphic representation of the electrodeposition thickness versus the process time, for the conditions described in Table 13, plus sample EP C09 from Table 12. The electrodeposition thickness is calculated by adding the ma-P 1275 +PR thickness (of approximately 8 μm) to the overplating thickness measured in the Profilometer. 107

Figure 74 - Schematic representation of the top-view electroplating gradient observed. Colors represent the height of each specific area of the sample in relation to the minimum height registered for each sample. Compilation of profilometric measurements of the surface of samples EP D04-D08, averaged into one representation. 108

Figure 75 - Comparison between the surface topography obtained from the electrodeposition processes using: (a) the PMMA holding system; and (b) the 3D printed setup. Colors represent the height of each specific area of the sample in relation to the minimum height registered for each sample. Compilation

of profilometric measurements of the surface of samples: (a) EP C05-C09; and (b) EP D04-D08, averaged into one representation. 109

Figure 76 - EDS analysis of electroplated silver produced through Solution #3. Pure Silver is observed in the data spectra. 109

Figure 77 - Schematic diagram representing the cross-section view of the microfabrication step #15. Unlike the tests performed with the dummy samples, the electrical charge travels from the metallic layer deposited on the back of Silicon sample and through its matrix, emerging in the bottom of the microfabricated pits..... 110

Figure 78 - Microscopic inspection of samples EP E01 ((a) and (b)); EP E02 ((c) and (d)); and EP E03 ((e) and (f)). The empty pits are represented by small, uniform black circles, whilst the electroplated structures are represented by either larger, non-uniform black circles under 10× amplifications ((a), (c) and (e)), or by bright, non-uniform shapes under 50× amplifications. In (d) and (f), no empty pits are presented..... 111

Figure 79 - Schematic representation of the cluster dispersion (white circles) throughout the patterned silicon matrix (grey area). Description of the cluster’s sizes, distancing, and position in the matrix, in relation to the 4 borders of the patterned matrix..... 112

Figure 80 - Schematic representation of a single cluster of electrodeposited structures. The circles represent overplated structures, whilst the squares represent non-electroplated structures. Each cluster is formed by 5×5 to 6×6 individual structures in a circular-type shape. 113

Figure 81 - Schematic diagram representing the cross-section view of the dummy samples used for the optimization of the contact patterning. All pits were filled with a Silver electrodeposit according to the EP Dxx series tests. 115

Figure 82 - Microscopic inspection of a sample containing a patterned 8 μm thick ma-P 1275 +PR with electrodeposits of Silver: (a) after electrodeposition; and (b) after exposure at Alcatel SCM for the deposition of a 3000 Å of SiO₂, without pre-heating. The black areas in the images consist of electroplated Silver. 116

Figure 83 - Schematic diagram representing the cross-section view of the dummy samples used for the optimization of the contact patterning. All pits were filled with a Silver electrodeposit according to the EP Dxx series tests. Simulation of step #16 - Silicon Dioxide deposition..... 116

Figure 84 - Microscopic inspection of a sample containing a patterned 8 μm thick ma-P 1275 +PR with electrodeposits of Silver and a 3000 \AA SiO_2 layer on top: (a) heated at a temperature of 65 $^\circ\text{C}$; and (b) heated at a temperature of 85 $^\circ\text{C}$. The black areas in the images consist of electroplated Silver. 117

Figure 85 - Microscopic inspection of a sample containing a patterned 8 μm thick ma-P 1275 +PR with electrodeposits of Silver and a 3000 \AA SiO_2 layer on top: (a) before development at the SVG track; and (b) after development at the SVG track. The black areas in the images consist of electroplated Silver. 118

Figure 86 - Schematic diagram representing the cross-section view of the dummy samples used for the optimization of the contact patterning. All pits were filled with a Silver electrodeposit according to the EP Dxx series tests. Simulation of step #17 and #18 - Lithographical patterning of PFR 7790 G +PR in DWL technology and Vias etching for electrical contact access through Reactive Ion Etching of SiO_2 119

Figure 87 - AutoCAD™ image representing the profile patterned through Direct Writing Lithography for Step #22: (a) overall profile; and (b) detail on the patterned lines and pads. The red area on (a) represent the individual Silver electrodes, patterned previously. All measures and dimensions are represented in micrometers. Mask name: TMpH_frontcontact. 120

Figure 88 - Schematic diagram representing the cross-section view of the dummy samples used for the optimization of the contact patterning. All pits were filled with a Silver electrodeposit according to the EP Dxx series tests. Simulation of step #19 to #21 - Aluminum deposition through Magnetron Sputtering, Lithographical patterning of PFR 7790 G +PR in DWL technology and profile definition through wet etching. 121

Figure 89 - Patterned Aluminum lines and pads (grey) over an 8 μm thick ma-P 1275 +PR layer (red). The SiO_2 layer is transparent, and thus, unobservable in this image. 122

Figure 90 - Schematic diagram representing the cross-section view of the dummy samples used for the optimization of the structure release. 124

Figure 91 - Sample RS 01. Major deformation is observable due to the low adhesion between the PDMS and the Aluminum layer caused by the incomplete curing of the PDMS layer. 128

Figure 92 - Uniform heating step formed inside an oven with a simultaneous stress release process aimed inwards (a), compared to a differential heating gradient formed on top of a hotplate with a progressive stress release process aimed outwards (b). 129

Figure 93 - Samples RS 04 (a) and RS 05 (b). Major cracks and deformations are observable in both samples, as a consequence of the PDMS malleability during the release process..... 130

Figure 94 - Sample RS 06. After release, the sample coiled intensively, requiring the use of tweezers to stretch the coiled surface and place it on top of another layer of PDMS coated on glass. Through this method, the sample suffers severe deformation and cracking..... 130

Figure 95 - Samples RS 07 (a) and RS 08 (b). The increased stiffness of the material used in Sample RS 07 promoted a better adherence to the Aluminum layer and prevented the deformation of the substrate, allowing for a complete transfer of the pattern without deformations or cracks. In Sample RS 09, the increased malleability of the substrate caused cracks to form during the release process..... 131

Figure 96 - Samples RS 09 (a) and RS 10 (b). Due to the higher thickness of the PDMS in the border of the silicon samples, bonding did not occur homogeneously throughout the entire surface. In sample RS 11, the appliance of pressure after bonding allowed for a minor deformation of the glass in the center, approximating the two substrates and promoting the bonding in the contact area. 132

Figure 97 - Samples RS 11a (a), RS 11b (b), RS 11c (c) and RS 12 (d). With the exception of Sample RS 11c, all remaining patterns present deformations caused by a bad adhesion between the PDMS, the Aluminum layer and the Glass. Sample RS 11c only presents minor cracks in the bonded area. This improve in uniformity can be attributed to the pre-curing clamping of both substrates, forcing the dispersion of the liquid PDMS and promoting a better area coverage. 133

Figure 98 - Sample RS 14. Minor cracks are observed on top of the samples, possibly caused by non-uniform pressure during the degassing process. A small smudge is also located inside the sample, most likely due to improper cleaning of either the sample or the glass surface..... 135

Figure 99 - Sample RS 15. Minor cracks are observed on top of the samples, possibly caused by non-uniform pressure during the degassing process..... 135

Figure 100 - Samples RS 16 (a) and RS 17 (b). Major deformation is most likely caused by a low PDMS dispersion. By spin coating the PDMS, the total volume of PDMS is not enough to cover the entire topography of the samples and promote the complete adhesion between the Glass and the Aluminum layer..... 136

Figure 101 - Sample RS 18 (a) and RS 19 (b). Cracks are observed across the samples, likely caused by non-uniform pressure during the degassing process..... 137

Figure 102 - Exposed electroplated Silver μ Needles (squared structure on the center), with underlying layers of 3000 Å Aluminum, $\approx 20 \mu\text{m}$ PDMS and Glass. No cracks are observed..... 138

Figure 103 - Schematic diagram representing the cross-section view of the complete system consisting in patterned μ Needle Silver electrodes connected through an Aluminum pathway and protected by an insulating Silicon Dioxide double layer. In this schematic, the sacrificial ma-P 1275 +PR layer is removed through the use of Acetone in room temperature..... 139

Figure 104 - Schematic diagram representing the cross-section view of the complete system consisting in patterned μ Needle Silver electrodes connected through an Aluminum pathway and protected by an insulating Silicon Dioxide double layer. In this schematic, the transferred system is detached from the Silicon mold and is available for functionalization and use. 140

Figure 105 - SEM inspection of the released μ Needles (top view). The tips of the pyramids are missing, possibly due to breaking during the release process. The structures present a base width of around $12 \mu\text{m}$, in par with the results obtained previously during the profile definition of the ma-P 1275 +PR... 141

Figure 106 - Schematic diagram representing the cross-section view of the complete system, with insets focusing on the possible *mesa* (a) or hanging mask layer (b) formations blocking the release of the structure. 142

TABLE INDEX

Table 1 - Compilation of the Nernstian properties of pH sensors fabricated with different materials and methods. All measurements were performed at 298.15 K (25 °C). Table sorted by sensitivity (Nernstian Slope).	15
Table 2 - Process steps for the optimization of the lithographical patterning through Direct Writing Lithography. Complete Runsheet in Annex 1.	40
Table 3 - Description of the profiles scripted in the AutoCAD™ mask TMpH_array04.....	45
Table 4 - Process steps for the optimization of the structure definition through Silicon Wet Etching. Complete Runsheet in Annex 1.	47
Table 5 - Experimental conditions used in the definition of 10 μm × 10 μm wide pyramidal structures through wet etching. IPA availability represents the predicted time at when all IPA would evaporate. Adapted from [93].	53
Table 6 - Description of the profiles scripted in the AutoCAD™ mask TMpH_array04.....	57
Table 7 - Experimental conditions used in MTS cell proliferation assay. Samples A-C and X consisted in control cells. Samples D-F consisted in lysed cells, in which a minimum absorbance should be read. In samples H-L and N-R, weights were added along with the described structure. In samples S-W, the weights alone were placed on top of the cells, without any structure underneath.....	66
Table 8 - Process steps for the microfabrication of the proposed system. Complete Runsheet in Annex 5. Complete schematic of the process in Annex 6.	73
Table 9 - Experimental conditions used in the electroless deposition of Silver.	93
Table 10 - Experimental conditions used in the electrodeposition of Silver using Solution #2 (diluted Silver Iodide with Potassium Iodide and Calcium Nitrate).....	97
Table 11 - Experimental conditions used in the electrodeposition of Silver using Solution #3 (diluted Silver Nitrate and Ammonium in water).....	99
Table 12 - Analysis of the electrodeposition overplating thickness of samples EP C05-C10.	103
Table 13 - Experimental conditions used in the electrodeposition of Silver using Solution #3 (diluted Silver Nitrate and Ammonium in water) and topographical analysis of the samples surface	106

Table 14 - Experimental conditions used in the electrodeposition of Silver using Solution #3 (diluted Silver Nitrate and Ammonium in water), in the Through-Silicon-Electroplating process. 110

Table 15 - Topographical analysis of the samples surface in the center profiles. Non-electroplated structures are not considered for the calculation of the table values. 114

Table 16 - Experimental conditions used in the release of the patterned structures. 125

INTRODUCTION

Science has seen the development of novel tools, techniques and procedures through the development of Micro- and Nanotechnologies. In biology, these technologies have granted access to a new realm of manipulation of both the basic molecules of life and complex living systems alike. A particularly interesting area of convergence between these two areas is the use of Micro- and Nanotechnologies for the further analysis and study of living tissues, cells and cells metabolism [1].

The miniaturization of complex devices, as well as the fabrication of completely new, and so thus far unavailable, Microelectromechanical Systems (MEMS), have offered access to substantially greater details of cellular and metabolic processes, when compared with traditional techniques. These systems also have a particular interest in medicine, supplying tools to doctors and practitioners to aid them achieve a better diagnostics and treatment with greater accuracy, better information and reduced diagnosing time.

MEMS can be fabricated with active dimensions in the same order of magnitude, or even smaller, than complex biological systems, such as a biological cells or tissues. These systems can be functionalized with bioactive micro- and nanoscale structures that offer a new insight to the metabolic conditions inside individual cells, either for scientific research, or for medical diagnosis [1, 2].

A new research focus has been applied to new systems that can analyze the intracellular environment of a biological cell (the cytoplasm). Intracellular sensing devices can provide a better understand of the cells internal state, of their physiological processes on how they interact with stimuli [3-12]. The intracellular analysis of single cells can also be used to assist in the characterization of complex dynamic systems, either for the research into heterogeneous living cell populations, or as a tool to detect and diagnose metabolic imparities inside tissues [11, 12].

Sensor miniaturization has also led to an improvement in response time, enhanced analytical performance, improved signal-to-noise ratio and increased sensitivity, when compared with conventional systems [12, 13].

Intracellular analysis can be performed mainly through two different approaches: by optical analysis of reactive bio-active compounds, or by cell penetration of bio-active MEMS.

The first process is widely known and used in all related scientific fields. A bio-active compound (usually referred as a biomarker) is inserted inside a living cell either through standard pathways (such as diffusion or active membrane transport) or through artificial methods (such as cell penetration techniques, lysosomal delivery systems, etc.). Inside the cytoplasm, the biomarker reacts to a given sensitive condition, modulating the optical output that can be read by spectrophotometric techniques. This method is widely applied for monitoring a series of complex cellular behavior by targeting specific biochemical molecules, but has limited use in the analysis of simple biochemical reactions, is considerably expensive for most cases, and may require a complex optical analysis apparatus [6, 14-18].

Although more complex in nature, bio-active MEMS with cell penetration capability can provide a unique response for the limitations found in the previous method. The bio-active structure of these systems is usually composed of a solid supportive structure (usually made of Silicon or Glass) functionalized with an active layer that reacts to electrochemical changes in the environment with an electrical response that can be measured by low-cost and miniaturizable apparatus [8-11, 19-21].

Cell penetration can be achieved through either membrane perforation or electroporation. Membrane perforation is a well-known technique adapted for IVF (in-vitro fertilization) and other research techniques. It consists in the manual penetration of the cellular membrane through a sharp micrometric needle (usually with a diameter equal or inferior to 5 μm , varying with the specific cell dimension and elasticity) [8-11, 19-21].

Electroporation, specifically, LOMINE, or Local Micro-Invasive Needle Electroporation, is a recently spread technique that promotes cell penetration for pharmacological delivery, cell ablation or intracellular analysis. A micrometric electrode (or needle) is positioned at the boundary of the cell membrane. An electrical pulse is applied between a micrometric electrode and the cytoplasm of a single cell. This electrical field overcomes the binding forces of the phospholipids forming the cell membrane and disrupts their cohesion. The phospholipids automatically reassemble around the electrode, ensuring the necessary sealing that prevents a cytoplasmic leaking. Although the concept is well known for several decades, more recent studies have focused on the application of this technique for intracellular analysis, optimizing the appropriate parameters for reversible, non-damaging electroporation of micro-fabricated sensors [8, 22-24].

Monitorization of intracellular environmental changes can assist in the diagnosis of metabolic imparities that can be attributed to a series of diseases. Recent studies have suggested that slight

metabolic changes, either as cause or consequence of, can lead to physiological abnormalities in human cells. A specifically interesting metabolic condition that has shown to be correlated with abnormal cell growth in humans, mainly in the formation of tumors, is the pH balance inside and outside cells. Therefore, pH can be used as both a marker and a tool for diagnosis and treatment of tumors [25-30].

The identification of most tumors can be achieved through a different set of imaging techniques. However, confirmation is always accomplished by microscopic, chemical and biological analysis of biopsies and requires specialized professionals to process and analyze the results in a pathology lab, which could take hours or days [31].

Recent studies have demonstrated the possibility for MEMS devices to penetrate individual cells and analyze the intracellular environment, namely for pH [12, 21, 32], or ionic imbalance characterization [3, 4, 33, 34]. However, these systems are designed for single-cell analysis, and cannot yet provide a complete analysis of an entire sample, such as a biopsy. MEMS devices designed for simultaneous analysis of the intracellular environment of a wide set of cells could provide more reliable information regarding the internal conditions of tissues.

A multi-layer detection system that could combine optical and chemical analysis of tissues, providing accurate results with haste for medical practitioners, could perform an important role in the detection of metabolic imbalances in routine check-ups where biopsies were taken.

Such a system could also be applied during surgical procedures in which tumors are removed. Having this tool at their disposal, surgeons can make an informed decision as to how far to excise tissues in order to confidently remove all tumorous cells. If, whilst in surgery and after a tumor is removed, a surgeon can perform a fast analysis of the surrounding tissues, the risk of relapse can be drastically reduced, reducing the need for further procedures.

In this thesis, the ambition is to develop a novel tool for in-vitro cell diagnosis, based on *micrometric needles where pH sensors can be integrated*. The measurement of pH at a cellular level is a non-complex chemical measurement that can provide information on the metabolic status of a given cell and can be correlated with abnormal cell growth in humans [25-30]. Therefore, this is the parameter we have chosen to be monitored with these needles.

Towards this objective, we developed and optimized the microfabrication protocol to realize a *solid-state micrometric array of Silver electrodes*. The entire system was then transferred to a clear glass substrate, providing compatibility, and allowing integration with subsequent lab-on-chip components, mainly optical processes for further biological and chemical analysis. A schematic is shown in Figure 1, with the silver needles.

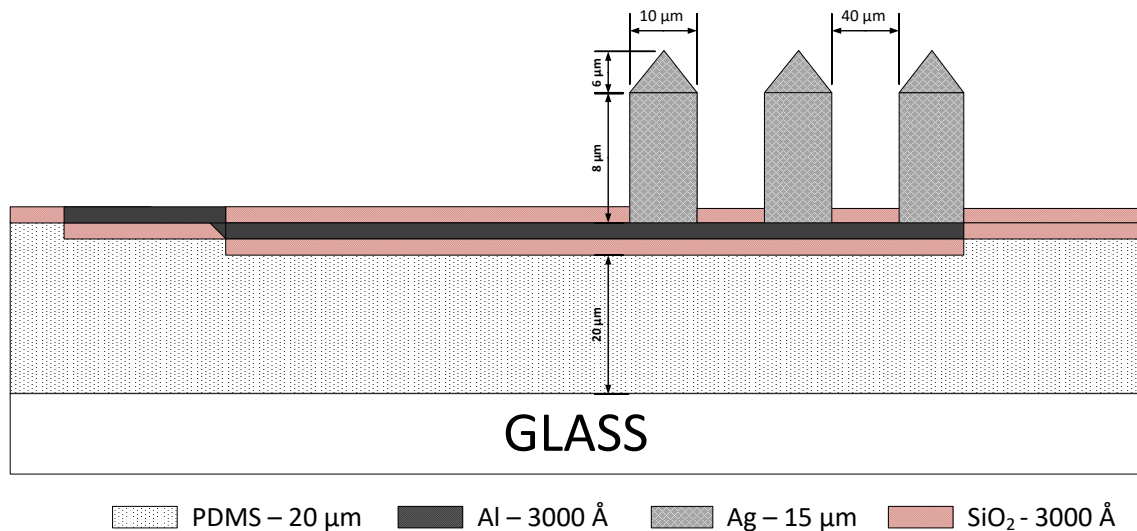


Figure 1 - Diagram of the microfabricated solid-state micrometric array of Silver electrodes, with Aluminum interconnections for electrical readout. The structure is supported by a flexible elastomer (PDMS) over a glass substrate so to enable further integration with microfluidics and other lab-on-chip components.

This work was performed using the Clean Room facilities at INESC-MN due to the unique equipment, expertise and know-how accumulated over the past 30 years in the areas of devices and advanced materials. This thesis describes novel methodologies which are combined with the existing set of Micro- and Nanofabrication techniques, allowing for a greater and unique fabrication output, particularly in removing dimensional constraints in profile patterning and reducing the processing time for most steps. The thesis is organized in 4 chapters:

Chapter I: Here, the concepts involving the measurement of pH are described. A correlation between pH variation and cellular metabolism is also explored in this chapter.

Chapter II: In this chapter, a theoretical description of the main methodologies is presented. Only the novel techniques and the crucial processing steps are explored, as all remaining processes are considered to be standard microfabrication techniques.

Chapter III: The research applied in the optimization of the processing steps is for the fabrication of the proposed system described in this chapter. The results are presented along the description of the optimization taking place, as both are directly correlated.

Finally, **Chapter IV** includes a summary of the work and most relevant results. The future research involving this work is suggested to be an in-vitro study of cell penetration and pH measurement so to adjust the system for intracellular analysis of cellular metabolism in human cells.

CHAPTER I

THEORETICAL CONCEPTS

PH THEORY

PH AND HUMAN CELLS

PH SENSORS

PH SENSORS FOR INTRACELLULAR MEASUREMENTS

CHAPTER I - THEORETICAL CONCEPTS

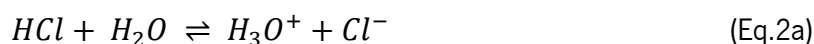
1.1 - pH theory

Water is the base molecule from which all biological reactions are dependent on. In its natural form, H_2O , it has a neutral electrical charge which allows acting as a solvent. However, water molecules can react with their surroundings, gaining or losing Hydrogen atoms, H^+ , and thus forming hydronium, in the form of H_3O^+ , or hydroxide, in the form of OH^- , as described by Equation 1, [35].



In a specific solution, the balance between H_3O^+ and OH^- molecules defines its *potential of hydrogen*, commonly known as **pH**. In pure water the hydronium ions are all neutralized by hydroxyl ions, which results in a solution with a neutral pH value. However, if the solution has a higher concentration of H_3O^+ atoms, it is considered *acidic*, whilst a higher concentration of OH^- atoms causes it to be considered *basic* [35].

Water molecules can both influence and be influenced by the remaining chemical species dissolved. Certain molecules can release or absorb hydrogen ions, or protons, when in contact with water, thus turning the solution either acidic (Equation 2a) or basic (Equation 2b), [35].



The pH measurement is defined by the negative logarithm of the activity of the H_3O^+ ion. For most applications, the activity correlates to the concentration of the ion and can be simplified by Equation 3. To bear in mind that minute changes in the pH value reveal exponential variations in the ionic balance of water molecules [35].

$$pH = -\log[H_3O^+] \quad (\text{Eq.3})$$

Since the concentration of hydronium and hydroxyl ions can be correlated by Equation 4, a dissociation constant, K_w can be written as the following [35]:

$$K_w = \frac{[H_3O^+][OH^-]}{[H_2O]} = [H_3O^+][OH^-] = 10^{-14} \text{ mol/L (25°C)} \quad (\text{Eq.4})$$

Through this, a conventional range from 1~14 can be observed in most pH scales for aqueous solutions. In equilibrium, when $[H_3O^+] = [OH^-] = 10^{-7}$ mol/L a pH value of 7 is obtained. Consequently, higher concentrations of H_3O^+ ions will drop the pH value below 7, whilst lower concentration values will raise it [35].

For more accurate measurements, the activity of H_3O^+ ions is used in the determination of a given pH sample, as described in Equation 5. Besides its concentration, given by the molality ($b = \text{mol/kg}$ solvent), an activity coefficient (γ_{H^+}) needs to be taken into consideration [35].

$$a_{H^+} = \gamma_{H^+} \cdot b_{H^+} \quad (\text{Eq.5})$$

The activity coefficient itself combines the effect of various factors, such as temperature, total ion strength, the dielectric constant, ion charge, the size of the ions (in Angstrom) and the density of the medium. One of the main effects to consider when performing pH measurements is called the *salt effect*. Dissolved salts can affect several of the factors influencing the activity coefficient, thus causing minor changes in the final measured pH.

Temperature also plays an important role in modulating the electrical response to pH variations (later seen in Equation 9 and 10 in Sub-Chapter 1.3). However, and for the applied system, this factor may not be of great influence since all measurements would be performed in biological samples that, by definition, require a specific temperature range to survive. Further analysis is required to infer about the temperature loss of excised cell tissues, the influence of room temperature in those cells and in the

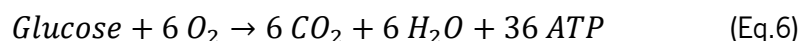
intracellular electrical measurements. Albeit, this research is beyond the scope of this thesis and will not be considered during its course.

For biological samples, other factors that may affect pH measurements have less impact, thus being disregarded in this study.

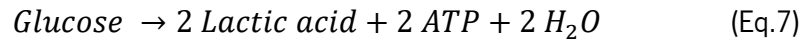
1.2 - pH and human cells

Human cells tend to regulate their internal and external environment to great extent, as they can only survive inside a narrow range of conditions, one of which being the pH. Changes in the environment pH of proteins can cause them to protonate or deprotonate, drastically changing their shape and function, which may lead to a fatal death for both the cell and the organism.

The pH of a given cell is affected mainly by its activity, namely through energy-based processes such as *respiration*. Under normal conditions, human cells undertake a process named *cellular respiration*, in which glucose, a molecule, is converted into biochemical energy in the form of adenosine triphosphate (ATP), consuming oxygen and releasing water and carbon dioxide in the process. The complete reaction can be summarized in the following Equation 6, [36]:



However, an increase in cellular metabolism forces the consumption of a growing amount of energy. Without the necessary means to release the waste products, or to incorporate more oxygen, the cellular respiration process can't occur with the same degree of efficiency. When that situation is presented, the cells can compensate by obtaining energy through either *anaerobic respiration* or *fermentation*. In either case, the glucose molecule is not completely decomposed into water and carbon dioxide. Instead, the cycle breaks after the complete glycolysis of glucose into *pyruvate*, which is then reduced to 2 *lactic acid* molecules through *lactate dehydrogenase* enzymes Equation 7, [36]. This last step is crucial in order to allow for the process to be restarted by regenerating the internal NAD^+ oxidizing agent and allowing for more glucose molecules to be processed. However, the lactic acid produced as waste acidifies the intracellular environment and can jeopardize protein function [30].



Prior to cancer, cells may undergo a stage of *neoplasia*, either by *hyperplasia* or *dysplasia*, in which abnormal changes in either number or shape of the cells, respectively, may be observed. Increased cellular activity and metabolism are two of the factors that may be used to detect these abnormal changes before cells fully transform into aggressive stages of tumors or cancer.

To maintain their intracellular environment stable, allowing for proteins to preserve shape and function, cells with increased respiratory rates that undergo lactic fermentation need to export an increasing amount of lactic acid, ejecting it into their extracellular environment. A study has shown that in order to survive and thrive, cancer cells perform exactly in that matter, being able to maintain a neutral intercellular environment (between 7.0 and 7.2 pH) whilst acidifying their extracellular environment (dropping it to 6.8 pH) [30]. Furthermore, evidences suggest the possibility to use pharmaceutical controlled release techniques based on specific pH patterns related with malign tumors or cancer cells [37, 38].

Eventually, tumor cells may develop a stage of *angiogenesis*, consisting in the creation of new blood vessels and capillaries surrounding their cells in order to maintain a prioritized supply of oxygen and nutrients, whilst being able to quickly remove the growing amount of waste products [39]. However, for cells in an early stage of neoplasia, the detection of small changes in the pH, both internally and externally, could provide a crucial tool for early cancer detection and treatment.

1.3- pH sensors

The ability to detect and measure pH is typically performed through electrical comparison between a sensor electrode (sensible to variations in the chemical concentration of H⁺ ions) and a stable reference sensor electrode (which is not), as a single electrode itself cannot perform the required electrical measurement. The galvanic potential between the two electrodes is therefore a function of the hydrogen ions concentration in the solution, given by the Nernst Equation (Equation 8) [35]:

$$E = E_0 + \frac{2.3RT}{nF} \cdot \log[a_{\text{H}^+}] \quad (\text{Eq.8})$$

Where E is the measured potential, E_0 is the standard potential, a_{H^+} is the activity coefficient for the H^+ ions (which for biological conditions can be read as the concentration in the solution), R is the universal gas constant, T is the Temperature in Kelvin, n is the number of electrodes transferred in the reaction and F is the Faraday constant.

Simplifying the terms in the Nernst Equation we can derive that:

$$\begin{cases} pH = \log(a_{H^+}) \\ 2.3 \cdot \frac{R \cdot T}{F} = k \cdot T \end{cases} \quad (\text{Eq.9})$$

And finally, we can obtain the following Equation:

$$E = E_0 - k \cdot T \cdot pH \quad (\text{Eq.10})$$

Through this mathematical expression we can infer that the measured electrical potential is linear to the solution pH, with a slope defined by $-kT$ and a deviation defined by the standard potential, E_0 .

To properly define and compare different electrode and reference systems, the Standard Hydrogen Electrode (SHE) was introduced as a universal reference electrode [40]. This system consists of a platinum sheet immersed in a solution of $a_{H^+} = 1.0$ and surrounded by hydrogen gas at 1 bar. At any given temperature, the SHE potential is always 0. Potentials of all other measurement systems are compared with that of the SHE at the same temperature, and defined as the standard potential, E_0 , for that system.

However, a standard galvanic electrochemical sensor supplies a combined electrical potential as a result of a series of internal potential points, as seen in Figure 2. To achieve and maintain a stable sensor, it's crucial to ensure that all internal potentials, with the exception of the membrane sensitive potential, are stable and can't affect the measurements in the defined conditions. In the showcase, a working and reference electrode are combined into the same system. A potential is measured between the working and reference electrodes on the top. Immersed in a solution, a diaphragm, or junction (defined in potential E_6) allows for an ionic pathway to be conducted between the reference electrode and the solution. At the working electrode, a sensitive membrane allows for a response to different H^+ activities.

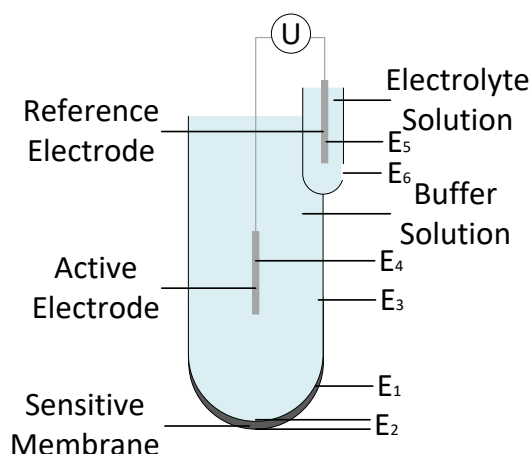


Figure 2 - Diagram of a standard galvanic electrochemical sensor. Description: E1 - Selective membrane potential; E2 - Asymmetry potential; E3 - Internal potential; E4 - Surface potential at the working electrode; E5 - Surface potential at the reference electrode; E6 - Diffusion potential.

In order to achieve a stable and reliable system, a few conditions should be met. If both electrodes are made from the same materials, and have similar electrical properties, then E_4 and E_5 cancel each other. Ensuring that no changes occur in the internal solution of the working electrode (usually referred as the inner buffer solution), such as leaks or contaminations; therefore, we can discard fluctuations in the E_3 potential as well. Although changes at the sensitive membrane, such as limitations to the ionic flux derived from differences of the membrane thickness may be observed when comparing different systems, internally, and during the lifetime of the system, they should remain constant. If so, the asymmetry potential, E_2 , should not influence the measurements as well. Finally, the diffusion potential is a result of the difficulty of the ionic flux between the electrolyte solution and the measured solution, through the diaphragm/junction. Ensuring that no clogging of the diaphragm/junction occurs, and that the internal electrolyte solution is not contaminated, allows for a steady diffusion potential across measurements.

Once these conditions are met, any variation in the measured potential is a result in the variation of the selective membrane potential, sensitive to H^+ ions, and can, therefore, supply a reliable pH value.

1.4 pH sensors for intracellular measurements

The common glass electrode, shown before in Figure 2, is proven ineffective for intracellular measurements due to size constraints, as the large bulk structure of the glass shell prevents cell penetration [12, 35]. To overcome this condition, two approaches have been pursued:

a) **Optical measurement of pH-sensitive molecules.** Most of the current methodologies used in this approach imply the use of a fluorescent pH-sensitive molecule that, once introduced inside the cell, can be detected and measured as a correlation between fluorescent signal intensity at a specific wavelength and the pH value. Despite the amount of research invested in this method, the entire apparatus and reagents remain complex and costly for standard applications [5, 7, 41];

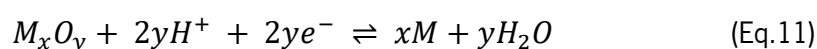
b) **Solid-state microelectrodes.** With this approach, small scale electrodes are fabricated and coated with a pH-sensitive layer, thus discarding the need for internal buffer solutions. These microelectrodes still present challenges in the microfabrication process and are characterized by having high electrical impedance. However, once manufactured, these electrodes could present a viable, cheap and long-term usage in the field [42-49].

Both applications have their own advantages and limitations. However, when looking for a device that can provide fast results and in the absence of specialized personnel or resources, a system consisting of an array of microelectrodes could be better appropriated. Furthermore, when analyzing complex samples, such as non-laminated tissues, optical systems may face additional challenges when obtaining results from multi-layer tissues, as the biological markers can, and will, penetrate all cells. Microelectrodes, though, only penetrate a limited number of layers, defined by their height, and therefore, should be more reliable when comparing samples from different sources.

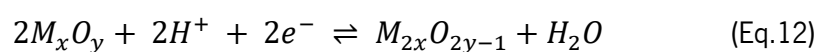
Although similar in concept, solid-state microelectrodes can be defined as Metal-Oxide or Metal-Metal Oxide electrodes, depending on the reaction that defines their potential-pH response. Under optimal conditions, these electrodes respond to pH in a Nernstian slope [48, 50]. The system includes one electrode to act as a reference, insensitive (or considerably less sensitive) to pH changes, and a primary electrode to act as a sensor (working electrode), providing an electric potential as a measure of pH.

b.1) Metal-Metal Oxide electrodes

Solid-state microelectrodes, specifically, metal-metal oxide electrodes are based in redox (reduction-oxidation) steps as the mechanism to react to the pH of their environment. Depending on the solution alkalinity/acidity, a metal element “*M*” can be a donor or receiver of Oxygen. Initial metal oxidation can be achieved by different techniques: thermal oxidation, electrolytic oxidation or sputtering. However, oxidation of the bulk material should be avoided entirely, as it drastically affects the internal electrical resistance and can limit the electrode potential response [49-53]. Equation 11 describes the interaction between these types of electrodes and water.

**b.2) Metal Oxide electrodes**

In solid-state metal oxide electrodes, redox reactions are also employed in pH measurements. However, in this case, a metal oxide/metal oxide (higher and lower valency) couple is involved in the pH-dependent response, rather than the complete oxidation/reduction of the electrode surface. The electrode usually displays a slightly non-stoichiometric composition in order to facilitate electronic conductivity. Fabrication of these electrodes can be achieved through the following techniques: thermal decomposition, cyclic voltammetry assisted electrodeposition or sputtering [49-53]. Equation 12 describes the interaction between these types of electrodes and water.



A vast array of metal oxides have been studied for their pH-response, such as IrO₂ [43, 52], Sb₂O₃ [50], PdO [50], SnO₂/Al [54], GaN [55], Al₂O₃ [56-59], Ta₂O₅ [60-63], ZrO₂ [64-66], among others.

A compilation of the pH response of some of these materials is compiled in Table 1. Not only the material, but also the method of fabrication, can influence both the Standard Potential (Potential measured at pH = 0 (or extrapolated to that point) against the Standard Hydrogen Electrode) and the Nernstian Slope (electrical response per unit of pH).

Table 1 - Compilation of the Nernstian properties of pH sensors fabricated with different materials and methods. All measurements were performed at 298.15 K (25 °C). Table sorted by sensitivity (Nernstian Slope).

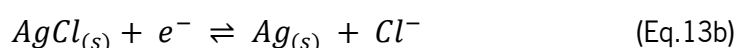
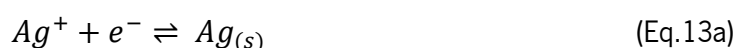
Material / Method	Standard Potential (mV)	Nernstian Slope (mV)	Reference
IrO ₂ (electrodeposition)	670 - 710	66 - 69	[43]
IrO ₂ (thermally deposited over a Ti support)	902 - 950	59	[67, 68]
TiO ₂ (thermally deposited over a Pt support)	642	59	[68]
Pt (oxidation)	982	59	[68]
ZrO ₂ (oxidation)	487	58.22	[66]
SnO ₃ /Al (RF sputtering)	1070	58	[54]
GaN/Ga ₂ O ₃ (sputtering / oxidation)	270	56.44 - 57.75	[55]
Ta ₂ O ₅ (RF sputtering)	1110	56-56.16	[63, 69]
Al ₂ O ₃	440	53.23	[59]
HfO ₂ (RF sputtering)	N/A	54.6	[69]
Si ₃ N ₄ (RF sputtering)	N/A	52.8	[69]
SiO ₂ (RF sputtering)	N/A	36	[69]

As presented in Table 1, most materials present a sensitivity (mV/pH) very close to the Nernstian slope of 59.16 mV/pH at 298.15 K, as derived previously from Equation 10. Some materials, or their manufacture process, allows even for a super-Nernstian response to be achieved by registering a sensitivity higher than the theoretical value of 59.16 mV/pH [70]. As seen from most materials displayed in Table 1, sensitivities do not vary significantly and all are compatible for the measurement of decimal pH variations. However, if higher sensitivity is required, which may be the case in this thesis, materials that display a super-Nernstian response should be sought after as potential candidates for final implementation.

b.3) Reference electrode

The potential of the reference electrode system is defined by the reference electrolyte and the reference element (the material consisting of the electrode itself). It's through a saturated concentration of a stable reference electrolyte solution that the reference electrode is able to provide a stable and consistent potential to compare with the working pH-sensitive electrode.

Most common reference electrodes for small quantitative analysis (including cellular measurements) are made of a silver (Ag) electrode, either in the form of a wire or solid-state microelectrode, covered by a layer of silver chloride (AgCl). The corresponding half-reactions of the electrode can be described as followed in Equation 13a and 13b:



When simplified, the reaction can be described as:



Through a concentrated electrolyte solution of potassium chloride (KCl), a steady supply of potassium and chloride ions can diffuse through the system without drastically change its concentration, allowing for electrons to be transferred in a controlled environment.

The contact with the external environment, from which the pH measurements are performed, usually occurs through a junction or diaphragm. This is a small opening that allows for an ionic pathway to be established between the reference electrolyte and samples to be measured, but with controlled ion mobility as to not affect the internal concentration. Ions possess specific mobility and diffuse through this junction in a determined velocity in accordance with their charge and size, considering its hydration cover. This means that small ions, such as lithium, that are highly hydrated, move slower than larger ions, such as potassium, that is only slightly hydrated. The electrolyte solution should be consisted of an ionic pair with similar ionic mobility, as to prevent a potential to be formed at the

junction during potentiometric measurements. K^+ and Cl^- ions present a similar mobility, of $7.62 \times 10^{-8} \text{ m}^2 \cdot \text{s}^{-1} \cdot \text{V}^{-1}$ against $7.91 \times 10^{-8} \text{ m}^2 \cdot \text{s}^{-1} \cdot \text{V}^{-1}$, respectively, at a temperature of $25 \text{ }^\circ\text{C}$ [71].

Different junction systems have been proposed and implemented commercially [72-76]. Some of these examples are the ceramic, sleeve, or open junctions. Each present specific advantages and limitations, according to the desired application. However, they may not be completely suitable for integration in a solid-state microelectrode system. An alternative method consists in the use of the capillary effect in polymeric microfluidic structures with a long ionic pathway. Due to the high surface tension of liquids inside microfluidic structures, dilution occurs at a slower rate, mostly due to diffusion [77, 78].

For micrometric applications, solid-state reference electrodes have been developed, with the Silver/Silver Chloride reference electrode presenting the easiest fabrication processes, whilst still being environmentally friendly. Although still not as reliable as conventional reference electrodes, some solid-state reference electrodes can be modulated and adapted to specific conditions, overcoming a few of the limitations regarding hydration, selectivity or long term stability [79, 80].

CHAPTER II

METHODOLOGIES

SILICON MICROMACHINING

SILICON WET ETCHING

ELECTRODEPOSITION

CHAPTER II - METHODOLOGIES

2.1- Silicon Micromachining

In order to achieve cell penetration capability, protuberant microelectrodes were envisioned to act in potentiometric pH analysis. The working electrode would consist of a microfabricated Silver microelectrode, functionalized with a pH-sensitive layer, whilst a reference electrode would be incorporated as a solid-state Ag/AgCl electrode immersed into a saturated KCl solution to ensure stability.

In a matrix, Silicon (Si) presents an FCC (*Face-Centered Cubic*) crystalline organization, where each unit cell is formed by 6 peripheral atoms coinciding with the center of each face of the cell, and 4 intrinsic atoms connecting the structure internally. The structure is replicated in all directions, forming a crystalline network, as shown in Figure 3.

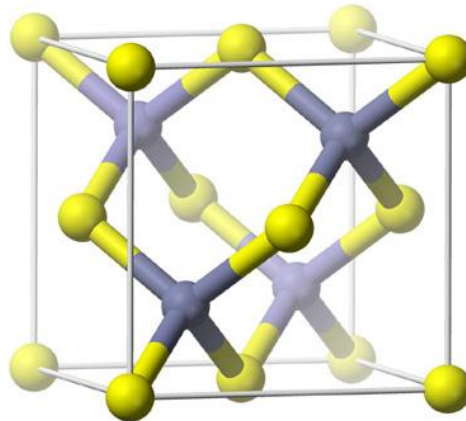


Figure 3 - Tridimensional representation of the crystallographic organization of Silicon atoms in a matrix. Grey dots represent inner atoms. Yellow dots represent atoms in plane [81].

Si micromachining (or Si etching) consists in the patterning removal of superficial Si atoms that are exposed to an etchant condition. A pattern is initially created on top of the sample surface through a lithographic process of a light-sensitive polymer (photoresist). However, standard photoresists used in the lithographic process for the pattern definition are usually affected by Si etching conditions.

To overcome this problem, the pattern can be transferred from the photoresist to a previously deposited masking layer, which in turn is unaffected by the etching conditions. Masking layers are

generally consisting of thin-films that are easily patterned by conventional microfabrication steps, such as lift-off, dry or wet etching. The specific patterned profile of the masking layer allows for only certain areas of the Si surface to be exposed to the etchant conditions, thus transposing the desired pattern [82].

Si etching usually requires the removal of large amounts of material from the Si matrix, which translates in long or highly energetic etching process. Due to this requirement, non-reactive dry etching techniques (such as sputtering etching) are not available, as they are characterized by generally-non-selective, small etching rates, that would not only require for a long etching period, as it would also etch the entire masking layer before the desired underlying Si pattern could be achieved [83].

Microfabrication of micrometric profiles in the Si matrix is, therefore, restricted to either: a) Reactive Ion Etching; or b) Wet Etching techniques.

Reactive Ion Etching (RIE) is a dry etching technique that applies the use of a Radio Frequency (RF) power source to form ionized reactive plasma that selectively targets exposed Silicon atoms. Standard RIE is an isotropic process that promotes a clear under-etch profile beneath the masked layer as a consequence of multidirectional reaction targeting from the plasma. This process can be of great interest in the formation of sharp tips, as the etching process is stronger near the surface of the sample, rather than in depth. However, isotropic etching promotes a widening of unused (etched) areas, especially for deep etching profiles [84], as illustrated further in Figure 5-B.

Anisotropy is achieved when different planes are etched at different rates. Direct manipulation of the etching profile can be achieved by protecting specific planes whilst others are etched. A practical example of this process is the Deep Reactive Ion Etching (DRIE) technique, demonstrated in Figure 5-A, which was developed for high depth etching without compromising the profile lateral dimensions. The most successful DRIE technique developed is the Bosch process [85]. In this microfabrication step, alternating cycles of standard isotropic RIE and passivation with an inert layer are used to protect the side walls, as the etching process is directed downwards through directional ion bombarding. This process can fabricate nearly vertical walls, which can then be sharpened with conventional RIE [11], as demonstrated in Figure 4. However, this process still requires considerable spacing between profiles, competing against the need for deeply compacted arrays of micrometric needles.

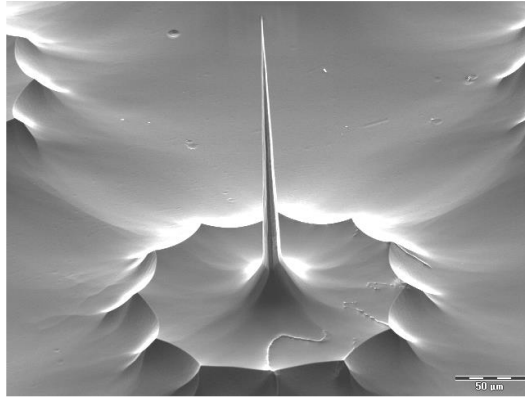


Figure 4 - RIE-sharpened silicon needle 230 μm tall and with a 200 nm wide tip. Authorized use by [11] ¹.

Silicon Wet Etching is a strictly chemical process that involves the use of a liquid etchant in the removal of exposed areas of the sample. Due to the Silicon crystal organization, the atoms in the different crystallographic planes possess different energetic levels, from which results the anisotropy of *Etching* processes in aqueous solutions, denominated by *Wet Etching*. This has been widely studied by other authors [86-89]. Depending on the crystalline orientation of the Silicon surface, and the materials used in the etchant solution, isotropic or anisotropic profiles can be obtained.

Isotropic Etching of Silicon is achieved by the constant oxidation of superficial atoms by dispersed Nitrogen Dioxide (NO_2), followed by etching through diluted Hydrofluoric Acid (HF). This procedure results in a symmetric etching pattern in all directions, as seen in Figure 5-B. This is an inexpensive, simple and highly selective process. However, the use of HF requires careful handling due to possible health hazards resulting from skin exposure, inhalation or reaction with secondary materials [90]. Furthermore, microloading effects can be aggravated due to the spatial competition of NO_2 and HF for tightly compacted active areas.

Another strategy for the fabrication of anisotropic structures in Silicon substrates is the use of the Silicon crystallographic structure to modulate the etching rate. Therefore, different planes are etched at different rates, forming non-rectangular shapes. An example of this process can be seen in Figure 5-C. For most Anisotropic Wet Etching processes, Potassium Hydroxide (KOH) is quite popular due to its low cost, low toxicity and ease to handle [86, 91]. Other etchant solutions, such as those containing organic compounds like Tetramethyl Ammonium Hydroxide (TMAH), have been demonstrated to produce better

¹ Reprinted from Journal of Micromechanics and Microengineering, Vol 13 / Number 4, Y Hanein¹, C G J Schabmueller¹, G Holman¹, P Lücke¹, D D Denton¹ and K F Böhringer¹, High-aspect ratio submicrometer needles for intracellular applications, Copyright (2003), © IOP Publishing. Reproduced with permission. All rights reserved

smoothness and lower roughness for the same process. However, they are considerably more costly and in most cases neurotoxic, thus presenting a huge health risk that requires the appropriate safety measurements [89, 91, 92]. To simplify the process and limit exposure to hazardous conditions, KOH was selected as the active etchant used in the micromachining of Si.

The different etching profiles can be observed in Figure 5.

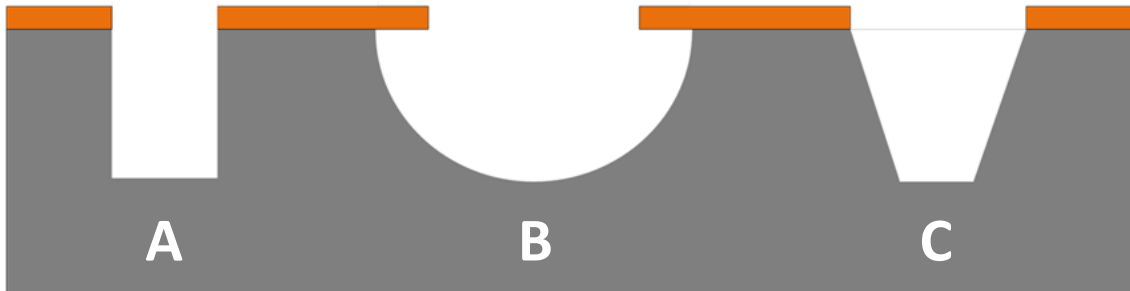


Figure 5 - Etching profile obtained by: A) Anisotropic RIE; B) Isotropic RIE or Wet Etching; C) Anisotropic Wet Etching (right).

2.2 - Silicon Wet Etching

The process at which KOH removes silicon atoms, through the nucleophilic reaction of Hydroxide radicals (OH^-), is well described in the literature [86]. The number of atoms at the surface of each crystallographic plane, as well as the energy of the specific atomic bond formed with the underneath atomic layers, play a crucial role in the definition of the etch rate. For this thesis, $\langle 100 \rangle$ oriented Silicon wafers are used in all processes. These have pronounced etching in the $\{100\}$ and $\{111\}$ planes, and as such, those will be discussed in further detail.

Etching in the $\{100\}$ plane

In this crystallographic plane, Si surface atoms are connected to 2 subjacent atoms through $\sigma(\text{Si-Si})$ backbonds, each filled with 2 electrons. However, the Si atom at the surface possesses a $3p(\text{Si})$ orbital fill with only 2 electrons, having the capacity to form 2 new bonds. Due to the high nucleophilicity of OH^- ions, one of their electrons can be transferred to the $3p(\text{Si})$ orbital through the Helmholtz layer. Such electric transfer allows for the pairing between a OH^- radical and the Si atom, forming a $\sigma(\text{Si-O})$ bond and filling the $3p(\text{Si})$ orbital with the remaining missing electrons. Through thermal excitation, one

3p(Si) orbital electron is shifted to the conduction band, thus allowing for a second OH⁻ radical to bond to the same Si atom, forming the Si(OH)₂⁺ complex [86].

Due to the high electronegativity of the oxygen atoms, the $\sigma(\text{Si-O})$ bonds possess a superior bond energy than those of the $\sigma(\text{Si-Si})$ bonds: 193 kcal/mol against 78 kcal/mol. This allows the shift of the $\sigma(\text{Si-Si})$ orbitals to a higher level, $\sigma(\text{Si-Si})'$. The thermal excitation of 2 electrons from these orbitals into the conduction band, combined with the presence of two other OH⁻ ions, leads to the formation of a silicon-hydroxide complex. This molecule ends up dissociating from the Si matrix, releasing 2 H⁺ ions due to the high pH (above 12), converting in a SiO₂(OH)₂⁻ molecule [86].

The excess electrons in the conduction band can then be transferred into the water molecules located around the surface of the wafer, dissociating the molecules into OH⁻ ions and hydrogen atoms, which therefore can recombine into molecular hydrogen (H₂). Whilst the hydroxide ions are reused in the etching reaction, the hydrogen ions can diffuse into the interior of the Si matrix, and particularly into the vicinity of the $\sigma(\text{Si-Si})$ bonds of the surface atoms, weakening them and assisting in the removal of the Si(OH)₂⁺ complex [86].

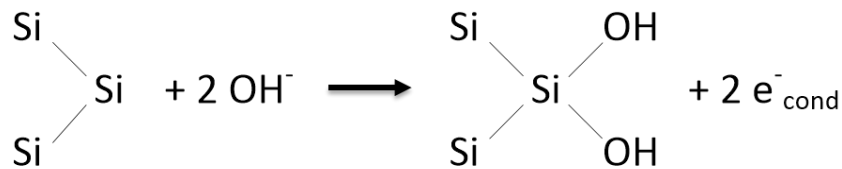


Figure 6 - Schematic diagram representing the chemical structure of the Silicon surface atoms and respective binding of hydroxide ions during a wet etch process for {100} silicon wafers.

Etching in the {111} plane

The etching process in this plane is similar as that described previously. However, the network crystalline orientation implies that each Si surface atom is connected covalently to 3 other Si atoms, forming 3 $\sigma(\text{Si-Si})$ bonds. Therefore, only one OH⁻ ion can be attached to the Si atom, projecting the $\sigma(\text{Si-Si})'$ bonds to a lower level than that of the {100} plane. Through this, the etching rate in the {111} is considerably slower, forming an incline profile towards the {100} plane with an approximate angle of 54.7° [86].

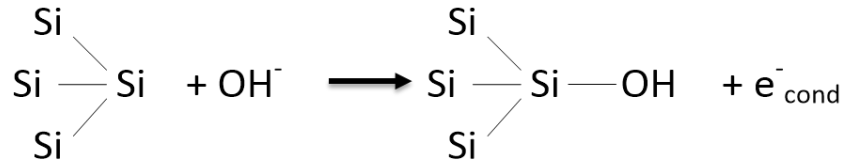


Figure 7 - Schematic diagram representing the chemical structure of the Silicon surface atoms and respective binding of hydroxide ions during a wet etch process for {111} silicon wafers.

Additives to the etchant solution

A standard KOH wet etching solution is composed of potassium hydroxide dissolved in water. However, other reagents can be added to the solution to influence the reaction. Isopropanol, or isopropyl alcohol (IPA), is a commonly used additive in this process that can assist in temperature regulation and affect the etching rate in different planes, although this process is not yet completely understood, despite various authors have suggested that. Although no chemical reaction between the Si atoms and the IPA molecules can be observed, IPA may limit the access of OH⁻ particles to the surface of the Si sample, thus acting as a pseudo-mask and a modulation agent [87, 88, 93, 94].

It has been proposed that, for a saturated concentration, i.e. once a thin film of IPA is formed on the top of the solution, a linear monolayer of alcohol molecules form at the surface of the Si sample, rather than being diluted in solution [88, 94].

In this work we have concluded that it's not IPA concentration, but availability, i.e., the amount of time that it's present in solution before complete evaporation, that plays the crucial role in the definition of the final structure. In this case, IPA directly reduces the etch rate for the (110) plane, comparatively to the (100) plane. If a steady supply of IPA is introduced into the system, to compensate for evaporation, this process will proceed indefinitely. However, once IPA completely evaporates, the etch rate for the (110) plane increases to standard levels, changing the etching profile of the structures [93].

Therefore, the final structure at which a silicon wafer is etched is intrinsically dependent on both the crystallographic orientation of the wafer and the type of chemicals used in the etching solution. Precisely controlling the availability of IPA at any given time is a crucial step in order to achieve a homogeneous etching process.

Dispersion methods and etching quality

The silicon wet etching reaction originates byproducts in the form of silicates, Si(OH)_4 , as demonstrated before. These molecules tend to adhere to the Si surface, acting as pseudo-masks that prevent the etching process in random locations, promoting a very rough and heterogeneous etching. Furthermore, hydrogen bubbles tend to form during the process, especially in hotspots of high etching activity, also naturally adhering to the Si surface. If not dissociated quickly, these bubbles also promote a mask-effect, affecting the overall quality of the etching process.

To promote the dissolution of silicates and the detachment of hydrogen bubbles, a dispersion method must be applied to the reaction. Magnetic stirring and ultrasonic agitation has been the subject of intensive study regarding etching homogeneity. Through magnetic stirring, an internal spiral flow is created that assists in the dilution of the etching byproducts and allows for continuous access to the silicon substrate. However, through this method is difficult to ensure a homogeneous distribution of energy throughout the entire sample, especially in larger samples. Some areas of the surface may be prone to higher quantity of silicates deposition, or hydrogen attachment, decreasing the overall quality of the etch process. Recent studies have demonstrated that ultrasonic agitation promotes greater quality in the overall process by distributing the same amount of vibrational energy throughout the entire solution [95], as observed in Figure 8.

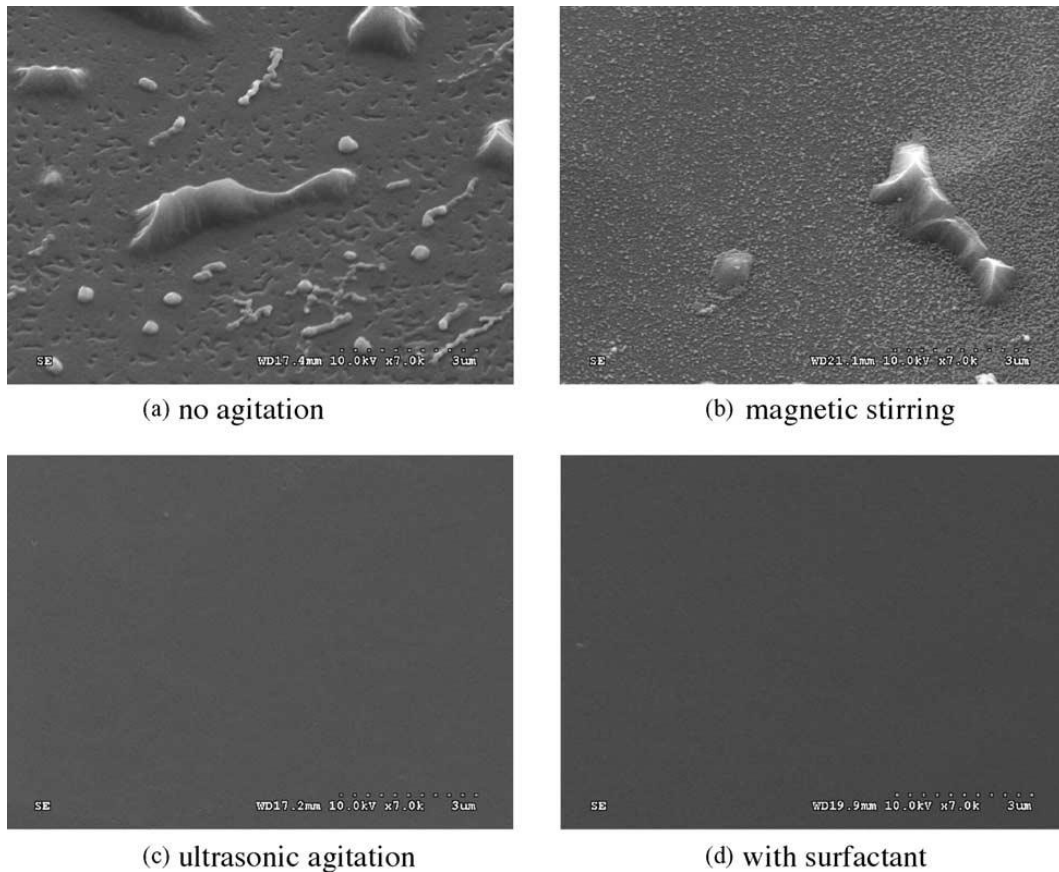


Figure 8 - Topology of the etched surface at various etching conditions. Authorized use by [95]².

Since both ultrasonic agitation and wet etching are exothermic processes, a minimum working temperature is always established. This temperature varies with the power applied through the agitation and the area of silicon atoms exposed to the etching process. Therefore, samples with considerable larger areas origin higher etching temperatures and, by consequence, higher etching and evaporation rates.

Temperature affects the etching rate through the increase of the system's free energy. Therefore, a higher temperature can both increase the free energy of Si atoms, making them more prone for break the bonds that connect them, but also increases the energy supplied to the chemical etching reaction that precedes the particle removal.

A typical Wet Etching setup, similar to what will be used in this thesis, is presented in Figure 9. In this apparatus, an opening on the top of the etching recipient allows for a dynamic control of the etching process, both through evaporation or through the addition of solvents during mid-process.

² Reprinted from Sensors and Actuators A: Physical, Vol 119 / Issue 1, C.-R. Yang, P.-Y. Chen, Y.-C. Chiou, and R.-T. Lee, Effects of mechanical agitation and surfactant additive on silicon anisotropic etching in alkaline KOH solution, Page No. 3, Copyright (2005), with permission from Elsevier."

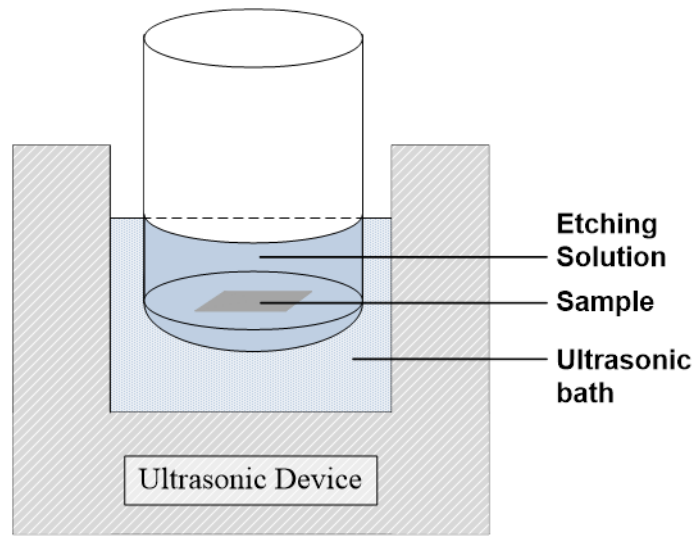


Figure 9 - Schematic diagram representing the Wet Etching Process with ultrasonic agitation.

2.3 - Electrodeposition

Electrodeposition, or electroplating, is a widely used technology that can be traced back to Michael Faraday and his laws of electrolysis. This process can be described as a charge transfer reaction that binds charged ions to reversely charged surfaces, inside an aqueous medium, through the application of an electrical current [96, 97]. In chemical terms, this process can be described as following:



Where M is the metal to be plated on the desired surface, n is the number of valence electrons of the specie and e represents the electrons being transferred in the process. To understand the effects of the electrical field in the electrodeposition process, we can summarize Faraday's laws into the following Equation:

$$m = \left(\frac{Q}{F}\right) \cdot \left(\frac{M}{z}\right) \quad (\text{Eq.15})$$

Where m is the mass of the substance deposited at an electrode, Q is the amount of electrical charge passed through the substance, F is the Faraday constant, M is the molar mass of the substance and z is the valency number of the ion.

According to Faraday's first law, the mass of the substance being deposited at an electrode is directly proportional to the quantity of electrical charge passed through the electrolyte. Those conditions are met if the medium of the electrodeposition does not change and the equivalent weight (M/z) remains equal, which is true for closed systems. For electrodeposition processes at a constant current, we can determine that:

$$Q = I \cdot t \quad (\text{Eq.16a})$$

$$n = \frac{m}{M} \quad (\text{Eq.16b})$$

And therefore:

$$n = \left(\frac{I \cdot t}{F}\right) \cdot \left(\frac{1}{z}\right) \quad (\text{Eq.16c})$$

Where n is the number of moles being deposited, I is the electrical current applied in the system and t is the process time. For electrodeposition processes with a variable electric current, the total charge is determined by integrating the electrical current over time. Since the only variable terms are the electrical current being applied and the process time, these two conditions correlate directly to the amount of material being electrodeposited.

An electrodeposition system consists in the following components, further depicted in Figure 10:

- a) **Electrodes.** These are electrical conductive materials that interact with the electrolyte bath, supplying the necessary electrical current to sustain the electrodeposition process. One of the electrodes, named the **Working Electrode**, acts as the electron donor, forcing the formation of ionic species in the electrolyte bath. On the other end, the **Counter Electrode** acts as the receiver of the transferred electron by adsorbing the ionic species into its own matrix, in a charge transfer reaction. Optionally, a third electrode, named the **Reference Electrode**, may be implemented near the Counter Electrode as to precisely measure the electrical potential formed during the electrodeposition process, granting additional inspection and control over the process.
- b) **Electrolyte.** This solution (or bath) provides the species to be deposited, usually complexed in the form of a salt. Through the application of an electrical current, the cations and anions dissociate and are transported to the corresponding polarized electrode. A crucial aspect for any electrolyte is its ability to be electrically conductive and allow for an easy ionic mobility. Optionally, some electrolytes may incorporate additives that can improve the quality of the electrodeposits, without affecting their composition.
- c) **Power supply.** The source of the power supply defines type of electrodeposition process. The electrical field can be applied through: a) a direct current at a constant voltage (Potentiostatic); b) a direct constant current (Galvanostatic); or c) a current or voltage waveform or pulse.

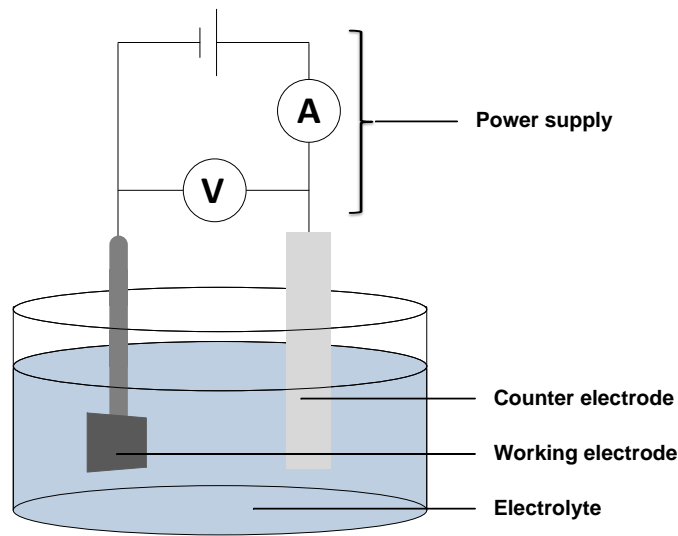


Figure 10 - Schematic diagram representing the Electrodeposition process in a two-electrode system.

The electrodeposition process begins with the application of an electrical field between the Working and Counter Electrodes, regardless of the power supply source. Through this electrical field, an electrical current is formed inside the Electrolyte, promoting the migration of cations and anions to the Cathodic and Anodic Electrodes, respectively. As most metal ions are positively charged, Cathodic Electrodeposition is more commonly used. Once the ionic species reach the reactant zone at the outer Helmholtz plane, a charge transfer process is performed between the ionic specie and the electrode, and the electrodeposition is performed.

Ultimately, this process conducts to the depletion of the ionic species in solution. To overcome this issue, sacrificial electrodes of the same species can be implemented, providing the necessary ions and maintaining a constant ionic concentration as the process is performed. If a sacrificial electrode can't be used or isn't available, manual replenishing of the salt could stabilize its concentration, although slight fluctuations in the Electrolyte concentration and density could alter the electrodeposition process [96, 97].

When using a sacrificial Working Electrode in Cathodic Electrodeposition, the supply of electrons is accompanied by the dissociation of the material from the electrode bulk, joining the remaining ionic species in the Electrolyte. In most electroplating setups, this electrode is commonly referred as the Anode. This process can be described as following:



The replenishment of the ionic species is crucial, not only on the bulk of the Electrolyte, but also at the reactant zones in both Electrodes. The relationship between the diffusion rate of the ionic species and the charge transfer rate determines the efficiency of the process. If the first is considerably higher than the latter, an over potential may be formed due to the accumulation of ions in the interface region. If otherwise, a depletion of the interface region will hinder the number of ions available for reaction. A balance between both factors can be obtained by [96, 97]:

- 1) Adjusting the concentration of the ionic species.
- 2) Adjusting the diffusion coefficient through temperature.
- 3) Adjusting the diffusion layer thickness by forced convection.

Another crucial aspect for the electrodeposition process is the choice of the substrate. As discussed previously, the deposition occurs at an Electrode. For such, a good conductivity is important for the application of the electrical field, as well as to improve the carrier collection efficiency. Furthermore, the substrate should also provide a scaffold for the electrodeposit that would match the requirements. Since the electrodeposition process tends to reproduce the surface morphology of the substrate, irregularities are amplified. In addition, the substrate should provide a good mechanical strength and matched thermal expansion, as to prevent cracking or peeling of the film. Amongst other factors that are process-specific, the substrate should also be stable and non-reactive with the electrolyte bath, as to prevent undesired chemical reactions non-related to the electrodeposition process [96, 97].

Alternatively, semiconductive materials can be used as substrate for the electrodeposition process, provided that an Ohmic contact is previously deposited on the back of the sample. It is this Ohmic contact that connects to the power supply. The electrical field then travels through the matrix of the semiconductor, finally reaching the Electrolyte. It's at this surface that the charge transfer process occurs, and thus, the electrodeposits adhere to the opposite side of where the conductive layer is deposited. [98] This process may be of interest for filling cavities and other tridimensional topographies where otherwise the conductive layer cannot reach.

Silver Electrodeposition

Several Electrolyte solutions have been studied for the electrodeposition of thick Silver films. The most successful solutions combine the use of Cyanide-based Silver compounds, such as Silver Cyanide (AgCN) [99-102] or Silver Potassium Cyanide (KAg(CN)₂) [103-105]. In such processes, a very thin silver layer is initially coated in low silver ion and high free-cyanide concentrations. This step is referred as a silver strike, and aims to prevent an electrochemical replacement reaction once the main electrodeposition process begins, with a more Silver-concentrated plating bath. These conditions provide high-speed plating with high-quality deposits, with decreased costs [97, 106].

However, health safety and environmental concerns have led to the substitution of Cyanide by Cyanide-free solutions, although they are yet to prove as efficient [107]. Some of the alternatives include the use of Thiosulfate [108, 109], Hydantoin derivatives [110, 111] or salts (such as Nitrate) [112, 113].

Most Silver salts and other derivatives are not entirely soluble in water. For that reason, most Silver-based electroplating solutions are composed of a mixture of other additives that increase solubility, wettability, grain sizes, among other factors. These additives may be specific for each silver-based solution, and a correct balancing should be implemented as to achieve quality plating. Furthermore, the bath main solvent should also be compatible with the targeted sample, as some solvents may directly (by chemically reacting with) or indirectly (through pH, for example) damage crucial components or layers.

Several studies have demonstrated the feasibility of fabricating Silver microelectrodes for diverse applications [79, 114, 115].

Through-Silicon Electrodeposition

As described previously, electrodeposition occurs as a charge transfer reaction at the surface of an electrode. Usually, this electrode consists of a metallic layer of the same material to be deposited as to facilitate adhesion and improve grain geometry. However, metal electroplating through semiconductive templates has proven to be possible [97, 116].

In this model, the metallic layer is set underneath or behind a semiconductive material and is otherwise insulated from the electroplating bath. Initially, the electrical current is transferred from the power source to the metallic layer through a uniform electric field distribution. The current then travels through the semiconductive material at a constant density throughout the entire surface, which is

crucial to guarantee a uniform deposition. Finally, the electrical current exits at the other side of the semiconductive material, and the electrodeposition occurs at the exposed surface.

A few studies can be found in the literature that focuses on the use of a patterned etched Silicon wafer as a mold for Electroplating [116]. Some of these studies consisted in the electrodeposition of the desired metallic species inside etched anisotropic silicon structures for uses in MEMS microfabrication as a substitute for LIGA processes [117], or as precursors for bottom-up self-assembly systems [98].

In both cases, the end product was separated from the Silicon mold through additional etching of the silicon matrix, either to completely detach and suspend the electroplated structures in a solution, or to release said structures and transfer them to another holding substrate maintaining their shape. Due to the weak interaction shown between silicon and deposited metals [118], no bond is formed between the two and the structures are easily detached.

Matrix doping type and concentration may affect electrodeposition in Silicon samples. For p-type doped samples, deposition of less-noble metals can only occur in the presence of photons that stimulate the generation of electrons at the conductive band. On the other hand, noble metals in p-type silicon samples and overall metals in n-type samples present no such limitations and the deposition occurs once a negative potential is applied. Depending on the position of the redox potential of the metal to be deposited on a n-type silicon sample, the charge transfer process may take place directly at the valence band (noble metals) or in the band gap through a reduced potential barrier (less noble metals) [116].

Furthermore, p-type silicon samples sensitivity to light can affect macropore (or cavity) filling. In the absence of photons, metal deposition begins and the bottom of the cavity and is grows upwards, limited only by the physical boundaries of the etched structures. With illumination however, electrons are generated over the wall area and allow for metal deposition to start at all exposed surface simultaneously. For etched profiles with a high aspect ratio, this may form porous structures once the electroplating bath can't physically reach the bottom of the cavity or is depleted at the top surface [24]. A description of this problem can be observed in Figure 11. One possible solution to overcome this problem may lay with passivation of the etched walls or the use of high aspect ratio insulating materials to define the electroplated height [117].

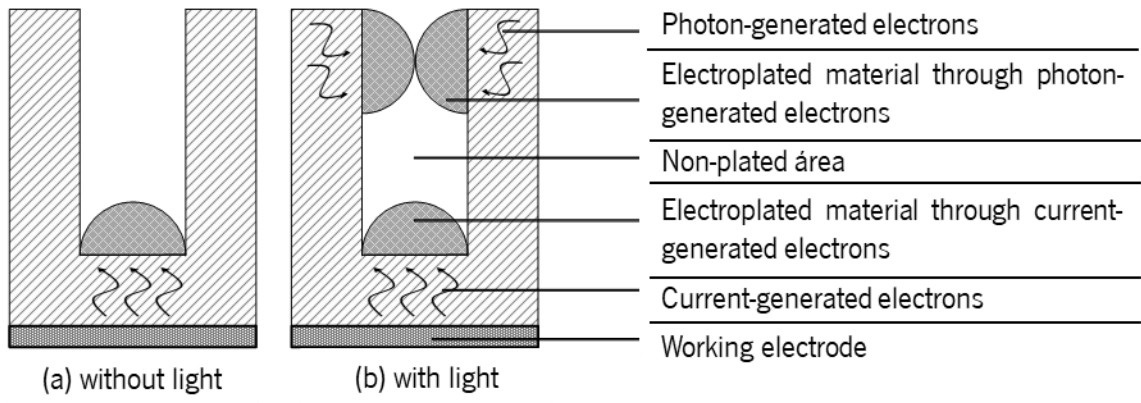


Figure 11 - Schematic diagram representing the effect of photons in the promotion of electroplating in non-desired areas through photon-generated electrons (b).

CHAPTER III

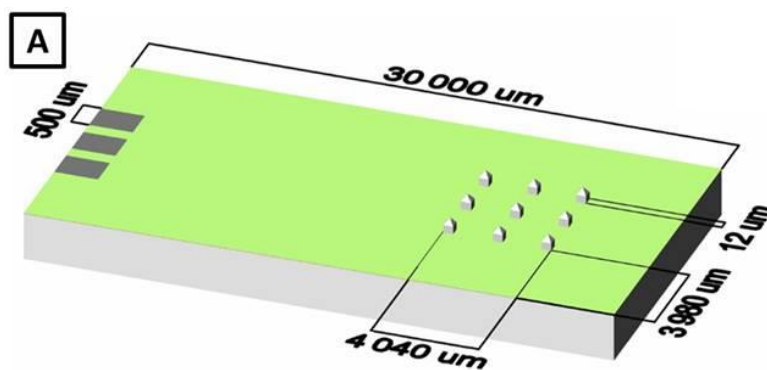
MICROFABRICATION PROCESS AND RESULTS

GENERAL PROCESS DESCRIPTION PROCESS DEFINITION

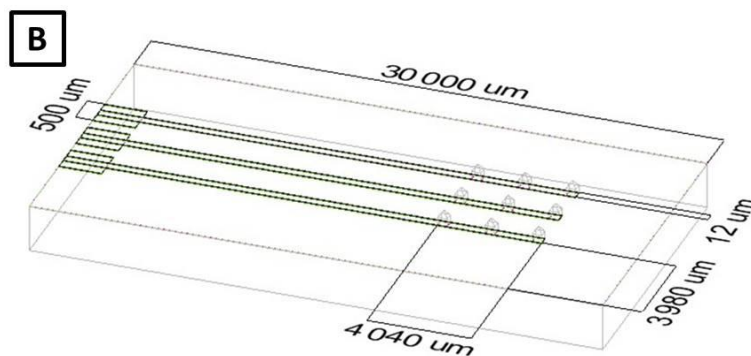
CHAPTER III - MICROFABRICATION PROCESS AND RESULTS

3.1 - General Process Description

The main goal of this work was to achieve a microfabricated system that could penetrate cells and perform intracellular pH measurements. To accomplish this goal, micrometric structures with a protuberant vertex were envisioned to achieve cell penetration, whilst their functionalization would allow for pH measurements to be performed. Ultimately, this system could include an integrated reference system. Figure 12 illustrates an example of the desired setup.



(a) view of top layers



(b) view of underneath components

Figure 12 - Schematic diagram representing a general layout of the proposed system: (a) - view of the top layers; and (b) - view of the microelectrodes and contact lines underneath the protective top layer. The individual components consist of: an array of pH sensitive (grey polygons – (a) and (b)); contact lines (green lines – (b)); contact pads (black – (a)); insulating and chemically resistant layer (green – (a)). The image is not to scale to allow for a better visual representation of the desired setup.

The fabrication of the working electrode (microelectrodes represented as grey polygons in Figure 12 a) and b)) could be achieved in one of two methods, either by: a) micromachining a hard surface with the desired pattern and coat it with an active electric layer; or b) creating a solid-state electrode through mold-filling or electroplating. Both approaches will be further studied in this chapter.

The fabrication steps take in consideration the compaction of an array of structures in tight formation to increase the yield of cell penetration in a given sample. This condition allows for a wide analysis of an entire tissue, rather than a single cell. The benefits from this includes error correction of individual electrodes (when performing data analysis of the entire array), a larger sample pool for analysis (which increases the confidence in the data collected) and possible the ability to detect data variation inside the sample (which could reflect variations on the metabolic states of different cells in the tissue sample).

A thin pH-sensitive layer, deposited over the working electrodes, grants sensibility to pH variations in the local active area. However, to prevent possible cross-contamination from the environment or from other individual electrodes, functionalization should occur only on the desired active area of the electrodes, and not through the entire system surface.

An insulating layer with chemical resistance and biological compatibility ensures electrical independence from each individual electrode, whilst providing erosion protection to the sensitive electric components underneath.

Optimization of the Silicon Wet Etching process was performed on 2 inch, 0,01-0,03 Ωcm , n-doped, $500 \pm 25 \mu\text{m}$ -thick polished silicon wafers with a monocrystalline <100> orientation (Sil'tronix, Silicon Technologies, Archamps, France).

All other experiments were carried out on 6 inches, 1–30 Ωcm , p-doped, $675 \pm 25 \mu\text{m}$ -thick polished silicon wafers with a monocrystalline <100> orientation (Si-Mat, Silicon Materials, Germany). The difference between the wafers does not affect the Si Wet Etching process conditions.

3.2 - Process Definition

As described in the previous sub-chapter, an array of cell penetrating structures with electroactive sensing capabilities could be manufactured either by: a) micromachining a hard surface with the desired pattern and coat it with an active electric layer; or b) creating a solid-state electrode through mold-filling or electroplating. These two approaches are reflected in Figure 13 and 14, respectively.

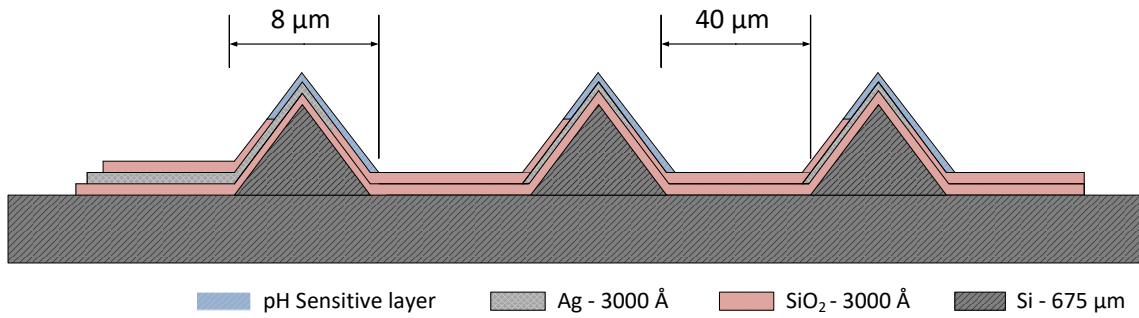


Figure 13 - Schematic diagram representing the cross-section view of the proposed sensor through Method a), depicting an array of microelectrodes fabricated through the functionalization of a micromachined Silicon surface.

The first approach (Figure 13) requires less microfabrication steps, is simpler and less expensive, as the desired pattern can be obtained by direct micromachining of a crystalline silicon substrate. However, the obtainable aspect-ratio is limited to the geometric configuration of the silicon crystallographic structure and cell penetration may not be achievable through this method. Furthermore, surface roughness on the etched profile may cause a high electric resistance on thin-film metallic layers deposited over, which could limit the effectiveness of the working electrode or require for considerable thicker layers to be deposited.

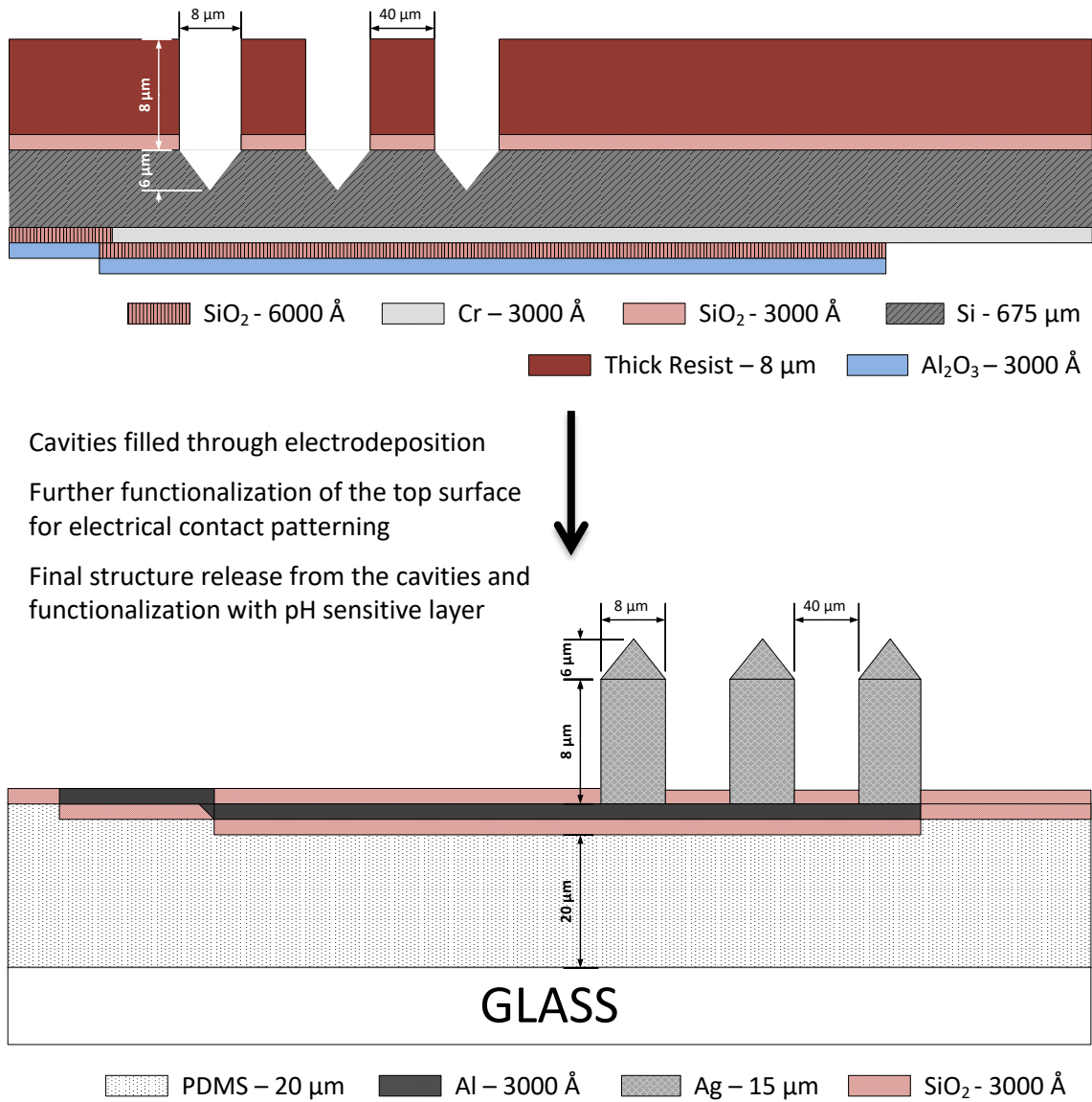


Figure 14 - Schematic diagram representing the cross-section view of the proposed sensor through Method b), depicting an array of microelectrodes fabricated through the electroplating (and later functionalization and detachment) of a series of cavities formed by micromachining a Silicon wafer and heightened artificially with a thick resist.

The second approach (Figure 14) is much more laborious-intensive, requires multiple sensitive steps to be overcome and relies on processes that are not well described in the literature and aren't a part of consolidated knowledge in the Laboratories where this work was performed.

Since both approaches require complete knowledge of the patterning of silicon structures, and the former can be directly correlated to this processing step alone, it was selected as the primary focus during the optimization of the lithographic and etching conditions.

3.2.1 - Lithographical patterning

Table 2 - Process steps for the optimization of the lithographical patterning through Direct Writing Lithography. Complete Runsheet in Annex 1.

#	TECHNIQUE	D	E	P	EQUIPMENT	MATERIAL	THICK
01	<u>Wafer dicing</u> Into ¼ of a 6" Silicon wafer			X	—	—	—
02	<u>Substrate cleaning</u> Remove any debris from the surface			X	Wet Bench	µ-Strip	—
03	<u>PVD – Magnetron Sputtering</u> Mask layer for Silicon wet etching process	X			Alcatel SCM 450	Chromium	3000 Å
04	<u>DWL – Lithography</u> Definition of Chromium pattern			X	DWL	PFR 7790 G +PR	1.4 µm
05	<u>Wafer dicing</u> Dicing saw that cuts individual dies for process			X	Disco DAD 231	—	—

For the initial optimization of this process, smaller, 2" Silicon wafers, were used for convenience, as they would fit inside most equipment chambers and would allow for smaller batches to test different masks and processing conditions. Therefore, during the optimization phase, processes #01 and #02 were discarded, as they were purposed to reduce the size of 6" Silicon wafers in order to fit Alcatel SCM 450 sample holders. The different steps of the process can be observed in Figure 15.

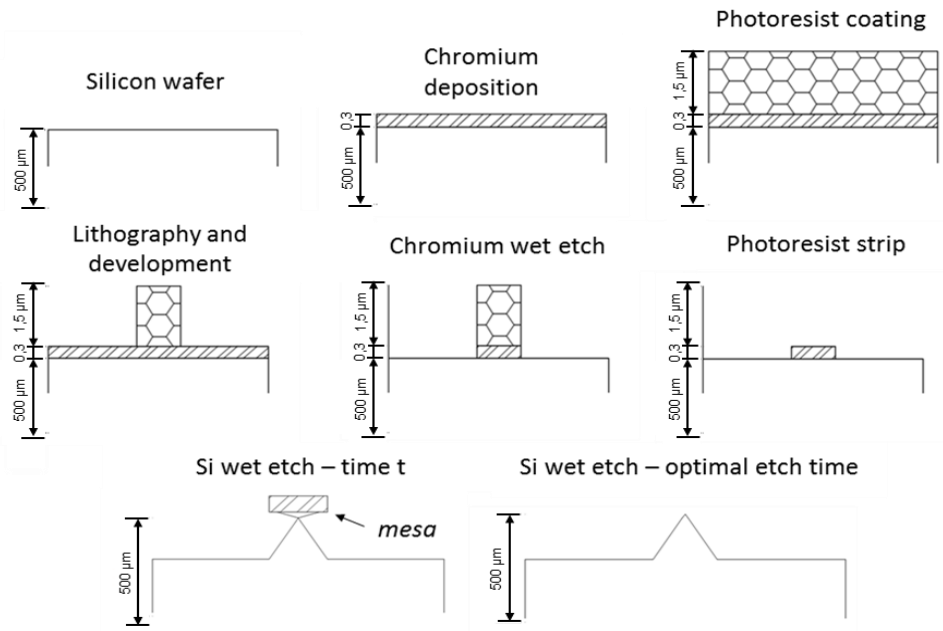


Figure 15 - Schematic diagram representing the microfabrication process of protuberant pyramidal structures through Silicon wet etching (cross-section view). A Chromium layer is used as a mask for the etching process. A sharp pyramidal structure is reached with the release of the mesa mask (optimal etch time). Adapted from [93].

Clean, 2'' Silicon wafers, were removed from the box and mounted on Alcatel SCM 450 sample holders. Previous to all processes, the samples were always cleaned with compressed air (blow dry) and inspected for potential contaminants. A Chromium layer was deposited by Magnetron Sputtering, under the following conditions: 3.07 mTorr, 20 sccm Argon, 20 W_{DC} . Controlling the sputtering time, different thicknesses can be obtained. Initial tests have demonstrated that thicknesses larger than $4000\ \text{\AA}$ tend to laminate in later processing, whilst thicknesses smaller than $2000\ \text{\AA}$ did not provided great chemical resistance to larger etching processes. An ideal $3000\ \text{\AA}$ thickness, achieved through 51 min of deposition, was set as the optimal condition. Figure 16 demonstrates one of the 2'' wafers, after Chromium deposition.

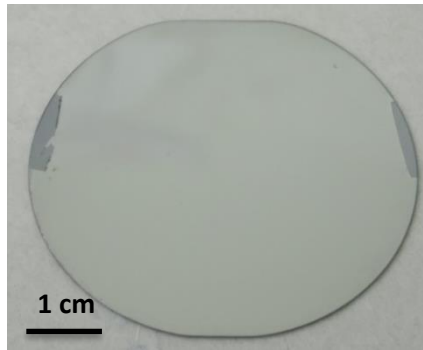


Figure 16 - Photograph of a 2" Silicon wafer after Step #03 - Chromium deposition. The darker spots on the wafer are the marks where Kapton tape was used to grab the wafer to the holder.

The samples were then coated with PFR 7790G +PR, a positive photosensitive polymer, or Photoresist (PR), which molecular bonds are weakened and broken by the combined effect of light intensity at 442 nm and a chemical solver. Therefore, exposure to the set wavelength in a defined and controlled manner allows for patterns to be scripted in the Photoresist.

The Photoresist was deposited on the surface of the wafers through injection (SVG track tool). During this step, the wafer was being spun to achieve a homogeneous covering, a procedure called spin-coating. The thickness of a specific Photoresist can be defined by controlling its viscosity (through temperature, such as that inside the room) and the velocity at which the wafer is being spun. Previous work developed at INESC-MN has concluded that a thickness of 1.5 μm for PFR 7790G Photoresist is optimal for standard lithographic processes at Lasarray Direct Writing Laser 2.0 system. This can be achieved through an initial 5 sec rotation at 800 rpm with acceleration of 500 rpm/s, and a second step of 40 sec rotation at 2800 rpm with identical acceleration. Baking the Photoresist at 85 $^{\circ}\text{C}$ for 60 sec after spin-coating is crucial to ensure a greater homogeneity by allowing the polymer to thermally expand and adjust to the surface roughness. Although this process produces a relatively flat surface, border thickness is always considerably higher due to surface tension. Due to this effect, a minimal distance of 3 mm to the wafer borders should be maintained during lithography as to achieve a homogenous profile, since different thicknesses require different exposure conditions.

Patterning was performed through direct writing laser lithography, consisting of a laser array with 200 photodiodes, with 1 μm resolution each, dispersed in a horizontal line. The system uses a converted AutoCAD mask to define scanning files, named as "*lics*". These represent 200 μm wide cross sections of the mask. By scanning through a "*lic*", each individual photodiode can be turned on

or off, thus creating the desired pattern. Since this process is light dependent, all processing was performed inside a “yellow room” with specific light and filters that do not affect the process. Profile alignment was performed using the wafers flat and the DWL2.0 software, to a maximum deviation of 0.02 rad. This ensures that the Si Wet Etching process can be adjusted to specific crystallographic orientations for the same wafer, just by aligning the patterned profiles with different angles towards the wafer flat. Laser energy and focus are constantly being optimized.

After exposure, the patterns are revealed through a development stage. An initial baking at 110 °C for 60 seconds hardens the Photoresist and prevents any additional energy dissipation throughout the matrix of the polymer that could degrade further molecular bonds. A 30 second cooling step is then applied and the sample is finally developed with a chemical solvent that removes any Photoresist that was exposed to the laser wavelength. For PFR 7790 G +PR, developer TMA 238 WA was applied for 60 seconds. After washing and spin drying the sample, the process is completed. All samples are then inspected at an optical microscope, using a green filter, for accessing the quality of the exposure and development, as shown in Figure 17. If remnants of unprocessed Photoresist were observed under the microscope, further development could be performed. However, once the sample was exposed to unfiltered light, no more development could be performed.

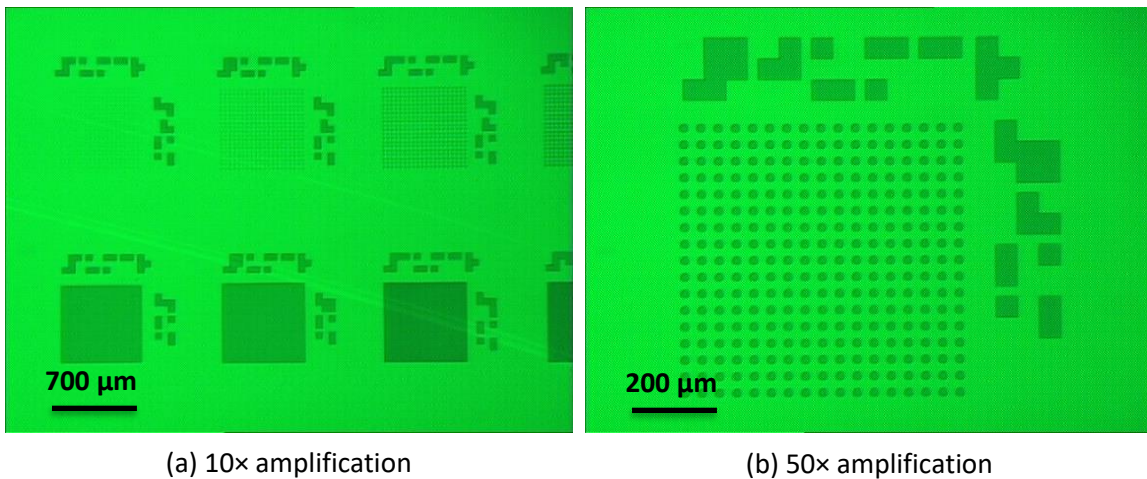


Figure 17 - Microscopic inspection of the patterning profile obtained in Step #04 through Direct Writing Laser. A green filter is used for microscopic inspection without affecting the Photoresist. The dark patterns represent hardened Photoresist, whilst the brighter areas represent the exposed Chromium surface. Mask name: TMpH_array04. The patterns in these arrays are presented in Table 3. (a) 10× amplification; (b) 50× amplification.

This mask possesses matrixes with specific geometries and dimensions, supplying important information regarding the etching process relating to critical dimensions for the process, minimal spacing between patterns and the influence of the geometric shapes and orientations.

A complete description of the patterns sizes and relative distances, i.e., the distance between the beginning of a given unit and the beginning of the next, can be observed in Table 3. The Honeycomb pattern was created by juxtaposing circles in a quadratic array, without any spacing between. The overall layout can be observed in Figure 18, whilst Figure 19 depicts a sample of each different type of patterns.

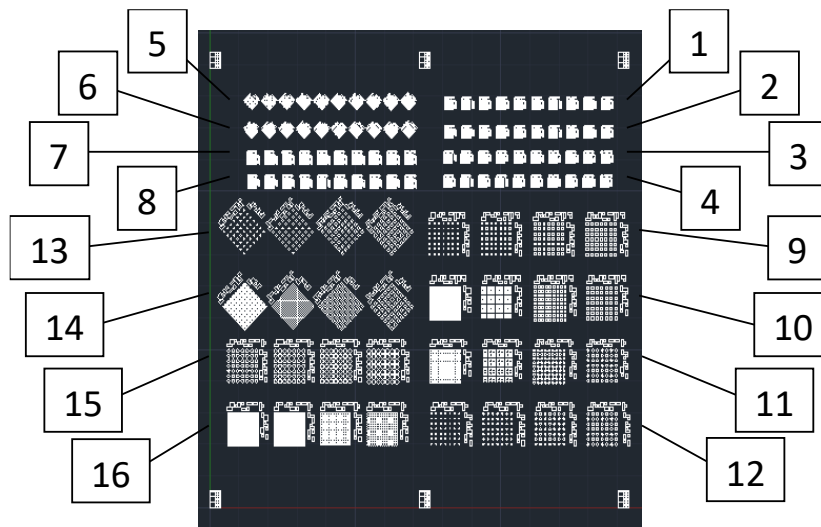


Figure 18 - AutoCAD™ image representing the profiles patterned through Direct Writing Lithography. Total patterned area of 9 × 9 mm. Complete description of each profile in Table 3. Mask name: TMpH_array04.

Table 3 - Description of the profiles scripted in the AutoCAD™ mask TMpH_array04.

#	Geometry	Size (μm)	Relative distance (μm)
1	Square	1-10	20
2			2-20
3	Circle	1-10	2-20
4			20
5	45° rotated square	1-10	20
6			2-20
7	Honeycomb	1-10	10
8			1-10
9	Square	20-50	100
10			40-100
11	Circle	20-50	40-100
12			100
13	45° rotated square	20-50	100
14			40-100
15	Honeycomb	60-90	100
16			20-50

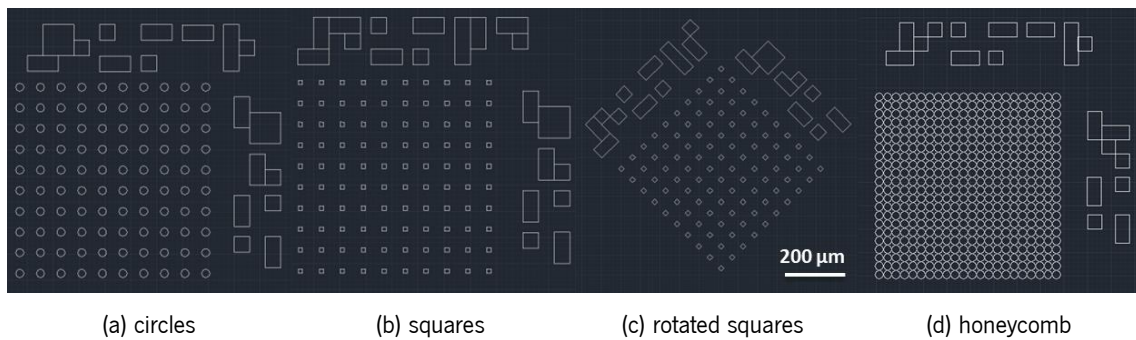


Figure 19 - AutoCAD™ image representing the profiles scripted in mask TMpH_array04 in greater detail: (a) Circles; (b) Squares; (c) Rotated Squares; and (d) Honeycomb pattern.

To assist in identifying the different patterns, a set of inscriptions based on braille language were added to each set, as seen in Figure 20 on the top and right margins. These set of inscriptions suffer the safe process of chemical corrosion as the patterns to be tested and analyzed. However, by having standard and recognizable patterns with larger dimensions, they are able to maintain a geometric shape similar to their starting point, allowing for a clear reading.

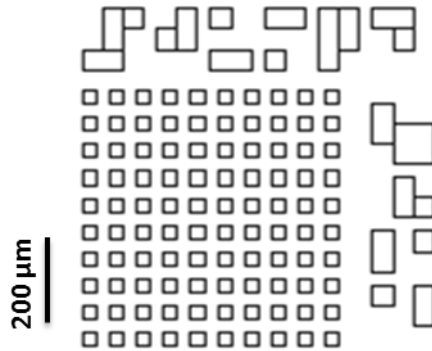


Figure 20 - AutoCAD™ image representing the profiles scripted in mask TMpH_array04, detailing the braille inscriptions. In this example it can be read “10 μm QD” on top and “20 μm ” on the side, which can be translated to “10 μm squares with a 20 μm relative distance”.

Finally, the wafer can be diced into individual dies for testing using Disco DAD 321 system. A 150 μm wide dicing saw is spun at 30 000 rpm in order to cut through the Silicon without breaking or cleaving. A constant streaming of water is crucial to prevent blade overheating and to remove any debris that could scratch and damage the surface of the sample. Once this process was completed, each 2” wafer provided 9 individual dies, with 9 \times 9 mm, all patterned with specific designs for Si Wet Etching, as seen in Figure 21 by the 9 squares in the center.

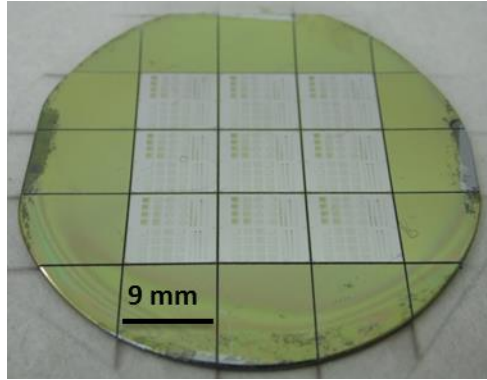


Figure 21 - Photography of a 2'' Silicon wafer after Step #5. In the middle, 9 individual dies contain the exact same profile, allowing for several samples to be fabricated from a single wafer. The bright color represents the exposed Chromium layer, whilst the darker-green color represents the hardened Photoresist.

Although the overlaying Photoresist had specific patterns, these were not yet transcript into the Chromium layer. That step was performed only moments previous to the Silicon Wet Etching to prevent surface oxidation of the Silicon due to long exposure to air. Therefore, each individual die was selected and processed thoroughly before a new one was picked.

3.2.2 - Silicon wet etching optimization

Table 4 - Process steps for the optimization of the structure definition through Silicon Wet Etching. Complete Runsheet in Annex 1.

#	TECHNIQUE	D	E	P	EQUIPMENT	MATERIAL	THICK
06	<u>Chromium Wet etching</u> Patterning of Chromium layer		X		Wet bench	Cr etchant	3000 Å
07	<u>Photoresist Stripping</u> Remove all the Photoresist from the die		X		Wet bench	Acetone	1.4 μm
08	<u>Silicon Wet etching</u> Patterning of protuberant pyramids		X		Wet bench	KOH solution	T.B.D.

To transfer the pattern to the Chromium layer, a specific etchant that selectively targets Chromium was applied (Sigma Aldrich 651826 Chromium Etchant, St. Louis, MO, USA). Both the Photoresist and the Silicon are unaffected by this etchant. The dies were immersed in a solution of Chromium Etchant until the patterns were completely revealed. This process generally takes 4 minutes, although different conditions could affect the process time, such as room temperature or solution dilution due to reuse. Considering that the thickness of the Chromium layer is considerably smaller than the diameter of the patterns, an overetching step can be applied safely to ensure the complete patterning of the surface.

After the pattern transfer, the Photoresist was removed with Acetone and IPA and the dies were inspected in an optical microscope for quality management. Figure 22 demonstrates one of the early masks used for Si Wet Etching optimization. The patterns observed in the Figure are consisted of the Chromium mask layer that was protected by the Photoresist. In a brighter tone, the Silicon surface is exposed.

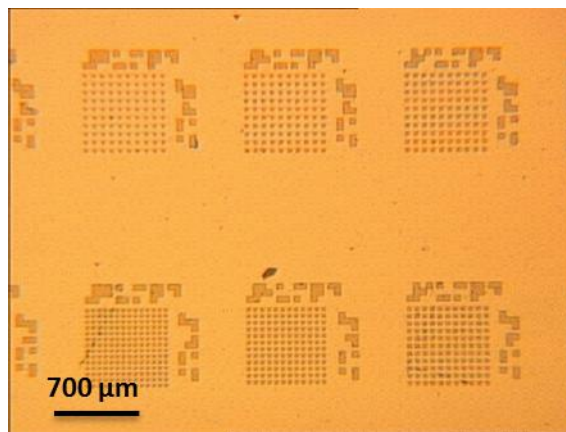


Figure 22 - Microscopic inspection of the patterning profile obtained in Step #07, after Chromium etching and Photoresist cleaning. The bright color represents the exposed Silicon surface, whilst the darker areas represent the patterned Chromium mask. Mask name: TMpH_array04.

From this step, optimization of the Si Wet Etching process took place. Initial testing was performed using the mask profiles presented previously in Table 3.

As the name of the technique suggests, Silicon Wet Etching is a chemical removal process performed under an aqueous solution, in this case, diluted Potassium Hydroxide (KOH). A 22 wt% solution was prepared by dissolving 70 g of KOH pellets (85% pure, Sigma Aldrich) into approximately 200 mL of distilled water. The dissolution of KOH in water is an exothermic process, hence the solution was left to cool down overnight before using.

Since it's an immersion chemical process, the removal of Silicon particles occurs in all directions at different etching rates, as explained in Chapter 2. However, etching also occurs underneath the masking layer, a process referred as *underetch*. If a given amount of time is allowed, the underetch process will progress gradually, under the same 54.7° inclination of the (111) plane, until it reaches the unit midpoint. During this stage, the structure formed on the top of the unit is referred as a *mesa*, as described in Figure 23.

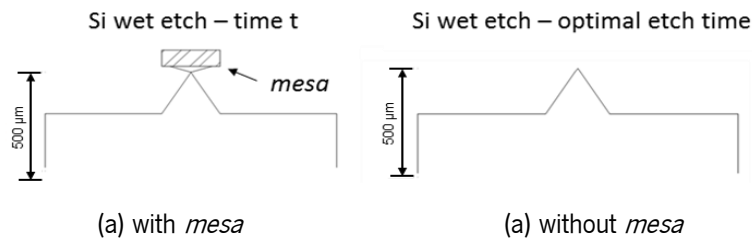


Figure 23 - Schematic diagram representing the: (a) dissociation of the top mesa mask; and (b) formation of a completed pyramidal structure. Adapted from [93].

For the desired purpose, the formation and consequential release of this *mesa* is crucial for the formation of sharp pyramidal structures. Subsequent etching does not affect the profile, rather just reduces the overall dimensions of the structure, as all planes would be then etched at the same exact rate.

Initial apparatus for Silicon Wet Etching consisted of a 250 mL, KOH-resistant, High Density Polyethylene (HDPE) flask with an exposed surface area of 28.27 cm^2 , placed on top of an orbital agitator at 150 rpm. The HDPE flask was filled with 20 mL of the KOH solution and the samples were immersed using a plastic tweezer.

Silicon Wet Etching through diluted KOH produces Silicates, as demonstrated in Chapter 2. Under the conditions and apparatus used, these adhered to the surface of the sample as soon as they were produced, acting as pseudo-masks and preventing from achieving a uniform and homogeneous etching profile, as seen in Figure 24, represented by the black smudges.

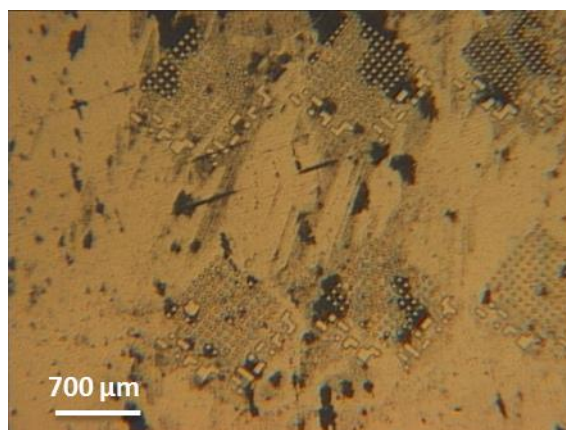


Figure 24 - Microscopic inspection of sample processed in Step #08 under an orbital agitator. Some of the Chromium mask profiles can be discerned in the image. The black smudges represent Silicate compounds that were formed as a by-product of Silicon wet etching and have adhered to the surface of the sample, acting as pseudo-masks and affecting the etching profile. Image obtained after 30 min process at room temperature.

To overcome this problem, the apparatus used in this process was adapted. An ultrasonic agitator (Fischer Scientific FB15047, 37 kHz, 30/90 W, Waltham, MA, USA) with controlled temperature was used. With this method, a constant state of agitation can be applied throughout the entire solution, promoting the dissolution of Silicates and other reaction by-products (such as hydrogen bubbles) and refreshing the etching solution at the reaction site. This results in a smoother surface without any Silicate adherence, as seen in Figure 25. Temperature management of the ultrasonic bath allows for a greater control of etching rates and total processing time as well, especially for deeper etching profiles.

A crucial parameter to control the etching process is the presence of additives. Since the process is run in an open system, it allows for the evaporation of solvents (in this case, IPA and water). Like discussed previously, IPA influences the etching rate of different crystallographic planes. As such, evaporation of IPA could affect the etching profile. To determine the influence of solvent evaporation in the Silicon Wet Etching process, a series of tests were conducted.

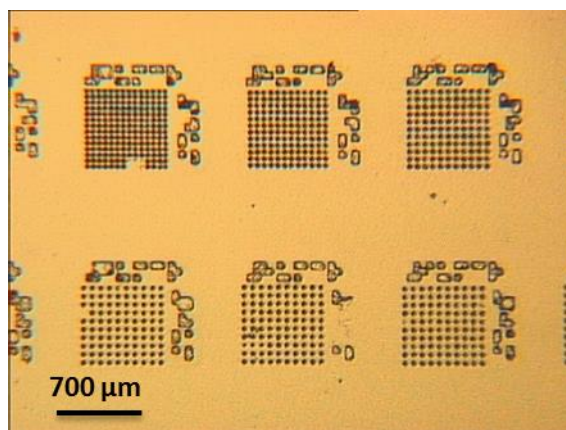


Figure 25 - Microscopic inspection of sample processed in Step #08 under an ultrasonic agitator. Although some of the profiles were affected and deleted in the process, the overall quality of the etching process increased considerably. Image obtained after 30 min process at room temperature.

To determine the standard evaporation of water during a wet etching process, a control sample was added to a flask containing 20 mL of 22 wt% KOH solution. No other additives were added. The sample was then processed with ultrasonic agitation for 120 min at 40 °C. In the end, the solution volume was measured again, registering 15 mL (as seen in Figure 26 A). This decline of 5 mL over the 120 min period consists solely of water evaporation, at a rate of 0.047 mL/min. Three other control samples were prepared and inserted in flasks containing 1, 3 and 5 mL of IPA added to the same 20 mL of 22 wt% KOH solution (Figure 26 B, C and D, respectively). All samples were processed in the same conditions as the first sample, and their final volumes were measured. Despite the different initial volumes of IPA added, all samples registered the exact same final volume of 15 mL. These results indicate that IPA is completely evaporated during the process, and that if sufficient time is given to evaporate all IPA, the final volume is independent of its initial added volume.

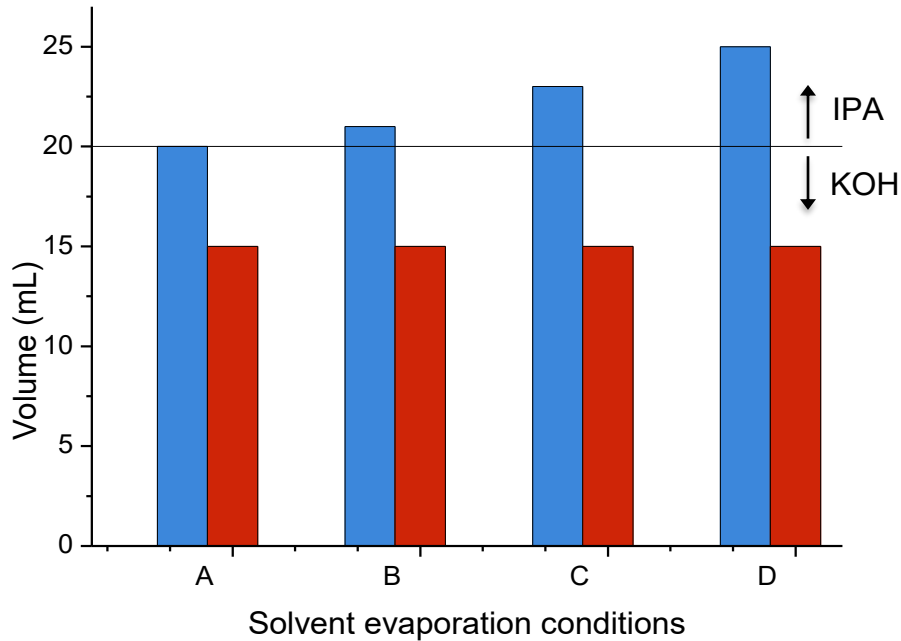


Figure 26 - Graphical representation of the total initial volume (blue), as a sum of initial KOH volume (20 mL) and IPA volume (ranging from 0 to 5 mL), *versus* the final volume (red) after a total etching time of 120 min. Adapted from [93].

To further determine IPA evaporation rate and influence over the etching process, four experiments were conducted as described in Table 5 (samples 1 to 4). All samples were processed in the same apparatus and under the same temperature. Etching time for each sample was determined by microscopic inspection, analyzing whenever the top *mesa* would detach from the remaining structure, thus forming the final pyramidal structure. The optimal etching time is dependent not only of the Temperature, KOH concentration and IPA availability, but the nominal size of the pattern as well. For that, 10 μm wide squares with a relative distance of 20 μm between were selected as the standard analysis structure to compare the different IPA conditions. In the end of each process, the final volume was once again measured. Since all volume measurements were made inside a graduated flask, a small error in measurement (in the order of a few hundred μL) can be expected.

Table 5 - Experimental conditions used in the definition of $10\ \mu\text{m} \times 10\ \mu\text{m}$ wide pyramidal structures through wet etching. IPA availability represents the predicted time at when all IPA would evaporate. Adapted from [93].

Sample	V_{KOH} (mL)	V_{IPA} (mL)	Etch Time (min)	Final Volume (mL)	IPA Availability (min)
1	20	0	40	18	0
2	20	3	50	18	17
3	20	5	60	17	29
4	20	20	60	27	114
5	20	2 + 2 (each 10min)	60	28	125

With the results obtained it was possible to observe that only samples 4 and 5 presented a final volume higher than that of the KOH solution, thus indicating that IPA would still be present in solution. Considering the evaporation rate of water of 0.0417 mL/min, calculated previously, we can infer that approximately 2.5 mL of water evaporated in the 60 min etching process. Therefore, the remaining 10.5 mL of volume missing from the initial measurement for sample 4 can be attributed to evaporated IPA, thus resulting in an evaporation rate of 0.175 mL/min.

Considering initial volumes of IPA and its evaporation rate, IPA availability can be calculated for each sample (last column in Table 5), representing the amount of time in which IPA is present inside the solution before complete evaporation.

In a parallel etching process, sample 5 was processed in a similar matter as the remaining. However, it started with only 2 mL of IPA, and additional volumes of 2 mL were added each 10 minutes. Considering IPA evaporation rate of 1.75 mL every 10 min, we could assure that IPA would remain constantly present in solution, independently of the concentration. In these conditions, both Sample 4 and 5 presented very similar macroscopic etching profiles, considerably distinguishable from the other samples. Therefore, IPA influence over the Silicon Wet Etching process can be address in terms of **availability**, rather than **concentration**.

We can infer that, once IPA evaporates completely, the wet etching process will continue in the same conditions as those observed for Sample 1 (without IPA). Therefore, we have two specific

moments that are particularly relevant to the etching process: when IPA is present in the solution, and when all IPA evaporates.

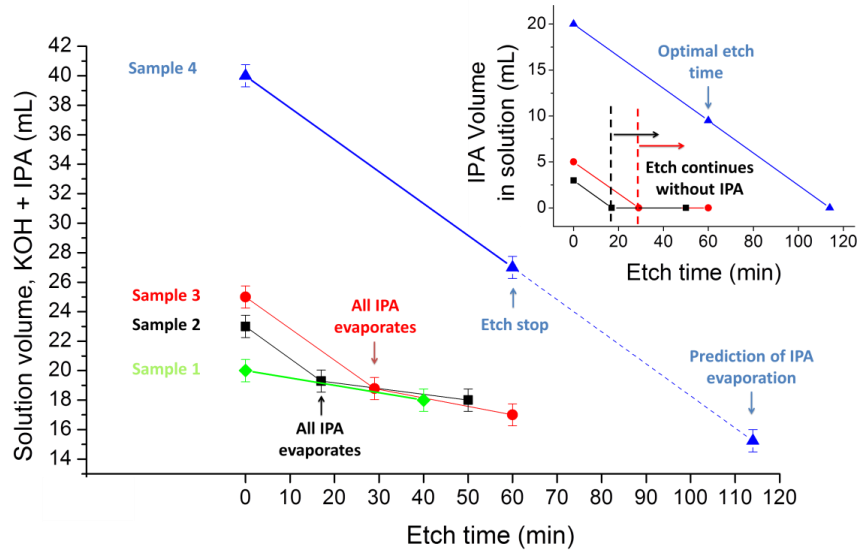


Figure 27 - Evolution of solution volume as a consequence of solvent evaporation. The main chart contains the total volume of the solution (sum of diluted KOH and IPA volume) across time, whilst the inset charts represents only the IPA volume in the solution, during the etch process. Samples 1-4 are represented in Table 5. Adapted from [93].

Under standard conditions, Silicon Wet Etching through diluted KOH promotes a higher etch rate for the (110) and (331) planes, when compared with the etch rate for the (100) plane (2× and 1.5×, respectively) [88]. This results in a very sharp, but irregular structure with a distinctive underetching profile that evolves into a shrunken structure. The obtained structures present an octagonal base with a basal diameter up to 1/3 and height up to 1/4 of the profile nominal size (mask size). However, the use of additives can modulate the etch rates of different planes. Under the presence of IPA, the (110) plane is predominantly protected, thus significantly increasing the base diameter of the structure, and reorienting it towards the (100) axis. Performing an etching of any structure, under IPA constant availability, results in a quadrilateral profile aligned with the axis with increased base width, as shown in Figure 28.

If enough time is given to the etching process under IPA availability, the progressive increase in base width may cause different structures to collide and merge, as seen in Figure 28 at the process end. Therefore, spacing between adjacent profiles needs to be carefully planned to prevent grouping.

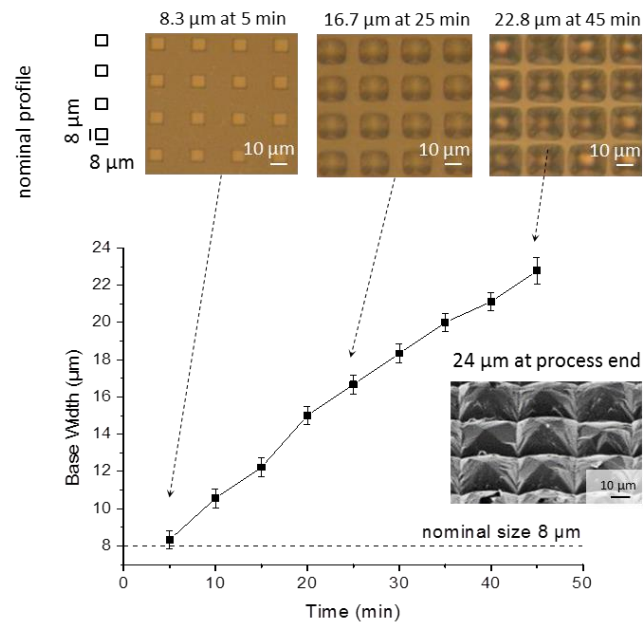


Figure 28 - Evolution of the base width of $8 \mu\text{m} \times 8 \mu\text{m}$ patterned square structures, spaced $16 \mu\text{m}$ apart, during a Silicon wet etching process under IPA saturated conditions (sample 4 in Table 5). Microscopic inspection demonstrates how the base of each individual profile widens consistently, ending up merging together. These results are a consequence of IPA availability during the entire process time. Adapted from [93].

After IPA completely evaporates from the solution, the etch rate for the (110) and (331) planes increases, promoting the transition from a quadrangular to an octagonal shaped structure, as seen in Figure 29. This transition occurs progressively and independently from the overlaying mask, since the structure base width has grown beyond the nominal size and is no longer defined by it. This effect can be observed in the images taken at 80 and 100 min, within Figure 29. Although the initial mask is still present and visible (shown as a bright square overlaid above the dark structure), the reorientation of the structure still occurs.

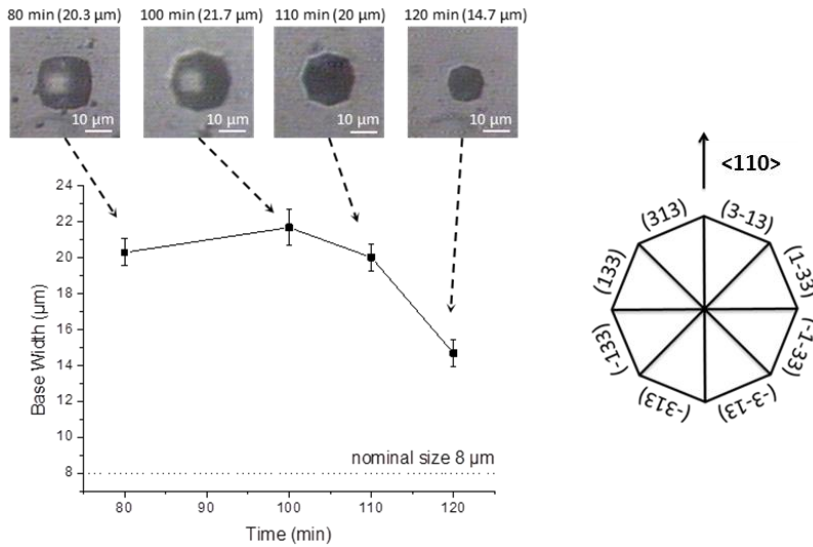


Figure 29 - Evolution of the base width of $8 \mu\text{m} \times 8 \mu\text{m}$ patterned square structures, spaced $40 \mu\text{m}$ apart, during a Silicon wet etching process under IPA saturated conditions (until minute 80) and under IPA depletion conditions (after minute 80). The results demonstrate that under the influence of IPA, the base width continuously widens under a square shape. Once transposed to a solution of diluted KOH without any IPA, an initial increase of the base width can be observed as a consequence of crystallographic reorientation towards the (331) plane. Once the reorientation is completed, continuous wet etching will cause the quickly decrease in base width. Adapted from [93].

A fine tune of the etching process, regarding structure shape and dimensions, can therefore be achieved by modulating the availability of IPA during the process. The volume required to ensure its availability is dependent not only on the exposed silicon area and the desired etch depth, but also on the evaporation rate of IPA itself, defined by both temperature and exposed surface area of the container, and the total volume of solution.

To determine the influence of IPA availability in the angles formed against the surface plane, a second profile mask was created following the exact same steps as before. This new mask possesses compact matrixes that can be easily analyzed under transversal SEM imaging for a precise observation of the structures profile. The profiles presenting the best results in the previous tests were selected in this new mask, which can be observed in Figure 30.

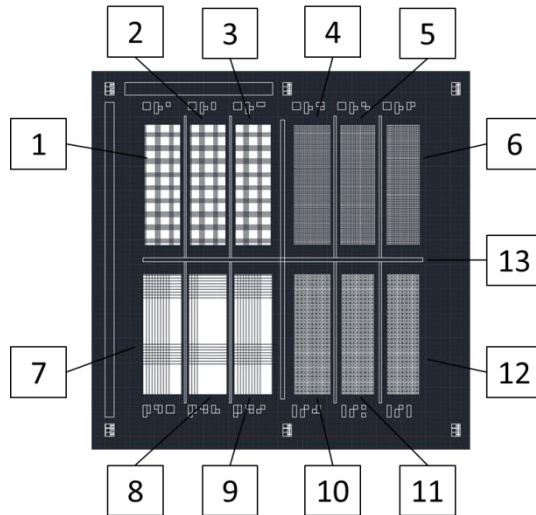


Figure 30 - AutoCAD™ image representing the profiles patterned through Direct Writing Lithography. Total patterned area of 9 × 9 mm. Complete description of each profile in table 6. Mask name: TMpH_array05.

Table 6 - Description of the profiles scripted in the AutoCAD™ mask TMpH_array04.

#	Geometry	Size (μm)	Relative distance (μm)
1		20	20
2		20	40
3	Inverted Square	10	20
4		10	50
5		8	20
6		8	40
7		10	10
8	Square	10	20
9		8	20
10		10	10
11	Rotated Square	10	20
12		8	20
13	Rectangular	200	200

Transversal SEM imaging was performed on samples patterned with three different mask profiles, as depicted in Figure 31. Each set of points for a given IPA availability period were extracted from the same sample containing the different masks, and therefore, processed in the exact same conditions. These results demonstrate a tendency of each structure towards a specific angle, and by consequence, a specific plane.

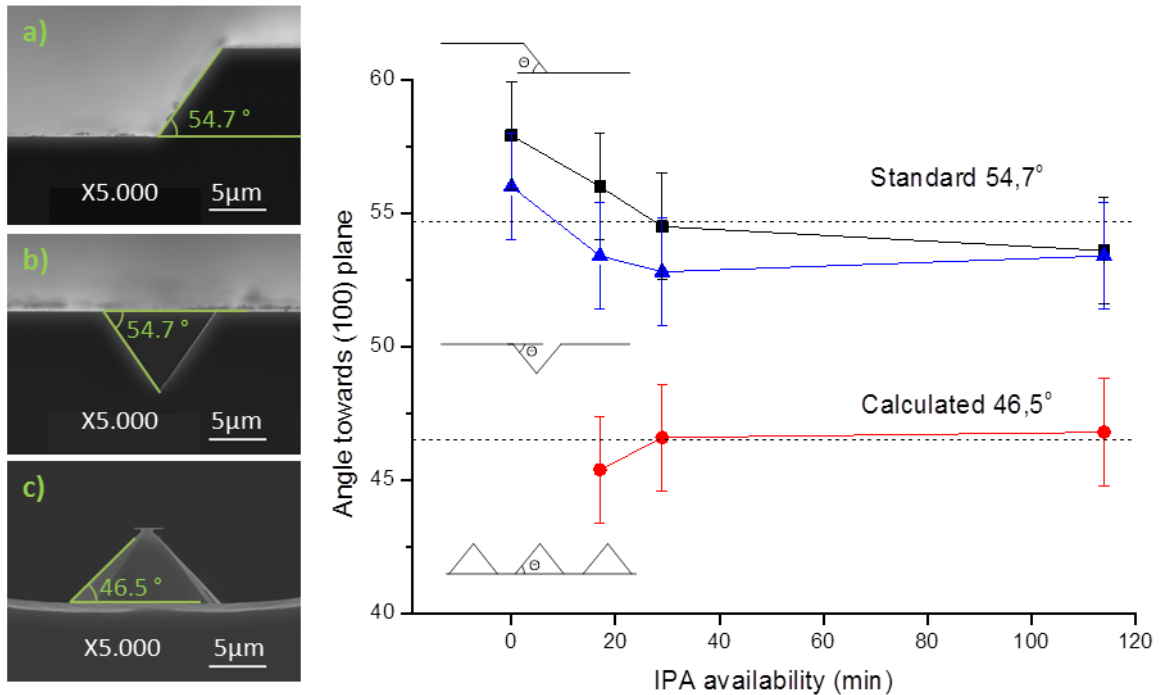


Figure 31 - Evolution of the measured pattern angle in different IPA availability conditions, obtained from (a) 200 μm wide rectangular mask (black); (b) 10 μm v-groove from a square mask with a spacing of 20 μm (blue); and (c) 10 μm square mask with a spacing of 20 μm (red). Adapted from [93].

As seen in Figure 31 a) and b), both structures present a $54.7^\circ \pm 2^\circ$ angle, characteristic of the (111) plane, as long as a minimum amount of IPA availability was observed. However, without IPA, the harsh conditions of the wet etching process form irregular structures with a steeper angle, although clearly close to the same 54.7° angle. We can infer that the variations in this case may be attributed to the aggressiveness of the etching itself, rather than a different etching plane.

When defining grooves and pits, the etched structure always orientates to align with the wafer flat, independently of the initial mask shape. This results in the formation of quadrangular pits with (111) planes. IPA influence on the final profile is negligible, either on the base width or profile topography.

However, dense structures, as those observed in Figure 31 c), are deeply influenced by the neighboring topography, which can be seen in the registered angle of 46.5° . Once again, IPA concentration plays little influence in the final profile, but its absence causes the formation of structures with an unmeasurable rough etch profile.

The discrepancy between the results observed in Figure 31 a) and c) is a direct consequence of the influence of the adjacent area around each of the structures. Whilst in Figure 31 a) the structure was patterned $200\ \mu\text{m}$ away from any other profile, the structure in Figure 31 c) was densely compacted in an array of similar structures. The difference in the etched result can be attributed to the **microloading** effect, in which etchants and byproducts of the reaction have more difficulty diffusing through smaller areas [119]. In dense arrays of structures, as soon as the wet etching starts, the (100) plane becomes less accessible than the (110) and the (331) planes. To overcome this situation, in order to promote consistent pyramidal structures with the desired 54.7° angle in dense arrays, other additives should be added in the etching solution as to increase the wettability of the sample surface. Alternatively, structures could be patterned further away from each other, although that would compete against the need for a densely patterned matrix. Figure 32 demonstrates in greater detail the profile obtained under the microloading effect.

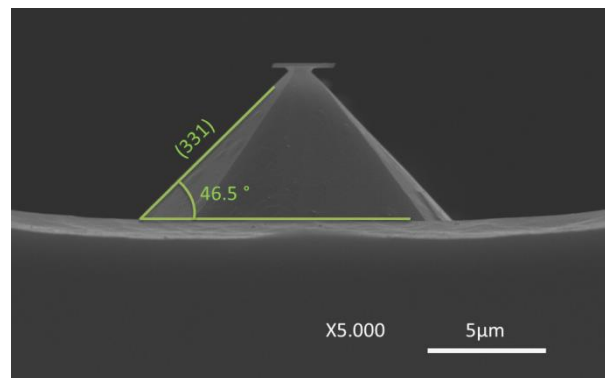


Figure 32 - SEM cross-section image of the (331) pyramidal structure obtained from a $10\ \mu\text{m} \times 10\ \mu\text{m}$ square mask, spaced $20\ \mu\text{m}$ apart (Sample 2 in Table 5). Adapted from [93].

Whilst compaction of pyramidal structures under the registered conditions is affected by this microloading effect, v-grooves and pits are not. In this situation, regardless of the amount of structures that are compacted, the final profile is unaffected by the microloading effect and present a much cleaner surface than any other structure. Furthermore, since the chemical etching occurs inside a

limited geographical location (defined by the area of the individual pits), the wafer surface retains its profile and smoothness, facilitating the further processing through standard microfabrication steps. Given enough time, all the structures created inside the pits will inevitably form inverted pyramids with a square base aligned with the axis, independently of the nominal profile shape (mask) or orientation.

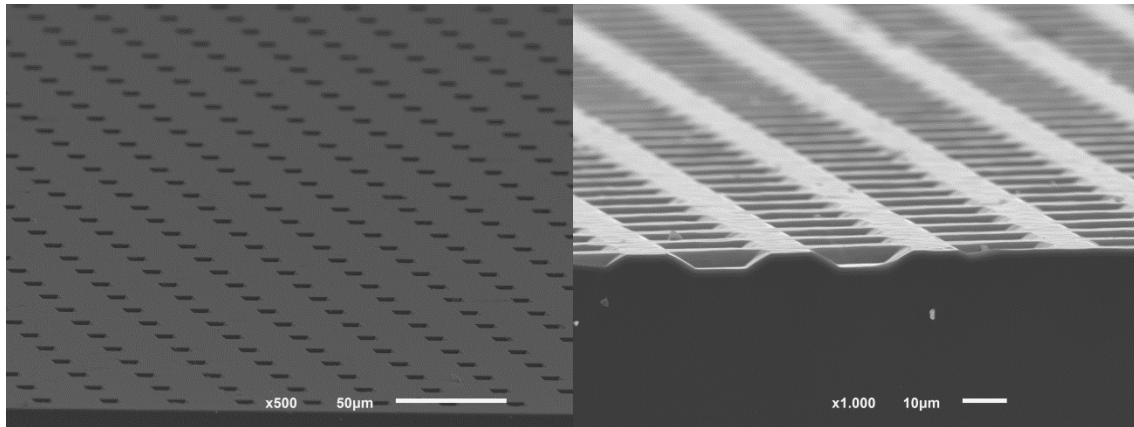


Figure 33 - SEM inclined image of (111) pits obtained from $10\ \mu\text{m} \times 10\ \mu\text{m}$ square inverted masks (holes), spaced $20\ \mu\text{m}$ apart. IPA plays little to no influence in this process (Sample 1 (left) and Sample 3 (right) from Table 5). Adapted from [93].

Further analysis of the IPA influence in the wet etching of Silicon has demonstrated that for v-grooves and pits, IPA plays little to no influence. However, for pyramidal structures formed by squares aligned with the wafer flat, etchings performed near the optimal volume of IPA force the reorientation of the structure towards the (331) plane. This reorientation will cause a shift in the number of sides the structure presents, from a square, through a dodecahedron, ending in an octagonal shape, as seen in Figure 34 a).

However, if the same profile is exposed with a tilt of 22.5° relatively to the wafer flat, as seen in Figure 34 b), no reorientation at all occurs, since the structure is already aligned with the (331) plane. Through this method it's possible to define the geometry of the desired pyramidal structures, from a squared or octagonal base, simply by defining the initial alignment tilt towards the wafer flat.

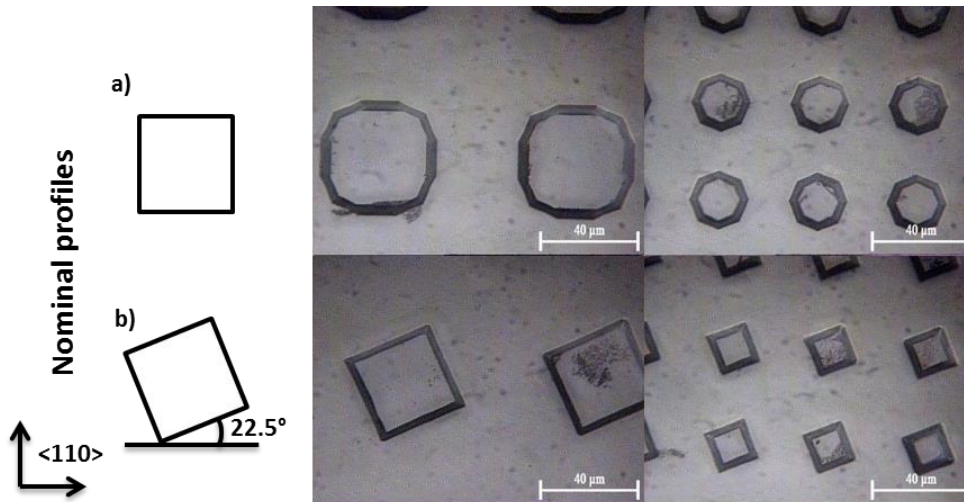


Figure 34 - Microscopic inspection of samples processed under the same conditions as Sample 2 (Table 5), after 20 minutes. Initial profile: (left) 40 μm and (right) 20 μm squares: (a) aligned with the wafer flat; and (b) misaligned 22.5 $^\circ$ with the wafer flat. Adapted from [93].

For longer IPA availability, the etched structures will form rounder shapes, independently of profile orientation, as shown in Figure 35. Although some of the tilt is observable, it is not significant in the overall profile. Furthermore, the surface topography of these structures is much rougher, making them undesirable for further processing.

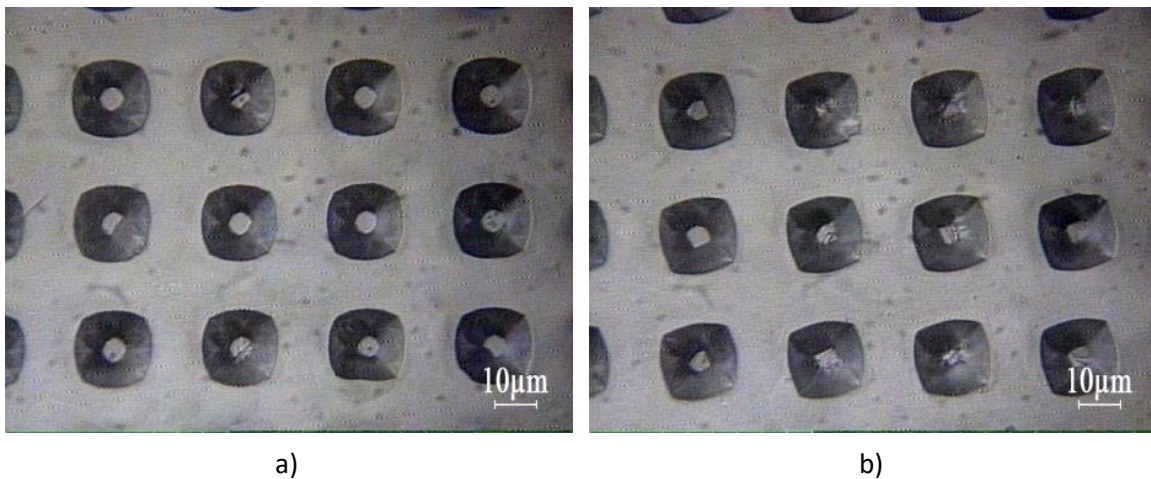


Figure 35 - Microscopic inspection of samples processed under the same conditions as Sample 4 (Table 5), after 50 minutes. Initial profile: 10 μm squares a) aligned and b) misaligned 22.5 $^\circ$ with the wafer flat. Adapted from [93].

An evolution of this process can be observed in Figure 36. In the lack of IPA, the (110) plane is predominantly etched, causing the visible undercut profile seen in Figure 36 a). A 17 min availability of IPA in the beginning of the process is sufficient to stabilize the etching rates for the (110) and (331) planes, thus allowing the formation of octagonal structures (Figure 36 b)). With the increase of IPA availability, the square profile is maintained with rounder edges, as observed in Figure 36 c) and d).

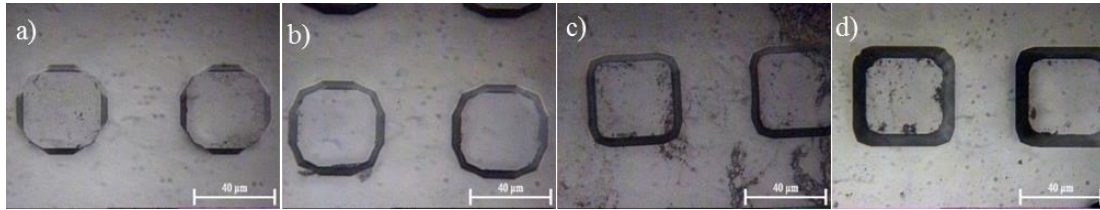


Figure 36 - Microscopic inspection of samples with an initial profile of 40 μm squares aligned with the flat. Conditions are as described in Table 5: (a) Sample 1; (b) Sample 2; (c) Sample 3; and (d) Sample 4. Adapted from [93].

Once IPA evaporates, all profiles tend to revert to initial situation with severe etching in the (110) plane. Controlling the correct conditions as to match the IPA evaporation with the required etching depth, as the etching profile reaches the mesa release stage, therefore allows for a wider range of profiles.

To assist in the choice of the optimal etching conditions, a summary of the research work was synthesized in Figure 37. The diagram is able to relate the IPA availability with the etching profile obtained the etching evolution time. If IPA availability is higher than its evaporation rate, square patterns are transferred to the silicon wafer under a square-based pyramid (transition from region A to B). However, if IPA is depleted mid-reaction, square based pyramids (region A) may rearrange along the etching time into n-side polygons (region C). This transition is gradual and the structure shape may undergo different profiles, depending on the profile size and etch rate. If enough time is allowed for the etching to proceed under IPA depletion conditions, the structure will eventually stabilize into an octagonal base pyramidal shape (region D). In this diagram, the optimal etch time is defined as the period in which the top *mesa* is released, for a 10 μm wide squared structure under the conditions defined in Table 5.

As shown before, this reorientation does not affect squared structures that are tilted 22.5° from the wafer flat. For those structures, independently of the IPA availability, the profile remains constant.

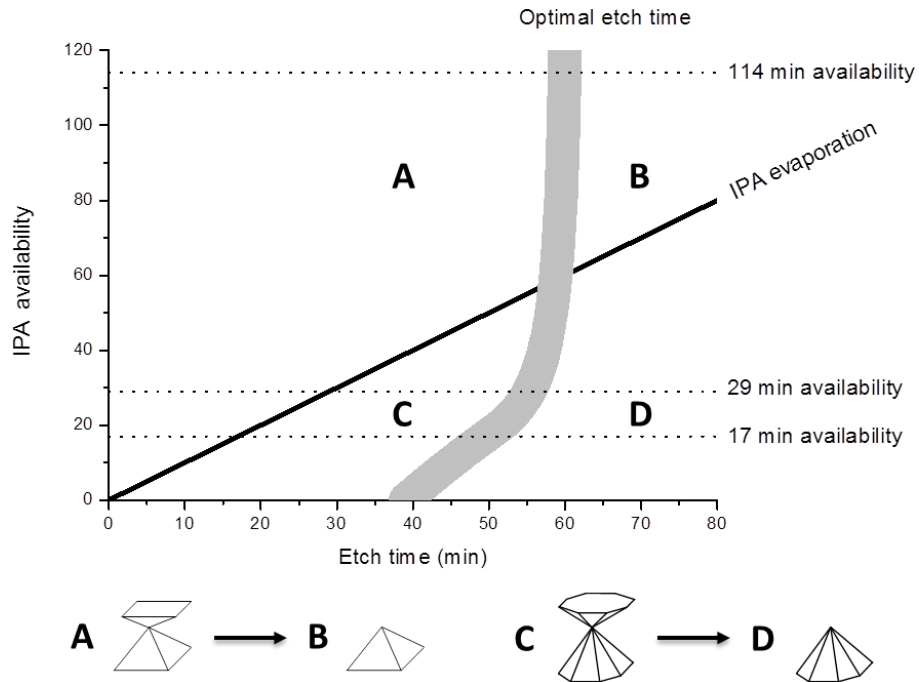


Figure 37 - Schematic diagram of the evolution of Silicon wet etched structures, under IPA influence, for a $10\ \mu\text{m}$ square mask and the conditions depicted in Table 5. Adapted from [93].

These experiments allowed for an important understanding of the Silicon wet etching process and how it can be modulated to our demands. In optimal conditions, large arrays of pyramidal structures could be achieved, as seen in Figure 38.

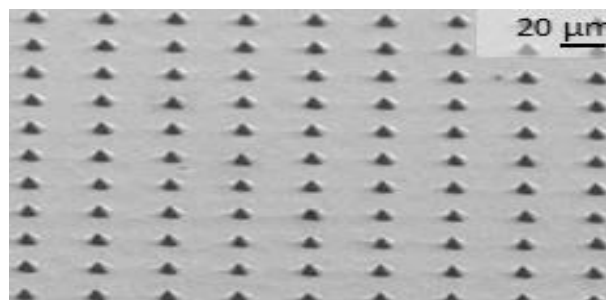


Figure 38 - SEM inclined view of a large array of standing octagonal pyramidal shaped structures, achieved under the conditions of Sample 2 (Table 5).

To prevent possible electrical coupling between structures, through the Silicon matrix itself, it's crucial to insulate the entire surface prior to any metallization. Due to the specific geometry of the manufactured structures, and to ensure that the entire surface is protected, a thin Silicon Dioxide film of 3000 Å was deposited through Chemical Vapor Deposition (CVD). This material is also biocompatible, which prevents cell damage during following processing and testing for cell penetration.

3.2.3 - Cell penetration assay

The microfabricated structures were tested for cell penetration capability, by performing biological assays of membrane integrity on 3T3 cell lines monolayer cultures (Fibroblast cells, embryonic tissue, Mouse from CCL 163, American Type Culture Collection). An array of octagonal pyramids with a base width of 13.7 µm and a height of 7.2 µm, at an angle of 46.5°, was used in this process (fabricated under the conditions of Sample 2 in Table 5).

By promoting the growth of a uniform layer of cells on the bottom of well plates (using a flat bottom 24-well plate), the aforementioned array of pyramidal structures could be tested for membrane penetration and cell viability through manual pressure. The purpose of this assay was to simulate the conditions in which the system would be implemented with biopsies. For that, membrane penetration is crucial for the measurement of cellular internal pH, whilst cell viability would infer about eventual damages to the cell membrane during the measurements.

To test cell viability, cell lines were unfrozen and grown in a Falcon flask with D-MEM_c culture media (without phenol, as to prevent contamination of colorimetric measurements later on), consisting of 84% D-MEM (Dulbecco's Modified Eagle's Medium), 15% FBS (Fetal Bovine Serum) and 1% antibiotic, until a cellular monolayer was formed (at least 80% confluency). Once cells matured and the desired confluency was achieved, the culture media was removed and the Falcon flask, containing a monolayer of adhered cells, was washed with a 0.1 M PBS (Phosphate Buffered Saline), pH 7.5, and treated with Trypsin, an enzyme that promotes cell dissociation by targeting protein hydrolization. By separating the cells, these could be transferred into well plates for testing. Incubation at 37 °C with D-MEM_c allowed for a new monolayer to form inside the testing well plates.

Once a monolayer of culture cells with at least 80% confluency had established inside the well plates, the microfabricated test samples with pyramidal structures were inserted into the well plates with the structures facing the cells. In some cases, metallic weights with fixed mass (Table 7) were

added as to simulate pressure, as described in Figure 39. Control test samples, consisting of a die of non-machined silicon, were used as a model of comparison. Samples D-F were added a lyse compound to burst the cell wall and destroy cell viability. After 30 seconds of exposure in each well, the structures and the solution media were removed, and the wells were washed with PBS. At this stage, MTS reagent was added to allow for a colorimetric cell proliferation assay and the entire well plate was covered with aluminum foil to prevent exposure to light. The complete procedure can be found in Annexes 2 to 4.

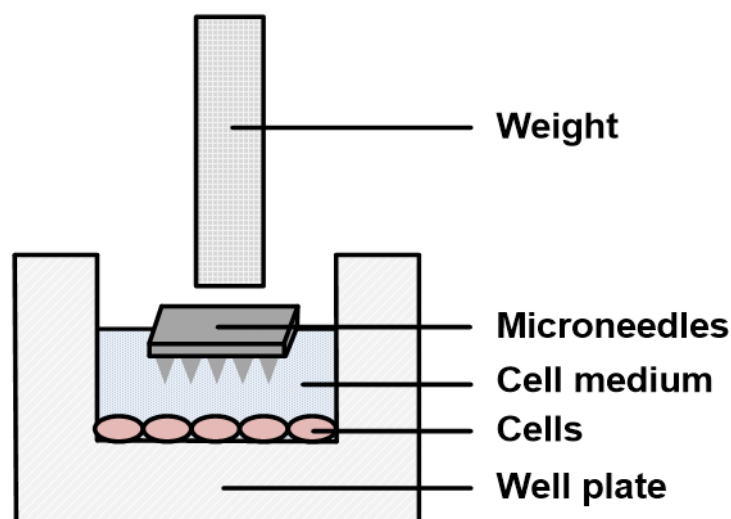


Figure 39 - Schematic diagram representing the setup used for the cell penetration assay using weights of fixed mass to simulate pressure.

All structures and weights were cleaned with PBS and DI water before and after use. Only the weights were re-used between samples, as they weren't in contact with cells except in samples S-W.

Table 7 - Experimental conditions used in MTS cell proliferation assay. Samples A-C and X consisted in control cells. Samples D-F consisted in lysed cells, in which a minimum absorbance should be read. In samples H-L and N-R, weights were added along with the described structure. In samples S-W, the weights alone were placed on top of the cells, without any structure underneath.

Sample #	Test condition	Puncture Force (N/m)	Sample #	Test condition	Puncture Force (N/m)
A	Control cells		M	Test structure	
B	Control cells		N	Test structure	2.54
C	Control cells		O	Test structure	4.23
D	Lyse cells		P	Test structure	6.17
E	Lyse cells		Q	Test structure	11.61
F	Lyse cells		R	Test structure	14.40
G	Control structure		S	Weight	2.54
H	Control structure	2.54	T	Weight	4.23
I	Control structure	4.23	U	Weight	6.17
J	Control structure	6.17	V	Weight	11.61
K	Control structure	11.61	W	Weight	14.40
L	Control structure	14.40	X	Control cells	

Puncture forces for biological cells strongly depend on the cell and tissue type. Researchers have estimated a puncture toughness for human cells ranging from $G_p = 1 \times 10^{-3}$ N/m [120] (human oocytes) to $G_p = 3 \times 10^4$ N/m [121] (human skin). Although there is still a lack of data regarding the puncture toughness of monolayer cultured cells, their morphology differs from the human skin, which is considerably stronger. Therefore, a more exact approximation would be towards the values registered for single cells, such as the oocytes. Penetration is achieved if the applied pressure is higher than the puncture toughness of the cell.

To ascertain the cell viability after the puncture and phase, the MTS cell proliferation assay was chosen as a quantitative colorimetric assay that promotes the reduction of the MTS tetrazolium compound by viable cells to generate a colored formazan product that is soluble in cell culture media. Only metabolic active cells, and thus undamaged cells, are able to carry out this conversion by the

NAD(P)H-dependent dehydrogenase enzymes. Irreversible cell damage, caused by the test structures, should provide lower readings of absorbance.

After a period of incubation of 1 hour at 37 °C, the well plate was then analyzed at a Synergy HT Reader for the Absorbance at 490 nm, at a temperature of 27.1 °C. The results can be observed in Figure 40.

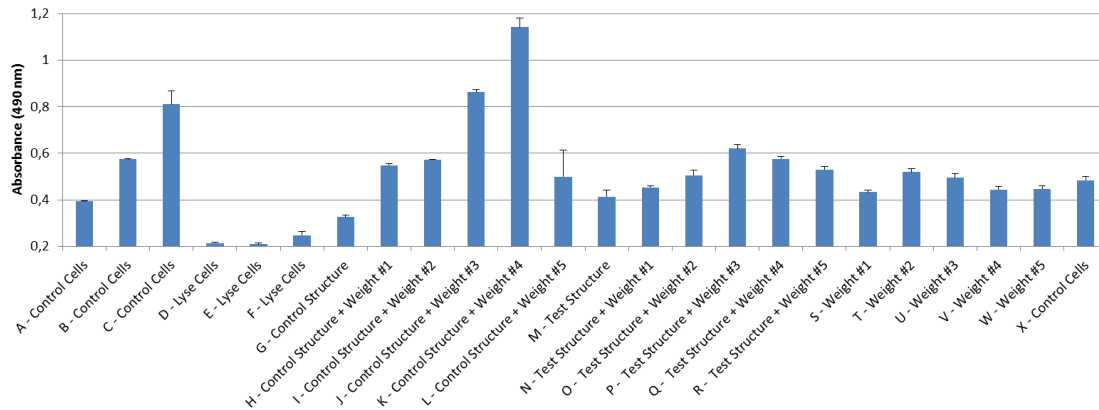


Figure 40 - Graphical representation of the absorbance results at 490 nm for the experiments described in Table 7.

The obtained results are mostly inconclusive and differ largely from what expected. Contrarily to the described results, samples A-C and X should present the highest absorbance value, since no damaging agent was applied in these wells. However, not only these 4 samples provide different readings (with sample A registering half the absorbance of sample C) but some of the testing samples provided a higher absorbance (such as samples J and K). Since different structures were used for each well, and the weights were only exposed directly to the cells at the last testing wells, it is unclear if a cross contamination occurred between wells. Furthermore, tests with added pressure show to increase cell viability, which is contrary to the expected results.

3.2.4 - Process assessment and redefinition

Without a clear notion of the explanation behind the results derived from the cell penetration assay, a new outlook on the approach to measure cell penetration and viability was required. Since the structures were microfabricated in Silicon, microscopic observation of cell penetration isn't possible. Therefore, a new strategy was devised:

1. New microfabricated structures should have a transparent base that would allow for microscopic observation of cell penetration.
2. Inverted confocal microscopy should be used, for accessing both cell membrane and structure tip simultaneously, allowing for a more precise observation of the process.

Further processing of the pyramidal structures would also be performed through the same lithographic steps defined previously. However, a few contemplations that could limit the success of the process were taken into consideration:

1. The standard PR used in the lithographic process could not achieve a thickness high enough to cover the newly created pyramidal structures.
2. Thicker PR was available, but the DWL system is optimized for a depth penetration of 1.5 μm . Deeper laser penetration could be achieved with consecutive sweeps, but at the expense of profile definition and laser focus.
3. Laser scattering could be a serious consequence of consequent sweeps through the pyramidal structures, affecting and damaging the PR in a wider area around them.
4. The produced patterns would have a severe inclination (wider at the surface, where the PR molecules would be more exposed to the laser, and narrower at the bottom), that would render the process unsuccessful for lift-off steps.
5. Without lift-off, patterning of metallic layers would require the use of dry etching techniques, which would be incompatible with the available equipment for the required thicknesses.
6. In order to achieve a stable electrode, a thick Silver layer would need to be deposited on top of the pyramidal structures. Without the ability to perform lift-off, or to use dry etching on thick layers, it would not be possible to follow the Runsheet processes as described.
7. To increase the chances for cell penetration, a high aspect ratio between height and width should be obtained.

8. Without the possibility to directly manipulate the Silicon substrate into vertical walls (without complex processing which was not available), nor increasing the etched angle of the μ -pyramids, an increase in height could only be achieved by depositing a thick layer that would grow upwards in the z-axis.
9. Electroplating could be used to both bolster the electrode thickness, and increase its height.
10. However, through electroplating, every surface irregularity is exponentially increased due to variances in the nucleation rate around those areas.
11. Furthermore, most electroplating processes form isotropic growths. Although the x/y-axis could be limited by a patterned photoresist encasement (limiting the lateral growth of the electrodes), growth in the z-axis would biasedly form rounded tips, not suitable for cell penetration.

Taking into account all of these considerations, a direct micromachining approach (i.e., functionalizing microfabricated silicon pyramidal structures) presented a greater challenge to the protocols and equipment available. Although more complex in processing, the fabrication of a solid-state electrode through mold-filling or electroplating of an inverted pattern met all the required criteria and was compatible with the available equipment, lacking the necessary adaptation to standard processing conditions.

In this approach, an array of pits would be created using the optimized conditions for the Silicon Wet Etching processing. A thick PR would then be coated on top and patterned as to open a pathway towards those pits, in order to attribute a higher depth penetration and perforation abilities to the microelectrodes. The total height of the electrodes would therefore consist in the sum of depth of the pit (which promotes a higher aspect-ratio by being formed at 54.7° , vs the aforementioned 46.5° registered for top-machined pyramids due to the microloading effect) and the height of the patterned PR.

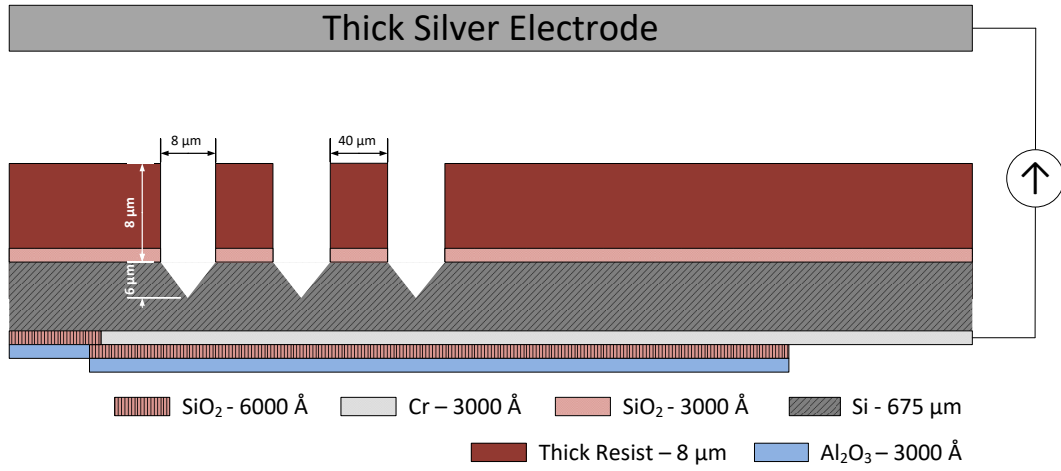
The empty space could then be filled through mold-filling or electroplating, creating the desired solid-state electrode. Mold-filling metals would require the pouring of the desired melted material over the substrate. Although Silicon itself could, theoretically, withstand the direct contact with molten Silver without suffering severe damage (melting point of 1414°C vs 961.8°C , respectively), the same can't be said regarding the available photosensitive polymers (maximum temperature of 140°C). An

Electrodeposition processing would be compatible with all the materials and requirements, and was therefore selected as the method of fabrication for the solid-state electrodes.

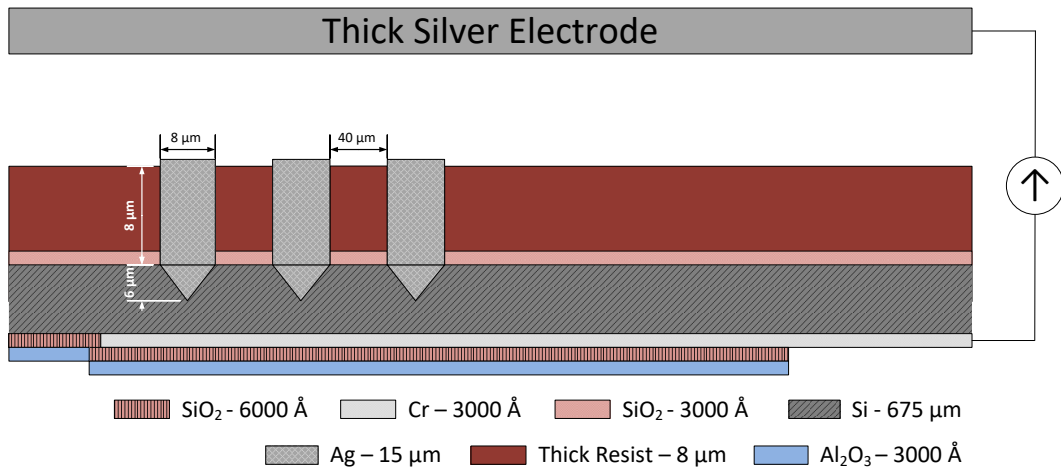
Silver was selected as the material to fill the cavities through Electrodeposition, with one of the electrodes engraved on the backside of the wafer and using the semiconductive properties of the Silicon to allow for an electrical pathway to be established. This process allows for the electrodeposition to begin in the lowest point of the cavity formed during the wet etching, and therefore, the bottom of the inverted pyramid. From this point, crystalline growth of the Silver matrix would be formed upwards, filling the empty space (Figure 41 (a) and (b)). By controlling the conditions of the process, a set-time can be defined for which the overplating of Silver is minimal, as to prevent increased topography at the surface of the wafer that could limit further microprocessing steps.

At the surface of the wafer, layers for insulation and electric contact would be deposited and patterned through small adaptations to the same microfabrication processes used before. Having the system completed, a final polymeric layer (PDMS - Polydimethylsiloxane), followed by the removal of the intermediary PR layer, would allow for the entire structure to be detached and expose the microfabricated solid-state Silver microneedles (Figure 41 (c) and (d)).

A



B



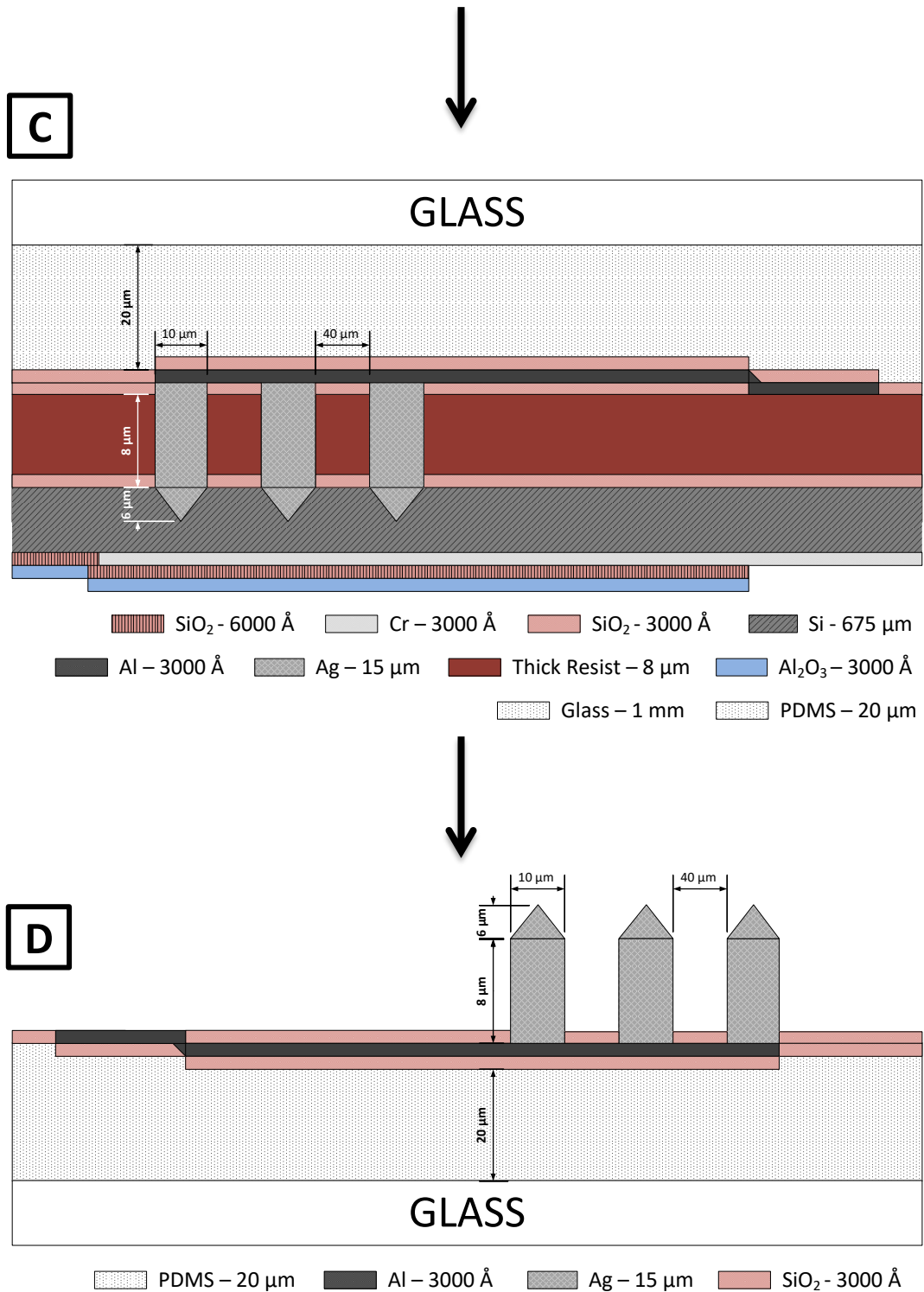


Figure 41 - Schematic diagram representing the cross-section view of the microfabrication steps for the proposed sensor, depicting the method to form solid-state Silver electrodes through electrodeposition and the release method with the assist of a transparent polymer. (a) Patterning of a mold for the; (b) Fabrication of thick Silver microelectrodes; (c) Vias patterning for contact signal acquisition and encapsulation with a solid substrate and a polymeric buffer; and (d) Structure release and functionalization.

A complete overhaul of the microfabrication process was required at this stage, since this strategy would require for dual-side processing of the silicon wafers. A 2-electrode system was implemented for the Silver electrodeposition process, using a solid Silver slab as the Counter Electrode, and an Ohmic electrical contact in the backside of an engraved Silicon wafer to act as the Working electrode. The working electrode patterning was required before engraving any structures in the Silicon matrix, as the wet etching process would damage the entire exposed surface, if not protected. Once completed, profile definition of the μ Needles structure was achieved through KOH wet etching, creating inverted pyramids with 4 identical {111} walls. An 8 μm thick PR was then coated and patterned on top of the engraved structures, creating a mold for the Silver plating process. Further processing consisted in the deposition of oxide and metallic layers for contact patterning, which can later be used for signal acquisition once the structure release and activation is completed.

To better track which side the processing was meant to take place in each step, the silicon wafers were defined as having a front side and a back side, being the former defined by the patterning of pyramidal pits.

A complete description of the microfabrication steps can be observed in Table 8. The next section details these steps.

Table 8 - Process steps for the microfabrication of the proposed system. Complete Runsheet in Annex 5. Complete schematic of the process in Annex 6.

#	TECHNIQUE	D	E	P	EQUIPMENT	MATERIAL	THICK	F	B
<u>WORKING ELECTRODE PATTERNING</u>									
01	<u>Wafer dicing</u> Into ¼ of a 6" Silicon wafer			X	—				
02	<u>PVD – Magnetron Sputtering</u> Mask layer for step #09	X			Alcatel	SiO ₂	3000 Å	X	
03	<u>PVD – Magnetron Sputtering</u> Electric contact for step #15	X			Alcatel	Cr	3000 Å		X

D - Deposition; E - Etching; P - Processing; F - Sample front side; B - Sample backside; Thick - Thickness; T.B.D. - To be defined. Shadings: Blue) steps performed on the sample backside; Grey) different sections of the microfabrication process.

Table 8 - (continuation)

#	TECHNIQUE	D	E	P	EQUIPMENT	MATERIAL	THICK	F	B
04	<u>DWL – Lithography</u> Definition of Chromium pattern			X	DWL	PFR 9950 G +PR	1.4 μm		X
05	<u>Chromium Wet etching</u> Patterning of Chromium layer		X		Wet bench	Cr etchant	3000 \AA		X
06	<u>PVD – Magnetron Sputtering</u> Protection from step #09	X			Alcatel	SiO_2	6000 \AA		X
<u>PROFILE DEFINITION</u>									
07	<u>DWL – Lithography</u> Patterning for step #09			X	DWL	PFR 9950 G +PR	1.4 μm	X	
08	<u>RIE</u> Mask definition for step #09		X		LAM	SiO_2	3000 \AA		X
09	<u>Silicon Wet etching</u> Patterning of inverted pyramids		X		Wet bench	KOH solution	5 μm		X
10	<u>PVD – Magnetron Sputtering</u> Stop current leakage on step #15	X			UHV 2	Al_2O_3	3000 \AA		X
11	<u>DWL – Lithography</u> Create pads for step #15			X	DWL	PFR 9950 G +PR	1.4 μm		X
12	<u>RIE – Vias etching</u> Open Vias for pads for step #15		X		LAM	SiO_2	6000 \AA		X
13	<u>DWL – Lithography</u> Thick PR to define needle height			X	DWL	ma-P 1275 +PR	8 μm	X	
<u>SILVER PLATING</u>									
14	<u>Wafer dicing</u> Into individual dies for process			X	Dicing Saw				
15	<u>Silver Electrodeposition</u> Create “solid-state Ag needles”	X			Electroplatin g Setup	AgNO_3 solution	15 μm	X	

D - Deposition; E - Etching; P - Processing; F - Sample front side; B - Sample backside; Thick - Thickness; T.B.D. - To be defined. Shadings: Blue) steps performed on the sample backside; Grey) different sections of the microfabrication process.

Table 8 - (continuation)

#	TECHNIQUE	D	E	P	EQUIPMENT	MATERIAL	THICK	F	B
CONTACT PATTERNING									
16	PVD – Magnetron Sputtering Insulation + protect from chemical attacks	X			Alcatel	SiO ₂	3000 Å	X	
17	DWL – Lithography Create access to needles and pads			X	DWL	PFR 9950 G +PR	1.4 μm	X	
18	RIE – Vias etching Open Vias for needs and pads		X		LAM	SiO ₂	3000 Å	X	
19	PVD – Magnetron Sputtering Deposit Al for electrical contact	X			N7000	Al	3000 Å	X	
20	DWL – Lithography Define Patterning for step #23			X	DWL	PFR 9950 G +PR	1.4 μm	X	
21	Aluminum Wet Etching Pattern Al layer		X		Wet bench	Al etchant	3000 Å	X	
22	PVD – Magnetron Sputtering Final electrical insulation	X			Alcatel	SiO ₂	3000 Å	X	
STRUCTURE RELEASE AND ACTIVATION									
23	PDMS pouring and baking To allow for step #26	X			Hot plate	PDMS	N/A	X	
24	Structure Release Detach the structures from the Si substrate			X	Wet bench	Acetone	N/A	X	
25	pH sensitive layer deposition Deposit pH sensitive layer over needles	X			T.B.D.	T.B.D.	T.B.D.	X	

D - Deposition; E - Etching; P - Processing; F - Sample front side; B - Sample backside; Thick - Thickness; T.B.D. - To be defined. Shadings: Blue) steps performed on the sample backside; Grey) different sections of the microfabrication process.

3.2.5- Working electrode patterning

As defined in subchapter 3.2.2, Silicon Wet Etching was used in the definition of the microelectrodes profile. However, as demonstrated in the optimization step, KOH wet etching causes profile roughness

at the surface of the wafer. Furthermore, only a few of the available materials are chemically resistant to it, from which we can highlight Chromium, Silicon Dioxide and Silicon Nitride.

To begin with, 6" Silicon wafers were diced in quarters, as to fit inside some of the microfabrication equipment. A Silicon Dioxide layer was deposited on top of the front surfaced at Alcatel SCM 450 Magnetron Sputtering (2.10 mTorr, 20 sccm Argon, 4 rpm, 140 W_{RF}, 107 min for a 3000 Å thick layer). This material was chosen over Chromium (used in the first process Runsheet) for two reasons:

1. Supplies an electrical insulation during the electroplating process, preventing crystal growth in areas that are not defined by the etched pattern.
2. Allows for Chromium to be used on the opposite side of the wafer as a conductive layer for the working electrode without the risk of damage during patterning (as a wet etch process, Chromium patterning removes all exposed material, including both sides of the wafer). For this situation, a secondary protective layer of Silicon Dioxide or Nitride could have been deposited on top of the Chromium, but with redundant results and overcomplicating the overall processing.

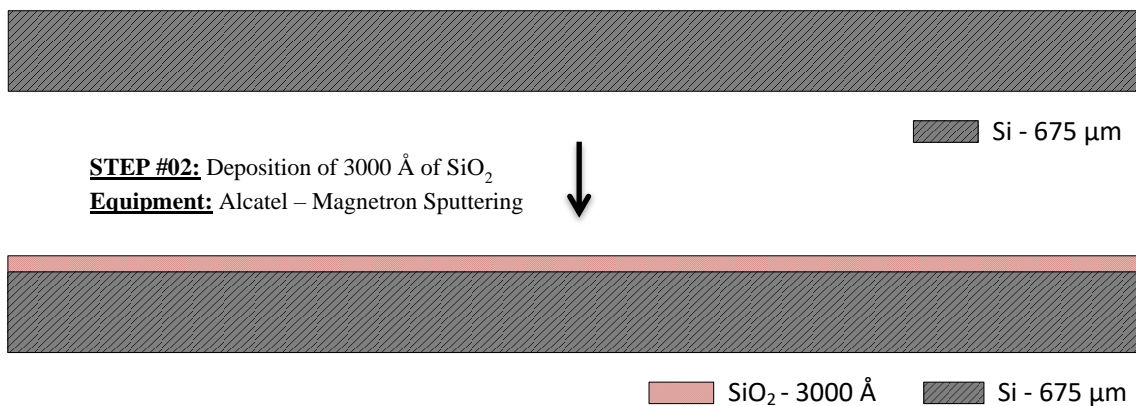


Figure 42 - Schematic diagram representing the cross-section view of the microfabrication steps for step #02: deposition of 3000 Å of Silicon Dioxide, through Magnetron Sputtering, on top of a Silicon Wafer with a thickness of 675 μm.

As stated, to ensure a good electrical contact during the electrodeposition step, a conductive layer of Chromium was deposited and patterned on the back side of the wafer, using the same equipment and process as before (Alcatel SCM 450 Magnetron Sputtering, under the following conditions: 3.07 mTorr, 20 sccm Argon, 20 W_{DC}, 51 min for a 3000 Å thick layer). A Resistivity of 471 ± 43 nΩ.m was

registered for the deposited samples, which can be compared for the Chromium bulk Resistivity of 130 nΩ.m at 20 °C [122]. Although a slight difference in electrical resistivity can be observed, it falls under an acceptable range.

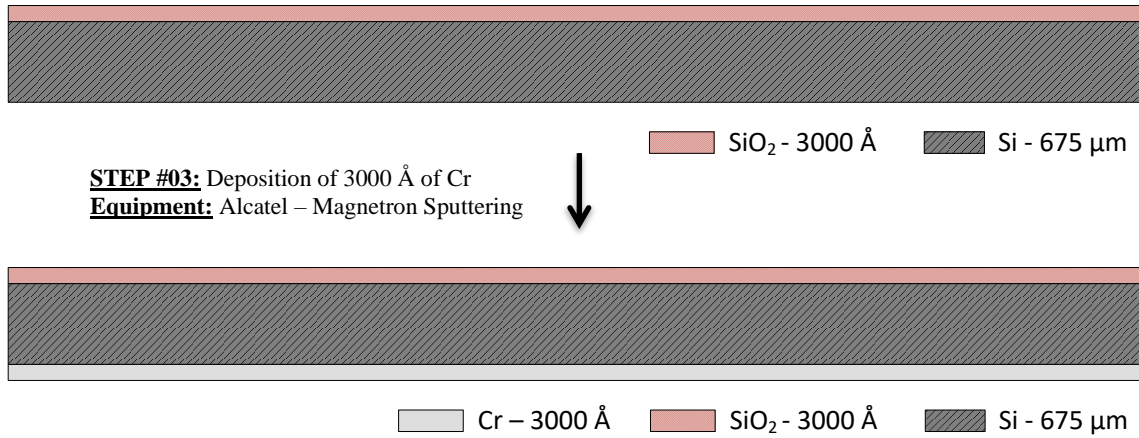


Figure 43 - Schematic diagram representing the cross-section view of the microfabrication steps for step #03: deposition of 3000 Å of Chromium, on the backside of the sample, through Magnetron Sputtering.

The Chromium layer was then patterned using the DWL system, according to standard Photoresist PFR 7790 G, 1.5 μm thick, lithography protocol. A rectangular profile (shown in Figure 44) was patterned for each individual die (a total of 8 dies were packed in each quarter of a 6'' Silicon wafer). The 30 × 12 mm will define the overall size of the die once diced, whilst the 27 × 6 mm rectangular space in the middle will be protected from etching, and therefore form the electrical contact pad. A 3 mm distance from the bottom and sides was kept assuring a more confined current density in the desired area, allowing for a direct control of the surface that is directly exposed to the electroplating process.

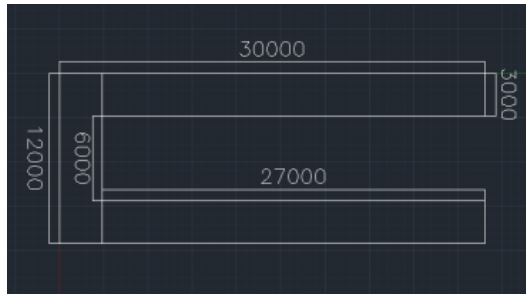


Figure 44 - AutoCAD™ image representing the profile patterned through Direct Writing Lithography for Step #04. Each ¼ of a 6" Silicon wafer contained 8 identical profiles, representing 8 different dies. All measures and dimensions are represented in micrometers. Mask name: TmPH_backcontact.

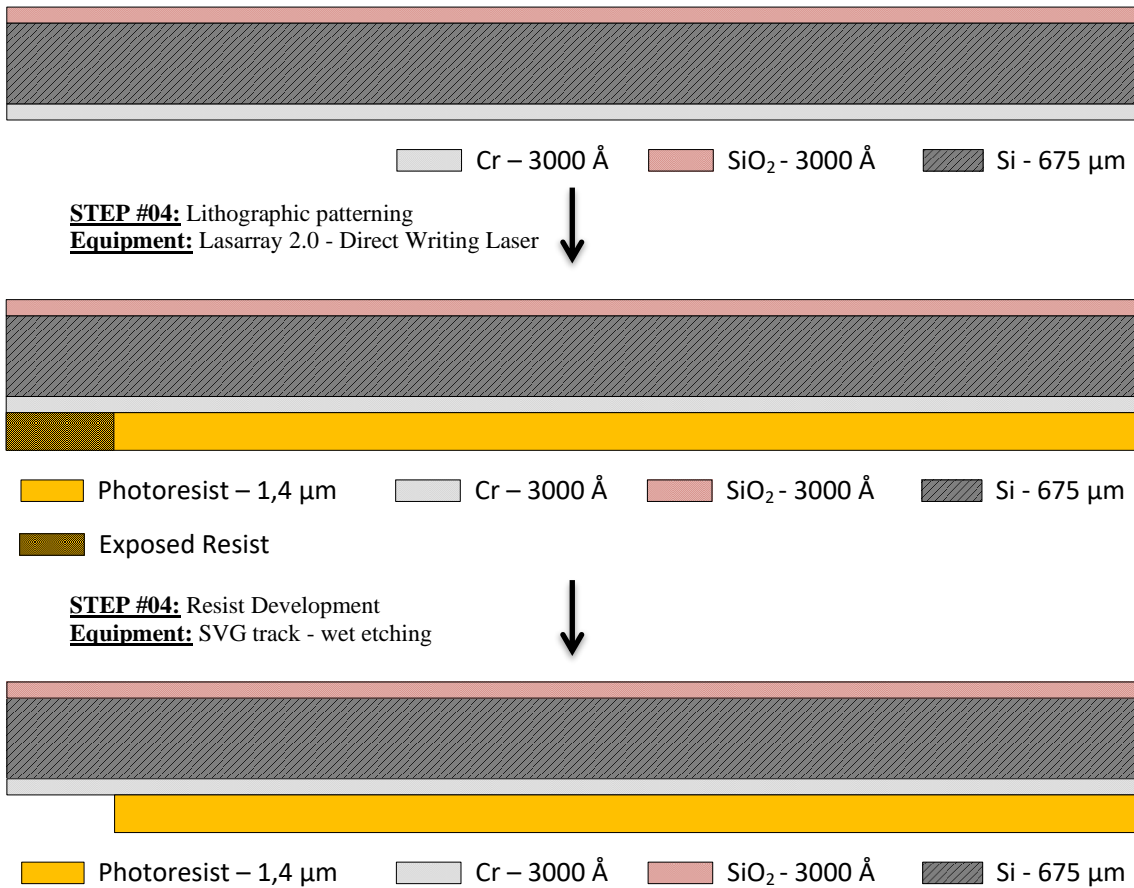


Figure 45 - Schematic diagram representing the cross-section view of the microfabrication steps for step #04: deposition of a 1.5 μm thick PFR 7790 G +PR, patterning through Direct Writing Laser, and resist development, on the backside of the sample.

With the profile patterned into the Photoresist, it was then transferred to the Chromium layer using the same wet etching process (Sigma Aldrich 651826 Chromium Etchant, St. Louis, MO, USA) with orbital rotation at room temperature until the profile became visible. After microscopic inspection, the 1.5 μm thick PFR 7790 G +PR was removed with Acetone and the sample was cleaned with IPA and DI water.

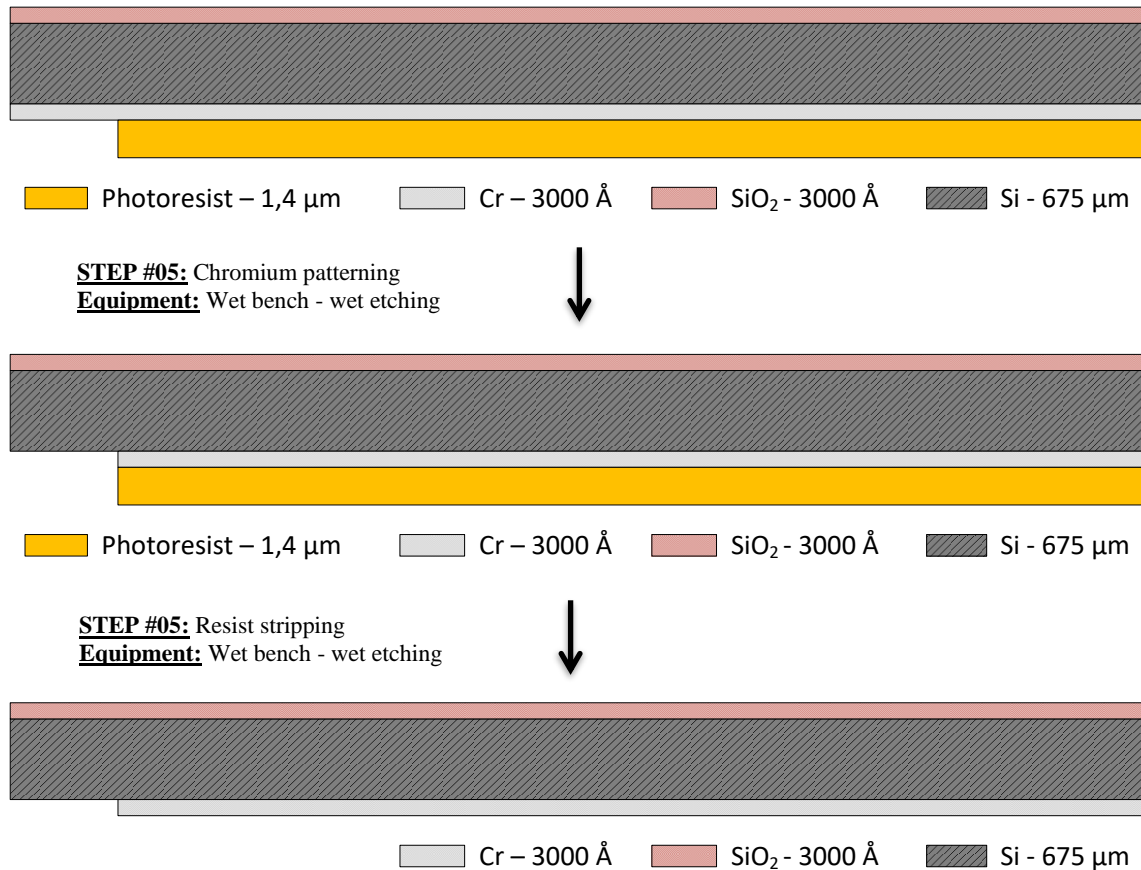


Figure 46 - Schematic diagram representing the cross-section view of the microfabrication steps for step #05: spin coating of a 1.5 μm thick PFR 7790 G +PR layer, patterning through Direct Writing Laser, and resist development, on the backside of the sample.

A layer of Silicon Dioxide was then deposited over the entire back surface of the wafer as to cover the Chromium and prevent any possible damage during the Silicon Wet Etching process that could affect the conductivity of the Chromium layer. This process was performed at Alcatel SCM 450 Magnetron Sputtering, under the following conditions: 2.10 mTorr, 20 sccm Argon, 140 W_{RF} , 4 rpm, 214 min for a 6000 \AA thick layer.

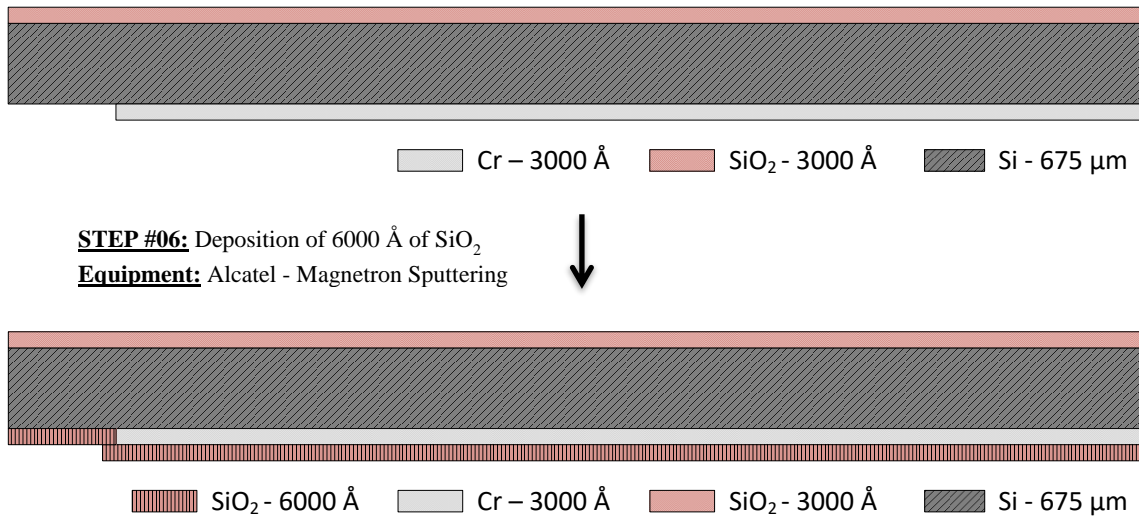


Figure 47 - Schematic diagram representing the cross-section view of the microfabrication steps for step #06: deposition of 6000 Å thick of Silicon Dioxide, on the backside of the sample, through Magnetron Sputtering.

3.2.6 - Profile Definition

Having the backside of the wafer patterned and protected, the frontside could be processed for etching. For that, a lithographic patterning at DWL allowed for the inscription of $8 \times 8 \mu\text{m}$ squares, distanced by $40 \mu\text{m}$, (as seen in Figure 48) on the surface of the frontside Silicon Dioxide layer. A total area of $4.624 \times 10^{-7} \text{ m}^2$ is created in this array of 85×85 square holes. Alignment marks, in the form of crosses, were also added for future mask to be perfectly aligned with the underlying profile. This process is performed automatically at the DWL station.

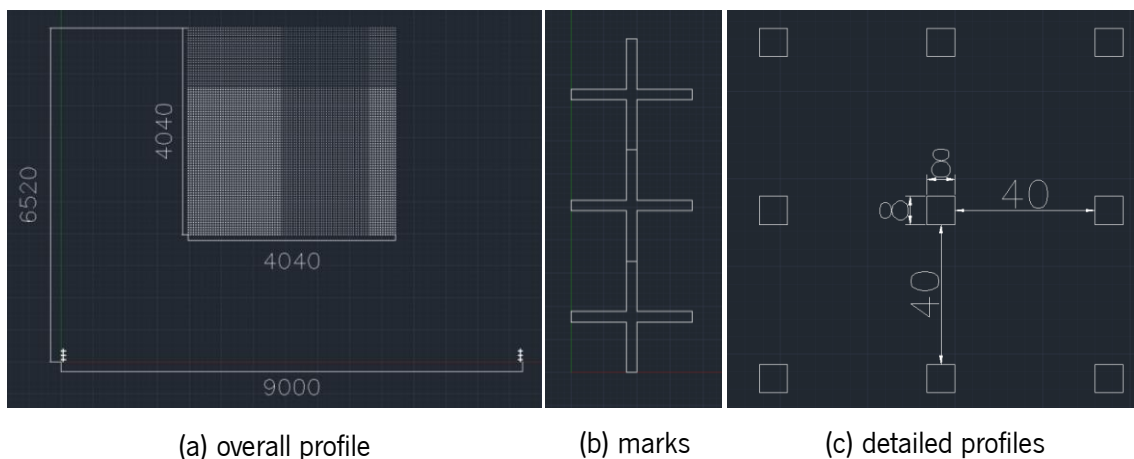


Figure 48 - AutoCAD™ image representing the profile patterned through Direct Writing Lithography for Step #07. Each ¼ of a 6" Silicon wafer contained 8 identical profiles, representing 8 different dies. (a) Overall profile; (b) detail on the alignment marks that would allow for a secondary lithography later on; and (c) detail on the matrix profile. All measures and dimensions are represented in micrometers. Mask name: TMpH_holes.

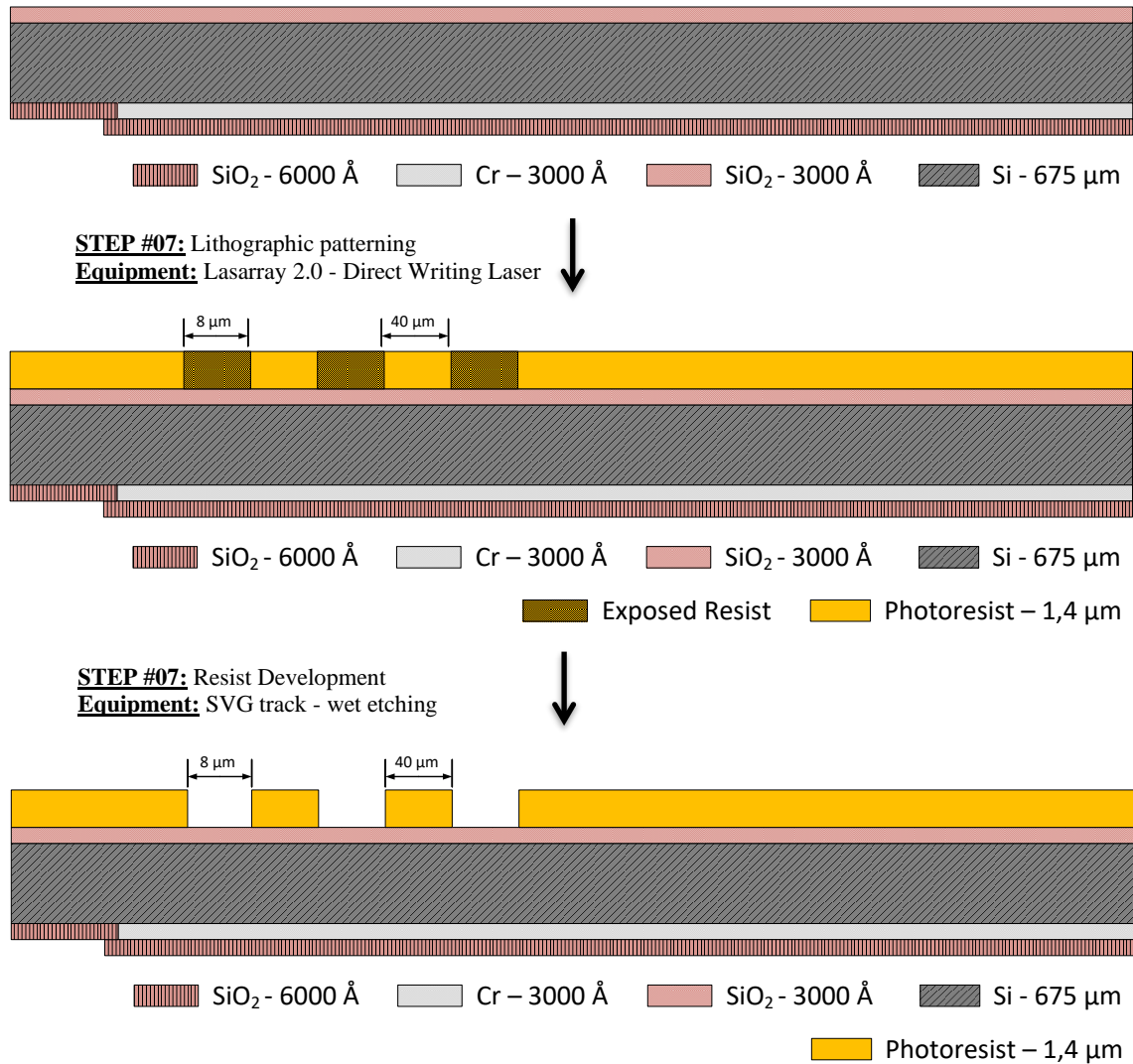


Figure 49 - Schematic diagram representing the cross-section view of the microfabrication steps for step #07: spin coating of a 1.5 μm thick PFR 7790 G +PR layer, patterning through Direct Writing Laser, and resist development.

Once patterned, the Silicon Dioxide layer was etched using LAM Rainbow 4400 Plasma Etching (pressure during process = 140 mTorr, wafer area pressure = 305 mTorr, 100 W_{RF}, 200 sccm Argon,

100 sccm CF_4 , 10 sccm O_2 , 6×150 seconds). In this process, a stream of plasma formed by the mixture of gases is directed towards the sample, reacting with it and forming volatile etch products that are removed from the sample. The main reactive gas used in Silicon Dioxide etching is CF_4 . Since this is a chemical process, only species that are reactive to the plasma mixture are affected by this process, granting a greater control of the etch depth by placing intermediary layers that are inert to the specific mixture. Once again, the PRF 7790 G +PR is removed through Acetone once the process is complete, and the sample is cleaned with IPA and DI water.

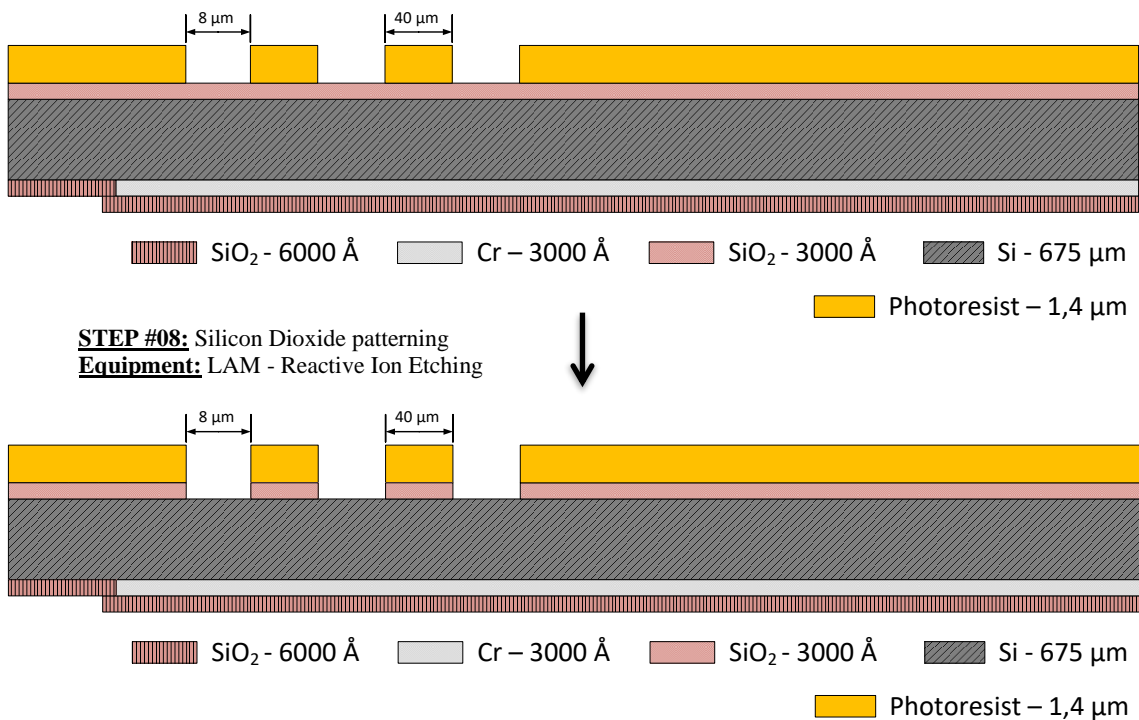


Figure 50 - Schematic diagram representing the cross-section view of the microfabrication steps for step #08: etching of the Silicon Dioxide layer, through Reactive Ion Etching.

For the present work, the material underlying the Silicon Dioxide layer was the Silicon wafer itself. In this situation, Silicon can be affected and removed, but at a considerably lower etch rate, thus working as a decent etch stop material.

However, this process tends to oxidize the surface of the Silicon matrix, which can hinder the efficiency of the Silicon Wet Etching process through diluted KOH solution. The same superficial oxide forms naturally and gradually with exposure to atmospheric air, as a consequence of the presence of Oxygen. Whilst in the previous Runsheet Chromium etching was performed in a non-oxidizing chemical

solution and Silicon wet etching was performed immediately after, for the present Runsheet surface oxidation is a factor to be taken into consideration before further processing.

To remove any residual surface oxidation, the sample was previously cleaned with Acetone, IPA and DI water (which also removed any residual photoresist that could block the access to the wafer surface), and then immersed inside a Buffered Oxide Etch (BOE) solution (Sigma-Aldrich™) for 1 minute, ensuring a constant manual agitation. Although this solution also reacts with the Silicon Dioxide layer that is acting as a mask, the immersion is performed in a considerably short amount of time and at room temperature, which ensures that only superficial oxidation is removed, and no major consequences are applied to the thicker 3000 Å layer.

Having the surface cleaned, Silicon wet etching through diluted KOH solution could be performed using the optimized conditions achieved previously. However, performing the etching process in a considerably larger sample (a quarter of a 6" Silicon wafer), the volumes were adjusted accordingly. Silicon wet etching was performed in a HDPE flask containing 120 mL of a 22% KOH solution and 10 mL of IPA. Although IPA did not influenced greatly the etch profile in pits, it did assisted as a surface buffer and cleaner [88, 91, 93, 94], removing any impurity from the previous cleaning process and allowing for a smoother etch start. The etching was performed during 40 minutes at 39 °C to achieve a complete profile definition. Over-etching plays a meaningless role in this method since the structures formed in the process are surrounded by the {111} plane, which in this situation have an etch rate nearly 100× slower than that for the {100} plane [88].

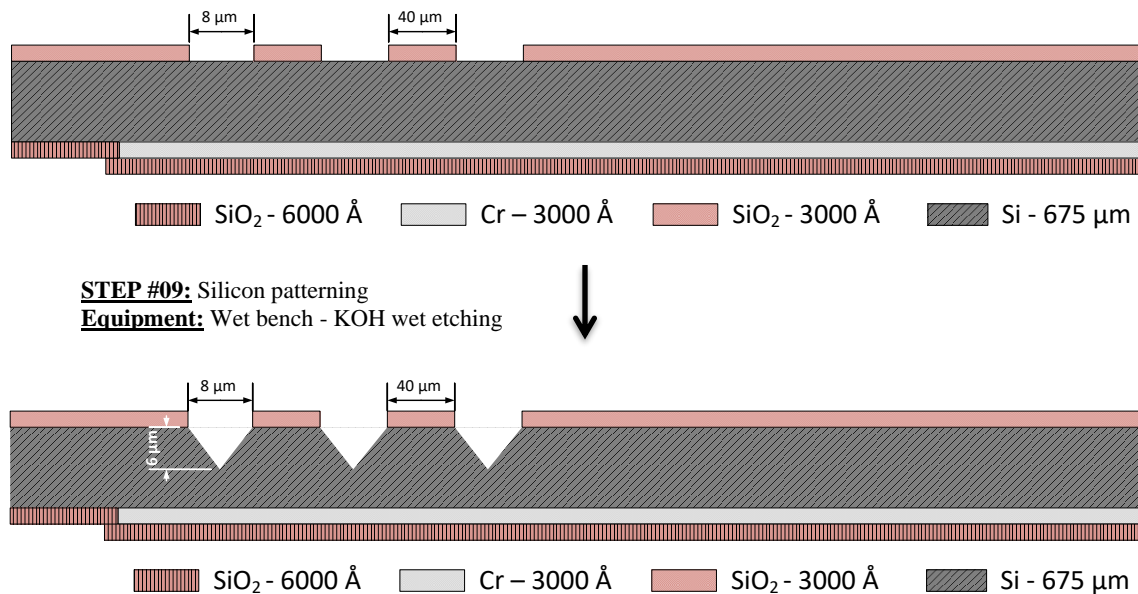


Figure 51 - Schematic diagram representing the cross-section view of the microfabrication steps for step #09: wet etching of the Silicon substrate, through a diluted KOH solution.

Microscopic inspection allowed for the assessment of etch quality and confirm etch time. By juxtaposing images at different focal points, we can analyze both the surface and the depth of the structures. In Figure 52 (a), we can observe the profiled pits (dark grey) opposing the wafer surface (bright brown). In Figure 52 (b), the same location is focused on a great depth, demonstrating 4 crossed lines that represent the light diffraction at the {111} walls of the newly formed pit (in this case, an inverted pyramidal structure).

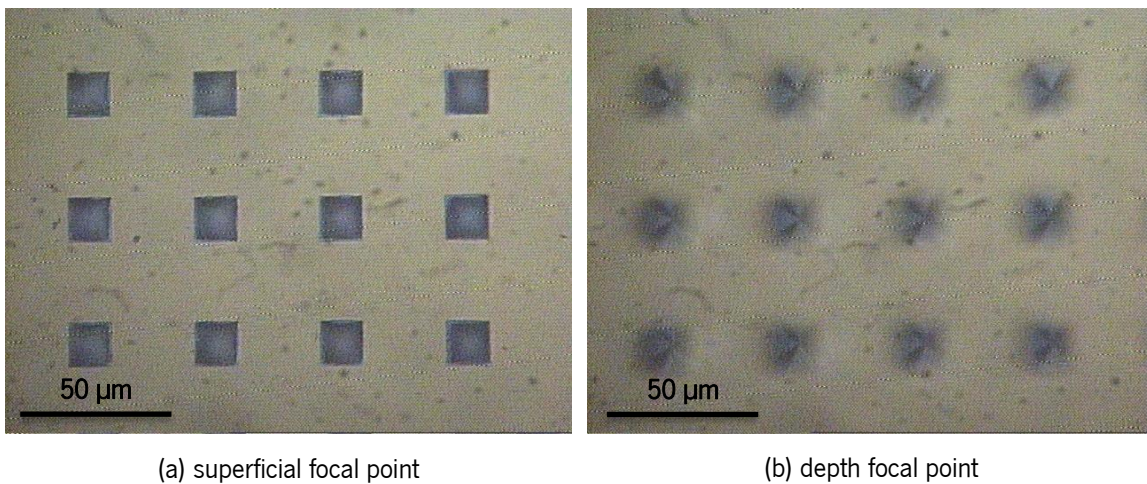


Figure 52 - Microscopic inspection of samples processed through Silicon wet etching (22% wt diluted KOH solution, 40 min at 39 °C with ultrasonic agitation). (a) Focal point at the surface of the Silicon wafer; and (b) at the bottom of the newly created pits. The intercross of the 4 walls at the center of the profiles, in (b), indicates the completion of the process. Slight offset of the intercross towards the profile position is due to optical misalignment of the microscope lenses.

After microscopic inspection and once the samples were cleared for defects, a 2000 Å layer of Alumina (Al_2O_3) was deposited on the backside of the wafer through Magnetron Sputtering PVD at UHV-2 (2.10 mTorr, 45 sccm_{Ar}, 200 W_{RF}, 165 min). This layer would cover any newly exposed area of the conductive inner layer as a consequence of KOH etching. A glass hard-mask would be carefully

positioned over the future pad area as to prevent Alumina deposition in this zone and reducing the number of steps required to open a Via to the conductive layer.

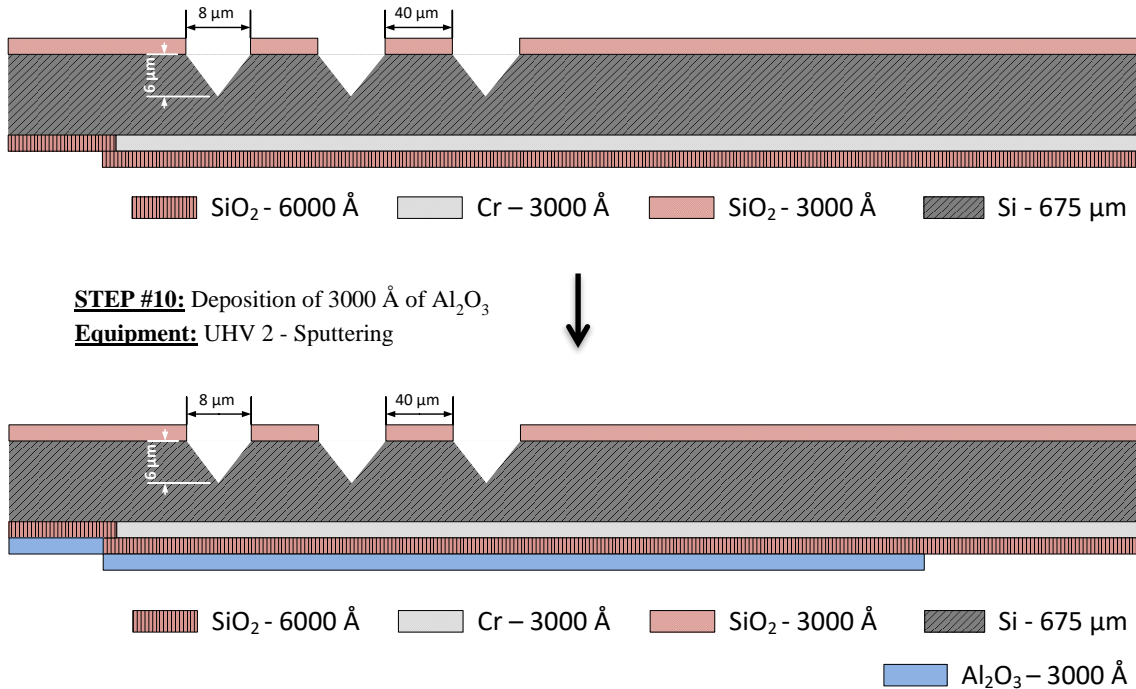


Figure 53 - Schematic diagram representing the cross-section view of the microfabrication steps for step #09: wet etching of the Silicon substrate, through a diluted KOH solution.

Once the process was completed, the backside of the sample would be coated again with the PFR 7790 G +PR under recipe 6/2 and exposed at the DWL. An area of 7 × 6 mm would be opened in the top of each individual die as to allow for access to the conductive layer. This access would be achieved after the removal of the SiO₂ layer through LAM etching, under similar conditions as before. Since Chromium isn't greatly affected by the plasma generated, it acts as a natural stop etch mask and no specific precautions need to be taken into consideration.

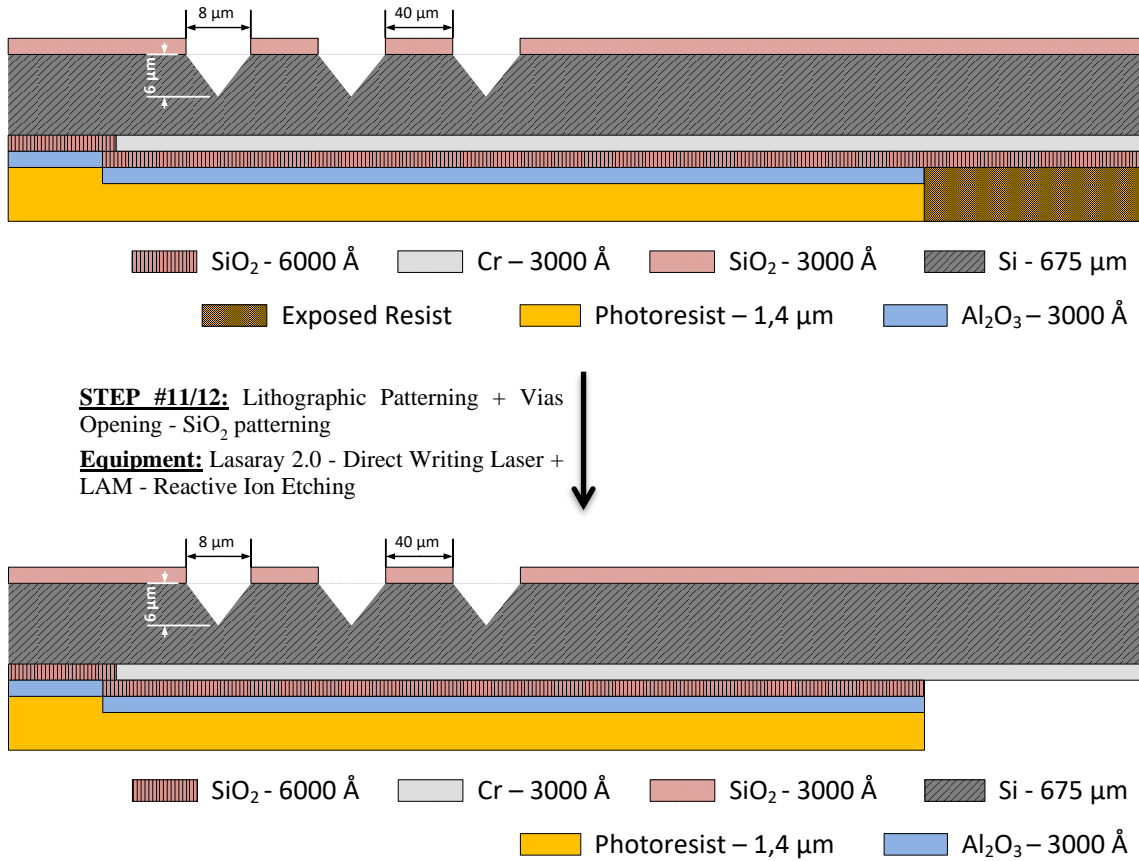


Figure 54 - Schematic diagram representing the cross-section view of the microfabrication steps for step #10: patterning and opening of the Vias through DWL lithography and RIE.

At this stage, with the removal of the excess Photoresist, the backside of the wafer is completely processed, with a defined conductive layer, a double electrical insulator layer (Silicon Dioxide and Alumina) and an open Vias.

To define the microelectrode height, and corresponding penetration depth, a thick PR would be spun on top of the Silicon front surface, covering the newly formed pits and their surroundings. This PR would need to fulfill the following requirements:

1. Be sensible to the same wavelength used in the Lasarray 2.0 DWL system, as it's the only lithographic system that comprises a precise alignment method compatible with the working dimensions of the microelectrodes.
2. Have a curing/development protocol compatible with the remaining materials deposited on the Silicon wafer (including temperature and solvents used).

3. Be resistant and inert to the electrodeposition process, preventing the adhesion of electrodeposition products to its surface and remaining unaffected by the overall process.
4. Be compatible with the standard microfabrication processes.
5. Be easily removed in conditions compatible with the remaining materials composing the microelectrodes (including temperature and solvents used).

From the available materials, ma-P 1275 +PR was selected for satisfying the noted requirements. Previous work developed at INESC-MN optimized the conditions for the deposition, patterning and development of the ma-P 1275 +PR. To achieve a thickness of $\sim 8 \mu\text{m}$ of PR, 10 mL of liquid ma-P 1275 +PR was poured on top of the sample ($\frac{1}{4}$ of a 6" Silicon wafer). The sample was then spun at 3000 rpm for 30 seconds, with an acceleration of 500 rpm/s, on the SVG track tool. Baking was performed on top of a hotplate, at 100 °C, for 10 minutes.

To ascertain the profile and dimensions of the ma-P 1275 +PR, a virgin Silicon sample was coated and patterned with mask **TMpH_holes**. To pattern such thick layers, the same mask needs to be used more than once in consecutive sweeps. With each sweep, an increasing amount of energy is transferred to the sample, in the exact same spot and pattern, which allows for the consecutive degradation of the molecules bond, whilst preventing charge accumulation at the surface or excessive heating of the material. For an 8 μm thick layer, a minimum of 5 sweeps is necessary to ensure complete patterning.

After exposure, the PR was developed manually by immersing the sample in the ma-D 1275 developer for 120 seconds. After rinsing with DI water, the samples were always inspected in the microscope. Once the PR hardened, the sample was then coated with a thick layer of PDMS (prepared by mixing 10:1 parts of pre-polymeric PDMS with curing agent (Sigma-Aldrich™)). The molded PDMS will be used to obtain clear SEM images of the patterned profiles. The liquid PDMS penetrates the exposed areas of the sample, including the profiles patterned through lithography, and creates a counter-mold of the entire sample surface. The PDMS was hardened inside an oven, at 70 °C, for 90 minutes. After hardening, the silicon sample was detached from the PDMS mold by removing the intermediary PR layer with Acetone. The cross-section view of the structure can be observed in Figure 55.

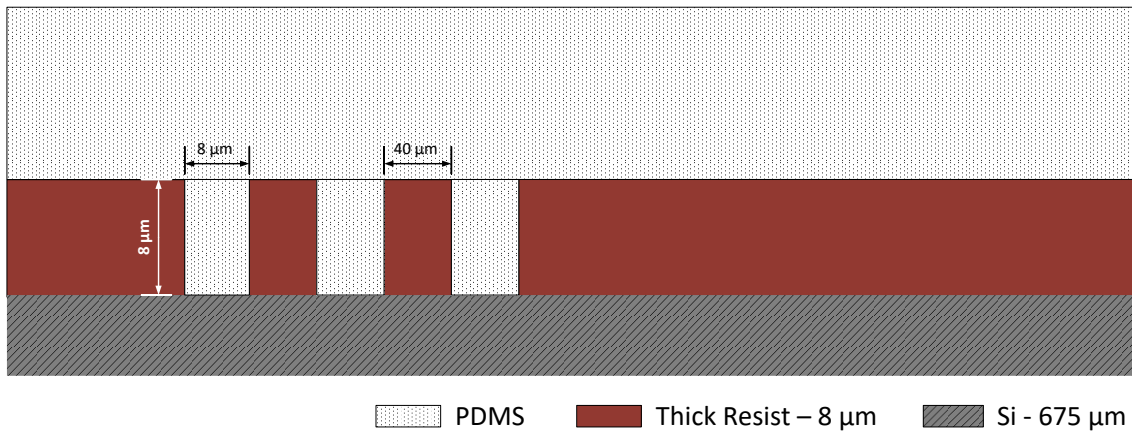


Figure 55 - Schematic diagram representing the cross-section view of the patterned structures filled with PDMS, as to ascertain the quality and dimensions of the TMpH_holes mask over the thick ma-P 1275 +PR.

The released PDMS mold was then coated with a thin layer of gold and analyzed in the SEM, as seen in Figure 56.

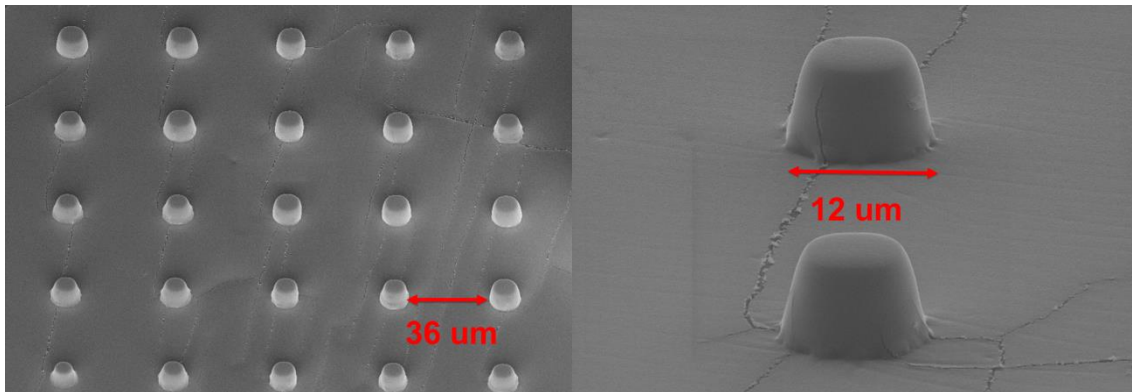


Figure 56 - SEM inspection of a PDMS counter-mold obtained from the patterning of an 8 μm thick ma-P 1275 +PR with the mask TMpH_holes. The base of the PDMS represents the surface of the PR, whilst the top of the PDMS represents the base (or pit) of the PR. The cracks seen in the image can be attributed to damage of the thin gold layer due to striation effects caused by the PDMS flexibility.

The SEM images show an increase in base width, from the projected 8 μm to a defined 12 μm, caused by the consecutive laser sweeps during the pattern exposure. Due to over-accumulation of energy in the same spot, part of the energy is dispersed laterally. As the laser is able to penetrate deeper into the PR, more and more energy is dispersed at the surface (top) of the PR, explaining the

profile obtained. To prevent cracks in the future, the PDMS can be hardened at higher temperatures (albeit that is limited by the thermal resistivity of the underlying materials, as will be seen in subchapter 3.2.9) or for longer periods of time.

3.2.7 - Silver plating

To test and optimize the electrodeposition process, dummy test samples, similar to the ones used in the complete process, were prepared. These samples lack the processing in the backside of the wafer and the pits created by Silicon wet etching, allowing for an extensive study of the electrodeposition process with lower costs and complexity. To prepare dummy samples, $\frac{1}{4}$ of 6" Silicon wafers were coated with two seed layers that facilitate the adhesion of further materials: a 500 Å thick Chromium layer, to act as an adhesive layer between the Silicon and sputtered Silver; and a 3000 Å thick Silver layer, to act as a conductive material and starting point for the electrodeposition process of Silver. By using the same material as the seed layer and the electrodeposition species, a stronger bond is created which prevents material dissociation from the sample surface during electrodeposition. Both materials were deposited on Alcatel SCM 450 Magnetron Sputtering, under the following conditions: a) 500 Å of Chromium: 2.10 mTorr, 20 sccm_{Ar}, 20 W_{DC}, 10 min; b) 3000 Å of Silver: 2.10 mTorr, 20 sccm_{Ar}, 20 W_{RF}, 140 V_{bias}, 33 min. Coating and patterning of ma-P 1275 +PR occurred as described before, using mask TMpH_holes. A schematic representation of the samples is depicted in Figure 57.

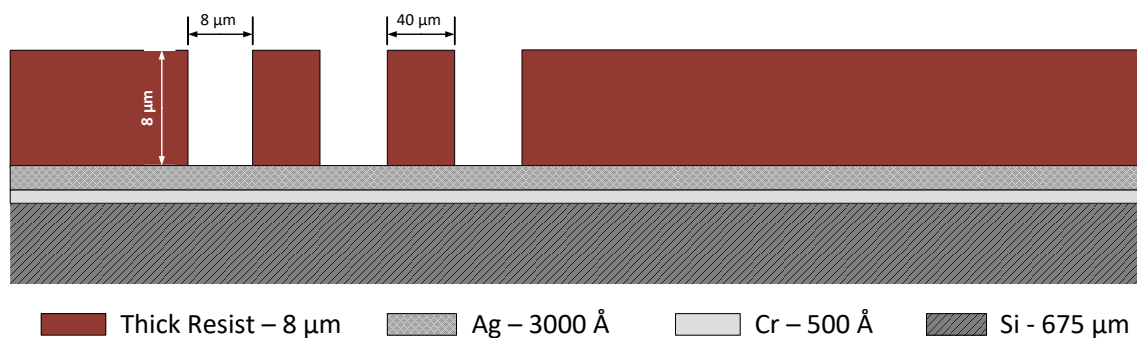


Figure 57 - Schematic diagram representing the cross-section view of the dummy samples used for the optimization of the Silver plating process.

As previously performed, the patterned Silicon samples with ma-P 1275 +PR could then be diced into individual dies for further processing, as the electrodeposition setup was unable to handle large

samples. The same Disco DAD 321 system was used for the dicing process, using a 150 μm wide dicing saw spun at 30'000 rpm and with a constant streaming of water.

For a thick Silver deposition process that could fulfill the 8 μm thick profile left by the patterning of the ma-P 1275 +PR, electro- and electroless deposition processes were studied. The best documented results for this process consist in cyanide-based silver solutions [96, 99, 103]. However, due to the lack of laboratorial facilities that could incorporate these solutions in a safe environment, a non-cyanide approach was preferable. For this, three different Silver-based solutions were prepared. A complete description of the Runsheet processes for the preparation of the solutions can be found in Annex 7.

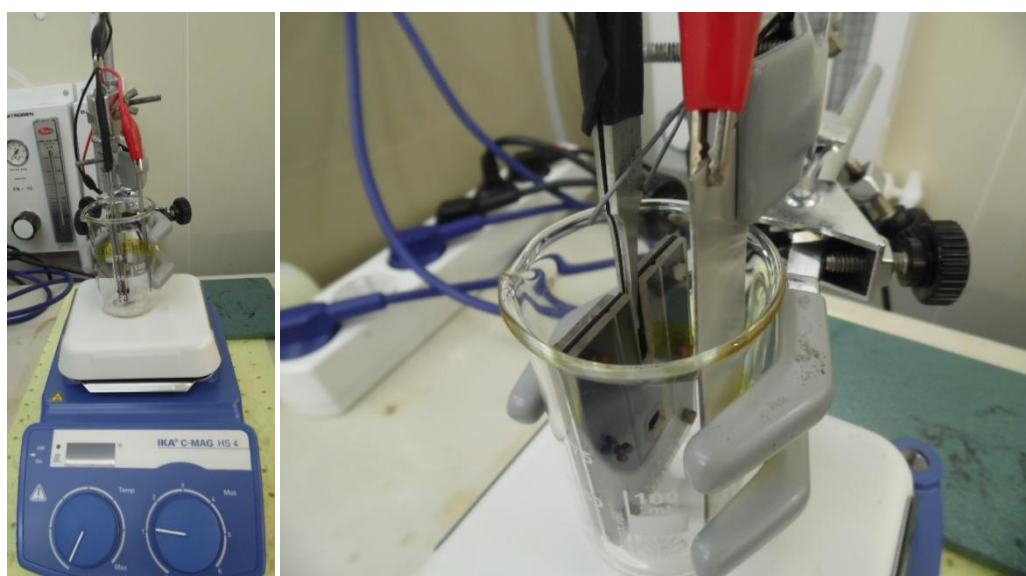
Solution #1 - An electroless plating solution consisting on the combination of lab-made Tollens' reagent (a mixture of Silver Nitrate, Sodium Hydroxide and diluted Ammonium) and Glucose. For this solution, Sodium Hydroxide is combined with Silver Nitrate to form a Silver Oxide (Ag_2O) precipitate. By adding enough Ammonium, the black precipitate is dissolved and combines into the Diamminesilver(I) complex ($[\text{Ag}(\text{NH}_3)_2]^+$). Glucose is added to the solution as a reducing agent that releases the Silver ions and promotes naturally occurring surface plating without the need for any electrical current.

Solution #2 - An electroplating solution consisting of diluted Silver Iodide, Potassium Iodide and Calcium Nitrate in water. The Silver ions, required to the electroplating process, would be provided by the Silver Iodide. However, Silver Iodide has a low solubility in water, requiring an additional component, such as Potassium Iodide, to improve dissolution. Calcium Nitrate acts as a surfactant to reduce surface tension between the solution and the cathode to be plated and improve overall plating.

Solution #3 - An electroplating solution consisting of diluted Silver Nitrate and Ammonium in water. In this solution, Silver Nitrate acts as the species donor for the electroplating process, whilst Ammonium increases its dissolution in water.

All solutions were prepared fresh in small, ready-to-use quantities, and had a lifetime inferior to 360 minutes of electroplating use, as to ensure quality control. After this period, a considerable change in color indicated chemical changes to the solution components derived from the accumulation of reaction by-products.

Electroless and Electroplating were conducted inside a 100 mL glass beaker, on top of a hotplate with magnetic agitation capability. For the electrodeposition process, a lab support stand and a set of tweezers were used to hold the samples and the counter electrode vertically inside the glass beaker, as seen in Figure 58 and represented in Figure 59. In the electroless deposition, the same system was used without the need for the counter electrode.



(a) overall setup

(b) reaction cup

Figure 58 - Laboratorial apparatus used for the electroless and electroplating deposition of Silver: (a) overall setup composed of a reaction cup, electrodes and heater/agitator equipment; (b) detail of the reaction cup with electrodes). A PMMA holder was used to assist in the electrodeposition process, whilst a solid Silver slat was used as the counter electrode.

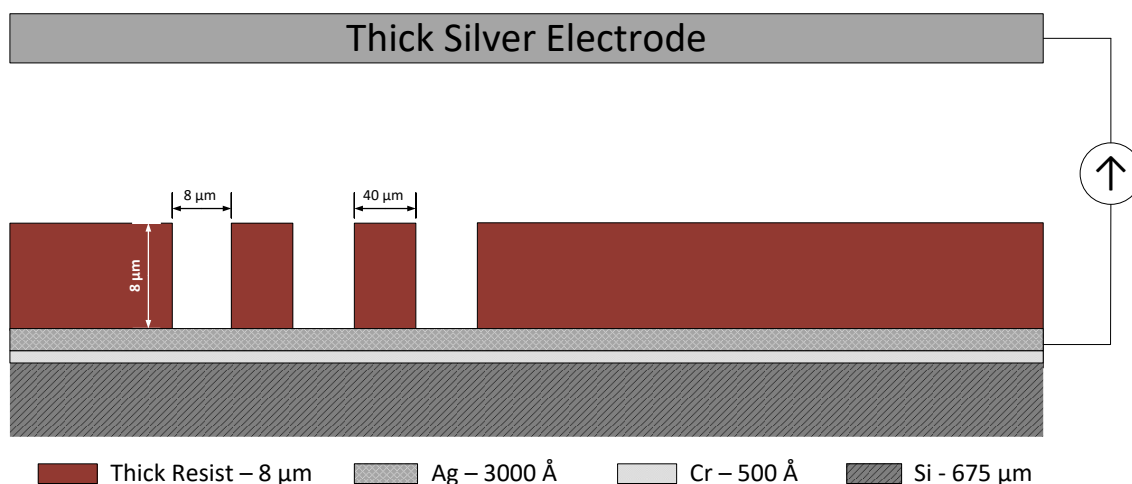


Figure 59 - Schematic diagram representing the cross-section view of the dummy samples used for the optimization of the Silver plating process, connected to the Working Electrode. The Silver layer acts as a seed layer for the electroplating process and as a conductor for the electrical charge applied in the process.

To perform the electroless deposition, the Tollens' solution (solution #1) was poured into the reaction cup and heated to above 40 °C, without any type of agitation. Afterwards, Glucose was added to the reaction cup and the solution was stirred to achieve a uniform dispersion. For samples ELP 04-06, a minute immersion in Buffer Oxide Etchant (BOE) was applied to assist in superficial oxide removal prior to the plating process. All samples were cleaned with DI water prior to any processing. The electroless plating conditions can be observed in Table 9. All samples were immersed approximately 2/3 of their length during the process.

Table 9 - Experimental conditions used in the electroless deposition of Silver.

Sample #	Solution	Substrate	BOE (min)	Agitation (rpm)	Temp. (°C)	Time (min)
ELP A01	Tollens' + Glucose	Pattern ma-P over Ag	0	0	42	10
ELP A02	Tollens' + Glucose	Pattern ma-P over Ag	0	0	42	15
ELP A03	Tollens' + Glucose	Pattern ma-P over Ag	0	0	48	20
ELP A04	Tollens' + Glucose	Pattern ma-P over Ag	1	0	46	10
ELP A05	Tollens' + Glucose	Pattern ma-P over Ag	1	0	46	15
ELP A06	Tollens' + Glucose	Pattern ma-P over Ag	1	0	46	20
ELP A10	Tollens' + Glucose	Pattern ma-P over Ag	0	0	46	30
ELP A11	Tollens' + Glucose	3000 Å Ag layer	0	0	46	30
ELP A12	Tollens' + Glucose	Glass	0	0	46	30

A macroscopic inspection of samples ELP A01-A02 demonstrated a visible smudge covering the area exposed to the solution, as seen in Figure 60 (a). Contrasting with these results, samples ELP A04-A06 showed a clean and reflective surface, as seen in Figure 60 (b). Profilometry measurements demonstrated that the reflective surface of samples ELP A04-A06 was in fact the underlying Silver layer deposited previously, and that the ma-P 1275 +PR layer was removed during the process. However, samples ELP A01-A02 registered no damage to the ma-P 1275 +PR layer. Instead, a thin Silver layer was deposited non-uniformly across the surface.

To review the results, a new Tollens' solution was prepared, and the reaction was repeated with samples ELP A10-A12, simultaneously. All three samples presented the same results as sample ELP A01-A02, characterized by a non-uniform smudge across the exposed surface.

These results indicate that independently of the surface used as a seed layer to the process, a non-uniform, thin layer of Silver atoms adhere during the initial 30 minutes of the process (Figure 60 (a)). For samples containing the ma-P 1275 +PR, those atoms protect the PR from the solution high pH of 14 and from NaOH molecules that affect and degrade the PR. However, if a new sample is placed after the depletion of all Silver atoms, no adhesion occurs and the PR is directly exposed to the high pH and NaOH molecules. This can be observed in Figure 60 (b), where the ma-P 1275 +PR was degraded and removed, revealing the underneath Silver layer deposited in previous steps.

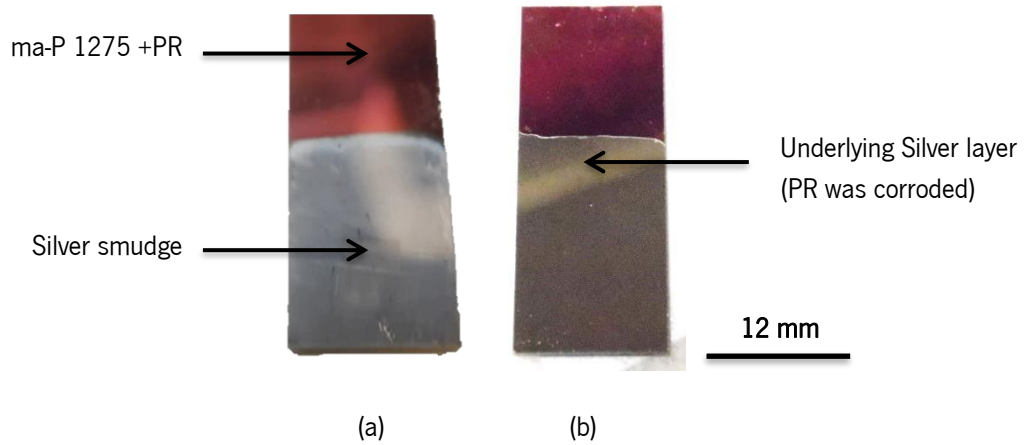


Figure 60 - Macroscopic inspection of samples ELP 01 (a) and ELP 06 (b). A white smudge of Silver can be observed in sample ELP 01 due to the adhesion of Silver molecules to the ma-P 1275 +PR surface. In sample ELP 06, Silver depletion had already occurred and no deposition was recorded.

During this process, all exposed surfaces are covered with a thin Silver layer, as observable in Figure 61. This represents a low yield of targeted deposition, as most Silver atoms are scattered throughout the entire system. Due to these results, this method was discarded.

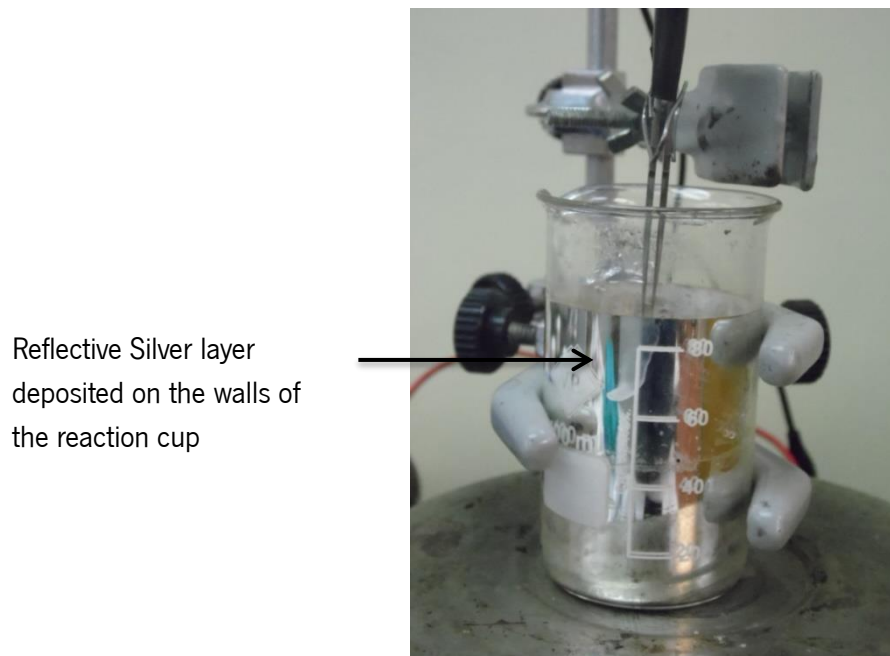


Figure 61 - A reflective, thin-layer of Silver atoms adhered to the inside wall of the reaction cup during the electroless deposition process.

For the electroplating system, a metallic tweezer acted as a conductive material to link the sample to the power source. The counter electrode, due to its length, extruded from the glass beaker, which meant that it could be directly linked to the power source through wired clamps. A schematic of the laboratorial apparatus used in this process can be observed in Figure 62.

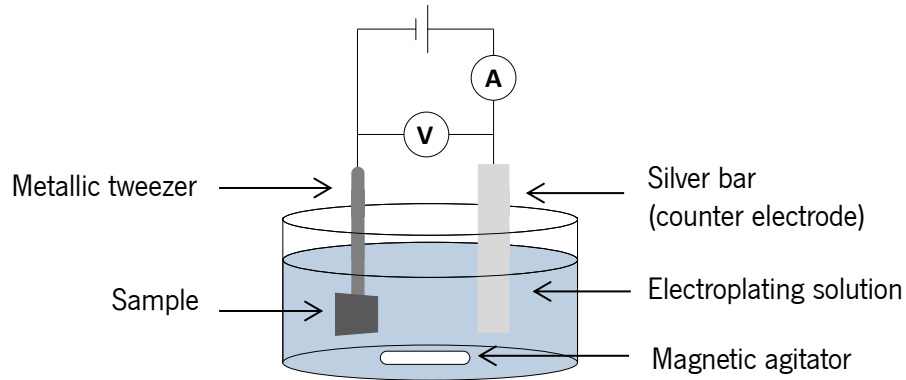


Figure 62 - Schematic diagram of the electroplating apparatus using a 2-electrode system.

To focus and assure current confinement to the desired area to be electroplated, a holding/protective system was projected and implemented.

An initial system consisted in a layer of rubber, 1 mm thick, set between 2 PMMA plaques, 2 mm thick. The samples would fit inside the back PMMA plaque, carved specifically to hold a 680 μm thick sample. A square slot was then carved in both the rubber layer and the front PMMA plaque, allowing access to the specific area to be plated, whilst protecting the remaining area of the sample. A rectangular slot was also carved on the top of all layers to facilitate the clamping of the sample. A set of PMMA milimetric screws and bolts was used to tighten the system together. A complete view of the system can be seen in Figure 63. The PMMA plaques were micromachined at Milling Machine (homemade). Although this system was partially successful in its purpose, a complete isolation was never achieved and leakage between the layers was common, as seen by the different color shades in the images.

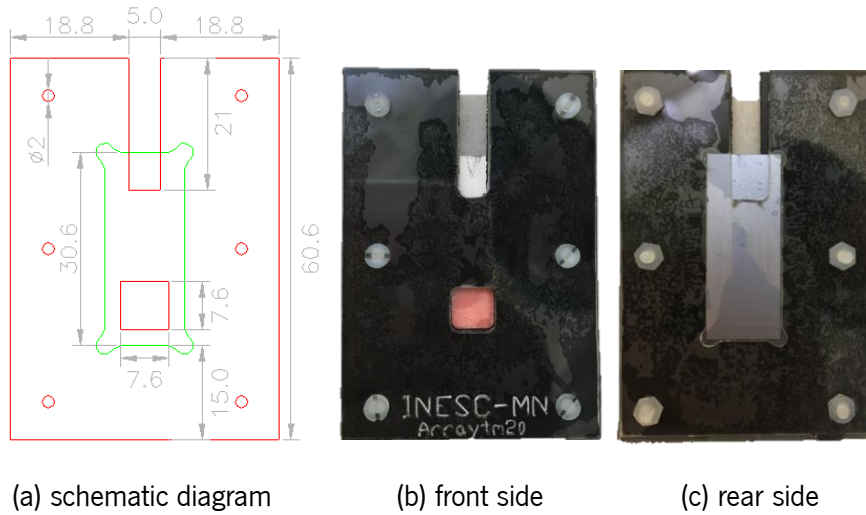


Figure 63 - PMMA holder used in the electrodeposition of Silver: (a) schematic diagram; (b) front side; (c) back side. The rectangular slot on the top allows for a metallic tweezers to be connected and transfer the electrical current to the power source. The square slot found in the middle of the front side (a and b) redirects the electroplating towards the desired area. All measures and dimensions are represented in millimeters.

A continuous current was applied through a Keithley 220 Programmable Current Source. To measure the voltage formed in the process, a Multimeter (Hewlett Packard 34401A) was attached, in parallel, to the circuit. A standard chronometer was used to time the process.



Figure 64 - Current source used in the electrodeposition process (Keithley 220 Programmable Current Source)

Solution #2 (consisting in a diluted Silver Iodide, Potassium Iodide and Calcium Nitrate solution) was used in the electroplating of Silver under the conditions in Table 10. All experiments were performed at room temperature (approximately 25 °C). A 1 minute immersion in BOE was applied to ensure that any superficial oxide was removed. All samples were cleaned with DI water and blown dried before and after immersion.

Table 10 - Experimental conditions used in the electrodeposition of Silver using Solution #2 (diluted Silver Iodide with Potassium Iodide and Calcium Nitrate).

Sample #	Solution	Substrate	BOE (min)	Agitation (rpm)	Temp. (°C)	Current Density (A/m ²)	Time (min)
EP B01	Agl	Pattern ma-P over Ag	1	150	RT	2.16×10 ³	20
EP B02	Agl	Pattern ma-P over Ag	1	150	RT	2.16×10 ²	20
EP B03	Agl	Pattern ma-P over Ag	1	150	RT	4.33×10 ²	20
EP B04	Agl	Pattern ma-P over Ag	1	150	RT	4.33×10 ³	20

Similarly to the causes in the previous results, the presence of nucleophile compounds (such as Iodide, in Solution #2 or Hydroxide, in Solution #1) promote the degradation of the ma-P 1275 +PR, causing severe damage to the exposed areas of the sample, as seen in Figure 65. However, contrary to the results obtained with Solution #1, the electroplating process does not promote the adhesion of Silver molecules on top of the ma-P 1275 +PR, as plating is selective only to conductive areas of the sample that are connected to the Current Source. Figure 65 (a) and (b) demonstrate a pale white coating of the sample surface obtained with samples EP B01-B02. Due to the low current used in both samples, Silver plating with smaller grain is dispersed through most of the samples surface, whilst a few areas of oxidized Silver and Photoresist remain with a black coloring. In Figure 65 (c) and (d), samples EP B03-B04 were processed with higher currents that caused the formation of larger grains of Silver plating with distinct fractal patterns (similar to tree branches). Due to the complete damaging of the patterned photoresist, this method was discarded as well.

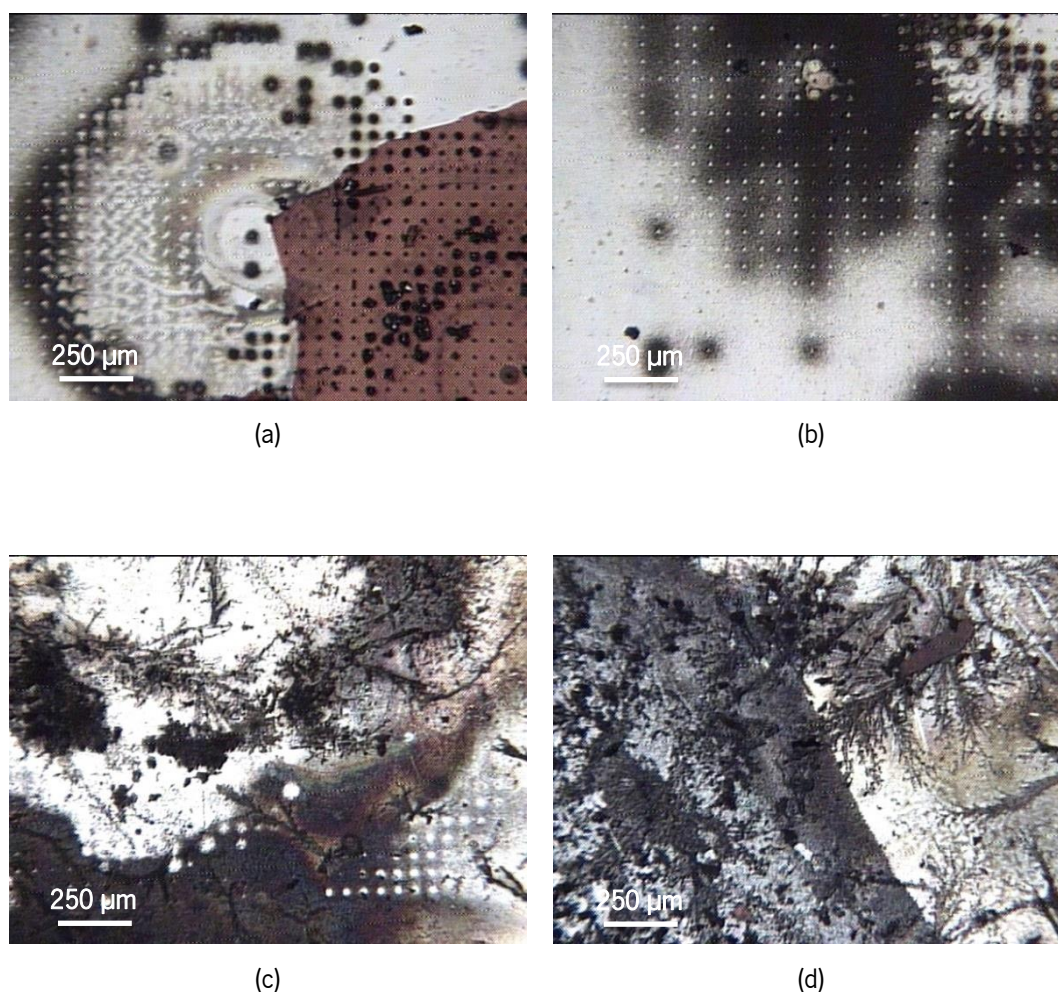


Figure 65 - Microscopic inspection of samples: (a) EP B01; (b) EP B02; (c) EP B03; and (d) EP B04. The red areas consist of ma-P 1275 +PR that survived the prolonged exposure. The black areas consist of oxidized molecules at the surface of the sample. The white areas consist of electroplated silver. The small circles/dots consist of the individual electroplated pits.

A final attempt to achieve the desired results was performed with Solution #3 (diluted Silver Nitrate and Ammonium in water). All samples were immersed in BOE for 1 minute prior to plating, as to remove any superficial oxide. Processing included washing with DI water and blow dry with compressed air before and after electroplating, as to remove any potential contaminants, dust particles or residues from the solutions. Temperature was applied through the hotplate and registered using a mercury thermometer. Magnetic agitation at 150 rpm was applied throughout all experiments. The experimental conditions can be observed in Table 11. Samples EP C02 and EP C06 were processed in two-step plating, performed subsequently.

Table 11 - Experimental conditions used in the electrodeposition of Silver using Solution #3 (diluted Silver Nitrate and Ammonium in water).

Sample #	Solution	Substrate	Temp. (°C)	Current Density (A/m ²)	Time (min)	Current Density (A/m ²)	Time (min)
EP C01	AgNO ₃	Pattern ma-P over Ag	RT	2.16×10 ³	40		
EP C02	AgNO ₃	Pattern ma-P over Ag	RT	2.16×10 ²	20	2.16×10 ³	20
EP C03	AgNO ₃	Pattern ma-P over Ag	RT	2.16×10 ²	40		
EP C04	AgNO ₃	Pattern ma-P over Ag	28	2.16×10 ³	30		
EP C05	AgNO ₃	Pattern ma-P over Ag	38	1.08×10 ³	40		
EP C06	AgNO ₃	Pattern ma-P over Ag	38	2.16×10 ²	40	4.33×10 ²	20
EP C07	AgNO ₃	Pattern ma-P over Ag	38	4.33×10 ²	40		
EP C08	AgNO ₃	Pattern ma-P over Ag	38	6.49×10 ²	40		
EP C09	AgNO ₃	Pattern ma-P over Ag	38	2.16×10 ²	80		
EP C10	AgNO ₃	Pattern ma-P over Ag	38	1,08×10 ²	80		
EP C11	AgNO ₃	Pattern ma-P over Ag	55	2.16×10 ³	20		
EP C12	AgNO ₃	Pattern ma-P over Ag	55	2.16×10 ⁰	240		

Silver Electroplating under room temperature (approximately 23 °C) produced a low yield with small aggregates of Silver deposits that overplate, whilst the large majority of the surface remains unplated, as observable in Figure 66. However, and contrarily to the previous results, the ma-P 1275 +PR withstood the electroplating process without any morphological changes and a clear electroplating result was achieved.

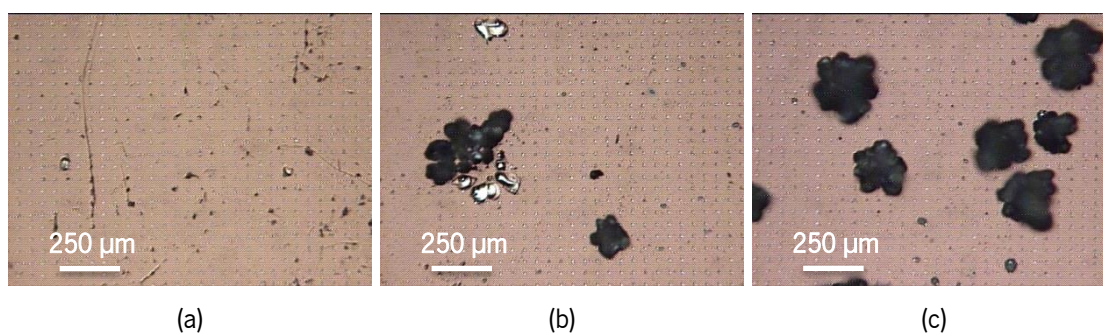


Figure 66 - Microscopic inspection of samples: (a) EP C01; (b) EP C02; (c) EP C03. The small dots consist of the patterned holes created in the ma-P 1275 +PR. The black areas in the images consist of large aggregates of electroplated Silver that prolong above the sample surface (overplating). In some cases, those aggregates would break, creating cleaved structures with a reflective surface, represented by the white areas.

Temperature was adjusted to improve the quality of the electroplating process, as it increases the average kinetic energy of the different molecules that make up the Solution and improves their solubility. A slight increase of temperature to 28 °C allowed for a greater yield of electroplated holes, although not through the entirety of the sample. An electroplating gradient was obtained throughout the sample surface, with one of the sides being nearly completely plated, whilst the opposite side still presented large gaps of unplated holes, as seen in Figure 67. Even though sample EP C04 was processed for a shorter period of time, smaller aggregates are formed which conclude that less material is wasted as overplating.

It is also possible to analyze the formation of larger aggregates in the areas of the sample that produced the lower yield of electroplated structures, when compared with the denser areas of the sample, possibly due to the lack of spatial competition for the available Silver ions [97].

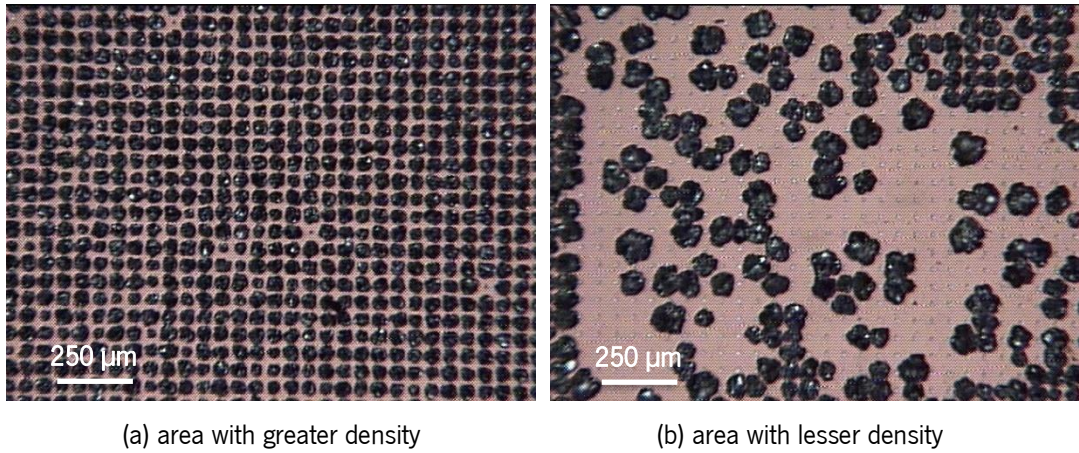


Figure 67 - Microscopic inspection of sample EP C04. The two images represent different areas of the same sample. The small dots represent the patterned holes created in the ma-P 1275 +PR. The black areas in the images consist of electroplated Silver that prolong above the sample surface (overplating).

Increasing the temperature by an additional 10 °C demonstrated to achieve a much higher uniformity in total area coverage, as Figure 68 shows. Although some specific points of the sample are not plated, those might be due to minor defects at the seed layer, flawed lithography, possible contaminants, or improper cleaning of the holes.

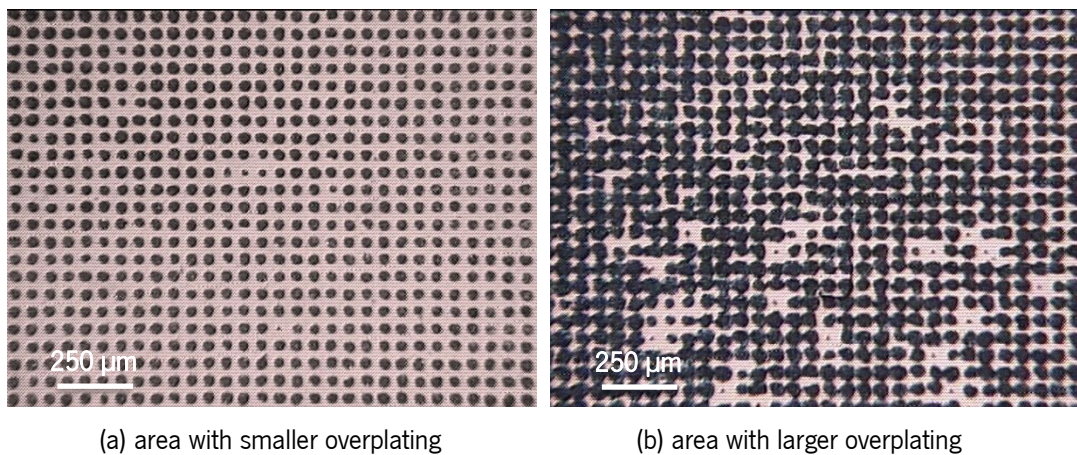


Figure 68 - Microscopic inspection of sample EP C09. The two images represent different areas of the same sample. The small dots represent the patterned holes created in the ma-P 1275 +PR. The black areas in the images consist of electroplated Silver that prolong above the sample surface (overplating).

However, a considerable difference in electroplating thickness was still observable in different parts of the samples, as a slight tilting occurred between the PMMA holder and the counter electrode due to manual positioning errors. Height measurements of the electrodeposition thickness, through Profilometer (Dektak 3030ST Profilometer), were performed at 5 points for each side of the electroplated samples, and each individual point was measured 5 times, for a total number of 100 measurements per sample. Since the ma-P 1275 +PR was still present in the samples, the measured heights (and thicknesses) represent the overplated Silver. The results were then compiled to represent the surface of the electroplated samples and demonstrate variations in thickness associated with tilting. Although samples had specific tilting (i.e., not all tilted to the same side/corner), the overall profile of samples EP C05-C09 averaged as described in Figure 69. The results demonstrate that some areas of the samples presented an overplated height 1.5× higher than that of the lowest overplated thickness.

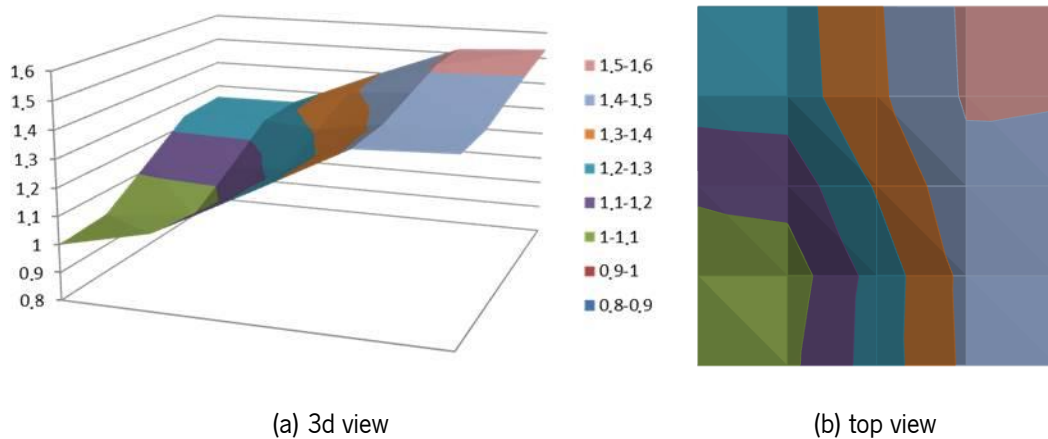


Figure 69 - Schematic representation of the top-view electroplating gradient observed due to manual positioning errors (tilting). Colors represent the height of each specific area of the sample in relation to the minimum height registered for each sample. Compilation of profilometric measurements of the surface of samples EP C05-C09, averaged into one representation.

Analysis of the profilometric results demonstrated that non-uniformity varies considerably between different samples, ranging from as low as 2.97 %, to as high as 18.46 %. Again, these results are a consequence of manual positioning errors of the electrodes, as no correlation could be found between non-uniformity and any other processing condition.

Contrary to the remaining samples presented at Table 12, sample EP C10 showed large areas of unplated surface, possibly due to low current density. The higher thickness registered, when comparing to sample EP C09, results from a more focused electroplating in fewer active areas of the sample, thus artificially manipulating the actual current density that affects each individual area.

By registering considerable overplating thicknesses, the experiments demonstrate that to achieve a complete electroplating of the patterned holes, considerably less time is required than that used for samples EP C05-C09.

For those reasons, the current density for future experiments was set at 2.16×10^2 A/m², as it provided the lowest energy with high yields, allowing for a precise control of the electroplating process in acceptable time frames.

Table 12 - Analysis of the electrodeposition overplating thickness of samples EP C05-C10.

Sample #	Temp. (°C)	Current Density (A/m ²)	Time (min)	Current Density (A/m ²)	Time (min)	Average Overplating Thickness (μm)	Standard Deviation (μm)	Non-uniformity (%)
EP C05	38	1.08×10^3	40			21.93	2.73	2.97
EP C06	38	2.16×10^2	40	4.33×10^2	20	16.41	2.07	4.95
EP C07	38	4.33×10^2	40			13.16	3.27	16.98
EP C08	38	6.49×10^2	40			17.69	4.64	18.46
EP C09	38	2.16×10^2	80			9.24	1.41	3.79
EP C10	38	1.08×10^2	80			12.68	2.20	9.08

A further increase of electroplating temperature to 55 °C, registered in samples EP C11-C12, not only decreased considerably the electroplating uniformity, when compared with the previous results, as it caused the deformation and cracking of the ma-P 1275 +PR, as seen in Figure 70. Even with a high current density, sample EP C11 (Figure 70 (a)) presents several blank spots of unplated surface, which when comparing with samples EP C05-C09 (Figure 68) indicate that, under the remaining conditions, an optimal temperature for the electroplating of Silver using Solution #3 is achieved around 38 °C.

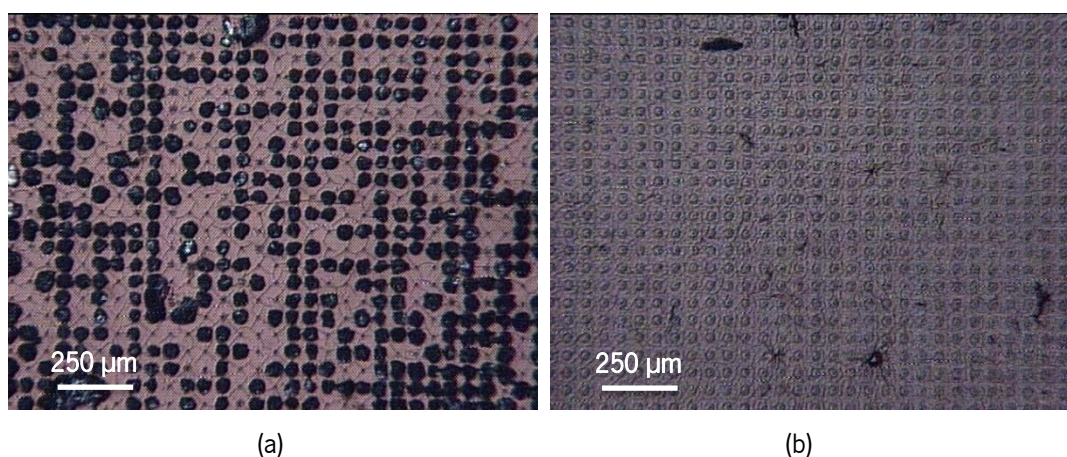


Figure 70 - Microscopic inspection of samples: (a) EP C11; and (b) EP C12. The small dots represent the patterned holes created in the ma-P 1275 +PR. The black areas in the images consist of electroplated Silver that prolong above the sample surface (overplating). Cracks and deformations are observable in the images due to prolonged exposure to the electroplating solution at 55 °C.

To correct and prevent some of the issues encountered in the previous results, namely the infiltrations found in the PMMA support system, the lack of uniformity in electroplating thickness across the surface between different samples due to manual positioning errors and eventual differences in regard to the distance between the electrodes, a new support system was designed in AutoCAD™ and created in a 3D Printer (BQ Witbox), as seen in Figure 71. Software conversion and printing conditions were defined in Cura™ 2.4.0, with a layer height of 0.2 mm, an infill density of 80 % and a printing speed of 20 mm/s at 210 °C.

The grey color represents the Silver counter electrode, which is inserted and maintained in place inside the overall support, illustrated in the color red in Figure 71 (a). This support also possesses a slot for an adaptor, illustrated in the colors green and blue (Figure 71 (b)), to be inserted. By maintaining both positions static, a fixed distance and tilt between both electrodes allows for a greater processing quality.

Like in the previous system, a square slot with the same dimensions (7.6×7.6 mm) is carved in the center of the blue layer, directing and controlling the electroplating only on the desired area of the sample, which is placed between the green and blue layers.

The orange structure was created to suspend the overall system at a fixed height, inside the reaction cup, allowing for a magnetic agitator to spin below, not affecting any of the created structures. The

structure represented in red also possesses slots below and in both sides, as to allow the circulation of the electroplating solution during the entire process.

The end result can be observed in Figure 72.

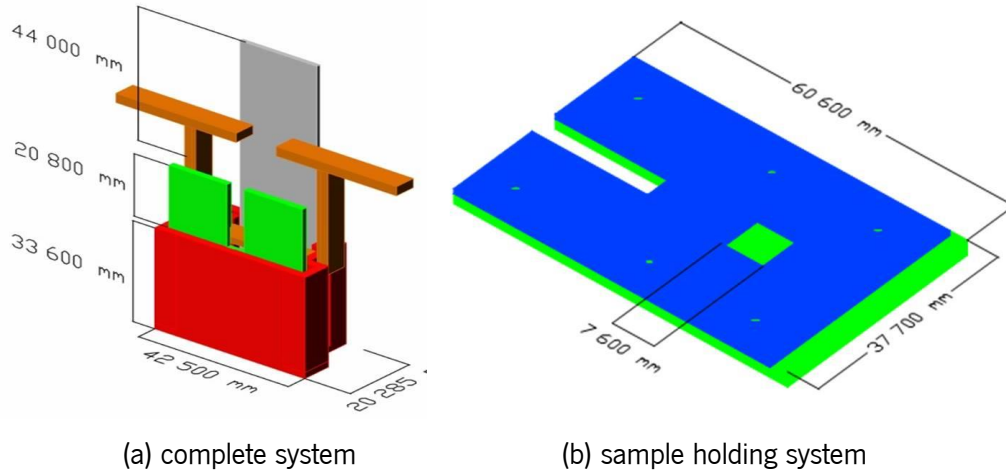


Figure 71 - Virtual representation of the complete electroplating support system designed in AutoCAD™ and created in a 3D Printer. The printed parts of the system are represented in the colors orange, red, blue and green. The grey color represents the Silver counter electrode.

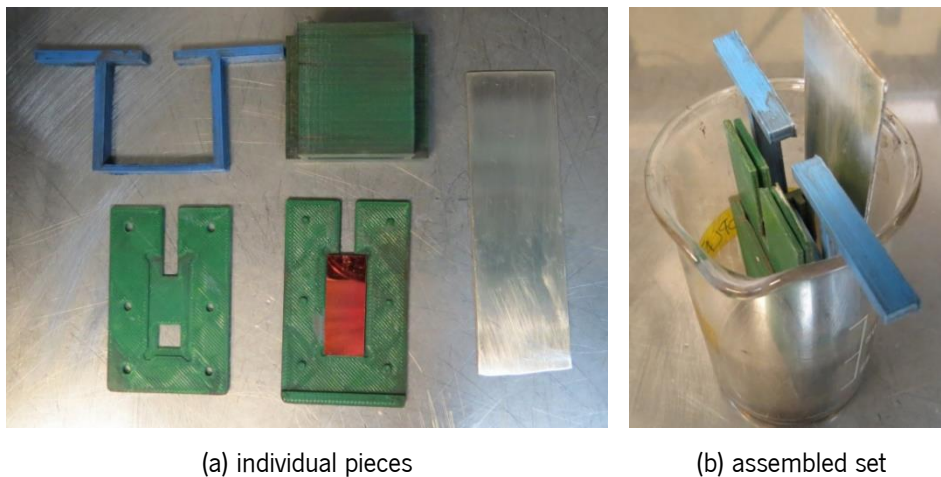


Figure 72 - 3D printed support system (green and blue), with corresponding Silver electrode (grey) and a dummy die (red). On (b), the complete system is assembled and placed inside a glass cup.

Optimization of the electroplating process was performed considering the previous results. Therefore, new samples were prepared and electroplated as described in Table 13. Samples EP D01-D03 were processed using the PMMA support system, whilst samples EP D04-D08 were processed using the 3D Printed support system. All samples were treated with BOE for 1 minute, prior to

electroplating, as to remove any superficial oxidation. Samples were also washed with DI water and blown dried with compressed air before and after electrodeposition. All samples were processed at 38 °C, with magnetic agitation at 150 rpm, and applying a current density of 2.16×10^2 A/m².

Table 13 - Experimental conditions used in the electrodeposition of Silver using Solution #3 (diluted Silver Nitrate and Ammonium in water) and topographical analysis of the samples surface

Sample #	Solution	Substrate	Current Density (A/m ²)	Time (min)	Average Overplating Thickness (μm)	Standard Deviation (μm)	Non-uniformity (%)
EP D01	AgNO ₃	Pattern ma-P over Ag	2.16×10^2	30	6.97	2.43	18.26
EP D02	AgNO ₃	Pattern ma-P over Ag	2.16×10^2	40	6.82	1.56	10.15
EP D03	AgNO ₃	Pattern ma-P over Ag	2.16×10^2	60	9.61	2.27	14.83
EP D04	AgNO ₃	Pattern ma-P over Ag	2.16×10^2	5	1.50	0.34	3.58
EP D05	AgNO ₃	Pattern ma-P over Ag	2.16×10^2	10	2.71	0.69	6.92
EP D06	AgNO ₃	Pattern ma-P over Ag	2.16×10^2	15	3.47	0.51	4.75
EP D07	AgNO ₃	Pattern ma-P over Ag	2.16×10^2	40	4.02	0.67	5.83
EP D08	AgNO ₃	Pattern ma-P over Ag	2.16×10^2	60	4.88	0.75	4.09

In overall, samples EP D04-D08, processed using the 3D Printed support system, demonstrate a greater uniformity, mainly due to the issues addressed when fixing the position of both electrodes. When comparing both systems, samples EP D04-D08 also present a lower deposition rate, possibly due to limitations in the flow and replenishing of solution between both electrodes. A logarithmic fitting to the results obtained with these samples, project a complete filling of the patterned holes in 90 seconds. The projected standard deviation for that time frame would fall under 0.300 μm, which would allow for compatibility with standard microfabrication processes for further layer processing. A graphical representation of the results can be observed in Figure 73.

The logarithmic evolution of the electrodeposition process is consistent with the increase of surface area as soon as overplating starts occurring. Until then, a linear progression can be idealized, with a growth rate of around 341 μm³/min. For the complete system with the patterned microneedles, a total

area of $\sim 632 \mu\text{m}^3$ would be required to be filled, which computes in a processing time of 1 minute and 51 seconds, considering that the deposition rate remains constant at those conditions.

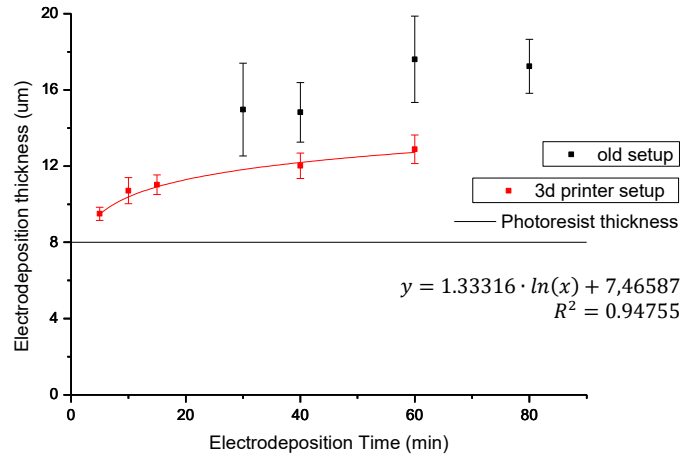


Figure 73 - Graphic representation of the electrodeposition thickness versus the process time, for the conditions described in Table 13, plus sample EP C09 from Table 12. The electrodeposition thickness is calculated by adding the ma-P 1275 +PR thickness (of approximately $8 \mu\text{m}$) to the overplating thickness measured in the Profilometer.

Surface mapping of samples EP D04-D08, through profilometric measurements, corroborate the increase in uniformity across the entire sample surface. The results shown in Figure 74 demonstrate that half of the samples surface remained inside a 10 % variation range, whilst the maximum registered height was of around $1.3\times$ higher, 0.2 points lower than for samples EP C05-C09 (which registered a maximum height of around $1.5\times$ higher).

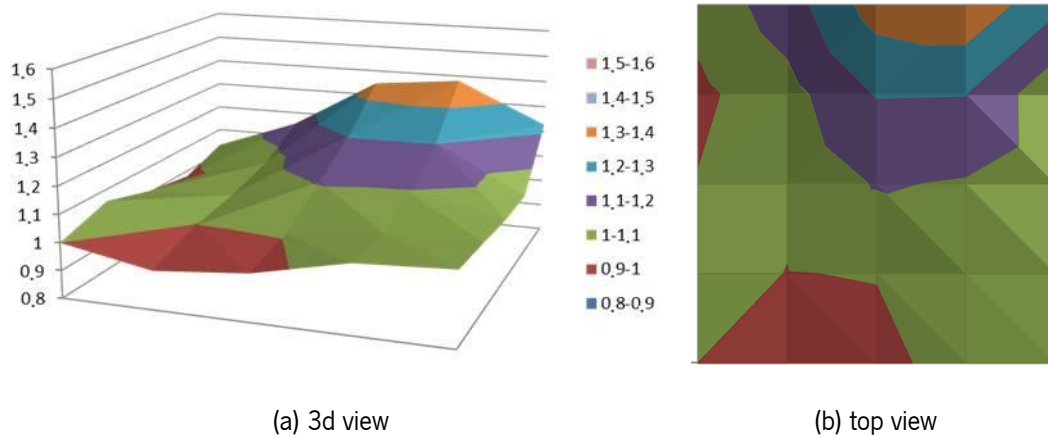


Figure 74 - Schematic representation of the top-view electroplating gradient observed. Colors represent the height of each specific area of the sample in relation to the minimum height registered for each sample. Compilation of profilometric measurements of the surface of samples EP D04-D08, averaged into one representation.

A direct comparison of the average overplating thickness between the use of the PMMA holding system and the 3D printed setup (Figure 75) demonstrates an improvement in both uniformity and maximum variation using the latter system (Figure 75 (b)). This can be mainly attributed to a more precise control of the sample tilting during electroplating. Whilst the PMMA holding system allows for a free positioning of both electrodes, the 3D printed setup holds both in place and at a fixed distance.

Despite the improvement, the 3D printed setup still presents considerable amplitude in the electrodeposits thickness. This may be caused by minor sample tilting inside the holding system - the 3D printed surfaces in contact with the sample are not 100% smooth - as well as defects or minor variations in the quality of the sample caused by the previous microfabrication steps.

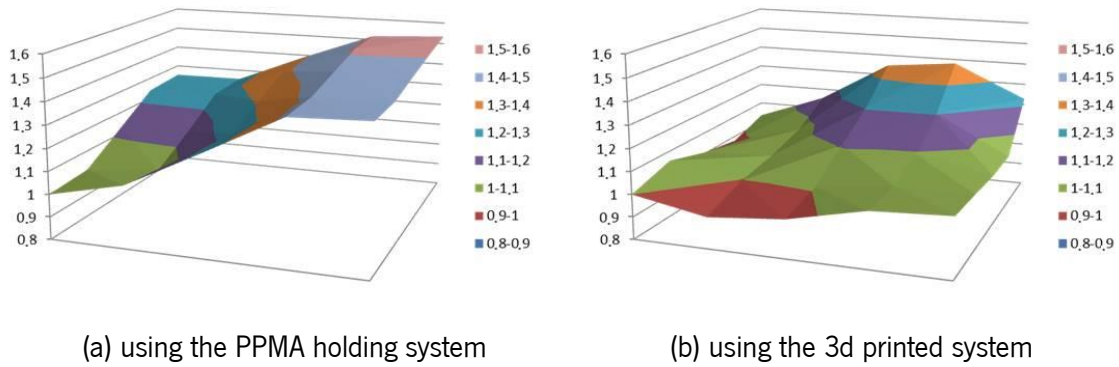


Figure 75 - Comparison between the surface topography obtained from the electrodeposition processes using: (a) the PMMA holding system; and (b) the 3D printed setup. Colors represent the height of each specific area of the sample in relation to the minimum height registered for each sample. Compilation of profilometric measurements of the surface of samples: (a) EP C05-C09; and (b) EP D04-D08, averaged into one representation.

To infer about the quality of the electroplating, Energy Dispersive x-ray Spectroscopy (EDS) was performed. The results demonstrate that pure Silver is obtained during the process, as seen in Figure 76. Although these results do not infer about the quality of the crystallographic growth, they confirm that no contaminants are being deposited simultaneously during the electroplating of Silver.

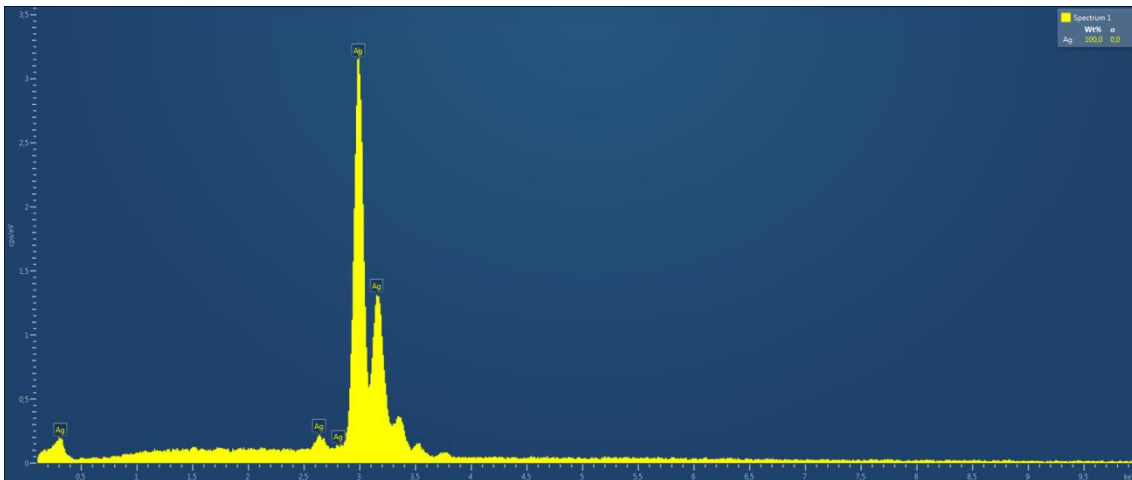


Figure 76 - EDS analysis of electroplated silver produced through Solution #3. Pure Silver is observed in the data spectra.

Once the electrodeposition process was optimized for the dummy samples, Through-Silicon-Electroplating was performed for the creation of solid-state Silver μ Needles. To test the process efficiency in this method (where the electrical current is travelling from the back of the Silicon sample and through its matrix, until it reaches the bottom of the microfabricated pits, as represented in Figure 77, different samples were tested as described in Table 14. A current density of 2.16×10^2 A/m² was used in Sample EP-01, based on the optimization tests performed previously, and as the baseline for comparison with the EP Dxx series. To account for possible efficiency loss, Samples EP E02-03 were electroplated with higher current densities, whilst maintaining the same process time at 5 minutes to allow for a recognizable overplating to be formed and analyzed.

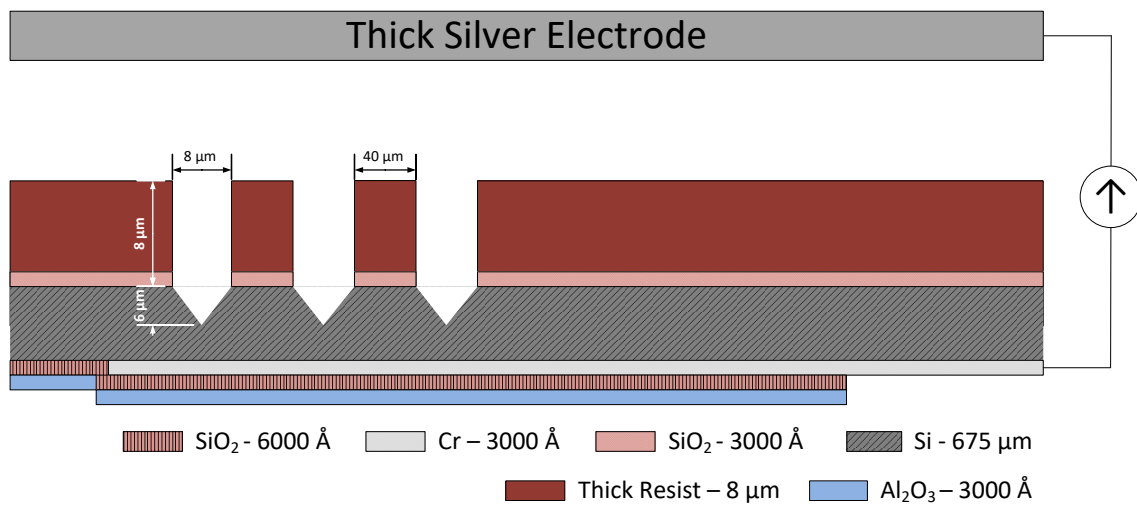


Figure 77 - Schematic diagram representing the cross-section view of the microfabrication step #15. Unlike the tests performed with the dummy samples, the electrical charge travels from the metallic layer deposited on the back of Silicon sample and through its matrix, emerging in the bottom of the microfabricated pits.

Table 14 - Experimental conditions used in the electrodeposition of Silver using Solution #3 (diluted Silver Nitrate and Ammonium in water), in the Through-Silicon-Electroplating process.

Sample #	Solution	Substrate	Temp. (°C)	Current Density (A/m ²)	Time (min)
EP E01	AgNO ₃	Pattern ma-P over patterned Silicon	38	2.16×10^2	5
EP E02	AgNO ₃	Pattern ma-P over patterned Silicon	38	1.08×10^3	5
EP E03	AgNO ₃	Pattern ma-P over patterned Silicon	38	2.16×10^3	5

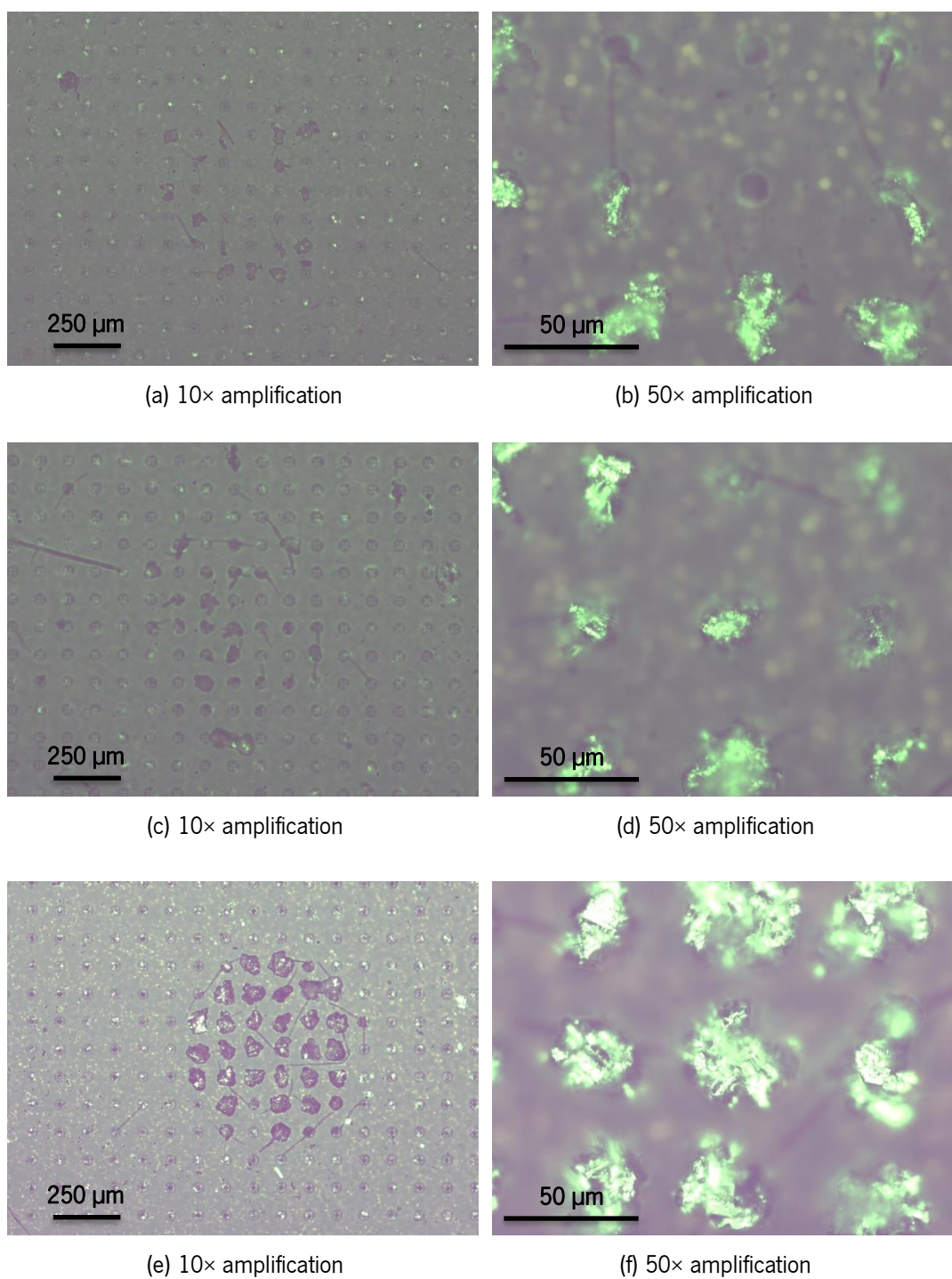


Figure 78 - Microscopic inspection of samples EP E01 ((a) and (b)); EP E02 ((c) and (d)); and EP E03 ((e) and (f)). The empty pits are represented by small, uniform black circles, whilst the electroplated structures are represented by either larger, non-uniform black circles under 10× amplifications ((a), (c) and (e)), or by bright, non-uniform shapes under 50× amplifications. In (d) and (f), no empty pits are presented.

Although electroplating was achieved using the Silicon wafer as a semiconductive substrate, the results under these conditions underperform from what expected. A complete surface analysis demonstrates that the profile of the electrodeposited areas forms a regular grid pattern of periodic clusters of about 5-7 individual structures (effective electrodeposition radius of $172\ \mu\text{m}$), distanced by 9-10 non-electroplated structures in both xx and yy axis (distance of $520\ \mu\text{m}$ between clusters), as seen in Figure 81.

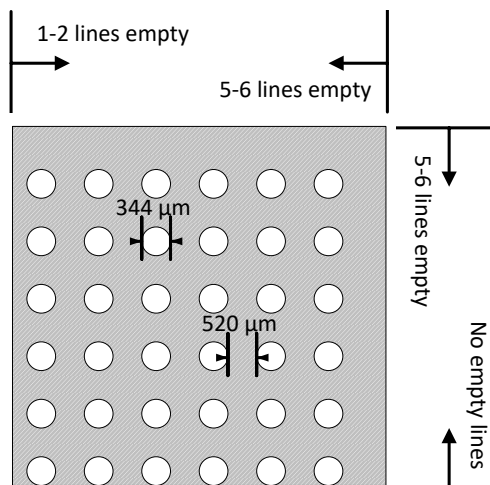


Figure 79 - Schematic representation of the cluster dispersion (white circles) throughout the patterned silicon matrix (grey area). Description of the cluster's sizes, distancing, and position in the matrix, in relation to the 4 borders of the patterned matrix.

The same pattern was observed for samples EP E02-03, with non-significant differences in relation to the clusters size, structure, or position in the matrix. All three samples are presented with 1-2 empty lines (i.e., columns of non-electroplated structures) in the left border and 5-6 empty lines in both the right and top border of the matrix. At the bottom border, electroplated structures can be observed at the very beginning, with possibly 1-2 structures missing (i.e., the clusters at the bottom border are smaller than those from any other position, possibly due to the lack of available electroplatable structures below). Furthermore, all clusters present a similar internal structure, as demonstrated in Figure 80.

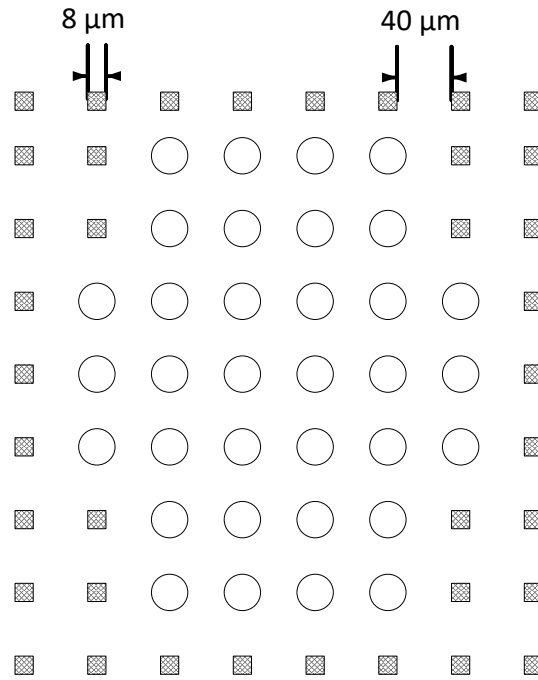


Figure 80 - Schematic representation of a single cluster of electrodeposited structures. The circles represent overplated structures, whilst the squares represent non-electroplated structures. Each cluster is formed by 5×5 to 6×6 individual structures in a circular-type shape.

These results reveal that only around 13% of the entire patterned surface is being electrodeposited (approximately 1224 from the total 9600 individual pits are electroplated).

Both the low yield and the grid-like pattern cannot be explained by problems in the photolithographic process. As the DWL system uses a 200 μm wide array of photodiodes that scan the surface in vertical patterns, not only the horizontal distance between the profiles is larger than each individual scan, as it would provide the same energy level to each individual profile in a given vertical column (and thus, no empty profiles in the vertical axis would be formed)

A poor dispersion of the photoresist during the coating cannot provide an explanation as well, as it would form a wave-like pattern of different thicknesses, closely aligned with the horizontal axis. Since there are empty profiles in the horizontal axis, these cannot be attributed to this event.

An eventual combination of both factors, coating dispersion of the photoresist and effect of the lithographic process fails to justify the clusters sizes and distancing, both above the individual lithographic scan of 200 μm.

When comparing these results with those obtained in the EP Dxx series, we can infer the cause to either the presence of the microfabricated pits that may be affecting the Photoresist dispersion in a regular pattern, or the current appliance process through the Silicon matrix, which may be conducting the electrical current in a non-direct pathway. Further experiments are required as to ascertain the cause of these results, namely:

1. Performing the electroplating process under the same scenario, but without the microfabricated pits.
2. Performing the electroplating process under the same scenario, but with a different substrate (doping, thickness or polishing of the silicon wafer).

Due to the low yield and small cluster size, a complete topographical analysis of the EP Exx series is not possible. However, careful analysis of the profilometric results obtained from these samples demonstrate significant differences in terms of electrodeposition thickness, as expected from the different applied current densities. An overall decrease in overplating thickness across the sample can also be observed and correlated to the distance from the center, adding another layer of complexity to the topographical analysis. Analysis of the center profiles (away from the edges) for each sample is demonstrated in Table 15:

Table 15 - Topographical analysis of the samples surface in the center profiles. Non-electroplated structures are not considered for the calculation of the table values.

Sample #	Solution	Substrate	Current Density (A/m ²)	Time (min)	Average Overplating Thickness (μm)	Standard Deviation (μm)	Non-uniformity (%)
EP E01	AgNO ₃	Pattern ma-P over Ag	2.16×10 ²	5	9.32	3.91	37.55
EP E02	AgNO ₃	Pattern ma-P over Ag	1.08×10 ³	5	12.53	2.97	26.01
EP E03	AgNO ₃	Pattern ma-P over Ag	2.16×10 ³	5	17.75	2.12	16.09

The efficiency loss in this process is considerable when comparing with the optimized results for the dummy samples. A brief calculation of the total amount of electroplated Silver between Samples EP

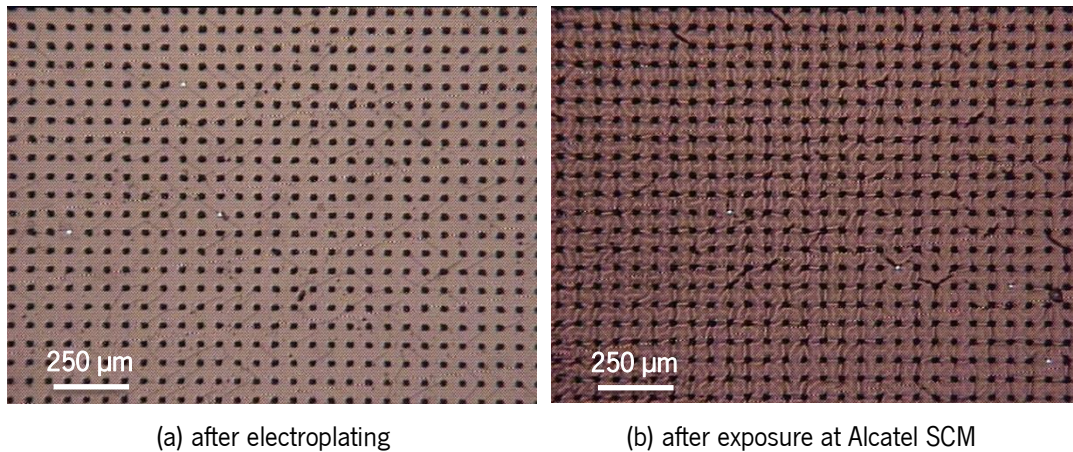


Figure 82 - Microscopic inspection of a sample containing a patterned 8 μm thick ma-P 1275 +PR with electrodeposits of Silver: (a) after electrodeposition; and (b) after exposure at Alcatel SCM for the deposition of a 3000 Å of SiO₂, without pre-heating. The black areas in the images consist of electroplated Silver.

To clear all contaminants, the samples are placed on top of a hotplate at 75 °C. The temperature is then increased to 110 °C at a rate of ~2 °C/min. Finally, the sample is held at 110 °C for 5 minutes and then left to cool down. A steeper slope of heating, or the appliance of higher temperatures, cause the natural occurrence of blisters and Resist burning. Once the cooling is completed, the sample can then be further processed. Silicon Dioxide was deposited on Alcatel SCM 450 Magnetron Sputtering (2.10 mTorr, 20 sccm_{Ar}, 4 rpm, 140 W_{RF}, 107 min for a 3000 Å thick layer).

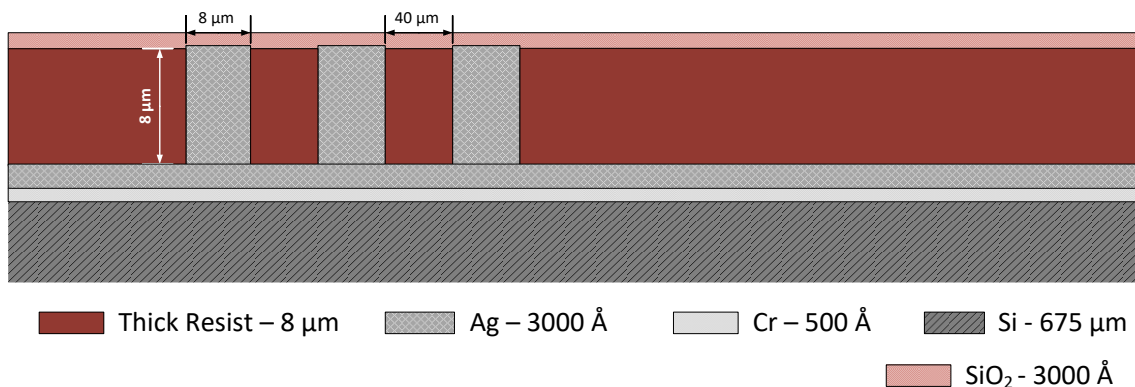


Figure 83 - Schematic diagram representing the cross-section view of the dummy samples used for the optimization of the contact patterning. All pits were filled with a Silver electrodeposit according to the EP Dxx series tests. Simulation of step #16 - Silicon Dioxide deposition.

Once protected, the sample was then patterned once again with mask **TMpH_holes** at DWL. However, conditions used in standard microfabrication steps are not compatible with the sample layout and damage to the ma-P 1275 +PR is common for most processes, as the sandwiching of the Resist layer prevents the efficient transferring of accumulated energy derived from localized heating processes, such as baking steps or plasma contact. Gradual increase of temperature on top of a hotplate as shown that the current layout is capable of withstanding a maximum temperature of 65 °C without the risk for severe morphological changes, which is considerably lower than the temperatures used in the standard lithographical process of 85 °C and 110 °C for the pre- and post-exposure baking, accordingly. Figure 84 demonstrates de morphological changes occurring due to heating at higher temperatures.

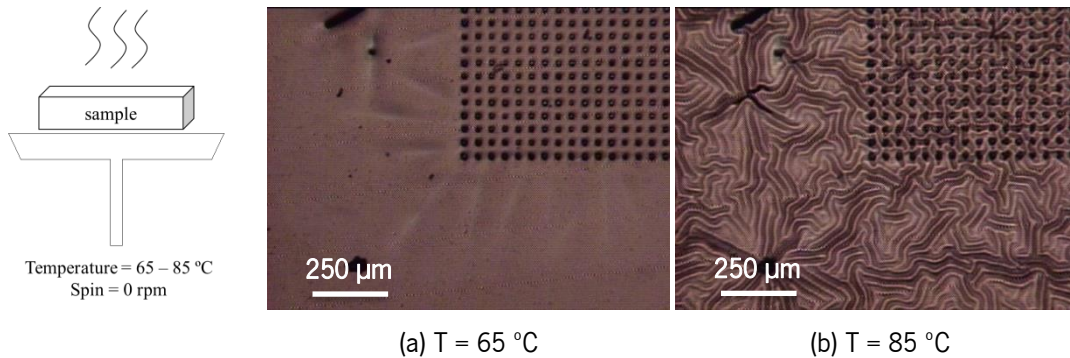


Figure 84 - Microscopic inspection of a sample containing a patterned 8 μm thick ma-P 1275 +PR with electrodeposits of Silver and a 3000 Å SiO₂ layer on top: (a) heated at a temperature of 65 °C; and (b) heated at a temperature of 85 °C. The black areas in the images consist of electroplated Silver.

PFR 7790 G +PR was spun at SVG track (initial 5 sec rotation at 800 rpm with acceleration of 500 rpm/s, and a second step of 40 sec rotation at 2800 rpm with identical acceleration) for an approximate thickness of 1.5 μm. Baking was performed manually on top of a hotplate at the designated maximum temperature of 65 °C for 180 seconds. Lithography was performed at DWL under standard conditions. After exposure, the sample was heated once again at 65 °C for a period of 180 seconds and then left to cool on top of a lab bench.

Although the layout system endured the initial spinning of the PFR 7790 G +PR, automatic development at the SVG track proved disastrous, as the high-speed rotation of the washing and cleaning process caused stress release by mechanical forces between the Silicon Dioxide and the ma-P 1275 +PR layers, creating cracks that the developer used to irremediably damage the thick Resist layer, as

seen in Figure 85. Therefore, development with TMA 238 WA was performed inside a HDPE beaker for 120 seconds with manual agitation. The sample was then rinsed with DI water and inspected at the optical microscope.

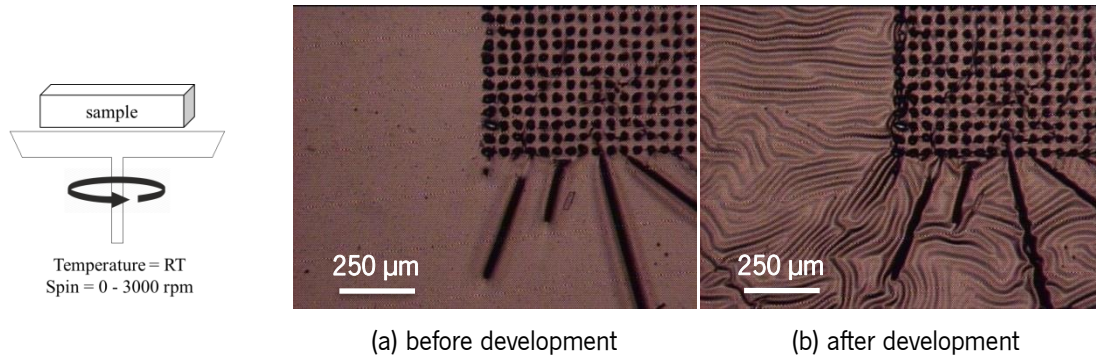


Figure 85 - Microscopic inspection of a sample containing a patterned 8 μm thick ma-P 1275 +PR with electrodeposits of Silver and a 3000 \AA SiO_2 layer on top: (a) before development at the SVG track; and (b) after development at the SVG track. The black areas in the images consist of electroplated Silver.

Vias etching of the patterned profile, to grant access to the Silver microelectrodes, was performed at LAM Rainbow 4400 Plasma Etching. However, due to the low thermal endurance of the stacked layers, standard processing conditions caused irremediable damage to the ma-P 1275 +PR layer. To overcome this problem, exposure to plasma was reduced to smaller intervals of time, preventing the overheating of the Resist layer and allowing enough time for the temperature to dissipate throughout the layer and into the sample holder. Therefore, using the standard conditions for SiO_2 etching (pressure during the process = 140 mTorr, wafer area pressure = 305 mTorr, 100 W_{rf} , 200 sccm Argon, 100 sccm CF_4 , 10 sccm O_2), exposure time was reduced from the usual 6×150 seconds, to alternated intervals of 25 seconds of exposure and 25 seconds of cooling. Considering the necessary time for the plasma to form and stabilize, the actual effective time of exposure was reduced to around 19-22 seconds per interval, which required a total number of 48 cycles to achieve the total necessary amount of 900 seconds of exposure to etch 3000 \AA of SiO_2 .

Once finished, the upper PFR 7790 G +PR layer was removed under a similar process, using an O_2 plasma recipe (pressure during the process = 275 mTorr, 30 steps of 25 seconds of exposure at 200 W, 20 sccm Φ_{O_2} , with 60 seconds cooling between steps) at LAM Rainbow 4400 Plasma Etching, as

conventional cleaning with solvents would damage the underlying ma-P 1275 +PR layer as well. The overall description of this process can be observed in Figure 86.

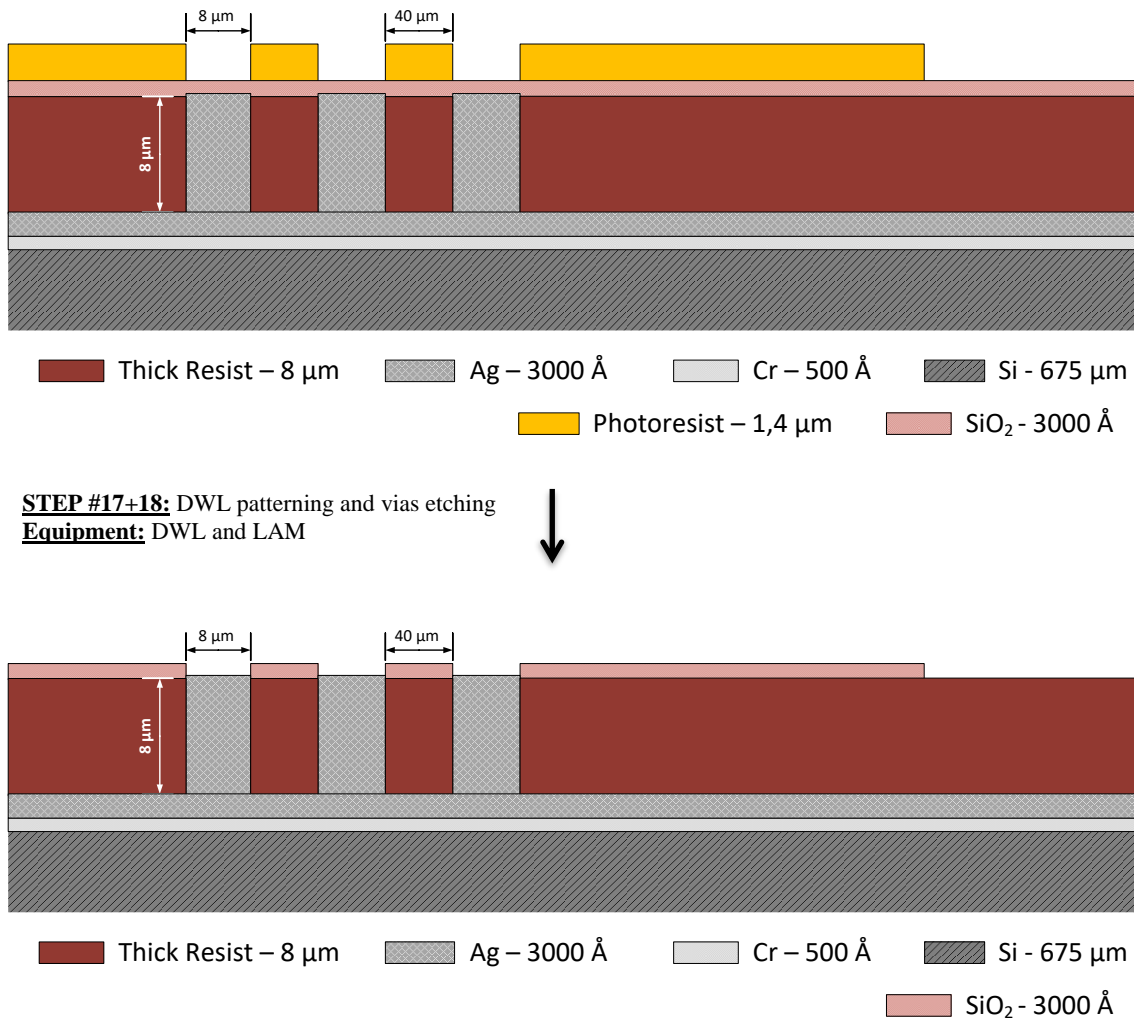


Figure 86 - Schematic diagram representing the cross-section view of the dummy samples used for the optimization of the contact patterning. All pits were filled with a Silver electrodeposit according to the EP Dxx series tests. Simulation of step #17 and #18 - Lithographical patterning of PFR 7790 G +PR in DWL technology and Vias etching for electrical contact access through Reactive Ion Etching of SiO₂.

The following step consisted in the deposition and patterning of Aluminum lines and pads that would form electrical contacts between the active area of the sensor and the external connectors. Due to the limitations registered before, lift-off processes could not be implemented as the solvents would damage all layers of Photoresist simultaneously. Instead, a chemical wet etching process was implemented as it is target-specific to Aluminum and does not damage or affect the other chemical species in the stack.

To perform this process, a 3000 Å thick Aluminum layer was deposited at Nordiko 7000. Similarly as before, exposure time was reduced as to prevent over-heating and consequential damage to the underlying Photoresist layer. Deposition occurred under the following conditions: 3.0 mTorr, 50.0 sccm_{Ar}, 2 kW, 5.12 A, 400 V, 3 × 27 sec of exposure with 150 sec of cooling in between steps. Once completed, patterning was performed as before, using controlled heating and manual development. A description of the patterned profiles can be seen in Figure 87, and a schematic representation in Figure 89.

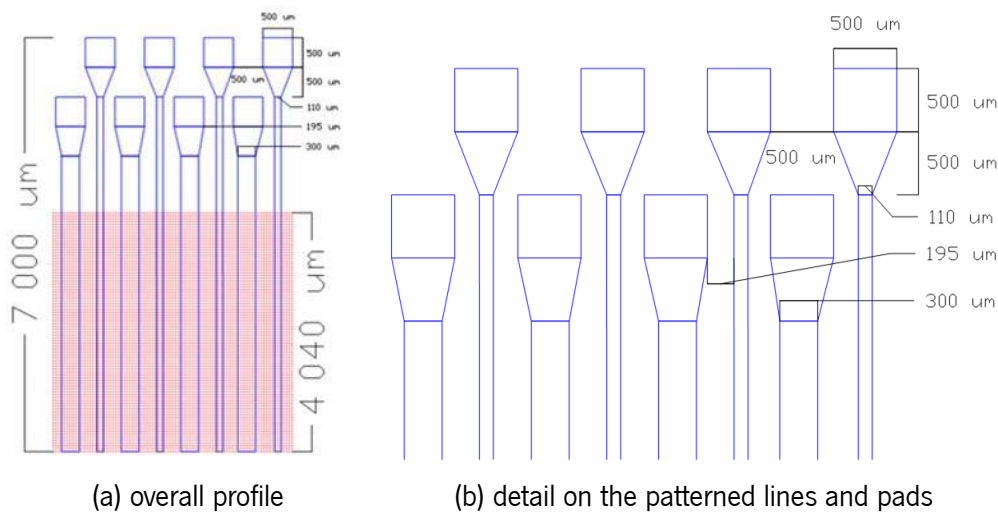


Figure 87 - AutoCAD™ image representing the profile patterned through Direct Writing Lithography for Step #22: (a) overall profile; and (b) detail on the patterned lines and pads. The red area on (a) represent the individual Silver electrodes, patterned previously. All measures and dimensions are represented in micrometers. Mask name: TMpH_frontcontact.

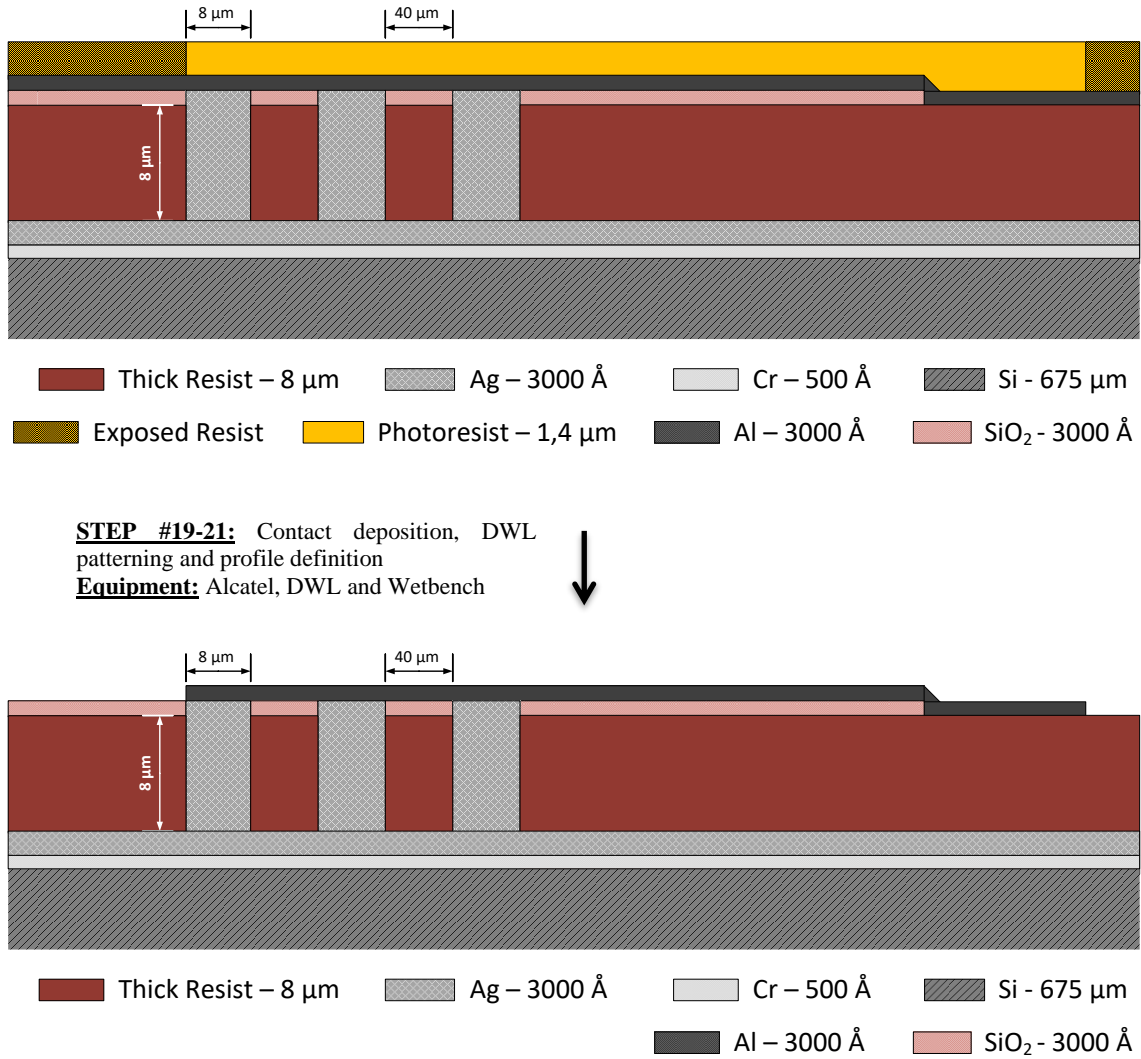


Figure 88 - Schematic diagram representing the cross-section view of the dummy samples used for the optimization of the contact patterning. All pits were filled with a Silver electrodeposit according to the EP Dxx series tests. Simulation of step #19 to #21 - Aluminum deposition through Magnetron Sputtering, Lithographical patterning of PFR 7790 G +PR in DWL technology and profile definition through wet etching.

An 8-line system was developed for initial testing in order to simplify reading and compact total area usage of the sample. Future iterations of this process can be designed in order to use a larger area of the sample in all directions for lines and pads.

The designed system includes four, 110 μm wide Aluminum lines that connects to a total amount of 255 individual Silver microelectrodes, and four 300 μm wide Aluminum lines that connects to a total amount of 595 individual Silver microelectrodes. The total contact area between the microelectrodes

and the metallic line is of $1.632 \times 10^2 \text{ mm}^2$ and $3.808 \times 10^2 \text{ mm}^2$, whilst the total area of the metallic line is of 0.99 mm^2 and 2.25 mm^2 , respectively.

Once patterned, the Aluminum layer was etched using commercial Aluminum etchant (Al80 from Technic™). Aluminum etchants contain mixtures of 1-5 % HNO_3^* (for Al oxidation), 65-75 % H_3PO_4^* (to dissolve the Al_2O_3), 5-10 % CH_3COOH^* (for wetting and buffering) and H_2O dilution to define the etch rate at given temperature. This process was performed at room temperature, under orbital agitation at 150 rpm, until the complete pattern was engraved. Due to slight fluctuations in room temperature and reuse of the etchant solution, etching times could vary and thus, required optical inspection at the confocal microscope to verify the progress of the process.

Having the profile completely patterned, the top PFR 7790 G +PR was once again removed using LAM Rainbow 4400 Plasma Etching O_2 plasma, as previously described. Although this process also oxidizes the Aluminum layer, this oxidation occurs at a superficial level. Since in the final step the entire layout will be flipped, this oxidized layer will remain in the bottom of the stack and will not interfere with either the contact with the Silver microelectrodes, or with the pad connection to the reading system. To completely insulate the contact lines, a 3000 \AA thick final layer of SiO_2 was deposited on top of the Aluminum, under the previous conditions. The final result can be observed in Figure 89.

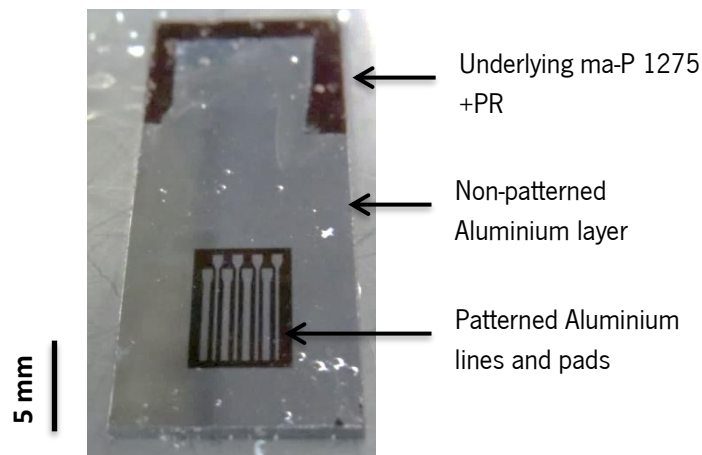


Figure 89 - Patterned Aluminum lines and pads (grey) over an $8 \mu\text{m}$ thick ma-P 1275 +PR layer (red). The SiO_2 layer is transparent, and thus, unobservable in this image.

3.2.9 - Structure release and activation

Once completed, a final step of transferring the stack to a clear substrate and releasing from the Silicon mold was required. For that, a set of different approaches were considered, as described in Table 16. These included the use of PDMS, Silicone and LOCTITE 1C Hysol (1:1). For some experiments, 10 × 10 mm pieces of Corning Glass were cleaned with Alconox™ solution for 30 minutes, at 65 °C, with ultrasonic agitation, and used as a solid substrate. All PDMS:curing-agent mixtures were prepared and degassed at a desiccator for about one hour, or until all the air bubbles were completely removed, prior to use. Both Silicone and LOCTITE 1C Hysol 1:1 were used directly. The releasing process was performed with Acetone, as to degrade the ma-P 1275 +PR layer, either on ultrasonic or orbital agitation (150 rpm in the latter case), until the complete detachment was achieved.

To facilitate the experiments, new dummy samples were created by depositing a stack layer of ma-P 1275 +PR (8 μm thick), Silicon Dioxide/Aluminum/Silicon Dioxide (3000 Å thick each) on top of a Silicon wafer. The wafer was then diced into individual dies with dimensions similar to those used in previous experiments. With this layout, the entire system was mimicked without the need for expensive and time-consuming samples. Furthermore, by having a linear Aluminum layer across the entire sample, deformations and fractures could be more easily observable, as to infer better quality. A schematic representation of the dummy samples used in this process can be observed in Figure 90.

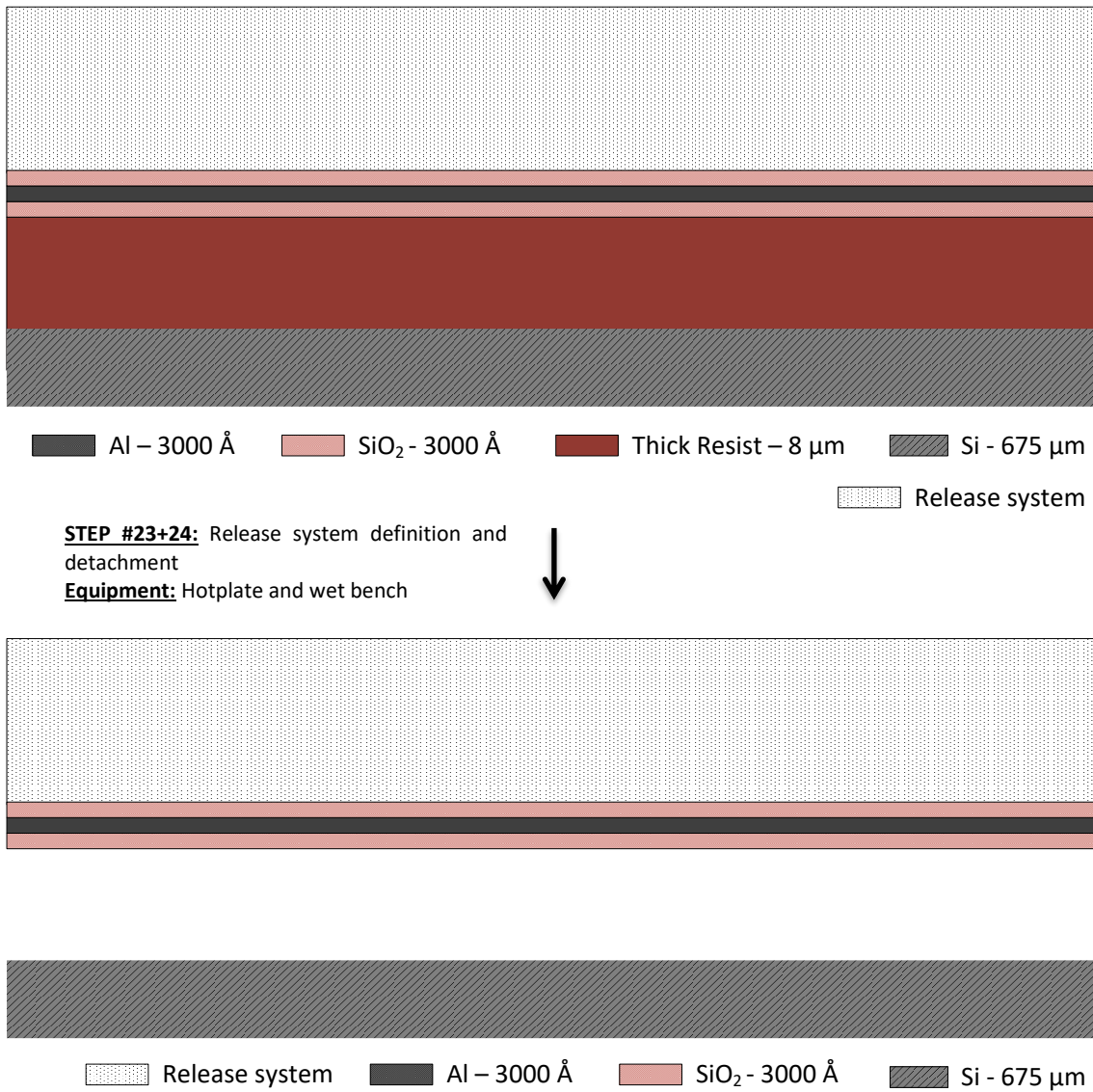


Figure 90 - Schematic diagram representing the cross-section view of the dummy samples used for the optimization of the structure release.

Table 16 - Experimental conditions used in the release of the patterned structures.

Sample #	PDMS on sample				PDMS on Glass					Extra Conditions	Release (agitation)	
	PDMS	Spin (rpm)	Time (sec)	Temp (°C)	Glass	PDMS	Spin (rpm)	Time (sec)	Temp (°C)		US	Orbital
RS 01	10:1	—	—	RT	—	—	—	—	—	—	yes	—
RS 02	10:1	—	—	70	—	—	—	—	—	—	—	—
RS 03	10:1	—	—	RT-70	—	—	—	—	—	—	—	—
RS 04	10:1	—	—	60	—	—	—	—	—	—	yes	—
RS 05	10:1	—	—	60	—	—	—	—	—	—	—	yes
RS 06	10:1	3000	30	60	—	—	—	—	—	—	—	yes
RS 07	—	—	—	—	—	—	—	—	—	LOCTITE 1C Hysol (1:1)	yes	—

(continuation of Table 16)

Sample #	PDMS on sample				PDMS on Glass					Extra Conditions	Release (agitation)	
	PDMS	Spin (rpm)	Time (sec)	Temp (°C)	Glass	PDMS	Spin (rpm)	Time (sec)	Temp (°C)		US	Orbital
RS 09	—	—	—	—	—	—	—	—	—	Silicone cured @ RT	yes	—
RS 10	10:1	3000	30	60	yes	10:1	3000	30	60	Plasma bond	—	yes
RS 11	10:1	3000	30	60	yes	10:1	3000	30	60	Plasma bond. Re-cure @ 60 °C for 4h	—	yes
RS 12a	10:1	3000	30	60	yes	—	—	—	—	Unite both substrates before curing	—	yes
RS 12b	10:1	3000	30	60	yes	10:1	3000	30	60	Unite both substrates before curing	—	yes
RS 12c	10:1	3000	30	60	yes	10:1	3000	30	60	Unite both substrates before curing and clamp both surfaces to increase pressure	—	yes
RS 13	—	—	—	—	yes	10:1	3000	30	60	Unite both substrates before curing	—	yes
RS 15	—	—	—	—	yes	10:1	500	30	60	Use larger glass substrate. Plasma bond and let it rest overnight with pressure	—	yes

(continuation of Table 16)

Sample #	PDMS on sample				PDMS on Glass					Extra Conditions	Release (agitation)	
	PDMS	Spin (rpm)	Time (sec)	Temp (°C)	Glass	PDMS	Spin (rpm)	Time (sec)	Temp (°C)		US	Orbital
RS 16	10:1	—	—	60	yes	—	—	—	—	Spill large amount of PDMS over the sample, unite and clamp both substrates	—	yes
RS 17	10:1	—	—	60	yes	—	—	—	—	Spill large amount of PDMS over the sample, unite and clamp both substrates. Place on desiccator for 2h before curing	—	yes
RS 18	—	—	—	—	yes	10:1	500	30	60	Use larger glass substrate, coat it with PDMS and place it on desiccator for 1h. Unite both substrates and place them on the desiccator overnight, before curing	—	yes
RS 19	—	—	—	—	yes	10:1	500	30	60	Use larger glass substrate, coat it with PDMS. Unite and clamp both substrates. Place both in desiccator overnight before curing	—	yes
RS 20	10:1	—	—	60	yes	—	—	—	—	Spill large amount of PDMS over the sample, unite and clamp both substrates. Place on desiccator overnight before curing	—	yes
RS 21	—	—	—	—	yes	10:1	—	—	60	Spill large amount of PDMS over the Glass, unite and clamp both substrates. Place on desiccator overnight before curing	—	yes

Initial study consisted in testing the reaction of the stacked layers to standard PDMS processing, namely the dispersion method and curing conditions. Samples RS 01-02 were prepared by dispersing the viscous PDMS on top of the processed samples until a ~5 mm thick layer was formed. Whilst sample RS 01 was left to cure at room temperature for 24 hours, sample RS 02 was baked at 70 °C inside an oven, for 75 minutes, and then left to rest at room temperature for the remaining period of time.

Preliminary analysis to the samples demonstrates that the curing process inside the oven is too aggressive for the stacked layers, causing massive damage to the underlying ma-P 1275 +PR. Moreover, the multilateral heating process occurring inside an oven could be causing the thermal expansion of the PR layer inwards, adding a cumulative stress to the center of the sample that would then erupt in bursts. However, curing at room temperature did not allow for the bonding of the PDMS layer to the top SiO₂ layer, causing a poor adhesion between both layers once attempted the release, as seen in Figure 91.

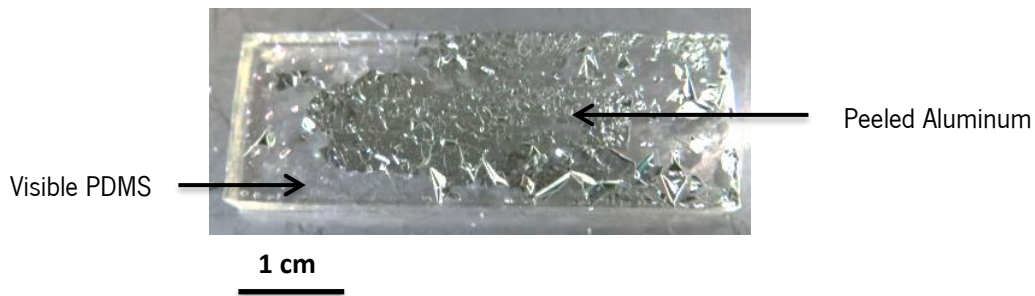


Figure 91 - Sample RS 01. Major deformation is observable due to the low adhesion between the PDMS and the Aluminum layer caused by the incomplete curing of the PDMS layer.

The curing process of the PDMS requires to be performed under compatible conditions with the limited thermal resistance/incompatibility of the stacked layers. Opting for a directional vertical heating source instead, a hotplate was tested as a tool for the baking process, aiming for a heating gradient that would be formed from the base of the sample and directed outwards, allowing for a free expansion of the ma-P 1275 +PR and evaporation of adhered gas molecules without deformation. Figure 92 demonstrates the difference between the heating appliance in both processes, as well as the direction of the stress release processes in each model.

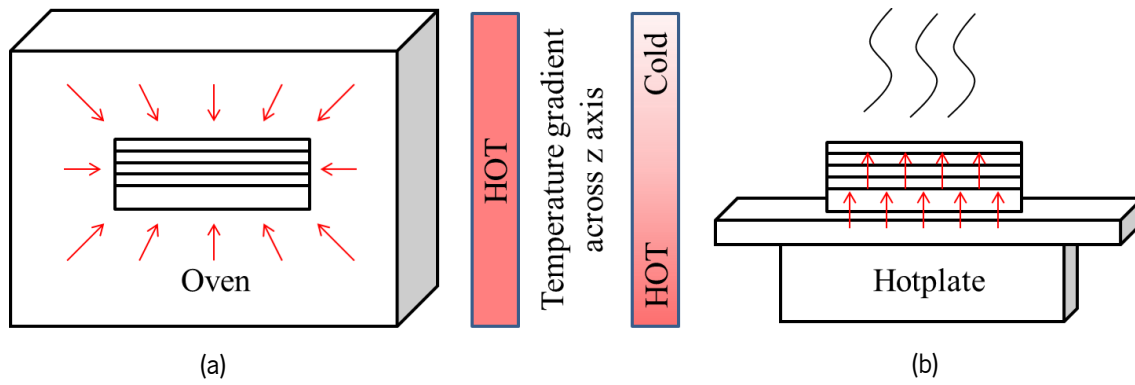


Figure 92 - Uniform heating step formed inside an oven with a simultaneous stress release process aimed inwards (a), compared to a differential heating gradient formed on top of a hotplate with a progressive stress release process aimed outwards (b).

A baking step with a gradient temperature increase was implemented as to infer the maximum temperature the Resist would endure before burning. Sample RS 03 was then processed with an increment of 5 °C every 15 minutes and inspected in an optimal microscope for visible deformations caused by overheating. The procedure demonstrated that after 65 °C, stress fractures and deformations would form on the Resist layer and would dissipate throughout the sample. Therefore, a maximum temperature of 60 °C was set for baking procedures on top of a hotplate.

Samples RS 04-05 (Figure 93) used the same procedure set previously to prepare identical samples that were tested in the release process through ultrasounds and orbital agitation, respectively. Both structures released completely, holding on to the patterned layers, once the ma-P 1275 +PR is degraded and removed. However, in both cases, massive stress fractures are registered as a consequence of the PDMS malleability. Once the structure would begin the detachment process, the PDMS would bend, allowing for Acetone to penetrate in between and deform the metallic layer.

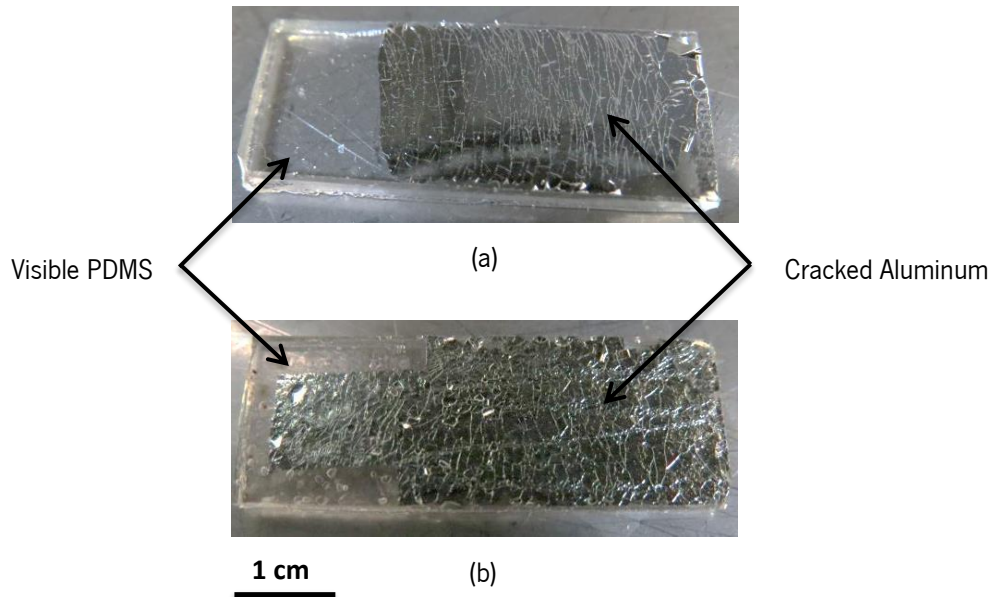


Figure 93 - Samples RS 04 (a) and RS 05 (b). Major cracks and deformations are observable in both samples, as a consequence of the PDMS malleability during the release process.

Alternatively, a contrasting strategy was tested with Sample RS 06. In this case, and in comparison with Samples RS 04-05, only a thin layer of PDMS was coated on top of the patterned silicon sample. The sample released perfectly, without apparent damage, but coils intensively, which prevents the correct “stretching” to allow for the bonding. A lot of effort needs to be put in order to place the sample correctly over the glass, which causes microstress fractures, as seen in Figure 94. Although the Sample could not be plasma-bonded to the Glass since it was constantly coiling, by placing it on top of another PDMS layer (coated on top of Glass), it was possible to adhere both samples.

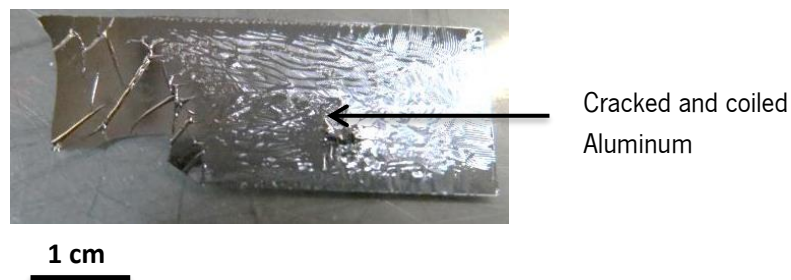


Figure 94 - Sample RS 06. After release, the sample coiled intensively, requiring the use of tweezers to stretch the coiled surface and place it on top of another layer of PDMS coated on glass. Through this method, the sample suffers severe deformation and cracking.

To improve the overall quality of the process, a harder substrate was tested, which would be able to withstand deformation whilst adhering to the stacked layers. Harder materials, such as LOCTITE 1C Hysol (1:1) and Silicone, were used for samples RS 07 and RS 08, respectively, and both cured at room temperature for 24 hours. The results can be observed in Figure 95. In both cases, release was performed through ultrasound agitation. Once cured, Silicone presented less flexibility than the PDMS with only slight improvement in the amount of defects transferred to the metallic layer. LOCTITE 1C Hysol (1:1) in the other hand, being a hardened epoxy, adhered intensively to the sample, taking a larger effort to detach. Once released, the underlying metallic layer presented only minor striations due to mechanical stress, presenting an overall improvement to the quality of the film.

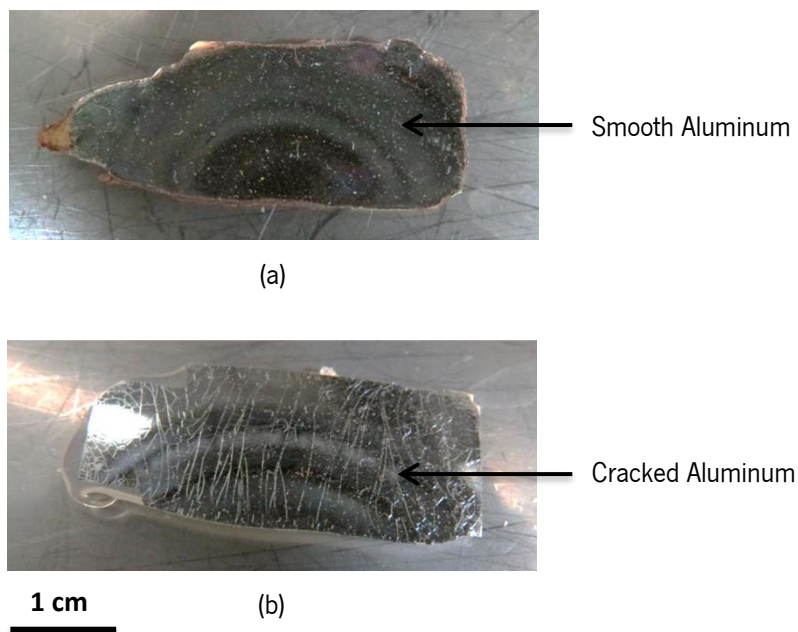


Figure 95 - Samples RS 07 (a) and RS 08 (b). The increased stiffness of the material used in Sample RS 07 promoted a better adherence to the Aluminum layer and prevented the deformation of the substrate, allowing for a complete transfer of the pattern without deformations or cracks. In Sample RS 09, the increased malleability of the substrate caused cracks to form during the release process.

Analyzing the results thus far, there is an apparent indication for the need of a solid substrate that could bond to the structured layer without any deformation. To attempt that, glass pieces were used together with PDMS to supply the needed solid substrate. In this process, the PDMS would create the bond between the fabricated structures and the glass. Furthermore, ultrasonic agitation provided the greatest fractures and deformations due to the highly entropic environment in which the samples are

presented. Therefore, future release processes relied only on the orbital agitation, at 150 rpm, immersed in Acetone.

Samples RS 9-10 were process simultaneously in a similar fashion. PDMS (10:1) was poured on top of the samples and the glass pieces and spun at 3000 rpm for 30 sec, followed by 240 minutes of baking on top of a hotplate at 60 °C. This resulted in the coating of a 100 μm thick layer. Once cured, the sample/glass pairs were bonded through Oxygen Plasma Bonding (Harrick Plasma Cleaner PDC-002-CE), at a Medium intensity, for 60 seconds, with an internal pressure of 800 mTorr. Sample RS 9 was re-baked on top of a hotplate at 60 °C, for an additional 240 minutes with pressure on top. Once completed, both samples were released on the orbital agitator. Due to surface tension effects at the border of the samples during the spin coating process, a peripheral topography is formed with an increased thickness of PDMS. Consequentially, the Plasma Bonding only occurred on the outer rim of the sample, as the higher thickness in that area prevented the contact between the two PDMS layers in the middle of both the sample and the glass piece. Once released, sample RS 09 presented a free-standing center area with a good outer rim bonding, as seen in Figure 96 (a). On the other hand, the pressure applied in sample RS 10 allowed for a partial bonding to occur in the center of the sample as well, as seen in Figure 97 (b).

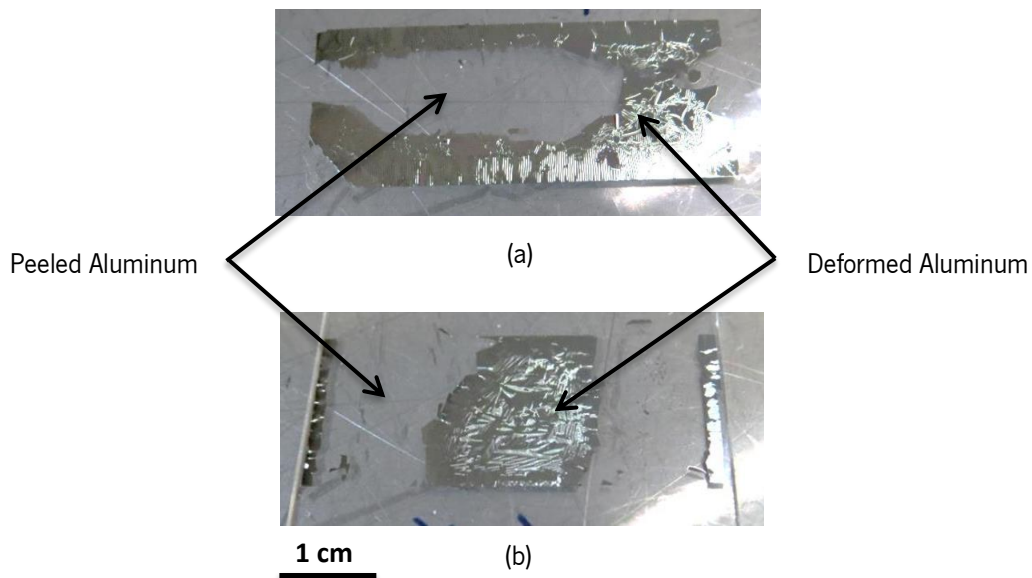


Figure 96 - Samples RS 09 (a) and RS 10 (b). Due to the higher thickness of the PDMS in the border of the silicon samples, bonding did not occur homogeneously throughout the entire surface. In sample RS 11, the appliance of pressure after bonding allowed for a minor deformation of the glass in the center, approximating the two substrates and promoting the bonding in the contact area.

To overcome the different thickness across the sample surface, Samples RS 11a-c and RS 12 were prepared by attempting to bond the 3 layers (Silicon sample with the patterned structures, PDMS and glass) before the curing process. In the first case, the PDMS was spun only on top of the silicon sample, whilst in the latter, only the glass substrate was coated. For samples RS 11b-c, both samples were coated with the PDMS. In all cases, once coated, the glass and the silicon were mounted together carefully, as to prevent the formation of air bubbles. For sample RS 11c, clamps were used to apply pressure and ensure the contact between all 3 layers. In all four cases, microbubbles were formed between the layers, causing deformations during the release process. Sample RS 11c however, presented the best results, as only a few imperfections could be detected, implying that clamping could allow for a greater uniformity in the PDMS dispersion and adhesion. Figure 97 presents the results obtained with these samples.

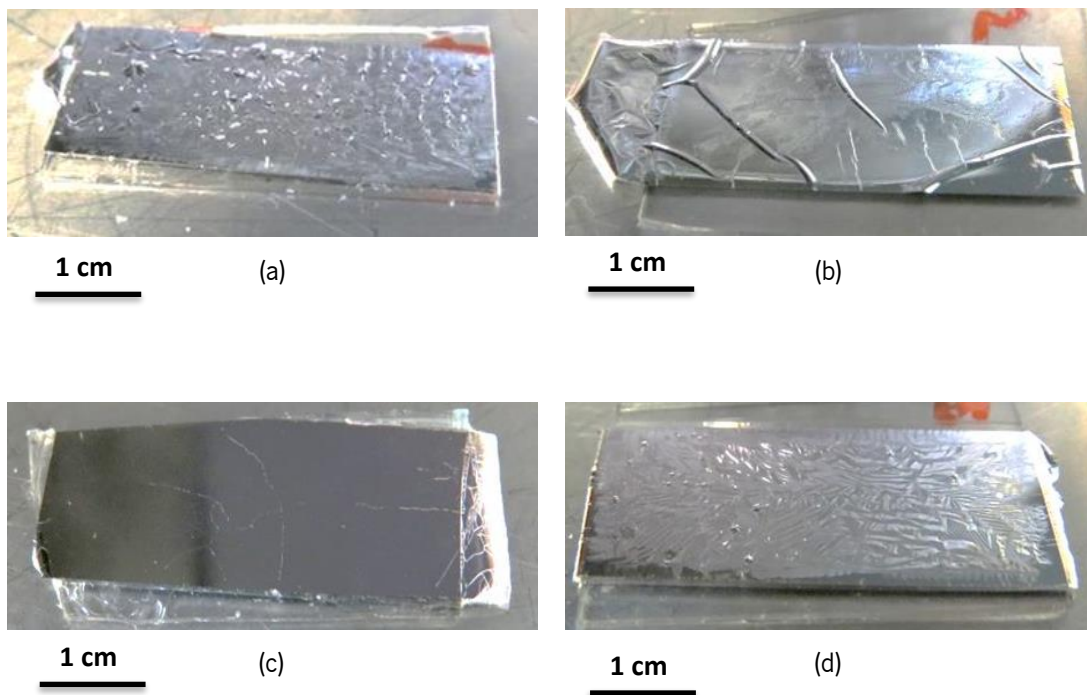


Figure 97 - Samples RS 11a (a), RS 11b (b), RS 11c (c) and RS 12 (d). With the exception of Sample RS 11c, all remaining patterns present deformations caused by a bad adhesion between the PDMS, the Aluminum layer and the Glass. Sample RS 11c only presents minor cracks in the bonded area. This improve in uniformity can be attributed to the pre-curing clamping of both substrates, forcing the dispersion of the liquid PDMS and promoting a better area coverage.

Taking into consideration all the previous results, two different approaches were taken into consideration for further studies:

- Bonding of the patterned silicon samples to larger pieces of glass coated with a thin film of PDMS, granting enough distance to the borders as to neglect the larger thickness at the borders.
- Usage of larger volumes of PDMS that would be compressed by pressure (clamping).

To test the first hypothesis, samples RS 13 was prepared by spin coating PDMS in a glass piece that was considerably larger than the silicon samples, as to avoid the previous problems with PDMS thickness around the borders of the glass. Applying a lower rotation to the spin coating of the PDMS, which resulted in a 250 μm thick layer, the coated glass piece was cured on top of a hotplate afterwards and Plasma Bonded to the Silicon Dioxide layer. A constant pressure was applied to the complete setup and left to rest overnight. Before the sample could be released, a visual inspection showed that an air bubble had formed between the two layers, which would signify a non-bonded area and a failed result.

Due to the large difficulties in ensuring a uniform and planar surface between the two layers to be bonded, and the eventual formation of air bubbles in between during the adhesion stage, this process was discontinued. A greater promise was found in the use of larger volumes of PDMS, poured or spun on top of the samples, and forcing the compression between the samples as to ensure that the excess PDMS would be dispersed and adapt to the topography of both surfaces.

An initial test was performed with sample RS 14 (figure 98). A large amount of PDMS was poured over the patterned silicon sample and a glass piece was then placed on top. The entire system was clamped and cured on top of a hotplate. Upon release, the sample took almost 2 days to completely detach from the silicon mold. This occurred due to the overspill of PDMS around the substrate, covering and blocking most access to the ma-P 1275 +PR layer, and hampering the dissolution of the resist layer. However, once detached, the sample presented the best yield so far, with only a fragment of imperfections and fractures being observed, possibly due to microbubbles formed between the PDMS and one of the substrates during the pouring stage.

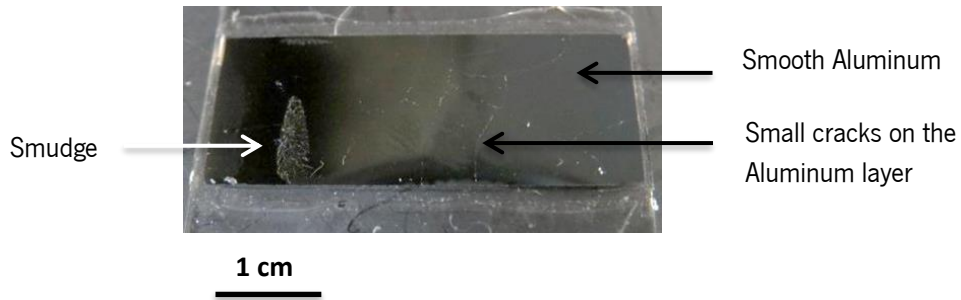


Figure 98 - Sample RS 14. Minor cracks are observed on top of the samples, possibly caused by non-uniform pressure during the degassing process. A small smudge is also located inside the sample, most likely due to improper cleaning of either the sample or the glass surface.

To improve on this result, sample RS 15 implied the same method as before, but the Glass/PDMS/Silicon set was placed inside a desiccator for 2 hours prior to curing. Although the release process took some effort as well, the sample detached without any signs of deformations, and only minor cracks along the surface, as seen in Figure 99. The use of the desiccator allowed for the microbubbles registered before to be removed, whilst the constant pressure applied by the clamps ensured that the PDMS would mold to the topography of both surfaces.

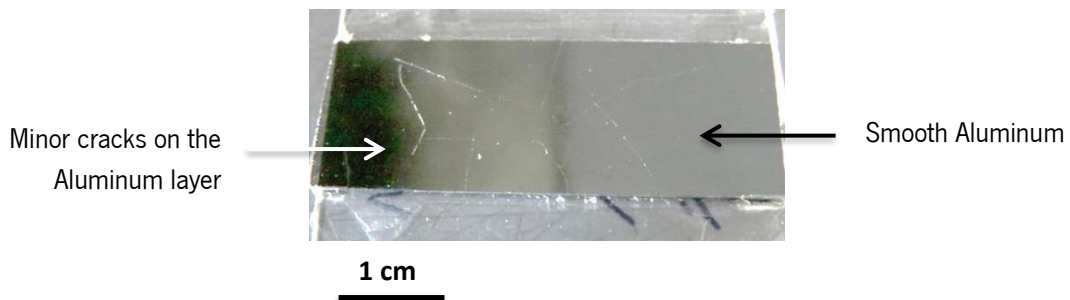


Figure 99 - Sample RS 15. Minor cracks are observed on top of the samples, possibly caused by non-uniform pressure during the degassing process.

To decrease the effort in the release process, several variations to the process used with RS 15 were applied. In samples RS 16-17, instead of pouring a large amount of PDMS that would then flow around the silicon sample and block the lateral access to the ma-P 1275 +PR, PDMS was spun on top of the glass pieces at similar conditions used in sample RS 13. Whilst in sample RS 17 both surfaces were clamped right after the PDMS coating, sample RS 16 was placed inside the desiccator for 1 hour prior

to that step. Afterwards, both samples were desiccated overnight before curing. The additional pre-clamping desiccation envisioned to facilitate the removal of microscopic air bubbles that could have formed during the spin coating process, as a greater surface area was available during this step. In both cases, some rugosity could be observed macroscopically throughout the samples surface, implying a low PDMS dispersion, as shown in Figure 100. Furthermore, a considerable amount of PDMS was still overlapping and covering the lateral walls of the silicon sample, hampering the access of the Acetone to the inner ma-P 1275 +PR layer. These results concluded that PDMS pouring, and not spinning, proved a better outcome in the transfer and release process.

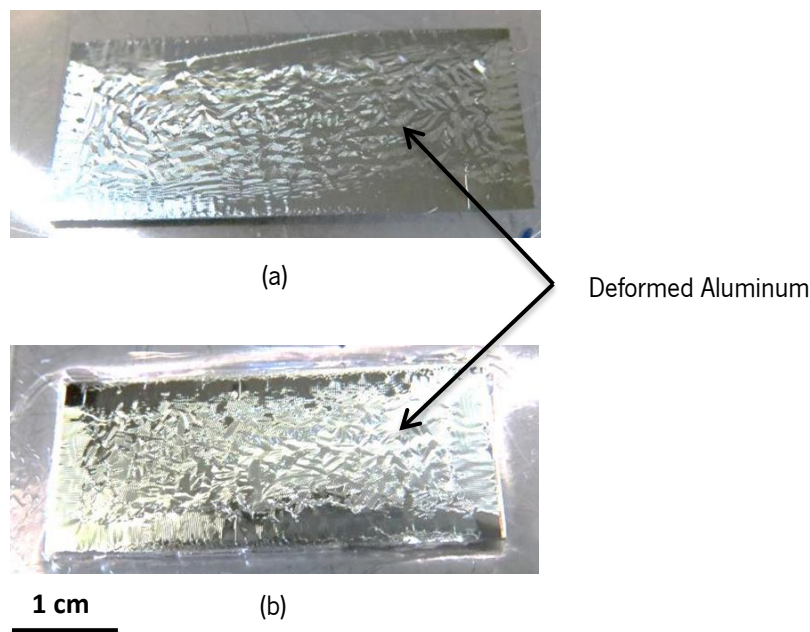


Figure 100 - Samples RS 16 (a) and RS 17 (b). Major deformation is most likely caused by a low PDMS dispersion. By spin coating the PDMS, the total volume of PDMS is not enough to cover the entire topography of the samples and promote the complete adhesion between the Glass and the Aluminum layer.

A final variation to the process was performed with samples RS 18-19 (figure 101). Whilst both samples were processed simultaneously, a difference relied on the recipient of the PDMS pouring, either the Silicon sample itself (sample RS 18), or the Glass piece (sample RS 19). After uniting and clamping the corresponding Silicon/PDMS/Glass setup, samples were placed on a desiccator overnight before curing on top of a hotplate. Prior to release, manually scrapping of the overlapping PDMS on the

lateral walls of the Silicon sample with a scalpel ensured a lateral pathway to the ma-P 1275 +PR. With this application, both samples detached in less than 6 hours, transferring the pattern with some cracks and defects, possibly caused by non-uniform pressure during the degassing process. Application of the PDMS on top of each substrate presented similar results. However, pouring on top of the -larger- Glass piece allowed for less PDMS to be wasted and overlapped after the clamping, as it possessed a larger area to expand before reaching the substrate rim.

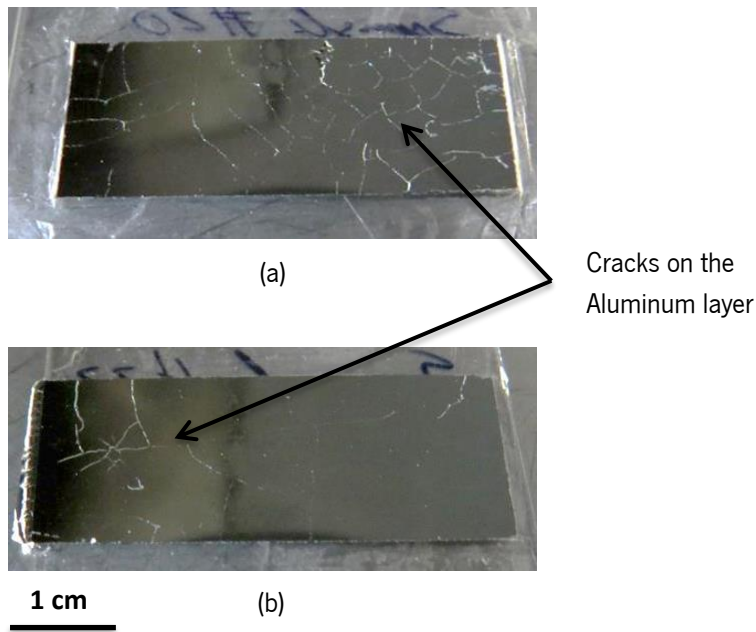


Figure 101 - Sample RS 18 (a) and RS 19 (b). Cracks are observed across the samples, likely caused by non-uniform pressure during the degassing process.

To compensate for the observable cracks, a better dispersion of the PDMS should be obtained during the curing process. This may be performed by improving the pressure, allowing for a longer degassing process, or using a more viscous PDMS. Using the gathered results, an electroplated sample was processed using the same conditions as sample RS 19, but applying a more uniform pressure. The result is a good pattern transfer, as seen in Figure 102 with a visible electroplated area (center-left) and a uniform Aluminum coating all around.

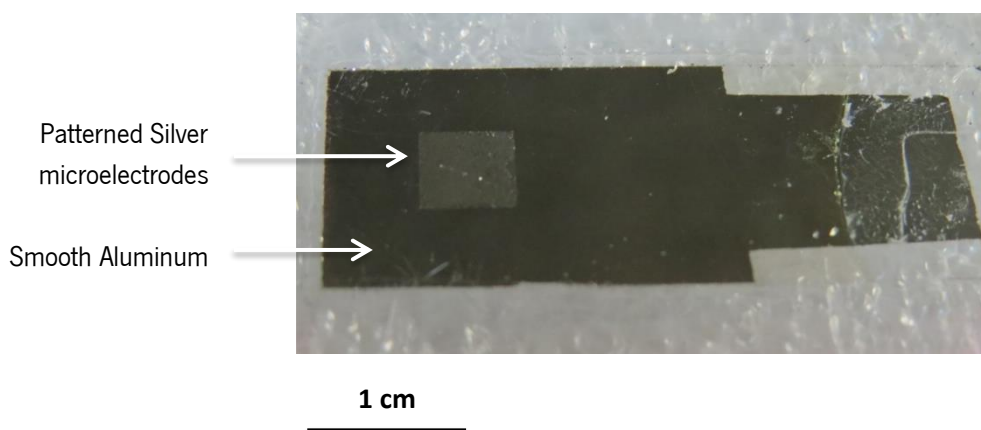


Figure 102 - Exposed electroplated Silver μ Needles (squared structure on the center), with underlying layers of 3000 Å Aluminum, $\approx 20 \mu\text{m}$ PDMS and Glass. No cracks are observed.

After the optimized conditions for the transferring of the patterns to a glass substrate were achieved, the complete system was manufactured according to the Runsheet, using all the process conditions optimized in the previous tests.

Samples EP Exx were used in this process as the final test samples. The different overplating thicknesses were used to analyze possible interferences to the overall process (particularly the electrical contact and shadowing effect with the Aluminum layer). Due to the process approach, all manufactured structures (particularly the μ Needles) should present the same profile and any variations in the visible profile thus far would be buried inside the PDMS layer once the structure was released.

Grain geometry between the EP Exx samples was not taken into consideration for this test, and thus, not analyzed. A description of the complete system and steps #23 and #24 are represented in Figures 103 and 104.

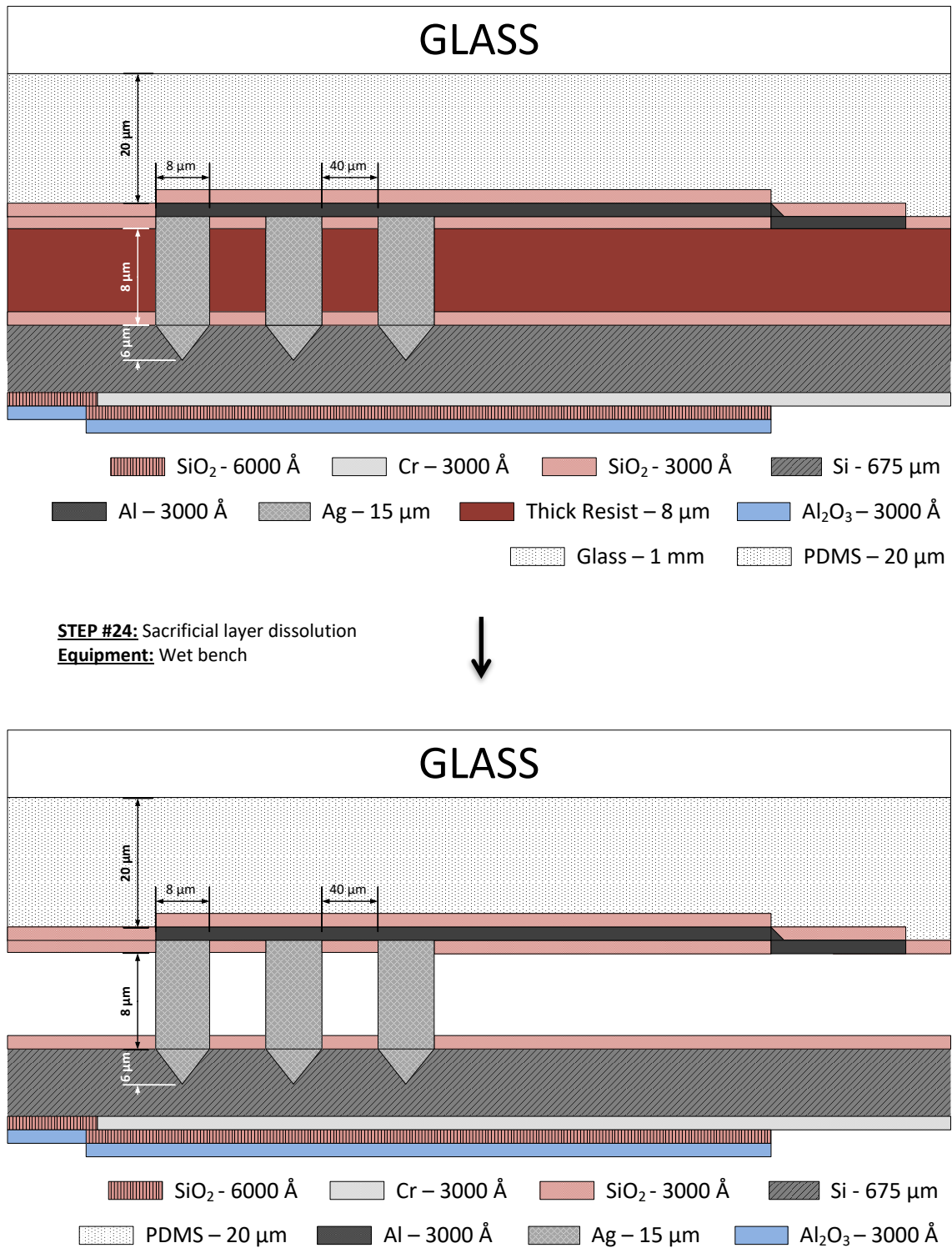


Figure 103 - Schematic diagram representing the cross-section view of the complete system consisting in patterned μ Needle Silver electrodes connected through an Aluminum pathway and protected by an insulating Silicon Dioxide double layer. In this schematic, the sacrificial ma-P 1275 +PR layer is removed through the use of Acetone in room temperature.

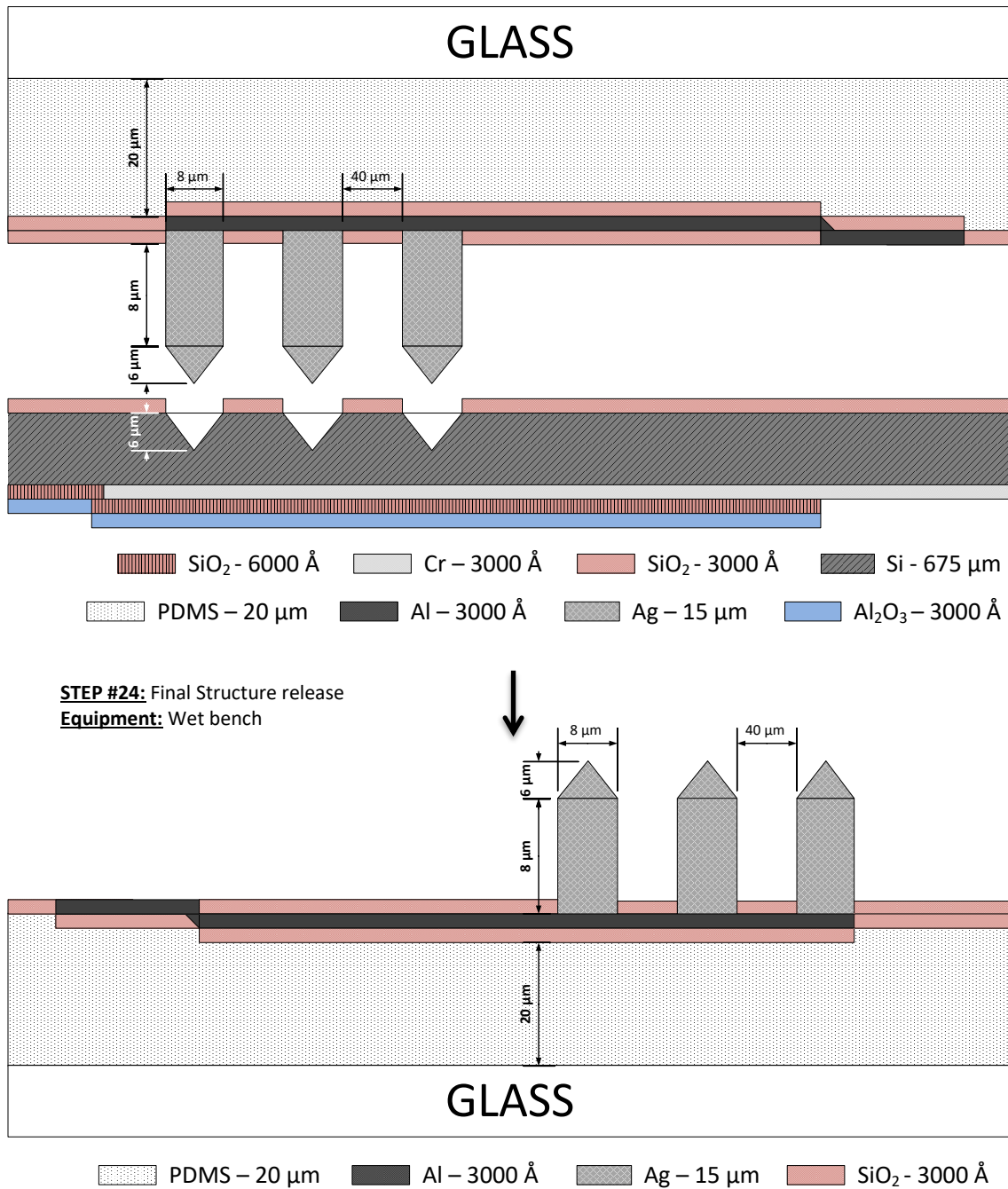


Figure 104 - Schematic diagram representing the cross-section view of the complete system consisting in patterned μ Needle Silver electrodes connected through an Aluminum pathway and protected by an insulating Silicon Dioxide double layer. In this schematic, the transferred system is detached from the Silicon mold and is available for functionalization and use.

Once released, the samples were analyzed at SEM for visual inspection of the μ Needles profile, and at a Profilometer to confirm the structures dimensions.

SEM analysis showed structures without a micrometric tip profile, as would be expected from the electrodeposition process, as demonstrated in Figure 105. All structures presented a square-like shape (promoted by the lithographic definition of the ma-P 1275 +PR), with a slight inclination near the top towards the center (caused by the width gradient formed during the consecutive laser scans during the lithographic process, demonstrated previously in Figure 56).

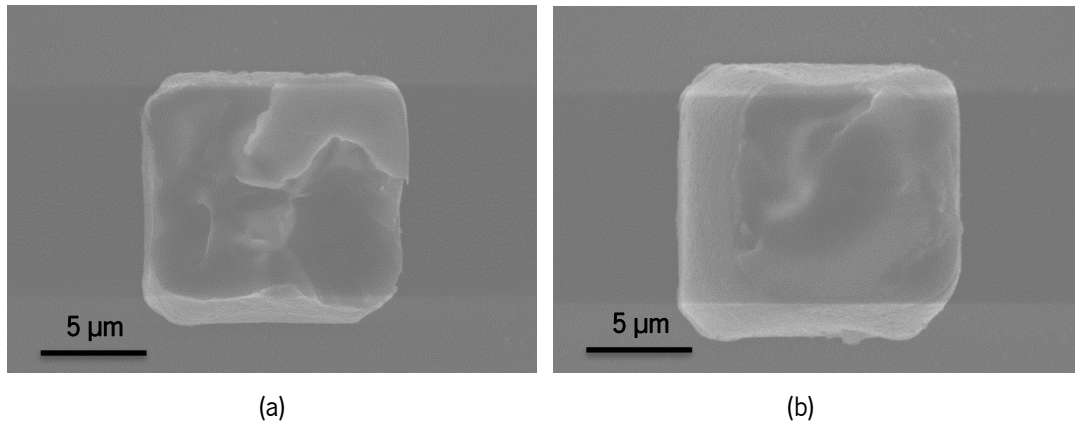


Figure 105 - SEM inspection of the released μ Needles (top view). The tips of the pyramids are missing, possibly due to breaking during the release process. The structures present a base width of around 12 μm , in par with the results obtained previously during the profile definition of the ma-P 1275 +PR.

Further analysis at the Profilometer revealed a height of only 8 μm across the entire sample. These two results combined demonstrate that the release process was unsuccessful to detach the electroplated tips and that a cleavage of the structures occurred at the interface between the silicon surface and the microfabricated pits.

A possible explanation for these results may lay with an underetching event. During the Silicon Wet Etching process, underetching may have one of two consequences: the creation of *mesa*-like structures similar to those observed in the formation of pyramids; or the direct etching beneath the mask layer, causing it to hang over the newly etched area.

As described previously, *mesas* are the consequence of underetching during the Silicon wet etching process, forming an undercut with an opposite inclination as that of the main etching plane. These *mesas* would act as physical barriers that prevent the dislodgment of material, entrapping the electroplated structures inside the pit, as seen in Figure 106.

Mesa formations are not common inside of pits formed by wet etching with KOH and weren't observed in the SEM inspection transversal images obtained during the optimization of the Silicon wet etching process.

For a focused analysis on the Silicon profile during the Wet Etching process, the Chromium masking layer was removed prior to SEM inspection. This prevented the observation of the hanging layer phenomenon at that period, which was later confirmed by further analysis from other projects at INESC-MN using the same technique, particularly for shallower etches.

To solve this issue, a simple step of removing the mask layer after the Silicon Wet Etching process is completed, following a soft overetching step to destroy the "*mesas*", should suffice. Although this layer was intended to provide an additional insulation against electroplating in non-desirable areas of the sample, the thick Photoresist should present a sufficient resistance to prevent that scenario, as proven during the Silver Electroplating optimization assay.

However, removing the Silicon Dioxide layer may prove a challenge. Typical processing at INESC-MN includes the use of a Reactive Ion Etching technique, as described previously. This technique also targets the exposed Silicon matrix (particularly the newly formed pits), extracting atoms in an isotropic configuration and possibly damaging both the final structural profile and the LAM Rainbow 4400 Plasma Etching equipment itself.

Another process could consist in the use of a shallow Dry Etching technique to sweep the surface of the sample, whilst avoiding the interior of the pits. However, this technique is usually applied to shallow etches (of a few hundred Angstroms) and most of the equipment at INESC-MN is not prepared for such long processes.

A final process to remove the Silicon Dioxide layer could consist in a Wet Etching process. Buffered Hydrofluoric Acid (BHF) is commonly used for this goal, although its use in this Runsheet could damage the remaining layers in the back of the Silicon wafer.

Alternatively, the mask layer could be changed completely. From the available materials, Chromium was the only element that was found to be resistant to the KOH process. However, manipulation of the topside Chromium layer could affect the backside layer previously deposited, especially if the protective layer does not have a good lateral coverage.

Further analysis is required to ascertain the optimal conditions for either removing or replacing the Silicon Dioxide layer used as a mask for the Silicon Wet Etching process. However, all of these steps are performed in the early stages of the Process Runsheet, and cannot be used to solve the problems for processed samples. Due to time constraints, it was not possible to recreate the setup with the proposed changes in the timeline for this thesis.

CHAPTER IV

CONCLUSIONS AND FUTURE WORK

CONCLUSIONS

FUTURE WORK

SCIENTIFIC PUBLICATIONS

CHAPTER IV - CONCLUSIONS AND FUTURE WORK

This thesis aimed for the fabrication of vertical micro-electrodes with cell penetration and pH quantitative sensing capabilities. A solid-state approach to this fabrication process was chosen over the direct functionalization of patterned surfaces due to limitations in the available processes, mainly the combination of several micrometric thick lithography with lift-off.

The chosen design included the fabrication of pyramidal pits that would be “artificially” increased in height with a PR spacing layer, electroplated with Silver to fill the empty cavities, and finally transferred to a transparent substrate for further integration with spectrometric analysis.

Silver was selected as the body of the micro-electrodes due to the extensive literature study of Silver/Silver-Chloride electrodes for pH measurements, as well as due to easy compatibility with the remaining microfabrication steps.

4.1 - Conclusions

Silicon Wet Etching allowed for a consistent and considerable uniform patterning of micrometric pyramidal structures, from which 4-sided pyramidal pits were selected for subsequent processing. The structures were designed and fabricated with dimensions of $8 \times 8 \times -5.6 \mu\text{m}$ (x/y/z) as proof of concept, granting considerable safety margins for subsequent lithographical processing. However, and for future iterations, the same structures may be fabricated with dimensions as small as $2 \times 2 \times -1.4 \mu\text{m}$ for the selected range of equipment and processes. A diluted Potassium Hydroxide (KOH) 22 wt% solution was used in this step. Isopropanol (IPA) was shown to influence the etching rate of the {110} and {331} crystallographic planes. Significant progress was made in the modulation of the etching conditions regarding the microloading effect, and in discovering that it's the IPA availability, and not concentration, that affects the etching rate of said planes.

Through the deposition and patterning of an $8 \mu\text{m}$ thick PR layer, the structure dimensions were increased to $12 \times 12 \times -13.6 \mu\text{m}$ (x/y/z). The increase in the base size was due to light scattering and heat dispersion during lithography, which mainly affects the areas closest to the light source, and thus, the base of the future structures. Further increase of the aspect ratio would be possible with a decrease of the pyramidal structure initial dimensions (as described in the previous paragraph), or by increasing the PR thickness (with consequential increase in the new base dimensions as well).

Silver electroplating was achieved using a 2-Electrode system in a novel technique that imposes a current transfer throughout the bulk of the Silicon wafer in order to promote crystalline growth in the opposite side of the applied current. Optimization of the electroplating conditions in dummy samples proved to achieve a decent homogeneity and a good yield, both compatible with further micrometric processing. However, the same conditions applied to the final design resulted in low-yield deposition with a distinctive and regular pattern that could not be explained. Further study and optimization of this process is required for future iterations. The electroplated profiles were proven to be composed of 100 % Silver, although not enough data was obtained regarding the crystallographic structure.

The biggest challenge in the reported microfabrication process was found around the low thermal conductivity of the sacrificial ma-P 1275 +PR, once other layers were already deposited on top. This forced the reconfiguration and optimization of standard microfabrication protocols to adapt to lower energetic output with higher cool down periods. Nevertheless, optimization of these conditions allowed for a multi-layer processing system to be implemented, mainly regarding the patterning and removal of top PR layers without interfering or damaging the underlying 8 μm thick PR that served as a sacrificial layer for height incrementation.

Structure release was accomplished by combining the use of liquid PDMS with hard glass substrates. Although great success was achieved with the optimization of this transferring and release protocol, the final structures were truncated near the start of the pyramidal features due to an unforeseen formation of *mesa* features during the Wet Etching process. This occurred due to the use of Silicon Dioxide as a mask layer, instead of Chromium, used in the optimization steps of that process. Several alternatives are discussed in this thesis that could overcome this problem and meet the required conditions for complete pattern transferring.

4.2 - Future work

Due to time limitations, the project could not be completed. However, a guideline of the necessary steps was predicted and presented.

For future work, an alternative thick sacrificial layer, compatible with photolithographic protocols, should be researched. This sacrificial layer would replace the ma-P 1275 +PR and should be processed in a way that isn't influenced by the developing solutions used for standard lithography processes, and can be easily removed with a solvent that does not damage any layer of the final structures.

Further analysis of the penetration capability of the fabricated microneedles is also required. For solid-state, micrometric needles, electroporation can be implemented as the primary cell penetration method. Alternatively, the profile of the microneedles may be adjusted for thinner lateral dimensions, although that may increase the likelihood of structural damage and breakage. Optimal conditions for the developed processes presume the possibility for $6 \times 6 \times -9.4 \mu\text{m}$ microneedles with a pyramidal tip structure of $2 \times 2 \times -1.4 \mu\text{m}$. Further modulation of those dimensions should be possible with other materials or techniques, aiming for a decrease in the structure base width and increase in the total height of the sacrificial layer.

With the MEMS transfer to a glass substrate, demonstrated in this thesis, this system may be implemented with spectroscopy systems. Metallic lines used for signal acquisition may be deposited using transparent materials, such as ITO, reducing the opacity of the system and limiting it to the microneedles themselves. This could allow for a complex dual analysis system with a cell-penetrating, solid-state pH sensing microneedles, and an absorbance or fluorescence conjugated apparatus.

A Reference Electrode could theoretically be integrated in this system during the electroplating step, by allowing for another electroplating area to be performed away from the patterned profiles. A PDMS-based microfluidic system could be implemented for limiting Silver Chlorination with Ferrous Chloride (FeCl_2) to the desired area of the Reference Electrode, as well as providing a medium for a liquid electrolyte solution for stabilization. A vertical outlet system compatible with this process was investigated in a parallel manner and presented in an Oral Communication.

Finally, the development of electronics and microelectronics is required, to acquire individual electric voltage from each needle in the matrix, compute pH values and apply individual calibration and corrections, and represent the pH map of the full electrodes matrix.

4.3 - Scientific publications

The work related with the optimization of the Silicon Wet Etching process was published in:

- T.S. Monteiro, P. Kastytis, L.M. Gonçalves, G. Minas, S. Cardoso, "Dynamic Wet Etching of Silicon through Isopropanol Alcohol Evaporation", *Micromachines* 2015, 6 (10), 1534-1545.

Poster communications related to that process were also presented in:

- T.S. Monteiro, L.M. Gonçalves, G. Minas, S. Cardoso, "Effect of Isopropanol evaporation on anisotropic etching of silicon in aqueous potassium hydroxide solutions", in 26th *Micromechanics and Microsystems Europe workshop*, Toledo, Spain, 2015.
- T.S. Monteiro, J.D. Santos, S. Cardoso, "Silicon wet etch micromachining for smart system integration", *IN Workshop*, Lisbon, Portugal, 2016.

Oral communications regarding different topics related with the thesis were presented in:

- T.S. Monteiro, L.M. Gonçalves, G. Minas, S.C. Freitas, "Silicon Probes as Biosensors for Intra- and Extracellular Measurement of pH for Early Detection of Dysplasia", 1st *Cluster Workshop in Material and Nanotechnology*, Lisbon, Portugal, 2013. http://1clustermn.ist.utl.pt/Book_of_Abstracts_1ClusterMN.pdf
- T.S. Monteiro, S. Cardoso, L.M. Gonçalves, G. Minas, "PDMS encasing system for integrated lab-on-chip Ag/AgCl reference electrodes", 4th *Portuguese BioEngineering Meeting*, Porto, Portugal, 26-28 February 2015. https://www.researchgate.net/publication/275410214_toc

Publications in scientific meetings were registered in:

- S.Pimenta, T.S. Monteiro, L.M. Gonçalves, G. Minas, "Spectroscopy and pH biosensors for the detection of gastrointestinal dysplasia", published in *Proceedings of IEEE-EMBS, 3rd Portuguese BioEngineering Meeting*, Braga, Portugal, 20-22 February 2013. <https://ieeexplore.ieee.org/document/6518407>
- T.S. Monteiro, S. Cardoso, L.M. Gonçalves, G. Minas, "PDMS encasing system for integrated lab-on-chip Ag/AgCl reference electrodes", published in *Proceedings of IEEE*, 4th

Portuguese BioEngineering Meeting, Porto, Portugal, 26-28 February 2015.
<https://ieeexplore.ieee.org/document/7088871>

Scientific publications, based on the processes developed on this thesis, but not related to it, are compiled in the following list:

- Scientific paper: M. Peres, A. J. S. Fernandes, F. J. Oliveira, L. C. Alves, E. Alves, T. S. Monteiro, S. Cardoso, M. Alonso-Orts, E. Nogales, B. Méndez, E. G. Villora, K. Shimamura, K. Lorenz, “Micro-Opto-Electro-Mechanical Device Based on Flexible β -Ga₂O₃ Micro-Lamellas”, ECS Journal of Solid State Science and Technology 2019, 8 (7), 3235-3241.
<https://iopscience.iop.org/article/10.1149/2.0441907jss>
- Book chapter: M.H.G. Costa, T.S. Monteiro, S. Cardoso, J. Cabral, F.C. Ferreira, C.L. da Silva, “Three-Dimensional Co-culture of Human Hematopoietic Stem/Progenitor Cells and Mesenchymal Stem/Stromal Cells in a Biomimetic Hematopoietic Niche Microenvironment”, Methods of Molecular Biology 2018.
<https://europepmc.org/article/med/30367359>
- Poster communication: A.V. Silva, R. Bastos, J. Santos, T.S. Monteiro, S. Cardoso, “Silicon groove etching for ASPIC encapsulation”, in 43rd Micro and Nano Engineering - MNE2017, Braga, Portugal, 2017
- Poster communication: J. Santos, T.S. Monteiro, S. Cardoso, “Integration of micromachined through silicon vias with TMR sensors”, in 43rd Micro and Nano Engineering - MNE2017, Braga, Portugal, 2017

BIBLIOGRAPHY

- [1] D. F. Emerich, and C. G. Thanos, "Nanotechnology and medicine," *Expert Opinion on Biological Therapy*, vol. 3, no. 4, pp. 655-663, 2003/07/01, 2003.
- [2] S. Bhansali, and A. Vasudev, *MEMS for biomedical applications*, 2012.
- [3] M. Asif, A. Razaq, S. Bhand, M. Willander, and B. Danielsson, "Biosensors for Intracellular and Less Invasive Measurements Based on Nanostructured Metal Oxides," pp. 29-49, 2018.
- [4] M. H. Asif, O. Nur, M. Willander, P. Strålfors, C. Brännmark, F. Elinder, U. H. Englund, J. Lu, and L. Hultman, "Growth and Structure of ZnO Nanorods on a Sub-Micrometer Glass Pipette and Their Application as Intracellular Potentiometric Selective Ion Sensors," *Materials*, vol. 3, no. 9, pp. 4657, 2010.
- [5] R. Orij, J. Postmus, A. Ter Beek, S. Brul, and G. J. Smits, "In vivo measurement of cytosolic and mitochondrial pH using a pH-sensitive GFP derivative in *Saccharomyces cerevisiae* reveals a relation between intracellular pH and growth," *Microbiology*, vol. 155, no. 1, pp. 268-278, 2009.
- [6] J. Lu, and Z. Rosenzweig, "Nanoscale fluorescent sensors for intracellular analysis," *Fresenius' Journal of Analytical Chemistry*, vol. 366, no. 6, pp. 569-575, March 01, 2000.
- [7] H. A. Clark, R. Kopelman, R. Tjalkens, and M. A. Philbert, "Optical Nanosensors for Chemical Analysis inside Single Living Cells. 2. Sensors for pH and Calcium and the Intracellular Application of PEBBLE Sensors," *Analytical Chemistry*, vol. 71, no. 21, pp. 4837-4843, 1999/11/01, 1999.
- [8] C. Tautorat, P. Koester, J. Held, J. Gaspar, P. Ruther, O. Paul, A. Cismak, A. Heilmann, J. Gimsa, H. Beikirch, L. Jonas, and W. Baumann, *Intracellular potential measurements of adherently growing cells using micro-needle arrays*, 2008.
- [9] S. J. Pearton, T. Lele, Y. Tseng, and F. Ren, "Penetrating living cells using semiconductor nanowires," *Trends in Biotechnology*, vol. 25, no. 11, pp. 481-482, 2007/11/01/, 2007.
- [10] T.-M. Fu, X. Duan, Z. Jiang, X. Dai, P. Xie, Z. Cheng, and C. M. Lieber, "Sub-10-nm intracellular bioelectronic probes from nanowire–nanotube heterostructures," *Proceedings of the National Academy of Sciences*, vol. 111, no. 4, pp. 1259-1264, 2014.
- [11] Y. Hanein, C. G. J. Schabmueller, G. Holman, P. L. Cke, D. D. Denton, and K. F. Bhringer, "High-aspect ratio submicrometer needles for intracellular applications," *Journal of Micromechanics and Microengineering*, vol. 13, no. 4, pp. S91-S95, 2003/06/13, 2003.
- [12] M. Willander, and S. Al-Hilli, "ZnO Nanorods as an Intracellular Sensor for pH Measurements," *Micro and Nano Technologies in Bioanalysis: Methods and Protocols*, R. S. Foote and J. W. Lee, eds., pp. 187-200, Totowa, NJ: Humana Press, 2009.
- [13] Y. Wang, H. Xu, J. Zhang, and G. Li, "Electrochemical Sensors for Clinic Analysis," *Sensors*, vol. 8, no. 4, pp. 2043, 2008.
- [14] Y. Shevchenko, G. Camci-Unal, D. Cuttica, M. Dokmeci, J. Albert, and A. Khademhosseini, *Surface Plasmon Resonance Fiber Sensor for Real-Time and Label-Free Monitoring of Cellular Behavior*, 2014.
- [15] C. Yu, X. Li, F. Zeng, F. Zheng, and S. Wu, "Carbon-dot-based ratiometric fluorescent sensor for detecting hydrogen sulfide in aqueous media and inside live cells," *Chemical Communications*, vol. 49, no. 4, pp. 403-405, 2013.
- [16] Y.-X. Wu, J.-B. Li, L.-H. Liang, D.-Q. Lu, J. Zhang, G.-J. Mao, L.-Y. Zhou, X.-B. Zhang, W. Tan, G.-L. Shen, and R.-Q. Yu, "A rhodamine-appended water-soluble conjugated polymer: an efficient ratiometric fluorescence sensing platform for intracellular metal-ion probing," *Chemical Communications*, vol. 50, no. 16, pp. 2040-2042, 2014.

- [17] R. Yan, J.-H. Park, Y. Choi, C.-J. Heo, S.-M. Yang, L. P. Lee, and P. Yang, "Nanowire-based single-cell endoscopy," *Nature Nanotechnology*, vol. 7, pp. 191, 12/18/online, 2011.
- [18] A. L. Sisson, D. Steinhilber, T. Rossow, P. Welker, K. Licha, and R. Haag, "Biocompatible Functionalized Polyglycerol Microgels with Cell Penetrating Properties," *Angewandte Chemie International Edition*, vol. 48, no. 41, pp. 7540-7545, 2009.
- [19] Y. Sun, and B. J. Nelson, "MEMS capacitive force sensors for cellular and flight biomechanics," *Biomedical Materials*, vol. 2, no. 1, pp. S16-S22, 2007/03, 2007.
- [20] Q. Qing, Z. Jiang, L. Xu, R. Gao, L. Mai, and C. M. Lieber, "Free-standing kinked nanowire transistor probes for targeted intracellular recording in three dimensions," *Nature Nanotechnology*, vol. 9, pp. 142, 12/15/online, 2013.
- [21] M. H. Asif, B. Danielsson, and M. Willander, "ZnO Nanostructure-Based Intracellular Sensor," *Sensors*, vol. 15, no. 5, pp. 11787, 2015.
- [22] O. P. Hamill, A. Marty, E. Neher, B. Sakmann, and F. J. Sigworth, "Improved patch-clamp techniques for high-resolution current recording from cells and cell-free membrane patches," *Pflügers Archiv*, vol. 391, no. 2, pp. 85-100, August 01, 1981.
- [23] A. Rolong, R. V. Davalos, and B. Rubinsky, "History of Electroporation," *Irreversible Electroporation in Clinical Practice*, M. R. Meijerink, H. J. Scheffer and G. Narayanan, eds., pp. 13-37, Cham: Springer International Publishing, 2018.
- [24] J. C. Weaver, and Y. A. Chizmadzhev, *Theory of Electroporation: A Review*, 1996.
- [25] G. Yang, L. Xu, J. Xu, R. Zhang, G. Song, Y. Chao, L. Feng, F. Han, Z. Dong, B. Li, and Z. Liu, "Smart Nanoreactors for pH-Responsive Tumor Homing, Mitochondria-Targeting, and Enhanced Photodynamic-Immunotherapy of Cancer," *Nano Letters*, vol. 18, no. 4, pp. 2475-2484, 2018/04/11, 2018.
- [26] F. Ai, N. Wang, X. Zhang, T. Sun, Q. Zhu, W. Kong, F. Wang, and G. Zhu, "An upconversion nanoplatform with extracellular pH-driven tumor-targeting ability for improved photodynamic therapy," *Nanoscale*, vol. 10, no. 9, pp. 4432-4441, 2018.
- [27] S. Liu, X. Luo, S. Liu, P. Xu, J. Wang, and Y. Hu, "Acetazolamide-Loaded pH-Responsive Nanoparticles Alleviating Tumor Acidosis to Enhance Chemotherapy Effects," *Macromolecular Bioscience*, vol. 19, no. 2, pp. 1800366, 2019.
- [28] X. Chen, Z. Chen, B. Hu, P. Cai, S. Wang, S. Xiao, Y.-L. Wu, and X. Chen, "Synergistic Lysosomal Activatable Polymeric Nanoprobe Encapsulating pH Sensitive Imidazole Derivative for Tumor Diagnosis," *Small*, vol. 14, no. 9, pp. 1703164, 2018.
- [29] H.-N. Liu, N.-N. Guo, T.-T. Wang, W.-W. Guo, M.-T. Lin, M.-Y. Huang-Fu, M. R. Vakili, W.-H. Xu, J.-J. Chen, Q.-C. Wei, M. Han, A. Lavasanifar, and J.-Q. Gao, "Mitochondrial Targeted Doxorubicin-Triphenylphosphonium Delivered by Hyaluronic Acid Modified and pH Responsive Nanocarriers to Breast Tumor: in Vitro and in Vivo Studies," *Molecular Pharmaceutics*, vol. 15, no. 3, pp. 882-891, 2018/03/05, 2018.
- [30] X. Zhang, Y. Lin, and R. J. Gillies, "Tumor pH and Its Measurement," *Journal of Nuclear Medicine*, vol. 51, no. 8, pp. 1167-1170, August 1, 2010, 2010.
- [31] U. National Cancer Institute. "How Cancer Is Diagnosed," October 18, 2020; <https://www.cancer.gov/about-cancer/diagnosis-staging/diagnosis>.
- [32] M. Willander, P. Klason, L. L. Yang, S. M. Al-Hilli, Q. X. Zhao, and O. Nur, "ZnO nanowires: chemical growth, electrodeposition, and application to intracellular nano-sensors," *physica status solidi c*, vol. 5, no. 9, pp. 3076-3083, 2008.
- [33] A. J. Miller, D. E. Carden, and D. Diamond, "An improved Na⁺-selective microelectrode for intracellular measurements in plant cells," *Journal of Experimental Botany*, vol. 52, no. 359, pp. 1353-1359, 2001.

- [34] H. Yamaguchi, "Recording of intracellular Ca^{2+} from smooth muscle cells by sub-micron tip, double-barrelled Ca^{2+} -selective microelectrodes," *Cell Calcium*, vol. 7, no. 4, pp. 203-219, 1986/08/01/, 1986.
- [35] M. Khan, K. Mukherjee, R. Shoukat, and D. Huang, "A review on pH sensitive materials for sensors and detection methods," *Microsystem Technologies*, 07/22, 2017.
- [36] G. Bergtrom, *Basic Cell and Molecular Biology: What We Know & How We Found Out*, 2nd Edition ed.: University of Wisconsin, Milwaukee, 2016.
- [37] L. Tian, and Y. H. Bae, "Cancer nanomedicines targeting tumor extracellular pH," *Colloids and Surfaces B: Biointerfaces*, vol. 99, pp. 116-126, 2012/11/01/, 2012.
- [38] Y. Bae, W.-D. Jang, N. Nishiyama, S. Fukushima, and K. Kataoka, "Multifunctional polymeric micelles with folate-mediated cancer cell targeting and pH-triggered drug releasing properties for active intracellular drug delivery," *Molecular bioSystems*, vol. 1, no. 3, pp. 242-250, 2005/09//, 2005.
- [39] F. Hillen, and A. W. Griffioen, "Tumour vascularization: sprouting angiogenesis and beyond," *Cancer Metastasis Reviews*, vol. 26, no. 3-4, pp. 489-502, 08/24, 2007.
- [40] "The absolute electrode potential: an explanatory note (Recommendations 1986)," *Journal of Electroanalytical Chemistry and Interfacial Electrochemistry*, vol. 209, no. 2, pp. 417-428, 1986/09/25/, 1986.
- [41] R. Pal, and D. Parker, "A ratiometric optical imaging probe for intracellular pH based on modulation of europium emission," *Organic & Biomolecular Chemistry*, vol. 6, no. 6, pp. 1020-1033, 2008.
- [42] A. Eftekhari, "pH sensor based on deposited film of lead oxide on aluminum substrate electrode," *Sensors and Actuators B: Chemical*, vol. 88, no. 3, pp. 234-238, 2003/02/10/, 2003.
- [43] K. Pásztor, A. Sekiguchi, N. Shimo, N. Kitamura, and H. Masuhara, "Iridium oxide-based microelectrochemical transistors for pH sensing," *Sensors and Actuators B: Chemical*, vol. 12, no. 3, pp. 225-230, 1993/04/15/, 1993.
- [44] O. Segut, B. Lakard, G. Herlem, J.-Y. Rauch, J.-C. Jeannot, L. Robert, and B. Fahys, "Development of miniaturized pH biosensors based on electrosynthesized polymer films," *Analytica Chimica Acta*, vol. 597, no. 2, pp. 313-321, 2007/08/10/, 2007.
- [45] A. M. Bond, "Past, present and future contributions of microelectrodes to analytical studies employing voltammetric detection. A review," *Analyst*, vol. 119, no. 11, pp. 1R-21R, 1994.
- [46] M. L. Lucas, W. Schneider, F. J. Haberich, and J. A. Blair, "Direct Measurement by pH-Microelectrode of the pH Microclimate in Rat Proximal Jejunum," *Proceedings of the Royal Society of London. Series B. Biological Sciences*, vol. 192, no. 1106, pp. 39-48, December 31, 1975, 1975.
- [47] I. A. Ges, B. L. Ivanov, D. K. Schaffer, E. A. Lima, A. A. Werdich, and F. J. Baudenbacher, "Thin-film IrO_x pH microelectrode for microfluidic-based microsystems," *Biosensors and Bioelectronics*, vol. 21, no. 2, pp. 248-256, 2005/08/15/, 2005.
- [48] W.-H. Choi, and I. Papautsky, *Fabrication of a needle-type pH sensor by selective electrodeposition*: SPIE, 2011.
- [49] A. Fog, and R. P. Buck, "Electronic semiconducting oxides as pH sensors," *Sensors and Actuators*, vol. 5, no. 2, pp. 137-146, 1984/02/01/, 1984.
- [50] S. Głab, A. Hulanicki, G. Edwall, and F. Ingman, "Metal-Metal Oxide and Metal Oxide Electrodes as pH Sensors," *Critical Reviews in Analytical Chemistry*, vol. 21, no. 1, pp. 29-47, 1989/08/01, 1989.
- [51] J. B. Goodenough, "Metallic oxides," *Progress in Solid State Chemistry*, vol. 5, pp. 145-399, 1971/01/01/, 1971.

- [52] S. Shahrestani, M. C. Ismail, S. Kakooei, M. Beheshti, M. Zabihiazadboni, and M. A. Zavareh, "Iridium Oxide pH Sensor Based on Stainless Steel Wire for pH Mapping on Metal Surface," *IOP Conference Series: Materials Science and Engineering*, vol. 328, no. 1, pp. 012014, 2018.
- [53] R. Koncki, and M. Mascini, "Screen-printed ruthenium dioxide electrodes for pH measurements," *Analytica Chimica Acta*, vol. 351, no. 1, pp. 143-149, 1997/09/30/, 1997.
- [54] Y.-L. Chin, J.-C. Chou, T.-P. Sun, H.-K. Liao, W.-Y. Chung, and S.-K. Hsiung, "A novel SnO₂/Al discrete gate ISFET pH sensor with CMOS standard process," *Sensors and Actuators B: Chemical*, vol. 75, no. 1, pp. 36-42, 2001/04/30/, 2001.
- [55] G. Steinhoff, M. Hermann, W. J. Schaff, L. F. Eastman, M. Stutzmann, and M. Eickhoff, "pH response of GaN surfaces and its application for pH-sensitive field-effect transistors," *Applied Physics Letters*, vol. 83, no. 1, pp. 177-179, 2003.
- [56] H. Abe, M. Esashi, and T. Matsuo, "ISFET's using inorganic gate thin films," *Electron Devices, IEEE Transactions on*, vol. 26, no. 12, pp. 1939-1944, 1979.
- [57] C. F. Chan, and M. H. White, "Characterization of surface and buried channel ion sensitive field effect transistors (ISFET's)." pp. 651-653.
- [58] L. Bousse, N. F. de Rooij, and P. Bergveld, "Operation of chemically sensitive field-effect sensors as a function of the insulator-electrolyte interface," *Electron Devices, IEEE Transactions on*, vol. 30, no. 10, pp. 1263-1270, 1983.
- [59] J.-C. Chou, and C.-Y. Weng, "Sensitivity and hysteresis effect in Al₂O₃ gate pH-ISFET," *Materials Chemistry and Physics*, vol. 71, no. 2, pp. 120-124, 2001/08/15/, 2001.
- [60] H. S. Wong, and M. H. White, "A CMOS-integrated 'ISFET-operational amplifier' chemical sensor employing differential sensing," *Electron Devices, IEEE Transactions on*, vol. 36, no. 3, pp. 479-487, 1989.
- [61] P. Gimmel, B. Gompf, D. Schmeisser, H. D. Wiemhöfer, W. Göpel, and M. Klein, "Ta₂O₅-gates of pH-sensitive devices: Comparative spectroscopic and electrical studies," *Sensors and Actuators*, vol. 17, no. 1, pp. 195-202, 1989/05/03/, 1989.
- [62] D. Wilhelm, H. Voigt, W. Treichel, R. Ferretti, and S. Prasad, "pH sensor based on differential measurements on one pH-FET chip," *Sensors and Actuators B: Chemical*, vol. 4, no. 1, pp. 145-149, 1991/05/01/, 1991.
- [63] M. Chen, Y. Jin, X. Qu, Q. Jin, and J. Zhao, "Electrochemical impedance spectroscopy study of Ta₂O₅ based EIOS pH sensors in acid environment," *Sensors and Actuators B: Chemical*, vol. 192, pp. 399-405, 2014/03/01/, 2014.
- [64] Y. Vlasov, A. Bratov, M. Sidorova, and Y. Tarantov, "Investigation of pH-sensitive ISFETs with oxide and nitride membranes using colloid chemistry methods," *Sensors and Actuators B: Chemical*, vol. 1, no. 1, pp. 357-360, 1990/01/01/, 1990.
- [65] T. Akiyama, Y. Ujihira, Y. Okabe, T. Sugano, and E. Niki, "Ion-sensitive field-effect transistors with inorganic gate oxide for pH sensing," *Electron Devices, IEEE Transactions on*, vol. 29, no. 12, pp. 1936-1941, 1982.
- [66] R. H. Zhang, X. T. Zhang, and S. M. Hu, "Zr/ZrO₂ Sensors for in Situ Measurement of pH in High-Temperature and -Pressure Aqueous Solutions," *Analytical Chemistry*, vol. 80, no. 8, pp. 2982-2987, 2008/04/15, 2008.
- [67] J. Augustynski, M. Koudelka, J. Sanchez, and B. E. Conway, "ESCA study of the state of iridium and oxygen in electrochemically and thermally formed iridium oxide films," *Journal of Electroanalytical Chemistry and Interfacial Electrochemistry*, vol. 160, no. 1, pp. 233-248, 1984/01/10/, 1984.
- [68] K. Kinoshita, "Electrochemical Measurements on Pt, Ir, and Ti Oxides as pH Probes," *Journal of The Electrochemical Society*, vol. 131, no. 5, pp. 1089, 1984.

- [69] J.-W. Kang, and W.-J. Cho, "Improved pH Sensitivity and Reliability for Extended Gate Field-Effect Transistor Sensors Using High-k Sensing Membranes," *Journal of Nanoscience and Nanotechnology*, vol. 19, no. 3, pp. 1425-1431, //, 2019.
- [70] M. Miyake, L. D. Chen, G. Pozzi, and P. Bühlmann, "Ion-selective electrodes with unusual response functions: simultaneous formation of ionophore-primary ion complexes with different stoichiometries," *Analytical chemistry*, vol. 84, no. 2, pp. 1104-1111, 2012.
- [71] J. Varcoe, P. Atanassov, D. Dekel, A. Herring, M. Hickner, P. Kohl, A. Kucernak, W. Mustain, K. Nijmeijer, K. Scott, T. Xu, and L. Zhuang, "Anion-exchange membranes in electrochemical energy systems," *Energy Environ. Sci.*, vol. 7, pp. 3135, 08/05, 2014.
- [72] S. Balslev, A. M. Jorgensen, B. Bilenberg, K. B. Mogensen, D. Snakenborg, O. Geschke, J. P. Kutter, and A. Kristensen, "Lab-on-a-chip with integrated optical transducers," *Lab on a Chip*, vol. 6, no. 2, pp. 213-217, 2006.
- [73] J. Melin, N. Roxhed, G. Gimenez, P. Griss, W. van der Wijngaart, and G. Stemme, "A liquid-triggered liquid microvalve for on-chip flow control," *Sensors and Actuators B: Chemical*, vol. 100, no. 3, pp. 463-468, 2004/05/15/, 2004.
- [74] H. J. Yoon, J. H. Shin, S. D. Lee, H. Nam, G. S. Cha, T. D. Strong, and R. B. Brown, "Solid-state ion sensors with a liquid junction-free polymer membrane-based reference electrode for blood analysis," *Sensors and Actuators B: Chemical*, vol. 64, no. 1, pp. 8-14, 2000/06/10/, 2000.
- [75] H. Suzuki, T. Hirakawa, S. Sasaki, and I. Karube, "An integrated three-electrode system with a micromachined liquid-junction Ag/AgCl reference electrode," *Analytica Chimica Acta*, vol. 387, no. 1, pp. 103-112, 1999/04/16/, 1999.
- [76] W. Vonau, and U. Guth, "pH Monitoring: A review," *Journal of Solid State Electrochemistry*, vol. 10, pp. 746-752, 01/09, 2006.
- [77] P. Novo, F. Volpetti, V. Chu, and J. P. Conde, "Control of sequential fluid delivery in a fully autonomous capillary microfluidic device," *Lab on a Chip*, vol. 13, no. 4, pp. 641-645, 2013.
- [78] A. Olanrewaju, M. Beaugrand, M. Yafia, and D. Juncker, "Capillary microfluidics in microchannels: from microfluidic networks to capillare circuits," *Lab on a Chip*, vol. 18, no. 16, pp. 2323-2347, 2018.
- [79] M. Sophocleous, and J. K. Atkinson, "A review of screen-printed silver/silver chloride (Ag/AgCl) reference electrodes potentially suitable for environmental potentiometric sensors," *Sensors and Actuators A: Physical*, vol. 267, pp. 106-120, 2017/11/01/, 2017.
- [80] T. Y. Kim, S. A. Hong, and S. Yang, "A Solid-State Thin-Film Ag/AgCl Reference Electrode Coated with Graphene Oxide and Its Use in a pH Sensor," *Sensors*, vol. 15, no. 3, pp. 6469, 2015.
- [81] "Silicon crystallographic structure," 2014-09-22; http://bazzim.mit.edu/oeit/OcwWeb/Materials-Science-and-Engineering/3-22Spring-2008/Projects/detail/iii_v_2.htm.
- [82] B. Ziaie, A. Baldi, and M. Z. Atashbar, "Introduction to Micro-/Nanofabrication," *Springer Handbook of Nanotechnology*, B. Bhushan, ed., pp. 231-269, Berlin, Heidelberg: Springer Berlin Heidelberg, 2010.
- [83] S. J. Pearton, and D. P. Norton, "Dry Etching of Electronic Oxides, Polymers, and Semiconductors," *Plasma Processes and Polymers*, vol. 2, no. 1, pp. 16-37, 2005.
- [84] H. Jansen, H. Gardeniers, M. d. Boer, M. Elwenspoek, and J. Fluitman, "A survey on the reactive ion etching of silicon in microtechnology," *Journal of Micromechanics and Microengineering*, vol. 6, no. 1, pp. 14-28, 1996/03/01, 1996.
- [85] Y. Q. Fu, A. Colli, A. Fasoli, J. K. Luo, A. J. Flewitt, A. C. Ferrari, and W. I. Milne, "Deep reactive ion etching as a tool for nanostructure fabrication," *Journal of Vacuum Science & Technology*

- B: Microelectronics and Nanometer Structures Processing, Measurement, and Phenomena*, vol. 27, no. 3, pp. 1520-1526, 2009.
- [86] H. Seidel, L. Csepregi, A. Heuberger, and H. Baumgärtel, "Anisotropic Etching of Crystalline Silicon in Alkaline Solutions: I. Orientation Dependence and Behavior of Passivation Layers," *Journal of The Electrochemical Society*, vol. 137, no. 11, pp. 3612-3626, November 1, 1990, 1990.
- [87] E. D. Palik, H. F. Gray, and P. B. Klein, "A Raman Study of Etching Silicon in Aqueous KOH" *Journal of The Electrochemical Society*, vol. 130, no. 4, pp. 956-959, April 1, 1983, 1983.
- [88] I. Zubel, and M. Kramkowska, "Etch rates and morphology of silicon (h k l) surfaces etched in KOH and KOH saturated with isopropanol solutions," *Sensors and Actuators A: Physical*, vol. 115, no. 2, pp. 549-556, 2004/09/21/, 2004.
- [89] R. Drago, D. Vrtacnik, U. Aljancic, and S. Amon, "Effective roughness reduction of {100} and {311} planes in anisotropic etching of {100} silicon in 5% TMAH," *Journal of Micromechanics and Microengineering*, vol. 13, no. 1, pp. 26, 2003.
- [90] C. f. D. C. a. Prevention. "HYDROGEN FLUORIDE/ HYDROFLUORIC ACID : Systemic Agent," 2020/08/25; https://www.cdc.gov/niosh/ershdb/emergencyresponsecard_29750030.html.
- [91] I. Zubel, and M. Kramkowska, "The effect of isopropyl alcohol on etching rate and roughness of (1 0 0) Si surface etched in KOH and TMAH solutions," *Sensors and Actuators A: Physical*, vol. 93, no. 2, pp. 138-147, 2001/09/30/, 2001.
- [92] S.-H. Park, J. Park, K.-H. You, H.-C. Shin, and H.-O. Kim, "Tetramethylammonium Hydroxide Poisoning during a Pallet Cleaning Demonstration," *Journal of Occupational Health*, vol. 55, no. 2, pp. 120-124, 2012.
- [93] T. Monteiro, P. Kastytis, L. Gonçalves, G. Minas, and S. Cardoso, "Dynamic Wet Etching of Silicon through Isopropanol Alcohol Evaporation," *Micromachines*, vol. 6, no. 10, pp. 1437, 2015.
- [94] K. P. Rola, and I. Zubel, "Impact of alcohol additives concentration on etch rate and surface morphology of (100) and (110) Si substrates etched in KOH solutions," *Microsystem Technologies*, vol. 19, no. 4, pp. 635-643, April 01, 2013.
- [95] C.-R. Yang, P.-Y. Chen, Y.-C. Chiou, and R.-T. Lee, "Effects of mechanical agitation and surfactant additive on silicon anisotropic etching in alkaline KOH solution," *Sensors and Actuators A: Physical*, vol. 119, no. 1, pp. 263-270, 2005/03/28/, 2005.
- [96] J. P. G. Farr, "Electroplating, electrode kinetics and electrocrystallisation," *Transactions of the IMF*, vol. 88, no. 5, pp. 262-265, 2010/09/01, 2010.
- [97] M. Schlesinger, *Modern Electroplating*, 5th ed., p. 131, Hoboken, USA: John Wiley & Sons, 2011.
- [98] Q. Xu, I. Tonks, M. J. Fuerstman, J. C. Love, and G. M. Whitesides, "Fabrication of Free-Standing Metallic Pyramidal Shells," *Nano Letters*, vol. 4, no. 12, pp. 2509-2511, 2004/12/01, 2004.
- [99] B. Wang, H. Wang, P. Cheng, Z. Yang, and G. Ding, "Optimizing the electroplating condition of an acid low cyanide silver bath and its application in micromachining." pp. 1-2.
- [100] Y. Zhou, and Y. Huo, "The comparison of electrochemical migration mechanism between electroless silver plating and silver electroplating," *Journal of Materials Science: Materials in Electronics*, vol. 27, no. 1, pp. 931-941, January 01, 2016.
- [101] P. Leisner, C. Zanella, I. Belov, C. Edström, G. Sandulache, and W. E. G. Hansal, "Control of silver throwing power by pulse reverse electroplating," *Transactions of the IMF*, vol. 95, no. 1, pp. 25-30, 2017/01/02, 2017.

- [102] A. Nevers, L. Hallez, F. Touyeras, and J.-Y. Hihn, "Effect of ultrasound on silver electrodeposition: Crystalline structure modification," *Ultrasonics Sonochemistry*, vol. 40, pp. 60-71, 2018/01/01/, 2018.
- [103] B. Zheng, L. P. Wong, L. Y. L. Wu, and Z. Chen, "Cyclic Voltammetric Study of High Speed Silver Electrodeposition and Dissolution in Low Cyanide Solutions," *International Journal of Electrochemistry*, vol. 2016, pp. 11, 2016.
- [104] V. S. Kublanovsky, and O. L. Bersirova, "Electrochemical behavior of silver in dicyanoargentate electrolytes." pp. 01PCSI21-1-01PCSI21-6.
- [105] F. Ulu, G. Demirci, M. Erdogan, and I. Karakaya, "The Role of Electrolyte Composition on Codeposited Ag and Cu," *ECS Transactions*, vol. 72, no. 21, pp. 35-44, July 28, 2016, 2016.
- [106] A. Blair, "Silver plating," *Metal Finishing*, vol. 93, no. 1, Supplement 1, pp. 290-297, 1995/01/01/, 1995.
- [107] J. Christophe, G. Guilbert, Q. Rayée, M. Poelman, M.-G. Olivier, and C. Buess-Herman, "Cyanide-Free Silver Electrochemical Deposition on Copper and Nickel," *Journal of The Electrochemical Society*, vol. 165, no. 14, pp. D676-D680, January 1, 2018, 2018.
- [108] D. G. Foster, Y. Shapir, and J. Jorné, "Scaling of Roughness in Silver Electrodeposition," *Journal of The Electrochemical Society*, vol. 150, no. 6, pp. C375-C380, June 1, 2003, 2003.
- [109] F.-z. Ren, L.-t. Yin, S.-s. Wang, A. A. Volinsky, and B.-h. Tian, "Cyanide-free silver electroplating process in thiosulfate bath and microstructure analysis of Ag coatings," *Transactions of Nonferrous Metals Society of China*, vol. 23, no. 12, pp. 3822-3828, 2013/12/01/, 2013.
- [110] A. Liu, X. Ren, J. Zhang, D. Li, and M. An, "Complexing agent study for environmentally friendly silver electrodeposition(ii): electrochemical behavior of silver complex," *RSC Advances*, vol. 6, no. 9, pp. 7348-7355, 2016.
- [111] A. Liu, X. Ren, J. Zhang, G. Yuan, P. Yang, J. Zhang, and M. An, "A composite additive used for an excellent new cyanide-free silver plating bath," *New Journal of Chemistry*, vol. 39, no. 4, pp. 2409-2412, 2015.
- [112] G. M. Zarkadas, A. Stergiou, and G. Papanastasiou, "Influence of citric acid on the silver electrodeposition from aqueous AgNO₃ solutions," *Electrochimica Acta*, vol. 50, no. 25, pp. 5022-5031, 2005/09/05/, 2005.
- [113] G. M. Zarkadas, A. Stergiou, and G. Papanastasiou, "Influence of tartaric acid on the electrodeposition of silver from binary water + dioxane AgNO₃ solutions," *Journal of Applied Electrochemistry*, vol. 31, no. 11, pp. 1251-1259, November 01, 2001.
- [114] B. Bao, B. Ji, M. Wang, K. Gao, B. Yang, X. Chen, X. Wang, and J. Liu, "Development and characterisation of electroplating silver/silver chloride modified microelectrode arrays," *Micro & Nano Letters*, vol. 14, no. 3, pp. 299-303, 2019.
- [115] S. Södergren, "Electrochemical microsensor with in-situ fabricated Ag/AgCl reference electrode for high-pressure microfluidics," Student thesis, UPTec Q, 2017.
- [116] Y. H. Ogata, K. Kobayashi, and M. Motoyama, "Electrochemical metal deposition on silicon," *Current Opinion in Solid State and Materials Science*, vol. 10, no. 3, pp. 163-172, 2006/06/01/, 2006.
- [117] D. Sander, R. Hoffmann, V. Reiling, and J. Muller, "Fabrication of metallic microstructures by electroplating using deep-etched silicon molds," *Journal of Microelectromechanical Systems*, vol. 4, no. 2, pp. 81-86, 1995.
- [118] I. F. Cheng, "Electrochemical Phase Formation and Growth: An Introduction to the Initial Stages of Metal Deposition By E. Budevski (Bulgarian Academy of Sciences) and G. Staikov and W. J. Lorenz (University of Karlsruhe). VCH: Weinheim. 1996. xi + 410 pp. DM188.00. ISBN 3-527-29422-8," *Journal of the American Chemical Society*, vol. 119, no. 22, pp. 5276-5276, 1997/06/01, 1997.

- [119] R. K. Waser, H.; Erb, U. , *Nanoelectronics and Information Technology: Advanced Electronic Materials and Novel Devices*, p.^pp. 1002, NJ, USA: John Wiley & Sons, Inc.: Hoboken, 2003.
- [120] M. Garcés-Schröder, M. Leester-Schädel, M. Schulz, M. Böhl, and A. Dietzel, "Micro-Gripper: A new concept for a monolithic single-cell manipulation device," *Sensors and Actuators A: Physical*, vol. 236, pp. 130-139, 2015/12/01/, 2015.
- [121] S. P. Davis, B. J. Landis, Z. H. Adams, M. G. Allen, and M. R. Prausnitz, "Insertion of microneedles into skin: measurement and prediction of insertion force and needle fracture force," *Journal of Biomechanics*, vol. 37, no. 8, pp. 1155-1163, 2004.
- [122] A. Misra, M. F. Hundley, D. Hristova, H. Kung, T. E. Mitchell, M. Nastasi, and J. D. Embury, "Electrical resistivity of sputtered Cu/Cr multilayered thin films," *Journal of Applied Physics*, vol. 85, no. 1, pp. 302-309, 1999.

ANNEXES

List of Annexes:

Annex 1 - Process Runsheet for the study and optimization of the Silicon Wet Etching process

Annex 2 - Cell proliferation protocol

Annex 3 - Homogeneous Membrane Integrity Assay Protocol

Annex 4 - MTS Cell Proliferation Assay Protocol

Annex 5 - Process Runsheet for the fabrication of Silver Microneedles

Annex 6 - Process Diagram for the fabrication of Silver Microneedles

Annex 7 - Process Runsheet for the preparation of Silver Electroplating Solutions

Annex 1 - Process Runsheet for the study and optimization of the Silicon Wet Etching process

#	TECHNIQUE	D	E	P	EQUIPMENT	MATERIAL	THICK
01	<u>Wafer dicing</u> Into ¼ of a 6" Silicon wafer			X	—	—	—
02	<u>Substrate cleaning</u> Remove any debris from the surface			X	Wet Bench	µ-Strip	—
03	<u>PVD – Magnetron Sputtering</u> Mask layer for Silicon wet etching process	X			Alcatel SCM 450	Chromium	3000 Å
04	<u>DWL – Lithography</u> Definition of Chromium pattern			X	DWL	PFR 7790 G +PR	1.4 µm
05	<u>Wafer dicing</u> Dicing saw that cuts individual dies for process			X	Disco DAD 231	—	—
06	<u>Chromium Wet etching</u> Patterning of Chromium layer		X		Wet bench	Cr etchant	3000 Å
07	<u>Photoresist Stripping</u> Remove all the Photoresist from the die		X		Wet bench	Acetone	1.4 µm
08	<u>Silicon Wet etching</u> Patterning of protuberant pyramids		X		Wet bench	KOH solution	T.B.D.

RUN SHEET – MICRONEEDLES SENSOR

RESPONSIBLE: TIAGO ALEXANDRE DA SILVA MONTEIRO

Sample ID: _____

STEP 1: Substrate preparation: Silicon 2" Wafer

Date: ___/___/___

Operator: _____

Machine: Wet Bench (Ultrasounds)

Conditions: Clean for 10 minutes in IPA solution with ultrasounds;
Clean with DI water and blow dry with compressed air gun.

Observations: _____

STEP 2: Metal deposition: Chromium 3000 Å

Date: ___/___/___

Operator: _____

Machine: Alcatel

Pre-Treatment: _____

Magnetron Sputtering: Yes

Material deposited: Chromium 3000 Å

Substrate: Silicon 2 inch Wafer

Conditions:

Chamber pressure before deposition: _____ Torr

Chamber pressure during deposition: _____ Torr

Substrate rotation: _____ rpm

Deposition Rate: _____ Å/s

Current: _____ mA

Voltage: _____ mV

Time: _____ sec

NOTE: Calibration sample required!

NOTE: Microscopic inspection required!

NOTE: Electrical measurements required!

$$\sigma = \ln 2VI$$

Measurements:

Current: _____ mA

Voltage: _____ mV

Resistance: _____ Ω

Film thickness: _____ Å

Observations: _____

STEP 3: Lithography patterning

Date: ___/___/___

Operator: _____

Machine: DWL

Photoresist coating conditions:

Pre-treatment/adhesion layer: HDMS for 5 min @ 130 °C (program 0)

Wafer dehydration:

Vacuum: 10 Torr for 2 min

N2 inlet: 760 Torr for 3 min

Heating to 130 °C

Priming:

Vacuum: 1 Torr for 3 min

HDMS: 6 Torr for 5min

Purge prime exhaust:

Vacuum: 4 Torr for 1 min

N2 inlet: 500 Torr for 2 min

Vacuum: 4 Torr for 2 min

Return to atmosphere:

N2 inlet: 3 min

Photoresist: PFR 7790 G Recipe: 6/2 Thickness: 1.3 µm

Step #1: time 5 s at speed 800 rpm with acceleration 50 rpm/s

Step #2: time 40 s at speed 2800 rpm with acceleration 50 rpm/s

Bake temperature: 85 °C for 60 sec

Other conditions: _____

Observations: _____

Exposing Conditions:

Map: 3x3 with 400 µm spacing in all 4 directions

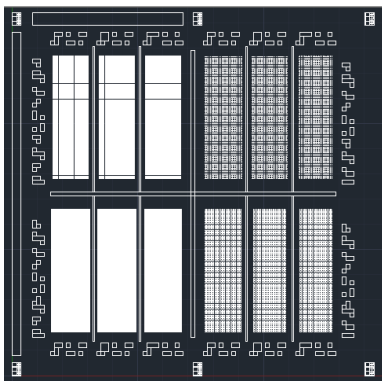
Map name: arraytm0

Die dimensions: [X: 9000.000 Y: 9000.000] µm

Alignment marks: [X=168, Y=163.7; X=4668, Y=163.7; X=8946, Y=163.7]

[X=168, Y=8839.7; X=4668, Y=8839.7; X=8946, Y=8839.7]

Mask name: ArrayTM04P.dxf **Layer:** SV **Alignment:** middle cross



DWL Energy: 100

DWL Focus: 60

Developer: TMA 238 WA

Development: Recipe: 6/2

Baking: 110 °C for 60 sec

Cooling: 30 sec

Development: 60 sec

Rinse: 15 sec

Spin: 30 sec

NOTE: Microscopic inspection required!

Observations: _____

STEP 4: Wafer Dicing

Date: ___/___/___

Operator: _____

Machine: Disco DAD 321

Pre-Treatment: _____

Conditions: Recipe # _____
Cut mode: A (semi-automatic)
Blade rotation = 30'000 rpm
Work thickness = 0,500 mm
Tape thickness = 0,150 mm
Blade height = 0,050 mm
Kerf width = 0,150 mm
Speed = 5 mm/s

Round:
Worksize = 70 mm

Index
CH1 = 9.4 mm
CH2 = 9.4 mm

NOTE: Microscopic inspection required! Some Silicon particles may adhere to the surface of the samples. If required, clean with DI water and apply blow dry. Do not use Acetone or IPA, since it may damage either the PR or Cr. Residues may be removed during the PR stripping and Chromium etching.

Observations: _____

STEP 5: Chromium Etching

Date: ___/___/___

Operator: _____

Machine: Wet Bench

Pre-Treatment: Blow dry

Conditions: Sigma Chromium Etchant @ RT

Etching rate: 15 Å.s⁻¹

Required Time: 240 sec

NOTE: Rinse samples thoroughly with DI Water twice after use

Observations: _____

STEP 6: Resist Stripping

Date: ___/___/___

Operator: _____

Machine: Wet Bench

Pre-Treatment: Blow dry

Conditions: Acetone @ RT

NOTE: PR is removed in contact with KOH solution. Resist stripping is optional.

NOTE: Microscopic inspection required!

NOTE: Profilometric measurements required!

Observations: _____

STEP 7: Wet Etching KOH

Date: ___/___/___

Operator: _____

Machine: Wet bench

Pre-Treatment: Blow dry

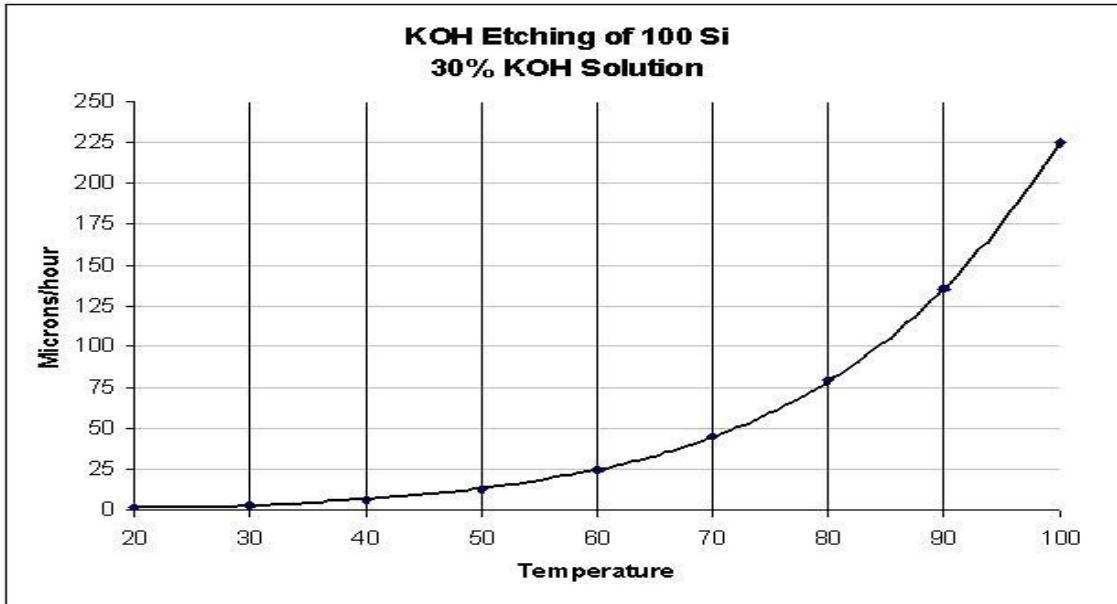
Conditions: Follow KOH Wet Etching Protocol

KOH Solution: 30%

Temperature: ___°C

Etch Rate: ___Å.s⁻¹

Exposition time: ___min



Observations: _____

Annex 2 - Cell proliferation protocol

Laboratório de Cultura de Células e Tecidos/ PROTOCOLO GERAL

ÍNDICE

PTO 001 Reabilitação de cultura de células animais.....	02
PTO 002 Contagem de células em câmara de Neubauer	04
PTO 003 Transferência de cultura de células animais	06
PTO 004 Criopreservação de cultura de células animais	09
PTO 005 Cultura das células em placa de 24 poços para a adesão de <i>Candida</i> sp.	12
PTO 006 Adesão de <i>Candida</i> sp. em células cultivadas em placa de 24 poços	15

CEB/LOCT/PTO GERAL

Executado por:
Melyssa Negri

Revisado por:
Mariana Henriques

Executado em:
Abril/2008

1/1

Laboratório de Cultura de Células e Tecidos/ PROTOCOLO GERAL

PTO 001 Reabilitação de cultura de células animais

0.1| MATERIAL E REAGENTE

Pipeta (10ml e 5ml)
 Falcon de 15 ml
 Frasco de cultura de 25 cm²
 Centrífuga
 D-MEM high glucose (D-MEM)
 Fetal Bovine Serum (FBS)
 Antibiótico

1| PREPARAÇÃO DO MEIO DE CULTURA

1. D-MEM completo para reabilitação de cultura de células animais

	Concentração (%)	Volume total (10ml)	Volume total (20ml)	Volume total (30ml)	Volume total (40ml)	Volume total (50ml)
D-MEM	84	8.4	16.8	25.2	33.6	42
FBS	15	1.5	3	4.5	6	7.5
Antibiótico	1	0.1	0.2	0.3	0.4	0.5

Preparar o meio em um Falcon estéril.

Armazenar a 4°C.

2| PROCEDIMENTO

1. Preparar o meio de cultura;
2. Retirar o criovial do azoto líquido e colocar num banho a 37°C;
3. Retirar todo o meio de dentro do criovial e colocar num falcon de 15 ml;
4. Adicionar 9 ml de meio;
5. Centrifugar 7 min a 1000 rpm e 4°C;
6. Descartar o sobrenadante por decantação;
7. Ressuspender as células em 3 ml de meio fresco;
8. Colocar 2 ml de meio num frasco de cultura de 25 cm²;
9. Colocar as células ressuspendidas neste frasco;
10. Colocar o frasco na estufa a 37°C e 5% de CO₂.

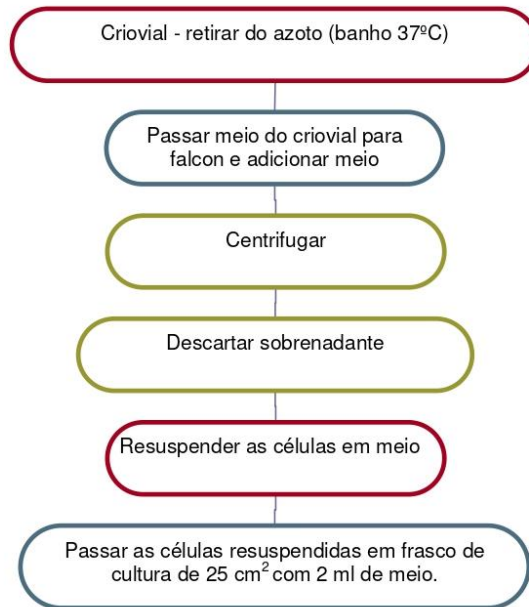
Observações

A descongelação das células deve ser um processo rápido de modo a minimizar a lesão das mesmas.

Dado que o meio de congelação contém DMSO (tóxico para as células).

Laboratório de Cultura de Células e Tecidos/ PROTOCOLO GERAL

2.1| DIAGRAMA ESQUEMÁTICO DO PROCEDIMENTO



Laboratório de Cultura de Células e Tecidos/ PROTOCOLO GERAL

PTO 002 Contagem de células em câmara de Neubauer

0.1| MATERIAL E REAGENTE

Câmara de Neubauer
Lamela
Eppendorfs
Pipetas
Pontas amarelas
Corante Azul de Tripán

1| PROCEDIMENTO

- Observações*
11. Colocar a lamela sobre a área de marcada na câmara de contagem. Usar lamelas especiais que fornecem a profundidade correcta da câmara de contagem.
12. Homogeneizar bem a suspensão celular e transferir com esterilidade 100µl para um Eppendorf e adicionar a mesma proporção de azul de tripán ao eppendorf diluição 1/2.
13. Misturar o conteúdo e retirar uma alíquota de 10µl com a pipeta.
14. Encostar a ponta da pipeta na borda da lamela, preencher cuidadosamente a câmara de contagem. O líquido deve preencher apenas um lado da câmara e não deve chegar aos canais de cada lado da área de contagem (Fig. 1). Deixar as células sedimentarem por 2 min.
15. Focalizar a área demarcada da câmara de contagem com a objectiva de menor ampliação (Fig.2). Nas áreas 1, 2, 3 e 4,
16. Critérios para a contagem (Fig. 3):
enumerar células com núcleo bem visível;
(a) contar células isoladas como 1 célula;
(b) contar grumos constituídos por células facilmente distinguíveis por seus núcleos e citoplasmas como grupos de células isoladas e contar cada célula;
(c) grumos, cujas células são difíceis de serem distinguidas umas das outras, devem ser contados como um único grupo.
17. Contar as células nas 4 áreas de um lado da câmara de contagem, seguindo o esquema da Fig.2, dividir o valor por 4 para obter a média e multiplicada pelo fator de diluição, no caso 2.
18. Para obter o número de células/ml, multiplicar corrigir o valor obtido por 10.000, pois:
1 ml = 1 cc
1 cc = 10 x 10 x 10 mm = 1.000 mm³
Na câmara de Neubauer obtemos o número de celular por 0,1 mm³, então devemos multiplicar por 10, portanto 10 x 1.000 = 10.000 o volume com a lamela colocada corresponde a 0,1 mm³
19. n° de células/ml = $\frac{n^{\circ} \text{ total de células} \times \text{fator de diluição} \times 10.000}{n^{\circ} \text{ de quadrantes contados}}$

CEB/LCCT/PTO GERAL

Executado por:
Melyssa Negri

Revisado por:
Mariana Henriques

Executado em:
Abril/2008

4/1

Laboratório de Cultura de Células e Tecidos/ PROTOCOLO GERAL

PTO 003 Transferência de cultura de células animais

0.1| MATERIAL E REAGENTE

Pipeta (10ml e 5ml)
 Falcon de 50 ml
 Frasco de cultura de 75 cm²
 Eppendorfs
 Pontas amarelas
 D-MEM completo
 Câmara de Neubauer
 Lamela
 Corante Azul de Tripán

1| PREPARAÇÃO DO MEIO DE CULTURA

2. D-MEM completo

Volume (mL)	D-MEM 84% (ml)	FBS 15% (ml)	Antibiótico 1% (µl)
10	8.4	1.5	100
20	16.8	3	200
30	25.2	4.5	300
40	33.6	6	400
50	42	7.5	500

Preparar o meio em um Falcon estéril.
 Armazenar a 4°C.

2| PREPARAÇÃO DO REAGENTE

3. Stock 0,1M Phosphate-Buffered Saline (PBS) pH 7,5 - 10x concentrado

Volume final (mL)	NaCl	KCl	K ₂ HPO ₄	NaHPO ₄ 12H ₂ O	Água ultrapura (mL)
100	8	0,2	0,2	2,85	100
500	40	1	1	14,25	500
1000	80	2	2	28,5	1000

Observação:

a. O reagente NaHPO₄ 12H₂O pode ser substituído por qualquer um destes dois reagentes a baixo:

Volume final (mL)	Na ₂ HPO ₄ 7H ₂ O (g)	Na ₂ HPO ₄ (g)	Água ultrapura (mL)
100	2,1	1,15	100
500	10,5	5,75	500
1000	21	11,5	1000

Adicionar 90% do volume de água e homogeneizar. Ajustar pH a 7,5 com HCl 37%.
 Acertar o volume. Esterilizar por filtração ou autoclavar (121 °C, 20).
 Armazenar a -20 °C em alíquotas de 10mL.
 Quando descongelar diluir 1/10 em água ultrapura estéril.

Laboratório de Cultura de Células e Tecidos/ PROTOCOLO GERAL

3| PROCEDIMENTO

- 20. Colocar a 37°C o meio de cultura completo, a tripsina e o PBS;
- 21. Observar 80% da confluência das células no microscópio invertido;
- 22. Retirar com auxílio da pipeta os 10 ml do meio do frasco de cultura de 75 cm²;
Para frasco de 25 cm² retira-se 5 ml de meio;
- 23. Colocar 2 ml de PBS no frasco de 75 cm², agitar suavemente e descartar;
Colocar 1 ml de PBS no frasco de 25 cm²
- 24. Colocar 2 ml de tripsina no frasco de 75 cm² colocá-lo na estufa a 37°C (máximo de 15 min);
Colocar 1 ml de tripsina no frasco de e 25 cm²
- 25. Verificar se as células estão destacadas do fundo do frasco, no microscópio invertido;
- 26. Colocar 4 ml de meio completo no frasco 75 cm² (4 ml de meio + 2 ml tripsina = 6ml);
Colocar 3 ml de meio completo no frasco 25 cm² (3 ml de meio + 1 ml tripsina = 4ml);
- 27. Contar o número de células viáveis em câmara de Neubauer (PTO 002)
- 28. Calcular o número de células presentes no frasco;
- 29. Calcular o volume de células a colocar em cada novo frasco para uma concentração final de 1 x 10⁵ cel/80 cm² e um volume total de 10 ml;
- 30. Completar o volume de cada frasco com meio de cultura;
- 31. Colocar o frasco na estufa a 37°C e 5% CO₂.

Observações

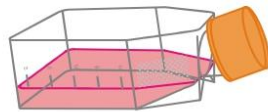
Lembre-se que tem que diluir o PBS

O soro inibe o efeito da tripsina. Esta fase (4) visa desactivar todo o soro.

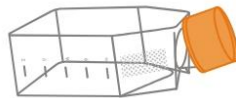
Laboratório de Cultura de Células e Tecidos/ PROTOCOLO GERAL

3.1| ESQUEMA DO PROCEDIMENTO

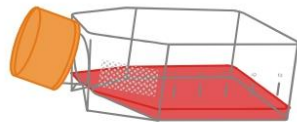
01 Frasco (75cm²) com 80% de confluência (10ml de meio).



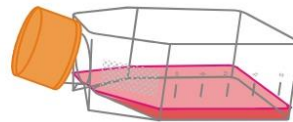
02 Retirar com pipeta todo o meio e colocar 2ml de PBS no frasco, agitar suavemente e descartar.



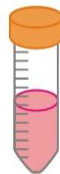
03 Colocar 2ml de tripsina e por na estufa a 37°C durante um máximo de 15 minutos.



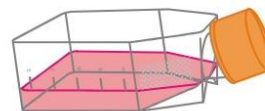
04 Verificar se as células estão destacadas do fundo do frasco e colocar 4ml de meio completo no frasco.



05 Transferir para um tubo 6ml da cultura, contar o número de células viáveis. Calcular o volume de 1×10^6 cel/80cm² em um volume total de 10ml.



06 Completar o volume de cada frasco com meio e colocar na estufa a 37°C e 5% CO₂.



Laboratório de Cultura de Células e Tecidos/ PROTOCOLO GERAL

PTO 004 Criopreservação de cultura de células animais**0.1| MATERIAL E REAGENTE**

Pipeta (10ml e 5ml)
 Falcon de 15 ml
 Criotubos
 Pontas amarelas
 Câmara de Neubauer
 Lamela
 Centrífuga
 Corante Azul de Tripán
 D-MEM completo
 Meio para congelação

1| PREPARAÇÃO DO MEIO 4. Meio de congelação

Volume (mL)	D-MEM 70% (ml)	FBS 20% (ml)	DMSO 10% (ml)
10	7	2	1
20	14	4	2
30	21	6	3
40	28	8	4
50	35	10	5

Preparar o meio em um Falcon estéril.

Armazenar a 4°C.

2| PROCEDIMENTO*Observações*

32. Preparar o meio de congelação;
33. Colocar em banho-maria a 37°C o meio de cultura completo, a tripsina e o PBS;
34. Observar 80% da confluência das células no microscópio invertido;
35. Retirar com auxílio da pipeta todo o meio do frasco de cultura de 75 cm²;
36. Colocar 2 mL de PBS no frasco, agitar suavemente e descartar;
37. Colocar 2 mL de tripsina no frasco e colocá-lo na estufa a 37°C (máximo de 15 min);
38. Verificar se as células estão destacadas do fundo do frasco, no microscópio invertido;
39. Colocar 4 mL de meio completo no frasco;
40. Contar o número de células viáveis em câmara de Neubauer (PTO 002)

CEB/LCCT/PTO GERAL

Executado por:
Melyssa NegriRevisado por:
Mariana HenriquesExecutado em:
Abril/2008

9/1

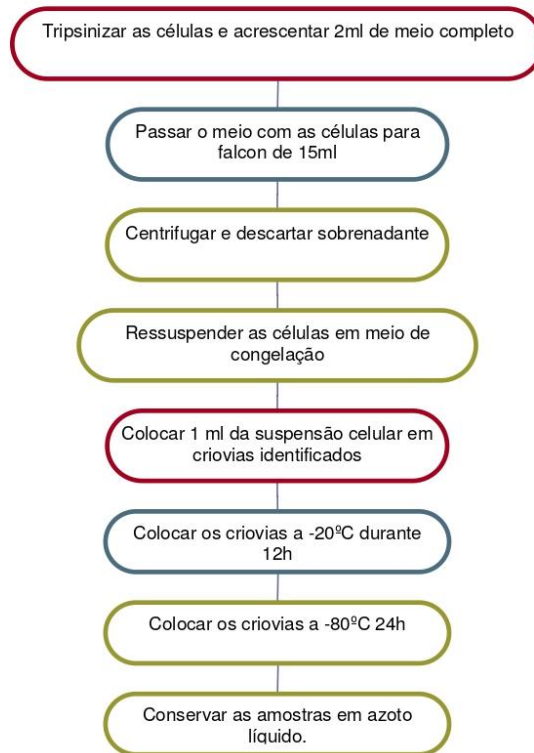
Laboratório de Cultura de Células e Tecidos/ PROTOCOLO GERAL

- 41. Retirar o meio contendo as células do frasco de cultura e colocar num falcon de 15 ml;
- 42. Centrifugar 7 min a 1000 rpm e 4°C;
- 43. Descartar o sobrenadante por decantação;
- 44. Ressuspender as células num volume de **meio de congelação** necessário para fazer uma concentração final de 1×10^6 cel/criovial (ml);
- 45. Colocar 1 ml da suspensão celular em criovias previamente identificados;
- 46. Colocar os criovias a -20°C durante 12h;
- 47. Colocar os criovias a -80°C durante 24h;
- 48. Conservar as amostras em azoto líquido.

O criovial tem que ter as seguintes identifições: nome da linhagem celular; data de congelação; nome do responsável.

Laboratório de Cultura de Células e Tecidos/ PROTOCOLO GERAL

2.1| DIAGRAMA ESQUEMÁTICO DO PROCEDIMENTO



Laboratório de Cultura de Células e Tecidos/ PROTOCOLO GERAL

PTO 005 Cultura das células em placa de 24 poços para a adesão de *Candida* sp.

0.1| MATERIAL E REAGENTE

Pipeta (10ml e 5ml)
 Falcon de 15 ml
 Pontas amarelas e pontas azuis
 Placa de 24 poços
 Câmara de Neubauer
 Lamela
 Corante Azul de Tripán
 D-MEM sem antibiótico
 Tripsina
 PBS

1| PREPARAÇÃO DO MEIO

5. Meio D-MEM sem antibiótico (TCC-SUP)

Volume (mL)	D-MEM 85% (ml)	FBS 15% (ml)
10	8.5	1.5
20	17	3
30	25.5	4.5
40	34	6
50	42.5	7.5

Preparar o meio em um Falcon estéril.
 Armazenar a 4°C.

2| PROCEDIMENTO

Observações

- 49. Preparar o meio sem antibiótico;
- 50. Colocar em banho-maria a 37°C a tripsina e o PBS;
- 51. Observar 80% da confluência das células no microscópio invertido;
- 52. Retirar com auxílio da pipeta todo o meio do frasco de cultura de 75 cm²;
- 53. Colocar 2 mL de PBS no frasco, agitar suavemente e descartar;
- 54. Colocar 2 mL de tripsina no frasco e colocá-lo na estufa a 37°C (máximo de 15 min);
- 55. Verificar se as células estão destacadas do fundo do frasco, no microscópio invertido;
- 56. Colocar 4 mL de meio sem antibiótico no frasco;

CEB/LCCT/PTO GERAL

Executado por:
 Melyssa Negri

Revisado por:
 Mariana Henriques

Executado em:
 Abril/2008

12/1

Laboratório de Cultura de Células e Tecidos/ PROTOCOLO GERAL

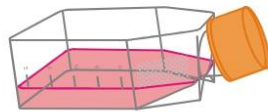
- 57. Passar todo o volume para um falcon de 50ml e contar o número de células viáveis em câmara de Neubauer (PTO 002)
- 58. Calcular o volume de células a colocar em cada poço para uma concentração final de 1×10^6 cel/cm² e um volume total de 500µl;
- 59. Completar o volume de cada poço com meio de cultura;
- 60. Colocar a placa na estufa a 37°C, 5% CO₂ por 24h.

É passado para um falcon para facilitar a pipetagem, a fim de evitar a contaminação

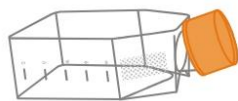
Laboratório de Cultura de Células e Tecidos/ PROTOCOLO GERAL

2.1| ESQUEMA DO PROCEDIMENTO

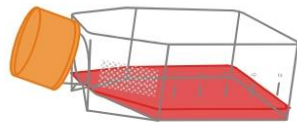
01 Frasco (75cm²) com 80% de confluência (10ml de meio).



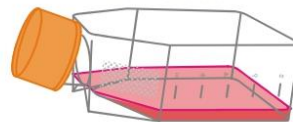
02 Retirar com pipeta todo o meio e colocar 2ml de PBS no frasco, agitar suavemente e descartar.



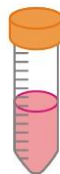
03 Colocar 2ml de tripsina e por na estufa a 37°C durante um máximo de 15 minutos.



04 Verificar se as células estão destacadas do fundo do frasco e colocar 4ml de meio sem antibiótico no frasco.



05 Transferir para um tubo 6ml da cultura, contar o número de células viáveis. Calcular o volume de 1x10⁶ cel/ml em um volume total de 12ml.



06 Transferir para uma placa com 24 poços 500µl em cada poço e colocá-la na estufa a 37°C e 5% CO₂, por 24 horas.



Laboratório de Cultura de Células e Tecidos/ PROTOCOLO GERAL

PTO 006 Adesão de *Candida* sp. em células cultivadas em placa de 24 poços

0.1| MATERIAL E REAGENTE

Pontas amarelas e pontas azuis
 Placa de 24 poços com cultura de células
 PBS estéril
 RPMI-1640 Sigma (R8758)

1| PREPARAÇÃO DOS REAGENTES

6. Violeta cristal 1% (v/v)

Volume (mL)	Violeta cristal (mL)	Água (mL)
100	1	99
500	5	495

7. Etanol Acetona 1:1 (v/v)

Volume (mL)	Etanol 100% (mL)	Acetona 100% (mL)
100	50	50
500	250	250

8. Ácido acético 33% (v/v)

Volume (mL)	Ácido acético glacial (mL)	Água (mL)
100	33	67
500	165	335

Conservar à temperatura ambiente.

2| PREPARAÇÃO DO MEIO

9. Meio RPMI-1640 Sigma (R8758)

Meio pronto

Realizar alíquotas do meio em um Falcon estéril.
 Armazenar a 4°C.

Laboratório de Cultura de Células e Tecidos/ PROTOCOLO GERAL

3| PROCEDIMENTO

- 61. Retirar o meio de cada poço (placa que foi realizada a cultura de células 24h antes);
- 62. Lavar uma vez cuidadosamente todos os poços com PBS;
- 63. Acrescentar 250µl de RPMI em todos os poços;
- 64. Levar a placa para o laboratório de microbiologia;
- 65. Passar 500µl de RPMI nos poços com apenas células (branco) ou leveduras (controle);
- 66. Passar 250µl de leveduras nos poços a fim de obter 1×10^7 de leveduras em 500µl;
- 67. Incubar por 2h, 37°C, 5% CO₂;
- 68. Retirar todo o meio de cada poço;
- 69. Lavar uma vez cuidadosamente todos os poços com PBS para retirar as leveduras não aderidas;
- 70. Fazer a coloração das células, adicionando 500 µL de violeta cristal 1 % a cada poço;
- 71. Deixar actuar durante 5 min a temperatura ambiente;
- 72. Remover a solução de coloração e lavar cada poço uma vez com PBS;
- 73. Para descorar as células e deixar corado apenas as leveduras, lavar uma vez com 500µl da solução de Etanol-acetona 1:1;
- 74. Para resolubilizar o corante ligado às leveduras, adicionar de imediato 500 µL de ácido 33% ;
- 75. Passar de imediato 200µl na placa de 96 poços (em triplicata de cada poço) e ler a densidade óptica a 570 nm.
- 76. O branco de cada ensaio será o poço que contiver apenas células;
- 77. A absorvância da solução de descoloração reflecte a quantidade de leveduras aderidas nas células.

Observações

Observar se as células estão com 90 a 100% de confluência em cada poço

É importante que o PBS e o RPMI estejam a 37°C.

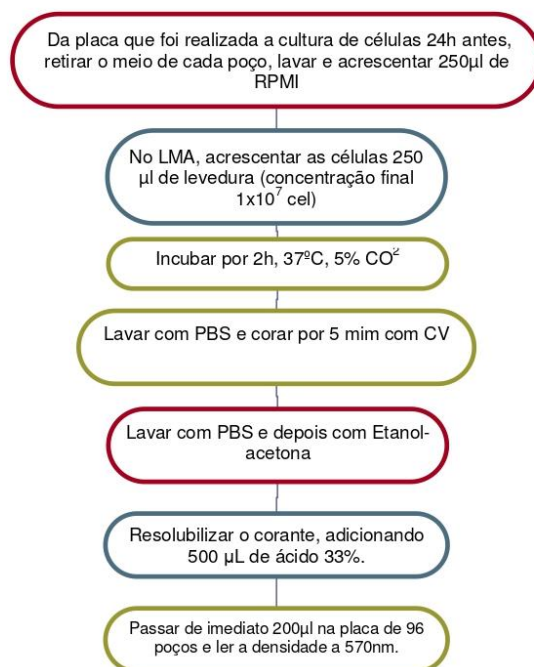
As leveduras terão que estar já diluídas em RPMI

Realizar este procedimento um poço de cada vez.

Lembre-se de subtrair dos resultados obtidos a abs do branco.

Laboratório de Cultura de Células e Tecidos/ PROTOCOLO GERAL

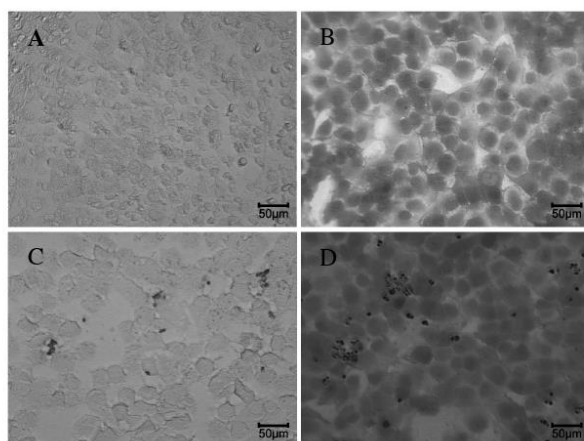
3.1| DIAGRAMA ESQUEMÁTICO DO PROCEDIMENTO



Laboratório de Cultura de Células e Tecidos/ PROTOCOLO GERAL

4| ANEXOS

4.1| MÉTODO CV PARA CONTAGEM DE LEVEDURAS ADERIDAS EM CÉLULAS



- A: Células TCC-SUP coradas com CV e descoradas com Etanol-acetona;
B: Células TCC-SUP coradas com CV;
C: Células TCC-SUP e leveduras coradas com CV e TCC-SUP descoradas com Etanol-acetona;
D: Células TCC-SUP e leveduras coradas com CV.

Annex 3 - Homogeneous Membrane Integrity Assay Protocol



PRINTED IN USA.
Revised 5/09

Technical Bulletin

CytoTox-ONE™ Homogeneous Membrane Integrity Assay

INSTRUCTIONS FOR USE OF PRODUCTS G7890, G7891 AND G7892.

www.promega.com

Part# TB306



CytoTox-ONE™ Homogeneous Membrane Integrity Assay

All technical literature is available on the Internet at www.promega.com/tbs
Please visit the web site to verify that you are using the most current version of this
Technical Bulletin. Please contact Promega Technical Services if you have questions on use
of this system. E-mail techserv@promega.com.

1. Description.....	1
2. Product Components and Storage Conditions	6
3. General Considerations	7
A. Background Fluorescence/Serum LDH.....	7
B. Temperature.....	7
C. Assay Controls.....	7
D. Considerations for the Maximum LDH Release Control.....	7
E. Light Sensitivity of Resazurin	8
F. Use of Stop Solution to Stop Development of Fluorescent Signal.....	8
G. Cell Culture Media Considerations.....	8
H. Use of Resazurin as an Indicator in both Cytotoxicity and Cell Viability Assays	9
I. Performing Other Multiplexed Assays in Combination with the CytoTox-ONE™ Assay	9
4. Protocols	10
A. Reagent Preparation.....	10
B. Recommended Controls.....	10
C. Example Cytotoxicity Assay Protocol.....	10
D. Calculation of Results	11
E. Proliferation Assay Protocol.....	12
5. Troubleshooting	13
6. References	14
7. Related Products	14

1. Description

The CytoTox-ONE™ Homogeneous Membrane Integrity Assay^(a) is a homogeneous, fluorometric method for estimating the number of non-viable cells present in multiwell plates. Cell viability is most often defined based on the integrity of the cell membrane and is most commonly measured by observing the exclusion of trypan blue or other vital dyes. Measurement of the leakage of components from the cytoplasm into the surrounding culture medium has been widely accepted as a valid method to estimate the number of non-viable cells.

Promega Corporation · 2800 Woods Hollow Road · Madison, WI 53711-5399 USA
Toll Free in USA 800-356-9526 · Phone 608-274-4330 · Fax 608-277-2516 · www.promega.com
Printed in USA. Part# TB306
Revised 5/09 Page 1



The CytoTox-ONE™ Assay is a rapid, fluorescent measure of the release of lactate dehydrogenase (LDH) from cells with a damaged membrane. LDH released into the culture medium is measured with a 10-minute coupled enzymatic assay that results in the conversion of resazurin into resorufin as shown in Figure 1. The CytoTox-ONE™ Reagent mix does not damage healthy cells; therefore the reactions to measure released LDH can be performed directly in a homogeneous format in assay wells containing a mixed population of viable and damaged cells.

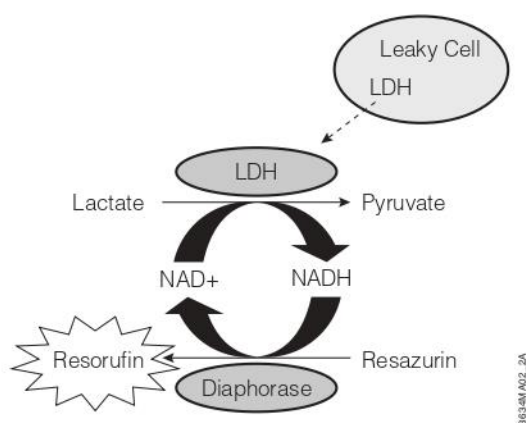


Figure 1. Release of LDH from damaged cells is measured by supplying lactate, NAD⁺, and resazurin as substrates in the presence of diaphorase. Generation of the fluorescent resorufin product is proportional to the amount of LDH.

The product is supplied as a lyophilized Substrate Mix that is reconstituted with Assay Buffer to form the CytoTox-ONE™ Reagent. A flow diagram summarizing the assay protocol is shown in Figure 2. Assay plates are allowed to equilibrate to ambient temperature, and CytoTox-ONE™ Reagent is added to each well and incubated for 10 minutes. Stop Solution is added, and the fluorescent signal is measured. Fluorescence data are collected using a standard 96- or 384-well fluorometer. The amount of fluorescence produced is proportional to the number of lysed cells using a 96- or 384-well format (Figure 3).

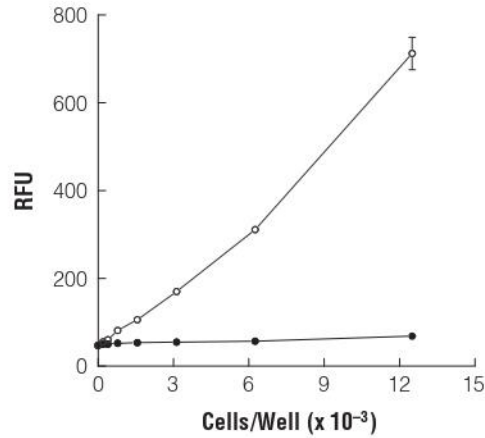
Methods for determining LDH release in conjunction with diaphorase have been used for several years. Variations on this technology have been reported for measuring natural cytotoxicity and have been demonstrated to be identical (within experimental error) to values determined in parallel ⁵¹Cr release assays (1,2).



Figure 2. The CytoTox-ONE™ Membrane Integrity Assay protocol. Assay plates are allowed to equilibrate to ambient temperature, and CytoTox-ONE™ Reagent is added to each well and incubated for 10 minutes. Stop Solution is added, and the fluorescent signal is measured.



A. 384-well plate



B. 96-well plate

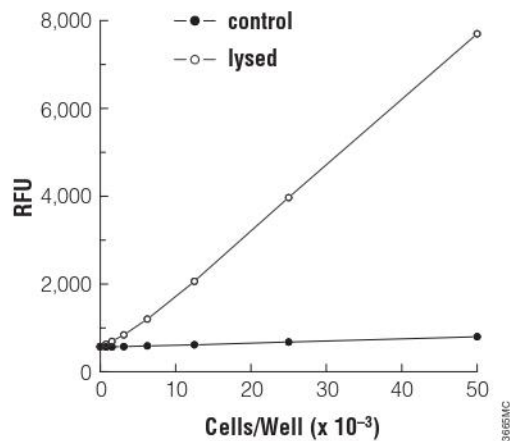


Figure 3. Linear relationship ($r^2 > 0.95$) between cell number and fluorescence (560_{Ex}/590_{Em}) using the CytoTox-ONE™ Assay in 384- and 96-well plate formats.

Serial twofold dilutions of L929 cells were made in a 384-well plate containing 25µl medium (**Panel A**) and a 96-well plate containing 100µl medium (**Panel B**). Wells were treated by addition of Triton® X-100 to produce "lysed" cells. Wells containing control cells received PBS as the vehicle control. CytoTox-ONE™ Reagent was added following treatments. Values represent the mean ± SD from 4 replicate wells for each cell number. The lowest values shown for each plate format (195 cells for 384-well format and 781 cells for the 96-well format) are significantly different than the "zero" cell background fluorescence.



The LDH release assay is commonly used for testing cytotoxicity of various experimental compounds. Figure 4 shows data generated using the CytoTox-ONE™ Assay and depicts the cytotoxic effect of TNF α on murine L929 cells. Increasing concentrations of TNF α are toxic to L929 cells, resulting in a loss of membrane integrity, release of LDH into the surrounding medium, and a greater fluorescent signal. Figure 4 also shows the results obtained using the CellTiter-Glo® Luminescent Cell Viability Assay to measure ATP content, which estimates the number of viable cells (3,4). Concentrations of TNF α that are toxic to L929 cells result in a loss of ATP and a reduced luminescent signal. The IC₅₀ values determined using both assays are similar.

The CytoTox-ONE™ Assay can also be used to determine the total number of cells present in wells at the end of a proliferation assay by adding a Lysis Solution to all wells (5).

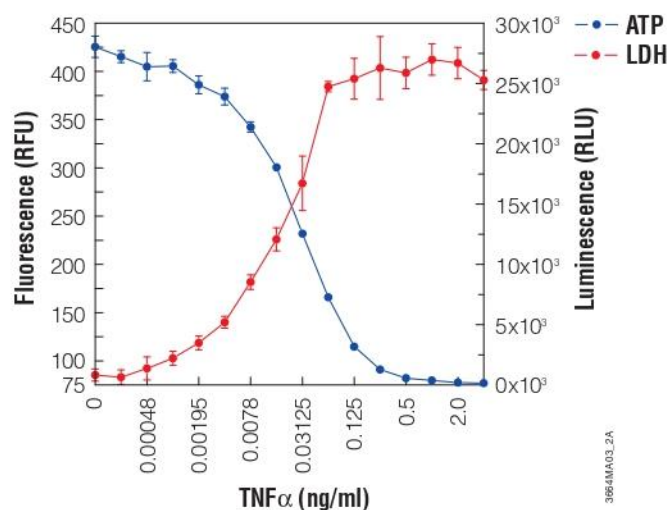


Figure 4. Half-maximal response variables correlate well between the CytoTox-ONE™ Assay and other assays. Murine L929 cells were seeded at 2,000 cells per well in a 384-well plate in serum-supplemented medium, cultured for 24 hours, then various amounts of TNF α were added and incubated overnight. Either CytoTox-ONE™ Reagent or CellTiter-Glo® Reagent was added to parallel sets of wells, and fluorescence (560_{Ex}/590_{Em}) or luminescence values, respectively, were recorded. (The CellTiter-Glo® Assay uses ATP content to indicate the number of viable cells.) The values represent the mean \pm SD of 4 replicate samples. The half maximal response values correlate well for the cytotoxicity and viability assays.



2. Product Components and Storage Conditions

Product	Size	Cat.#
CytoTox-ONE™ Homogeneous Membrane Integrity Assay	200-800 assays	G7890

Each vial contains sufficient reagents to perform 100 assays in a 96-well format or 400 assays in a 384-well format when the recommended volumes are used. Includes:

- 2 vials Substrate Mix
- 24ml Assay Buffer
- 0.5ml Lysis Solution
- 11ml Stop Solution

Product	Size	Cat.#
CytoTox-ONE™ Homogeneous Membrane Integrity Assay	1,000-4,000 assays	G7891

Each vial contains sufficient reagents to perform 100 assays in a 96-well format or 400 assays in 384-well format when the recommended volumes are used. Includes:

- 10 vials Substrate Mix
- 120ml Assay Buffer
- 0.5ml Lysis Solution
- 60ml Stop Solution

Product	Size	Cat.#
CytoTox-ONE™ Homogeneous Membrane Integrity Assay, HTP	1,000-4,000 assays	G7892

Each vial contains sufficient reagents to perform 500 assays in a 96-well format or 2,000 assays in a 384-well format when the recommended volumes are used. Includes:

- 2 vials Substrate Mix
- 120ml Assay Buffer
- 0.5ml Lysis Solution
- 60ml Stop Solution

Storage Conditions: Store all components frozen at -20°C protected from light. Reconstituted CytoTox-ONE™ Reagent may be stored without loss of activity for up to 3 days at room temperature (22-25°C), up to 1 week at 4°C, or 6-8 weeks at -20°C, protected from light.



3. General Considerations

3.A. Background Fluorescence/Serum LDH

Animal serum used to supplement tissue culture medium may contain significant amounts of LDH that can lead to background fluorescence. The quantity of LDH in animal sera will vary depending on several factors, including the species and the health or treatment of the animal prior to collecting serum. Background fluorescence can be corrected by including a control to measure the fluorescence from serum-supplemented culture medium in the absence of cells. The fluorescence value determined from this control is used to normalize the fluorescence values obtained from other samples. Using reduced serum concentrations or serum-free medium can reduce or eliminate background fluorescence resulting from LDH in serum and improve assay sensitivity.

3.B. Temperature

The generation of fluorescent product in the CytoTox-ONE™ Assay is proportional to the quantity of LDH. The enzymatic activity of LDH is influenced by temperature. We recommend equilibrating the temperature of the assay plate and the CytoTox-ONE™ Reagent to 22°C (20–30 minutes) prior to adding the CytoTox-ONE™ Reagent to initiate the reaction.

The recommended incubation period for the CytoTox-ONE™ Reagent is 10 minutes when reagents and samples are at 22°C. At longer incubation times or higher temperatures, assay linearity may decrease due to substrate depletion. In some situations, the time required for manual or robotic addition of CytoTox-ONE™ Reagent to the assay plate may be a significant portion of the 10-minute incubation period. To minimize the difference in incubation interval among wells within a plate, we recommend adding Stop Solution using the same sequence used for adding the CytoTox-ONE™ Reagent.

3.C. Assay Controls

In a standard cytotoxicity assay, it may be desirable to perform a 100% cell lysis control to determine the maximum amount of LDH present. Individual laboratories may prefer to use a positive control that is known to be toxic for their specific conditions, depending on the cell type, culture conditions, and assay model system. For convenience, we include the Lysis Solution, which is a 9% (weight/volume) solution of Triton® X-100 in water. Use of Lysis Solution at the recommended dilution will result in almost immediate lysis of most cell types and subsequent release of cytoplasmic LDH into the surrounding culture medium. Use of Lysis Solution at the recommended dilution is compatible with the CytoTox-ONE™ Assay chemistry.

3.D. Considerations for the Maximum LDH Release Control

Experimental design will influence the values for the Maximum LDH Release control. The mechanism of cytotoxicity, and thus the kinetics of release of LDH, may vary widely for different experimental compounds being tested.



3.D. Considerations for the Maximum LDH Release Control (continued)

The method by which the Maximum LDH Release Control is prepared as well as the timing of the addition of Lysis Solution (i.e., beginning, middle, or end of experimental/drug treatment period) may both affect the value obtained for 100% LDH release. For example, if the indicator cells are growing throughout the duration of exposure to test compounds, untreated control wells may have more cells and thus may have more LDH present at the end of the exposure period. Adding Lysis Solution after cultured cells are exposed to test compounds may give a different Maximum LDH Release Control value than adding Lysis Solution prior to exposure period.

The half-life of LDH that has been released from cells into the surrounding medium is approximately 9 hours. If Lysis Solution is added at the beginning of an experimental exposure period, the quantity of active LDH remaining in the culture medium at the end of the experiment may underestimate the quantity of LDH present in untreated cells.

The recommended dilution of Lysis Solution is compatible with the enzymatic reactions and fluorescence of the assay. Using higher concentrations of Lysis Solution may increase the rate of enzymatic reactions and inflate maximum cell lysis values.

3.E. Light Sensitivity of Resazurin

The resazurin dye in the CytoTox-ONE™ Reagent and the resorufin product formed during the assay are light-sensitive. Prolonged exposure of the Assay Buffer or reconstituted CytoTox-ONE™ Reagent to light will result in increased background fluorescence in the assay and decreased sensitivity.

3.F. Use of Stop Solution to Stop Development of Fluorescent Signal

The Stop Solution provided is designed to rapidly stop the continued generation of fluorescent product and allow the plate to be read at a later time. There may be situations where the researcher will want to take multiple kinetic reads of the same plate and not stop the assay. After adding the Stop Solution, provided that there is some serum (5-10%) present in the samples, the resulting fluorescence is generally stable for up to two days if the assay plate has been protected from light exposure and the wells have been sealed with a plate sealer to prevent evaporation. If no serum is present, the resulting fluorescence is stable for 1-2 hours.

3.G. Cell Culture Media Considerations

Pyruvate-supplemented medium is recommended for some cell lines. Common examples of culture media that contain pyruvate include: Ham's F12, Iscove's, and some formulations of DMEM. Culture media containing pyruvate may cause a reduction in the fluorescent signal due to product inhibition of the LDH reaction catalyzing conversion of lactate to pyruvate.



For most situations, the recommended assay conditions of 10 minutes at 22°C will provide adequate signal. However, assay conditions can be empirically optimized.

To increase the fluorescent signal, we recommend determining if the cell line requires pyruvate supplementation during the assay period. Alternatively, conditions known to increase the fluorescent signal include increasing the time of incubation with the CytoTox-ONE™ Reagent prior to adding Stop Solution or incubating the assay at temperatures above the recommended 22°C (up to 37°C). In all cases, all samples should be assayed under the same conditions.

3.H. Use of Resazurin as an Indicator in both Cytotoxicity and Cell Viability Assays

Resazurin reduction is a common reporter for both cytotoxicity and cell viability assays. Using the reaction conditions recommended for the CytoTox-ONE™ Assay (i.e., reduced temperature and short incubation time), only a negligible amount of resazurin is reduced by the viable cell population. Figure 3 (Section 1) shows only a very slight increase in fluorescence in the control (viable) cells. In the CytoTox-ONE™ Assay, the rate of the LDH reaction is increased by providing excess substrates (pyruvate, NAD⁺, and diaphorase) so that the reaction proceeds relatively quickly (10 minutes at ambient temperature). By contrast, the CellTiter-Blue® Cell Viability Assay requires longer incubation times (1-4 hours) and a higher incubation temperature (37°C). Additionally, the concentration of resazurin is different between the two assays.

3.I. Performing Other Multiplexed Assays in Combination with the CytoTox-ONE™ Assay

It is possible to remove a portion of the medium from each well to a separate multiwell plate to measure LDH release using the CytoTox-ONE™ Assay followed by performing a separate assay on the sample remaining in the original well. Some examples of this application include estimating the number of viable cells by measuring the ATP content using CellTiter-Glo® Assay or by measuring tetrazolium reduction using the CellTiter 96® AQueous One Solution Assay. Alternatively, the level of apoptosis could be determined by measuring the caspase activity using the Apo-ONE® Homogeneous Caspase-3/7 Assay.



4. Protocols

Materials to Be Supplied by the User

- 96- or 384-well opaque-walled tissue culture plates compatible with fluorometer (clear or solid bottom)
- multichannel pipettor
- reservoirs to hold CytoTox-ONE™ Reagent and Stop Solution
- fluorescence plate reader with excitation 530–570nm and emission 580–620nm
- plate shaker

4.A. Reagent Preparation

Equilibrate Substrate Mix and Assay Buffer to 22°C. A 37°C water bath may be used to thaw the Assay Buffer, but the Assay Buffer should not be left at 37°C longer than necessary. For Cat.# G7890 and G7891, prepare CytoTox-ONE™ Reagent by adding 11ml of Assay Buffer to each vial of Substrate Mix. Gently mix to dissolve the substrate.

For Cat.# G7892, add 55ml of Assay Buffer to each vial of Substrate Mix. Gently mix to dissolve the substrate.

Protect the reagent from direct light. Unused portions of the CytoTox-ONE™ Reagent may be stored tightly capped at -20°C for 6–8 weeks.

4.B. Recommended Controls

Each of these controls should be performed on each plate being assayed.

No-Cell Control: Set up triplicate wells without cells to serve as the negative control to determine background fluorescence that might be present.

Untreated Cells Control: Set up triplicate wells with untreated cells to serve as a vehicle control. Add the same solvent used to deliver the test compounds to the vehicle control wells.

Maximum LDH Release Control: Set up triplicate wells to determine the Maximum LDH Release Control. Add 2µl of Lysis Solution to the positive control wells before addition of reagent. See Considerations for the Maximum LDH Release Control (Section 3.D) concerning timing of addition.

4.C. Example Cytotoxicity Assay Protocol

1. Set up 96-well assay plates containing cells in culture medium.
Note: For 384-well plates, the recommended culture volume is 25µl per well.
2. Add test compounds and vehicle controls to appropriate wells so the final volume is 100µl in each well (25µl for a 384-well plate).
3. Culture cells for desired test exposure period.



4. Remove assay plates from 37°C incubator and equilibrate to 22°C (approximately 20-30 minutes).
Note: If samples cannot be equilibrated to 22°C, reduce incubation time to 5 minutes.
5. **Optional:** If Lysis Solution is used to generate a Maximum LDH Release Control, add 2µl of Lysis Solution (per 100µl original volume) to the positive control wells. If a larger pipetting volume is desired, use 10µl of a 1:5 dilution of Lysis Solution.
6. Add a volume of CytoTox-ONE™ Reagent equal to the volume of cell culture medium present in each well and mix or shake for 30 seconds (e.g., add 100µl of CytoTox-ONE™ Reagent to 100µl of medium containing cells for the 96-well plate format or add 25µl of CytoTox-ONE™ Reagent to 25µl of medium containing cells for the 384-well format).
7. Incubate at 22°C for 10 minutes.
8. Add 50µl of Stop Solution (per 100µl of CytoTox-ONE™ Reagent added) to each well. For the 384-well format (where 25µl of CytoTox-ONE™ Reagent was added), add 12.5µl of Stop Solution. This step is optional but recommended for consistency.
Note: We recommend adding the Stop Solution to the wells using the same order of addition that was used for adding the CytoTox-ONE™ Reagent. This is especially important if manual addition of reagent takes a significant amount of time.
9. Shake plate for 10 seconds and record fluorescence with an excitation wavelength of 560nm and an emission wavelength of 590nm.
Note: If the plate is not protected from light, the data should be recorded within one hour to avoid increased background fluorescence.

4.D. Calculation of Results

1. Subtract the average fluorescence values of the culture medium background from all fluorescence values of experimental wells.
2. Use the average fluorescence values from experimental, maximum LDH release, and culture medium background to calculate the percent cytotoxicity for a given experimental treatment.

$$\text{Percent cytotoxicity} = 100 \times \frac{(\text{Experimental} - \text{Culture Medium Background})}{(\text{Maximum LDH Release} - \text{Culture Medium Background})}$$



4.E. Proliferation Assay Protocol

The CytoTox-ONE™ Assay can be used to estimate the total number of cells in assay wells at the end of a proliferation assay. The procedure involves lysing all the cells to release LDH followed by adding the CytoTox-ONE™ Reagent. The total number of cells present will be directly proportional to the background-subtracted fluorescence values, which represent LDH activity.

1. Set up 96-well assay plates containing cells in culture medium.
2. Add test compounds and vehicle controls to appropriate wells so the final volume is 100µl in each well (25µl per well for 384-well plates).
3. Culture cells for desired test exposure period.
4. Add 2µl of Lysis Solution (per 100µl of original volume) to all wells. If a larger pipetting volume is desired, use 10µl of a 1:5 dilution of Lysis Solution.
5. Remove assay plates from 37°C incubator and equilibrate to 22°C (approximately 20–30 minutes).
Note: If samples cannot be equilibrated to 22°C, reduce incubation time to 5 minutes.
6. Add a volume of CytoTox-ONE™ Reagent equal to the volume of cell culture medium present in each well and mix or shake for 30 seconds (e.g., add 100µl of CytoTox-ONE™ Reagent to 100µl of medium containing cells for the 96-well plate format or add 25µl of CytoTox-ONE™ Reagent to 25µl of medium containing cells for the 384-well format).
7. Incubate at 22°C for 10 minutes.
8. Add 50µl of Stop Solution (per 100µl of CytoTox-ONE™ Reagent added) to each well in the 96-well format. For the 384-well format (where 25µl of CytoTox-ONE™ Reagent was added), add 12.5µl Stop Solution. This step is optional but recommended for consistency.
Note: We recommend adding the Stop Solution to the wells using the same order of addition that was used for adding the CytoTox-ONE™ Reagent. This is especially important if manual addition of reagent takes a significant amount of time.
9. Shake plate 10 seconds and record fluorescence 560/590nm.
Note: If the plate is not protected from light, the data should be recorded within one hour to avoid increased background fluorescence.



5. Troubleshooting

For questions not addressed here, please contact your local Promega Branch Office or Distributor. Contact information available at: www.promega.com. E-mail: techserv@promega.com

Symptoms	Causes and Comments
High background	Endogenous LDH in animal sera in culture medium. This background absorbance is normally subtracted as the culture medium background. To reduce the background absorbance, change the source of serum or reduce the serum concentration. LDH activity in sera varies with human AB serum, horse serum, fetal bovine serum and calf serum containing increasing levels of LDH activity. In general, decreasing serum concentration to 5% will significantly reduce background without affecting cell viability.
Low percent cytotoxicity	Percent cytotoxicity too low for convenient quantitation. In cases where it is desirable to increase percent cytotoxicity, increase the incubation time with cytotoxic compounds.
Fluorescence values above linear range of plate reader	Too much LDH activity. Repeat assay and shorten LDH reaction time to 5 minutes. Be sure temperature is equilibrated to 22°C.
Low overall fluorescence	Cell culture medium contains pyruvate. Pyruvate may cause a reduction in the fluorescent signal because of product inhibition of the LDH reaction. Determine if the cell line requires pyruvate supplement during the assay period. Conditions known to increase signal are increasing incubation time with CytoTox-ONE™ Reagent and incubating the assay above the recommended 22°C. Plate reader set at incorrect gain. Adjust gain setting. Improper filter set. Choose appropriate excitation and emission filters. The excitation wavelength should be 560nm, and the emission wavelength should be 590nm.
Unexpected high fluorescence	Experimental compound being tested may be fluorescent. Perform control without addition of CytoTox-ONE™ Reagent to test fluorescence of compound.



5. Troubleshooting (continued)

Symptoms	Causes and Comments
Unexpected high fluorescence (continued)	Experimental compound being tested may interfere with assay chemistry. Test combination of experimental compound and CytoTox-ONE™ Reagent without cells.

6. References

1. Korzeniewski, C. and Callewaert, D.M. (1983) An enzyme-release assay for natural cytotoxicity. *J. Immunol. Meth.* **64**, 313-20.
2. Decker, T. and Lohmann-Matthes, M.L. (1988) A quick and simple method for the quantitation of lactate dehydrogenase release in measurements of cellular cytotoxicity and tumor necrosis factor (TNF) activity. *J. Immunol. Meth.* **115**, 61-9.
3. *CellTiter-Glo® Luminescent Cell Viability Assay Technical Bulletin #TB288*, Promega Corporation.
4. Crouch, S.P. *et al.* (1993) The use of ATP bioluminescence as a measure of cell proliferation and cytotoxicity. *J. Immunol. Meth.* **160**, 81-8.
5. Moravec, R. (1994) Total cell quantitation using the CytoTox 96® Non-Radioactive Cytotoxicity Assay. *Promega Notes* **45**, 11-2.

7. Related Products

Product	Size	Cat.#
CytoTox 96® Non-Radioactive Cytotoxicity Assay*	1,000 assays	G1780
CellTiter-Glo® Luminescent Cell Viability Assay* (ATP, luminescent)	10ml	G7570
	10 × 10ml	G7571
	100ml	G7572
	10 × 100ml	G7573
CellTiter-Blue® Cell Viability Assay (resazurin, fluorometric)	20ml	G8080
	100ml	G8081
	10 × 100ml	G8082
CellTiter 96® AQueous One Solution Cell Proliferation Assay* (MTS, colorimetric)	200 assays	G3582
	1,000 assays	G3580
	5,000 assays	G3581
CellTiter 96® Non-Radioactive Cell Proliferation Assay* (MTT, colorimetric)	1,000 assays	G4000
	5,000 assays	G4100

*For Laboratory Use.



Product	Size	Cat.#
Apo-ONE® Homogeneous Caspase-3/7 Assay	1ml	G7792
	10ml	G7790
	100ml	G7791
Caspase-Glo® 3/7 Assay* (luminescent)	2.5ml	G8090
	10ml	G8091
	10 × 10ml	G8093
	100ml	G8092
Caspase-Glo® 8 Assay* (luminescent)	2.5ml	G8200
	10ml	G8201
	100ml	G8202
Caspase-Glo® 9 Assay* (luminescent)	2.5ml	G8210
	10ml	G8211
	100ml	G8212

*For Laboratory Use.



[®]U.S. Pat. No. 6,982,152 B2 has been issued to Promega Corporation for cytotoxicity assay. Other patents are pending.

© 2002-2004, 2007, 2009 Promega Corporation. All Rights Reserved.

Apo-ONE, Caspase-Glo, CellTiter 96, CellTiter-Blue, CellTiter-Glo and CytoTox 96 are registered trademarks of Promega Corporation. CytoTox-ONE is a trademark of Promega Corporation.

Triton is a registered trademark of Union Carbide Chemicals & Plastics Technology Corporation.

Products may be covered by pending or issued patents or may have certain limitations. Please visit our Web site for more information.

All prices and specifications are subject to change without prior notice.

Product claims are subject to change. Please contact Promega Technical Services or access the Promega online catalog for the most up-to-date information on Promega products.

Promega Corporation · 2800 Woods Hollow Road · Madison, WI 53711-5399 USA
Toll Free in USA 800-356-9526 · Phone 608-274-4330 · Fax 608-277-2516 · www.promega.com
Part# TB306 Printed in USA.
Page 16 Revised 5/09

Annex 4 - MTS Cell Proliferation Assay Protocol



PRINTED IN USA.
Revised 12/12

Technical Bulletin

CellTiter 96[®] AQueous One Solution Cell Proliferation Assay

INSTRUCTIONS FOR USE OF PRODUCTS G3580, G3581 AND G3582.

www.promega.com

Part# TB245



CellTiter 96[®] AQ_{ueous} One Solution Cell Proliferation Assay

All technical literature is available on the Internet at: www.promega.com/protocols/
Please visit the web site to verify that you are using the most current version of this
Technical Bulletin. Please contact Promega Technical Services if you have questions on use
of this system. E-mail: techserv@promega.com.

1. Description.....	1
2. Product Components and Storage Conditions	4
3. Protocols	5
A. General Protocol	5
B. Example of a Protocol for Bioassay of IL-6 Using B9 Cells	5
4. General Considerations	6
A. Background Absorbance	6
B. Optional Wavelengths to Record Data	7
C. Lymphocyte Assays	8
D. Reagent Optimization.....	8
E. Cell Number Optimization.....	8
5. References	9
6. Related Products	9

1. Description

The CellTiter 96[®] AQ_{ueous} One Solution Cell Proliferation Assay^(a) is a colorimetric method for determining the number of viable cells in proliferation or cytotoxicity assays. The CellTiter 96[®] AQ_{ueous} One Solution Reagent contains a novel tetrazolium compound [3-(4,5-dimethylthiazol-2-yl)-5-(3-carboxymethoxyphenyl)-2-(4-sulfophenyl)-2H-tetrazolium, inner salt; MTS^(a)] and an electron coupling reagent (phenazine ethosulfate; PES). PES has enhanced chemical stability, which allows it to be combined with MTS to form a stable solution. This convenient "One Solution" format is an improvement over the first version of the CellTiter 96[®] AQ_{ueous} Assay, where phenazine methosulfate (PMS) is used as the electron coupling reagent, and the PMS Solution and MTS Solution are supplied separately.

The MTS tetrazolium compound (Owen's reagent) is bioreduced by cells into a colored formazan product that is soluble in tissue culture medium (Figure 1, 1). This conversion is presumably accomplished by NADPH or NADH produced by dehydrogenase enzymes in metabolically active cells (2). Assays are performed by adding a small amount of the CellTiter 96[®] AQ_{ueous} One Solution Reagent directly to culture wells, incubating for 1–4 hours and then recording the absorbance at 490nm with a 96-well plate reader (3,4).



1. Description (continued)

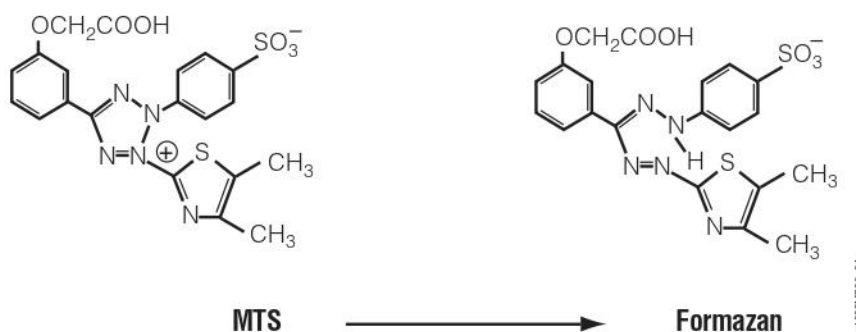


Figure 1. Structures of MTS tetrazolium and its formazan product.

The quantity of formazan product as measured by the absorbance at 490nm is directly proportional to the number of living cells in culture (Figure 2). Because the MTS formazan product is soluble in tissue culture medium, the CellTiter 96® AQ_{ueous} One Solution Assay requires fewer steps than procedures that use tetrazolium compounds such as MTT or INT (5,6). The formazan product of MTT reduction is a crystalline precipitate that requires an additional step in the procedure to dissolve the crystals before recording absorbance readings at 570nm (7).

If you currently use a [³H]thymidine incorporation assay, addition of the CellTiter 96® AQ_{ueous} One Solution Reagent can be substituted for the pulse of [³H]thymidine at the time point in the assay when the pulse of radioactive thymidine is usually added. Bioassay data comparing [³H]thymidine incorporation to the MTS-based CellTiter 96® AQ_{ueous} Assay and the original MTT-based CellTiter 96® Assay demonstrate that tetrazolium reagents can be substituted for [³H]thymidine incorporation (4,7).

Advantages of the CellTiter 96® AQ_{ueous} One Solution Assay include:

- **Easy-to-Use:** Add the CellTiter 96® AQ_{ueous} One Solution Reagent to cells, incubate and read absorbance.
- **Convenient:** Supplied as a single solution, filter-sterilized and ready for adding to assay plates.
- **Fast:** Perform the assay in a 96-well plate with no washing or cell harvesting. Also eliminates solubilization steps normally required for MTT assays.
- **Non-Radioactive:** Requires no scintillation cocktail or radioactive waste disposal.



- **Flexible:** Plates can be read and returned to incubator for further color development.
- **Safe:** Requires no volatile organic solvent to solubilize the formazan product (unlike MTT).

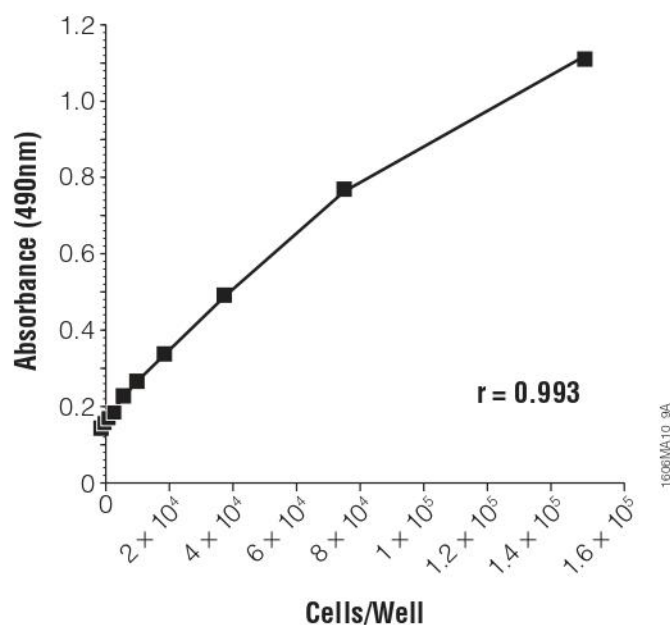


Figure 2. Effect of cell number on absorbance at 490nm measured using the CellTiter 96® AQ_{ueous} One Solution Assay. Various numbers of B9 hybridoma cells were added to the wells of a 96-well plate in RPMI containing 50μM 2-mercaptoethanol and supplemented with 5% FBS and 2ng/ml IL-6. The medium was allowed to equilibrate for 1 hour, then 20μl/well of CellTiter 96® AQ_{ueous} One Solution Reagent was added. After 1 hour at 37°C in a humidified, 5% CO₂ atmosphere, the absorbance at 490nm was recorded using an ELISA plate reader. Each point represents the mean ± SD of 4 replicates. The correlation coefficient of the line was 0.993, indicating a linear response between cell number and absorbance at 490nm. The background absorbance shown at zero cells/well was not subtracted from these data.



2. Product Components and Storage Conditions

Product	Size	Cat.#
CellTiter 96 [®] AQ _{ueous} One Solution Cell Proliferation Assay	200 assays	G3582

Includes:

- 4ml CellTiter 96[®] AQ_{ueous} One Solution Reagent

Product	Size	Cat.#
CellTiter 96 [®] AQ _{ueous} One Solution Cell Proliferation Assay	1,000 assays	G3580

Includes:

- 20ml CellTiter 96[®] AQ_{ueous} One Solution Reagent

Product	Size	Cat.#
CellTiter 96 [®] AQ _{ueous} One Solution Cell Proliferation Assay	5,000 assays	G3581

Includes:

- 100ml CellTiter 96[®] AQ_{ueous} One Solution Reagent

Storage Conditions: For long-term storage, store the CellTiter 96[®] AQ_{ueous} One Solution Reagent at -20°C, protected from light. See the expiration date on the Product Information Label. For frequent use, solutions may be stored at 4°C, protected from light, for up to 6 weeks.

Note: The performance of CellTiter 96[®] AQ_{ueous} One Solution Reagent after 10 freeze-thaw cycles was demonstrated to be equal to that of freshly prepared solution.

Safety: To the best of our knowledge, the chemical, physical and toxicological properties of this product have not been thoroughly investigated; therefore, we recommend the use of gloves, lab coats and eye protection when working with these or any chemicals.

Light-Sensitivity: The CellTiter 96[®] AQ_{ueous} One Solution Reagent is light-sensitive and is supplied in an amber container. Discoloration may occur if solutions are exposed to light outside of the container for several hours. This discoloration may cause slightly higher background 490nm absorbance readings, but it should not affect the performance of the CellTiter 96[®] AQ_{ueous} One Solution Assay.



3. Protocols

Materials to Be Supplied by the User

- 96-well plates suitable for tissue culture
- repeating pipettes, digital pipettes or multichannel pipettes
- 96-well plate reader

3.A. General Protocol

1. Thaw the CellTiter 96[®] AQ_{ueous} One Solution Reagent. It should take approximately 90 minutes at room temperature, or 10 minutes in a water bath at 37°C, to completely thaw the 20ml size.

2. Pipet 20µl of CellTiter 96[®] AQ_{ueous} One Solution Reagent into each well of the 96-well assay plate containing the samples in 100µl of culture medium.

Note: We recommend repeating pipettes, digital pipettes or multichannel pipettes for convenient delivery of uniform volumes of CellTiter 96[®] AQ_{ueous} One Solution Reagent to the 96-well plate.

3. Incubate the plate at 37°C for 1-4 hours in a humidified, 5% CO₂ atmosphere.

Note: To measure the amount of soluble formazan produced by cellular reduction of MTS, proceed immediately to Step 4. Alternatively, to measure the absorbance later, add 25µl of 10% SDS to each well to stop the reaction. Store SDS-treated plates protected from light in a humidified chamber at room temperature for up to 18 hours. Proceed to Step 4.

4. Record the absorbance at 490nm using a 96-well plate reader.

3.B. Example of a Protocol for Bioassay of IL-6 Using B9 Cells

1. Maintain stock cultures of B9 cells in RPMI 1640 medium containing 5% FBS, 50µM 2-mercaptoethanol (2-ME) supplemented with 5ng/ml human recombinant IL-6. Subculture the stock cultures of cells to 2 × 10⁴ cells/ml, and refeed with human recombinant IL-6 every 3 days or when a density of 2 × 10⁵ cells/ml is reached.

Note: B9 cells used for the bioassay should be from stock cultures 2 days after the last subculture (feeding with IL-6).

2. Add 50µl/well of IL-6 samples or standards to be measured, diluted in RPMI 1640 medium containing 5% FBS and 50µM 2-ME. Start the titration of the IL-6 standard at 4ng/ml in column 12, and perform serial twofold dilutions across the plate to column 2 (to 4pg/ml). (After the cell suspension is added in Step 5 below, the final concentration of the titrated standard will be 2ng/ml in column 12 to 2pg/ml in column 2.) Use column 1 for the negative control: RPMI 1640 medium (and supplements) without IL-6. Equilibrate the plate at 37°C in a humidified, 5% CO₂ atmosphere while harvesting the cells for assay.



3.B. Example of a Protocol for Bioassay of IL-6 Using B9 Cells (continued)

3. Wash the B9 cells twice in RPMI 1640 containing 5% FBS and 50 μ M 2-ME by centrifugation at 300 \times g for 5 minutes.
4. Determine cell number and viability (by trypan blue exclusion), and resuspend the cells to a final concentration of 1 \times 10⁵ cells/ml in RPMI 1640 supplemented with 5% FBS and 50 μ M 2-ME.
5. Dispense 50 μ l of the cell suspension (5,000 cells) into all wells of the plate prepared in Step 2. The total volume in each well should be 100 μ l.
6. Incubate the plate at 37°C for 48–72 hours in a humidified, 5% CO₂ atmosphere.
7. Add 20 μ l per well of CellTiter 96[®] AQ_{ueous} One Solution Reagent.
8. Incubate the plate at 37°C for 1–4 hours in a humidified, 5% CO₂ atmosphere.
Note: To measure the amount of soluble formazan produced by cellular reduction of MTS, proceed immediately to Step 9. Alternatively, to measure the absorbance at a later time, add 25 μ l of 10% SDS to each well to stop the reaction. Store SDS-treated plates protected from light in a humidified chamber at room temperature for up to 18 hours. Proceed to Step 9.
9. Record the absorbance at 490nm using a 96-well plate reader.
10. Plot the corrected absorbance at 490nm (Y axis) versus concentration of growth factor (X axis). Determine the X-axis value corresponding to one-half the difference between the maximum (plateau) and minimum (no growth factor control) absorbance values; this is the ED₅₀ value (ED₅₀ = the concentration of growth factor necessary to give one-half the maximum response.)

4. General Considerations

4.A. Background Absorbance

A small amount of spontaneous 490nm absorbance occurs in culture medium incubated with CellTiter 96[®] AQ_{ueous} One Solution Reagent. The type of culture medium used, type of serum, pH and length of exposure to light are variables that may contribute to the background 490nm absorbance. Background absorbance is typically 0.2–0.3 absorbance units after 4 hours of culture. Background absorbance may result from chemical interference of certain compounds with tetrazolium reduction reactions. Strong reducing substances, including ascorbic acid, or sulfhydryl-containing compounds, such as glutathione, coenzyme A and dithiothreitol, can reduce tetrazolium salts nonenzymatically and lead to increased background absorbance values. Culture medium at elevated pH or extended exposure to direct light also may cause an accelerated spontaneous reduction of tetrazolium salts and result in increased background absorbance values. If phenol red containing medium is



used, an immediate change in color may indicate a shift in pH caused by the test compounds. Specific chemical interference of test compounds can be confirmed by measuring absorbance values from control wells containing medium without cells at various concentrations of test compound.

Background 490nm absorbance may be corrected as follows: Prepare a triplicate set of control wells (without cells) containing the same volumes of culture medium and CellTiter 96[®] AQ_{ueous} One Solution Reagent as in the experimental wells. Subtract the average 490nm absorbance from the “no cell” control wells from all other absorbance values to yield corrected absorbances.

4.B. Optional Wavelengths to Record Data

Figure 3 shows an absorbance spectrum of the formazan product resulting from reduction of MTS. We recommend recording data at the absorbance peak of 490nm; however, if your 96-well plate reader does not have a 490nm filter, data can be recorded at wavelengths of 450–540nm. Absorbance may be recorded at other wavelengths if necessary, but loss in sensitivity will result. A reference wavelength of 630–700nm may be used to subtract background contributed by excess cell debris, fingerprints and other nonspecific absorbance.

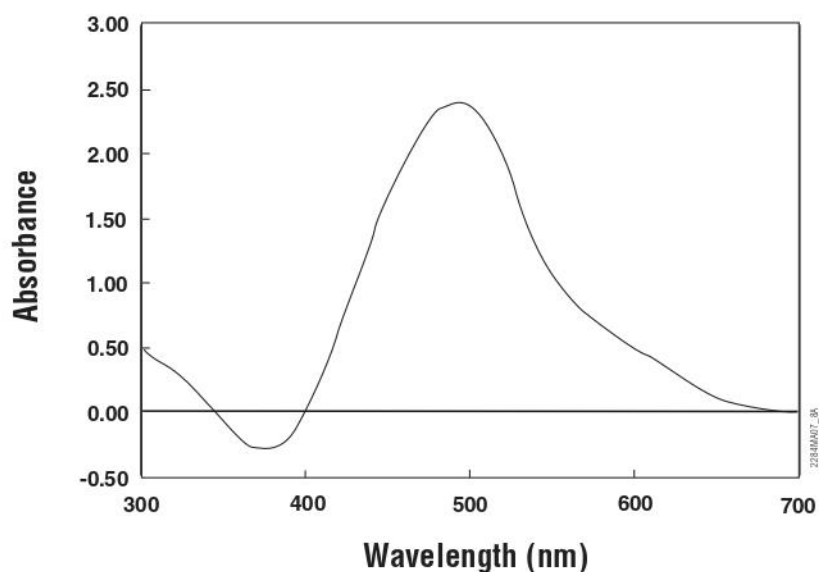


Figure 3. Absorbance spectrum of MTS/formazan. The absorbance spectrum of the formazan product resulting from reduction of the MTS tetrazolium compound shows an absorbance maximum at 490nm. The negative absorbance values (382nm) correspond to the disappearance of MTS as it is converted into formazan.



4.C. Lymphocyte Assays

Lymphocytes may produce less formazan than other cell types (8). To achieve significant absorbance changes with lymphocytes, increase the number of cells to approximately $2.5-10 \times 10^4$ cells/well and incubate the plate with CellTiter 96[®] AQueous One Solution Reagent for the entire 4-hour period.

4.D. Reagent Optimization

The concentrations of tetrazolium and electron transfer reagents have been optimized for general use with a wide variety of cell lines cultured in 96-well plates containing 100 μ l of medium. If different volumes of culture medium are used, adjust the volume to maintain a ratio of 20 μ l CellTiter 96[®] AQueous One Solution Reagent per 100 μ l culture medium. This reagent:medium ratio results in a final concentration of 317 μ g/ml MTS in the assay wells. Minor variations in the optimum concentrations of tetrazolium and electron transfer reagents occur with different cell lines; however, assay sensitivity is seldom compromised using the formulation in the CellTiter 96[®] AQueous One Solution Reagent. If reagent optimization is critical to your assay procedure, we recommend using the CellTiter 96[®] AQueous Non-Radioactive Cell Proliferation Assay (Cat.# G5421, G5430, G5440) or the CellTiter 96[®] AQueous MTS Reagent Powder products (Cat.# G1111, G1112) that supply the chemicals separately.

4.E. Cell Number Optimization

Cell proliferation assays require cells to grow over a period of time. Therefore, choose an initial number of cells per well that produces an assay signal near the low end of the linear range of the assay. This helps to ensure that the signal measured at the end of the assay will not exceed the linear range of the assay. This cell number can be determined by performing a cell titration as shown in Figure 2.

Different cell types have different levels of metabolic activity. Factors that affect the metabolic activity of cells may affect the relationship between cell number and absorbance. Anchorage-dependent cells that undergo contact inhibition may show a change in metabolic activity per cell at high densities, resulting in a nonlinear relationship between cell number and absorbance. Factors that affect the cytoplasmic volume or physiology of the cells will affect metabolic activity.

For most tumor cells, hybridomas and fibroblast cell lines, 5,000 cells per well is recommended to initiate proliferation studies, although fewer than 1,000 cells can usually be detected. The known exception to this is blood lymphocytes, which generally require 25,000–250,000 cells per well to obtain a sufficient absorbance reading.



5. References

1. Barltrop, J.A. *et al.* (1991) 5-(3-carboxymethoxyphenyl)-2-(4,5-dimethylthiazolyl)-3-(4-sulfophenyl)tetrazolium, inner salt (MTS) and related analogs of 3-(4,5-dimethylthiazolyl)-2,5-diphenyltetrazolium bromide (MTT) reducing to purple water-soluble formazans as cell-viability indicators. *Bioorg. Med. Chem. Lett.* **1**, 611-4.
2. Berridge, M.V. and Tan, A.S. (1993) Characterization of the cellular reduction of 3-(4,5-dimethylthiazol-2-yl)-2,5-diphenyltetrazolium bromide (MTT): Subcellular localization, substrate dependence, and involvement of mitochondrial electron transport in MTT reduction. *Arch. Biochem. Biophys.* **303**, 474-82.
3. Cory, A.H. *et al.* (1991) Use of an aqueous soluble tetrazolium/formazan assay for cell growth assays in culture. *Cancer Commun.* **3**, 207-12.
4. Riss, T.L. and Moravec, R.A. (1992) Comparison of MTT, XTT, and a novel tetrazolium compound for MTS in *in vitro* proliferation and chemosensitivity assays. *Mol. Biol. Cell (Suppl.)* **3**, 184a.
5. Mosmann, T. (1983) Rapid colorimetric assay for cellular growth and survival: Application to proliferation and cytotoxicity assays. *J. Immunol. Methods* **65**, 55-63.
6. Bernabei, P.A. *et al.* (1989) *In vitro* chemosensitivity testing of leukemic cells: Development of a semiautomated colorimetric assay. *Hematol. Oncol.* **7**, 243-53.
7. CellTiter 96® Non-Radioactive Cell Proliferation Assay Technical Bulletin #TB112, Promega Corporation.
8. Chen, C.-H., Campbell, P.A. and Newman, L.S. (1990) MTT colorimetric assay detects mitogen responses of spleen but not blood lymphocytes. *Int. Arch. Allergy Appl. Immunol.* **93**, 249-55

6. Related Products

MTS/MTT-Based Cell Viability Assay Systems

Product	Size	Cat.#
CellTiter 96® AQueous Non-Radioactive Cell Proliferation Assay	1,000 assays	G5421
	5,000 assays	G5430
	50,000 assays	G5440
CellTiter 96® AQueous MTS Reagent Powder*	250mg	G1112
	1g	G1111
CellTiter 96® Non-Radioactive Cell Proliferation Assay	1,000 assays	G4000
	5,000 assays	G4100

*PMS is not supplied with MTS Reagent Powder and must be obtained separately.



6. Related Products (continued)

Luminescent-Based Cell Viability Assay System

Product	Size	Cat.#
CellTiter-Glo® Luminescent Cell Viability Assay	10ml	G7570
	10 × 10ml	G7571
	100ml	G7572
	10 × 100ml	G7573

Resazurin-Based Cell Viability Assay System

Product	Size	Cat.#
CellTiter-Blue® Cell Viability Assay	20ml	G8080
	100ml	G8081
	10 × 100ml	G8082

Fluorescent-Based Cell Viability Assay

Product	Size	Cat.#
CellTiter-Fluor™ Cell Viability Assay	10ml	G6080
	5 × 10ml	G6081
	2 × 50ml	G6082

Cytotoxicity Assay Systems (LDH)

Product	Size	Cat.#
CytoTox-ONE™ Homogeneous Membrane Integrity Assay	200–800 assays	G7890
	1,000–4,000 assays	G7891
CytoTox 96® Non-Radioactive Cytotoxicity Assay	1,000 assays	G1780
CytoTox-Glo™ Cytotoxicity Assay	10ml	G9290
	5 × 10ml	G9291
	2 × 50ml	G9292



Apoptosis Assay Systems

Product	Size	Cat.#
Apo-ONE® Homogeneous Caspase-3/7 Assay	1ml	G7792
	10ml	G7790
	100ml	G7791
Caspase-Glo® 2 Assay	10ml	G0940
	50ml	G0941
Caspase-Glo® 6 Assay	10ml	G0970
	50ml	G0971
Caspase-Glo® 3/7 Assay	2.5ml	G8090
	10ml	G8091
	100ml	G8092
Caspase-Glo® 8 Assay	2.5ml	G8200
	10ml	G8201
	100ml	G8202
Caspase-Glo® 9 Assay	2.5ml	G8210
	10ml	G8211
	100ml	G8212
CaspACE™ Assay System, Colorimetric	50 assays	G7351
	100 assays	G7220
DeadEnd™ Fluorometric TUNEL System	60 reactions	G3250
DeadEnd™ Colorimetric TUNEL System	40 reactions	G7130
	20 reactions	G7360

Apoptosis Reagents

Product	Size	Cat.#
CaspACE™ FITC-VAD-FMK In Situ Marker	50µl	G7461
	125µl	G7462
Anti-ACTIVE® Caspase-3 pAb	50µl	G7481
Anti-Cytochrome c mAb	100µg	G7421
Anti-pS ⁴⁷³ Akt pAb	40µl	G7441
Anti-PARP p85 Fragment pAb	50µl	G7341
Caspase Inhibitor Z-VAD-FMK	125µl	G7232
	50µl	G7231
Caspase Inhibitor, Ac-DEVD-CHO	100µl	G5961



6. Related Products (continued)

Viability and Cytotoxicity Assay

Product	Size	Cat. #
MultiTox-Fluor Multiplex Cytotoxicity Assay	10ml	G9200
	5 × 10ml	G9201
(live/ dead cell protease activity determination)	2 × 50ml	G9202
CytoTox-Fluor™ Cytotoxicity Assay	10ml	G9260
	5 × 10ml	G9261
(dead cell protease activity determination)	2 × 50ml	G9262
MultiTox-Glo Multiplex Cytotoxicity Assay	10ml	G9270
	5 × 10ml	G9271
(live/ dead cell protease activity determination)	2 × 50ml	G9272

⁽⁴⁾The MTS tetrazolium compound is the subject of U.S. Pat. No. 5,185,450 assigned to the University of South Florida and is licensed exclusively to Promega Corporation.

© 1996-2012 Promega Corporation. All Rights Reserved.

Anti-ACTIVE, Apo-ONE, Caspase-Glo, CellTiter 96, CellTiter-Blue, CellTiter-Glo and CytoTox 96 are registered trademarks of Promega Corporation. CaspACE, CellTiter-Fluor, CytoTox-Fluor, CytoTox-Glo, CytoTox-ONE and DeadEnd are trademarks of Promega Corporation.

Products may be covered by pending or issued patents or may have certain limitations. Please visit our Web site for more information.

NEN is a registered trademark of NEN Life Science Products, Inc.

All prices and specifications are subject to change without prior notice.

Product claims are subject to change. Please contact Promega Technical Services or access the Promega online catalog for the most up-to-date information on Promega products.

Promega Corporation · 2800 Woods Hollow Road · Madison, WI 53711-5399 USA
 Toll Free in USA 800-356-9526 · Phone 608-274-4330 · Fax 608-277-2516 · www.promega.com
 Part# TB245 Printed in USA.
 Page 12 Revised 12/12

Annex 5 - Process Runsheet for the fabrication of Silver Microneedles

#	TECHNIQUE	D	E	P	EQUIPMENT	MATERIAL	THICK	F	B
<u>WORKING ELECTRODE PATTERNING</u>									
01	<u>Wafer dicing</u> Into ¼ of a 6" Silicon wafer			X	—				
02	<u>PVD – Magnetron Sputtering</u> Mask layer for step #09	X			Alcatel	SiO ₂	3000 Å	X	
03	<u>PVD – Magnetron Sputtering</u> Electric contact for step #15	X			Alcatel	Cr	3000 Å		X
04	<u>DWL – Lithography</u> Definition of Chromium pattern			X	DWL	PFR 9950 G +PR	1.4 µm		X
05	<u>Chromium Wet etching</u> Patterning of Chromium layer		X		Wet bench	Cr etchant	3000 Å		X
06	<u>PVD – Magnetron Sputtering</u> Protection from step #09	X			Alcatel	SiO ₂	6000 Å		X
<u>PROFILE DEFINITION</u>									
07	<u>DWL – Lithography</u> Patterning for step #09			X	DWL	PFR 9950 G +PR	1.4 µm	X	
08	<u>RIE</u> Mask definition for step #09		X		LAM	SiO ₂	3000 Å		X
09	<u>Silicon Wet etching</u> Patterning of inverted pyramids		X		Wet bench	KOH solution	5 µm	X	
10	<u>PVD – Magnetron Sputtering</u> Stop current leakage on step #15	X			UHV 2	Al ₂ O ₃	3000 Å		X
11	<u>DWL – Lithography</u> Create pads for step #15			X	DWL	PFR 9950 G +PR	1.4 µm		X
12	<u>RIE – Vias etching</u> Open vias for pads for step #15		X		LAM	SiO ₂	6000 Å		X
13	<u>DWL – Lithography</u> Thick PR to define needle height			X	DWL	ma-P 1275 +PR	8 µm	X	

#	TECHNIQUE	D	E	P	EQUIPMENT	MATERIAL	THICK	F	B
<u>SILVER PLATING</u>									
14	<u>Wafer dicing</u> Into individual dies for process			X	Dicing Saw				
15	<u>Silver Electrodeposition</u> Create "solid-state Ag needles"	X			Electroplating Setup	AgNO ₃ solution	15 μm	X	
<u>CONTACT PATTERNING</u>									
16	<u>PVD – Magnetron Sputtering</u> Insulation + protect from chemical attacks	X			Alcatel	SiO ₂	3000 Å	X	
17	<u>DWL – Lithography</u> Create access to needles and pads			X	DWL	PFR 9950 G +PR	1.4 μm	X	
18	<u>RIE – Vias etching</u> Open vias for needs and pads		X		LAM	SiO ₂	3000 Å	X	
19	<u>PVD – Magnetron Sputtering</u> Deposit Al for electrical contact	X			N7000	Al	3000 Å	X	
20	<u>DWL – Lithography</u> Define Patterning for step #23			X	DWL	PFR 9950 G +PR	1.4 μm	X	
21	<u>Aluminum Wet Etching</u> Pattern Al layer		X		Wet bench	Al etchant	3000 Å	X	
22	<u>PVD – Magnetron Sputtering</u> Final electrical insulation	X			Alcatel	SiO ₂	3000 Å	X	
<u>STRUCTURE RELEASE AND ACTIVATION</u>									
23	<u>PDMS pouring and baking</u> To allow for step #26	X			Hot plate	PDMS	N/A	X	
24	<u>Structure Release</u> Detach the structures from the Si substrate			X	Wet bench	Acetone	N/A	X	
25	<u>pH sensitive layer deposition</u> Deposit pH sensitive layer over needles	X			T.B.D.	T.B.D.	T.B.D.	X	

RUN SHEET – Ag μ-NEEDLES FOR PH ANALYSIS

RESPONSIBLE: TIAGO ALEXANDRE DA SILVA MONTEIRO

Sample ID: _____

STEP 1 - Wafer Dicing

Date: ___/___/___	Operator: _____
Machine: none	
Pre-Treatment: none	
<p>INSTRUCTIONS: Using a diamond tip, cleave the wafer into 4 identical quarters using the wafer flat as a guideline to create parallel and perpendicular cuts.</p>	
Observations: _____	

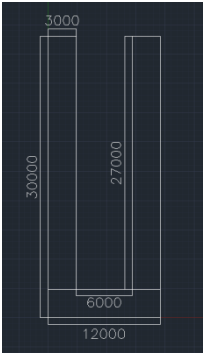
STEP 2 - Silicon Oxide deposition: SiO₂ 3000 Å

Date: ___/___/___	Operator: _____		
Machine: Alcatel (Magnetron Sputtering)			
Pre-Treatment: Blow-dry			
Material deposited: Silicon Oxide 3000 Å			
Conditions	Experimental	Aimed	
Chamber pressure before deposition	Torr	1x10 ⁻⁶	Torr
Chamber pressure during deposition	Torr	2x10 ⁻³	Torr
RF Power	W	140	W
Φ _s	sccm	20	sccm
Rotation	rpm	4	rpm
Time	min		min
Observations: _____			

STEP 3 - Chromium deposition: Cr 3000 Å (BACK SIDE)

Date: ___/___/___	Operator: _____		
Machine: Alcatel (Magnetron Sputtering)			
Pre-Treatment: Blow-dry			
Magnetron Sputtering: Yes			
Material deposited: Chromium 3000 Å			
Conditions	Experimental	Aimed	
Chamber pressure before deposition	Torr	1x10 ⁻⁶	Torr
Chamber pressure during deposition	Torr	2x10 ⁻³	Torr
DC Power	W	20	W
Φ _s	sccm	20	sccm
Rotation	rpm	0	rpm
Time	min		min
Observations: _____			

STEP 4 - Lithography patterning for backside contacts (BACK SIDE)

Date: ___/___/___	Operator: _____
Machine: DWL	
Photoresist coating conditions:	
Photoresist: PFR 7790 G	Recipe: 6/2
Step #1: time <u>5</u> s at speed <u>800</u> rpm with acceleration <u>500</u> rpm/s	Thickness: 1.3 μm
Step #2: time <u>40</u> s at speed <u>2800</u> rpm with acceleration <u>500</u> rpm/s	
Bake temperature: 85 °C for 60 sec	
Exposing Conditions:	
Mask dimensions: [X: 12'000; Y: 30'000] μm	
Dies dimensions: [X: 12'000; Y: 30'000] μm	
Map name: Arraytm1	Mask name: TMpH_backcontact.dxf
Layer: SV	Alignment: none
	Pattern: non-inverted
 INSTRUCTIONS: Align sample from the flat and move to the bottom-left corner . From that position, move the plate in the following directions: X: 5'000 μm; Y: 5'000. Set (0,0) and start exposure.	
 NOTE: Resist will remain OUTSIDE.	
	<p>DWL Energy: ____</p> <p>DWL Focus: ____</p> <p>Developer: TMA 238 WA</p> <p>Development: Recipe: 6/2</p> <p style="padding-left: 20px;">Baking: 110 °C for 60 sec</p> <p style="padding-left: 20px;">Cooling: 30 sec</p> <p style="padding-left: 20px;">Development: 60 sec</p> <p style="padding-left: 20px;">Rinse: 15 sec</p> <p style="padding-left: 20px;">Spin: 30 sec</p>
Observations:	

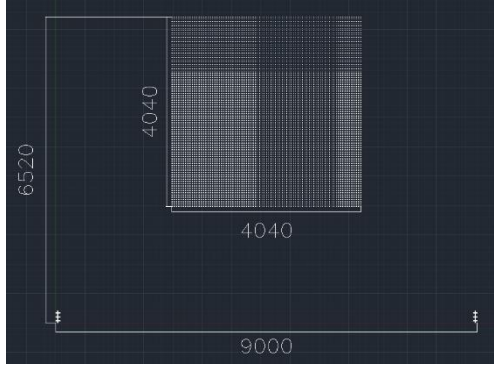
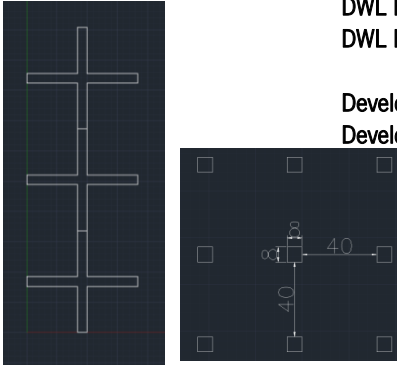
STEP 5 - Chromium etching

Date: ___/___/___	Operator: _____
Machine: Wet bench	
Pre-Treatment: Blow-dry	
Material Etched: Chromium 3000 Å	
 INSTRUCTIONS: Insert sample inside beaker containing Chromium Etchant solution. Apply mechanical agitation until pattern is completely revealed. Wash with IPA and water. After the process is completed, remove the Photoresist with Acetone and clean with IPA and water once again.	
Observations:	

STEP 6 - Silicon Oxide deposition: SiO₂ 6000 Å (BACK SIDE)

Date: ___/___/___		Operator: _____		
Machine: Alcatel (Magnetron Sputtering)				
Pre-Treatment: Blow-dry				
Material deposited: Silicon Oxide 3000 Å				
Conditions	Experimental		Aimed	
Chamber pressure before deposition		Torr	1x10 ⁶	Torr
Chamber pressure during deposition		Torr	2x10 ³	Torr
RF Power		W	140	W
φ _s		sccm	20	sccm
Rotation		rpm	4	rpm
Time		min		min
Observations:				

STEP 7 - Lithography patterning for Silicon wet etching process

Date: ___/___/___		Operator: _____		
Machine: DWL				
Photoresist coating conditions:				
Photoresist: PFR 7790 G		Recipe: 6/2		Thickness: 1.3 μm
Step #1: time <u>5</u> s at speed <u>800</u> rpm with acceleration <u>500</u> rpm/s				
Step #2: time <u>40</u> s at speed <u>2800</u> rpm with acceleration <u>500</u> rpm/s				
Bake temperature: 85 °C for 60 sec				
Exposing Conditions:				
Mask dimensions: [X: 9'000; Y: 6'520] μm				
Dies dimensions: [X: 12'000; Y: 30'000] μm				
Map name: Arraytm2		Mask name: TMpH_holes.dxf		Pattern: non-inverted
Layer: LINHAS		Alignment: none		
INSTRUCTIONS: Align sample from the flat and move to the bottom-right corner . From that position, move the plate in the following directions: X: -15'500 μm; Y: 6'500. Set (0,0). Then, move the plate in the X-direction as many dies as to be exposed, minus one (X: 4 x -12'000 for a total of 5 dies) and start exposure.				
NOTE: overall die layout (left image) and detail profile (right). Resist will remain OUTSIDE.				
				
Observations:		Developer: TMA 238 WA		
		Development: Recipe: 6/2		
_____		Baking: 110 °C for 60 sec		
		Cooling: 30 sec		
		Development: 60 sec		
		Rinse: 15 sec		
_____		Spin: 30 sec		

STEP 8 - Vias etching: SiO₂ ~3000 Å

Date: ___/___/___		Operator: _____		
Machine: LAM				
Pre-Treatment: Blow-dry				
Material Etched: Silicon Oxide 3000 Å		Recipe: <u>low power no O2</u>		
Conditions	Experimental	Aimed		
Chamber pressure during deposition	Torr	1,40x10 ⁻¹	Torr	
Wafer area pressure	Torr	3,05x10 ⁻¹	Torr	
Power	W	100	W	
Φ_{Ar}	sccm	200	Sccm	
Φ_{CF_4}	sccm	100	sccm	
Φ_{O_2}	sccm	10	sccm	
Etching Rate	Å/sec	20	Å/sec	
Time	sec		sec	
Observations: _____ _____				

STEP 9 - Silicon Wet Etching (KOH)

Date: ___/___/___		Operator: _____		
Machine: Wet-bench				
Pre-Treatment: Remove any existent Photoresist. Apply sample inside BOE solution for 1 min with agitation.				
Material Etched: Silicon				
INSTRUCTIONS:				
#1 - Turn on and Pre-heat and the Ultrasonic bath to the desired temperature. #2 - Insert a HDPE container with KOH solution inside the US bath and wait for thermal stabilization. #3 - Add the desired IPA volume inside the container immediately before inserting the sample inside. #4 - Insert the sample inside the KOH bath and time the process. #5 - Remove the sample and wash it thoroughly with DI water. #6 - Perform microscopic inspection and, if necessary, repeat steps #4 to #6.				
KOH Solution: ___ %				
Conditions:				
Test sample #	V _{KOH} (mL)	V _{IPA} (mL)	Temperature (°C)	Time (min)
Aim parameters				
Observations: _____ _____				

STEP 10 - Alumina deposition: Al2O3 2000 Å (BACK SIDE)

Date: ___/___/___	Operator: _____
-------------------	-----------------

Machine: UHV-2
Pre-Treatment: Blow-dry
Material deposited: Alumina 2000 Å

Conditions	Experimental	Aimed
Chamber pressure before deposition	Torr	Torr
Chamber pressure during deposition	Torr	Torr
RF Power	W	W
ϕ_s	sccm	sccm
Rotation	rpm	rpm
Time	min	min

NOTE: Place a piece of glass on top of the sample in order to protect the Pads area from being covered with Alumina. This will prevent an unnecessary Alumina etching process in Step #12. The glass should cover only the area delimited, as it will not be in contact with the electrodeposition solution. The remaining sample should be coated as to prevent electrical flow of current through the damaged SiO₂ layer.

Observations:

STEP 11 - Lithography patterning for backside Vias opening (BACK SIDE)

Date: ___/___/___

Operator: _____

Machine: DWL

Photoresist coating conditions:

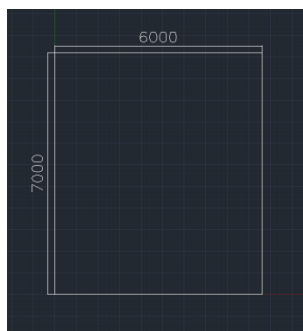
Photoresist: PFR 7790 G Recipe: 6/2 Thickness: 1.3 µm
 Step #1: time 5 s at speed 800 rpm with acceleration 50 rpm/s
 Step #2: time 40 s at speed 2800 rpm with acceleration 50 rpm/s
 Bake temperature: 85 °C for 60 sec

Exposing Conditions:

Mask dimensions: [X: 6'000; Y: 7'000] µm
Dies dimensions: [X: 12'000; Y: 30'000] µm
Map name: Arraytm3 **Mask name:** TMpH_backvias.dxf
Layer: SV **Alignment:** none **Pattern:** non-inverted

INSTRUCTIONS: Align sample from the flat and move to the **bottom-left corner**. From that position, move the plate in the following directions: X: 8'000 µm; Y: 28'000. Set (0,0) and start exposure.

NOTE: Resist will remain **OUTSIDE**.



DWL Energy: ____

DWL Focus: ____

Developer: TMA 238 WA

Development: Recipe: 6/2

Observations:

STEP 12 - Vias etching: SiO₂ ~ 3000 Å (BACK SIDE)

Date: ___/___/___

Operator: _____

Machine: LAM

Pre-Treatment: Blow-dry

Material Etched: Silicon Oxide 3000 Å

Recipe: low power no O2

Conditions	Experimental	Aimed	
Chamber pressure during deposition	Torr	1,40x10 ⁻¹	Torr
Wafer area pressure	Torr	3,05x10 ⁻¹	Torr
Power	W	100	W
Φ_{Ar}	sccm	200	Sccm
Φ_{CF_4}	sccm	100	sccm
Φ_{O_2}	sccm	10	sccm
Etching Rate	Å/sec	20	Å/sec
Time	sec	150	sec

Observations:

STEP 15 - Silver electrodeposition: AgNO₃ electroplating solution

Date: ___/___/___

Operator: _____

Machine: Electrodeposition apparatus

Pre-Treatment: Remove surface oxide in BOE for 1 min with mechanical agitation and washing in DI water.

INSTRUCTIONS:

- #1 - Turn on the magnetic agitation and Pre-heat the electroplating solution to the desired temperature.
- #2 - Clean the Silver counter-electrode thoroughly with soft sand paper and DI water.
- #3 - Place the sample inside the PLA holder.
- #4 - Place the PLA holder and the Silver counter-electrode inside the PLA support system.
- #5 - Place the PLA support system inside the electroplating solution.
- #6 - Place a metallic tweezer directly above the sample and clamp it to the metallic support.
- #7 - Add both electrical wires to the top of the metallic tweezer (black) and counter-electrode (red).
- #8 - Turn on the power source and apply the desired current.
- #9 - Time the process.
- #10 - Turn off the power source, remove the electrical wires and the PLA support system.
- #11 - Remove all the components and clean them thoroughly with DI water

CAUTION!!!: Silver Nitrate stains both cloth and SKIN! Always use the necessary protective equipment!

Solution: 0.3M of AgNO₃ in 1M NH₃ (diluted in water)

Conditions:

Test sample #	Current (mA)	Agitation (rpm)	Temperature (°C)	Time (min)
Aim parameters				

Observations:

At this step, **microscopic inspection** and **profilometric measurements** are required to ensure that the electrodeposited Silver respects all conditions. The over-deposition of Silver should be limited to the minimum possible in order to prevent “*shading*” during the subsequent steps. All samples should be inspected for **electrodeposited clusters** that could appear due to improper electrical insulation. If that occurs, the deposition rate inside the pits will change, and thus, the process will not be homogeneous and replicable. A support for electrodeposition is available, or can be manufactured with PLA in the BQ Witbox 3D printer. A support system is currently available under the following names:

- **TMpH_e-platingsupport**
- **TMpH_e-platingadaptor**

STEP 16 - Passivation: SiO₂ 3000 Å

Date: ___/___/___		Operator: _____		
Machine: ALCATEL				
Pre-Treatment:		Place sample over hotplate at Room Temperature		
		Increase the temperature to 75 °C		
		Increase the temperature from 75 °C to 110 °C at a rate of ~2 °C.min ⁻¹		
		Allow the sample to cool down		
		Place the sample inside ALCATEL as soon as possible		
Magnetron Sputtering: Yes				
Material deposited: Silicon Oxide (3000 Å)				
Conditions		Experimental		Aimed
Chamber pressure before deposition			Torr	1,2x10 ⁶ Torr
Chamber pressure during deposition			Torr	2,9x10 ³ Torr
RF Power			W	140 W
φ _s			sccm	20 sccm
Rotation			rpm	4 rpm
Time			min	min
Observations:				

STEP 17 - Lithography patterning for Vias opening

Date: ___/___/___

Operator: _____

Machine: DWL

Photoresist coating conditions:

Photoresist: PFR 7790 G Recipe: 6/3 Thickness: 1.4 μm
 Step #1: time 5 s at speed 800 rpm with acceleration 500 rpm/s
 Step #2: time 40 s at speed 2800 rpm with acceleration 500 rpm/s
 Bake temperature: MANUAL - 65 °C for 180 sec

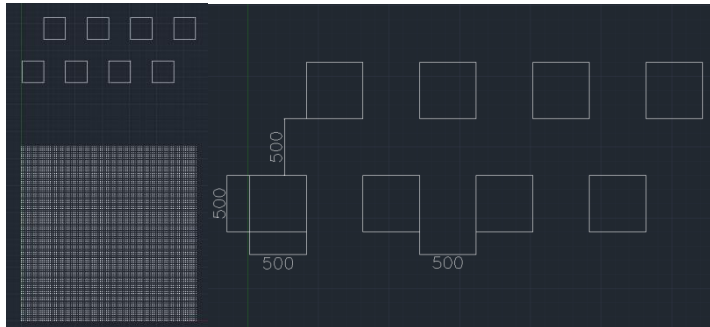
Mark #	Offsets	
	XX	YY
L-T	+ 2434	+ 2312
L-C	+ 2434	+ 2354
L-B	+ 2434	+ 2438
R-T	- 6474	+ 2312
R-C	- 6474	+ 2354
R-B	- 6474	+ 2438

Exposing Conditions:

Mask dimensions: [X: 4'000; Y: 7'000] μm
 Dies dimensions: [X: 12'000; Y: 30'000] μm
 Map name: Arraytm5 Mask name: TMpH_frontvias.dxf
 Layer: SV Alignment: alignment marks Pattern: non-inverted

INSTRUCTIONS: Align sample from the flat and move to the **bottom-right corner**. From that position, move the plate in the following directions: X: -15'500 μm; Y: 6'500. Set (0,0). Then, move the plate in the X-direction as many dies as to be exposed, minus one (X: 4 x -12'000 for a total of 5 dies). Proceed to a secondary alignment using the alignment marks created during the Silicon wet etch process. Mark the centre of any of the alignment marks, Set (0,0), compensate the offset and start exposure.

NOTE: overall die layout (left image) and detail profile (right). Resist will remain OUTSIDE.



DWL Energy: ____
 DWL Focus: ____

Developer: TMA 238 WA
 Development: **MANUAL DEVELOPMENT**
 Baking: @ 65 °C for 180 sec
 Cooling: until cold
 Development: 120 sec
 Rinse with DI water

Observations:

STEP 18 - Vias etching: SiO₂ ~ 3000 Å

Date: ___/___/___		Operator: _____		
Machine: LAM				
Pre-Treatment: Blow-dry				
Material Etched: Silicon Oxide 3000 Å		Recipe: low power no O2 25sec 6steps		
Conditions	Experimental	Aimed		
Chamber pressure during deposition	Torr	1,40x10 ⁻³	Torr	
Wafer area pressure	Torr	3,05x10 ⁻³	Torr	
Power	W	100	W	
Φ_{Ar}	sccm	200	Sccm	
Φ_{CF_4}	sccm	100	sccm	
Φ_{O_2}	sccm	10	sccm	
Etching Rate	Å/sec	20	Å/sec	
Time	sec	6 x 25	sec	
Cooling	sec	25	sec	
Cycles	#	8	#	
Observations: _____ _____				

STEP 19 - Metal deposition: Al 3000 Å

Date: ___/___/___		Operator: _____		
Machine: Nordiko 7000				
Magnetron Sputtering: Yes				
Material deposited: Aluminum 3000 Å (3x1000 Å)		Recipe: Al3000Å withcool		
Conditions	Experimental	Aimed		
Chamber pressure during deposition	Torr	3x10 ⁻³	Torr	
Φ_{Ar}	Sccm	50	sccm	
Power	kW	2,00	kW	
Current	A	5,12	A	
Voltage	V	400	V	
Deposition Rate	Å/sec	37,5	Å/sec	
Time	sec	27	sec	
Cooling	sec	150	sec	
Steps of Deposition	steps	3	steps	
Observations: _____ _____				

STEP 20 - Lithography patterning for Contact deposition

Date: ___/___/___

Operator: _____

Machine: DWL

Photoresist coating conditions:

Photoresist: PFR 7790 G Recipe: 6/3 Thickness: 1.4 μm
 Step #1: time 5 s at speed 800 rpm with acceleration 500 rpm/s
 Step #2: time 40 s at speed 2800 rpm with acceleration 500 rpm/s
 Bake temperature: **MANUAL - 65 °C for 180 sec**

Mark #	Offsets	
	XX	YY
L-T	+ 2434	+ 2312
L-C	+ 2434	+ 2354
L-B	+ 2434	+ 2438
R-T	- 6474	+ 2312
R-C	- 6474	+ 2354
R-B	- 6474	+ 2438

Exposing Conditions:

Mask dimensions: [X: 4'000; Y: 7'000] μm
 Dies dimensions: [X: 12'000; Y: 30'000] μm
 Map name: Arraytm6 Mask name: TMpH_frontcontact.dxf
 Layer: SV Alignment: alignment marks Pattern: inverted

INSTRUCTIONS: Align sample from the flat and move to the **bottom-right corner**. From that position, move the plate in the following directions: X: -15'500 μm; Y: 6'500. Set (0,0). Then, move the plate in the X-direction as many dies as to be exposed, minus one (X: 4 x -12'000 for a total of 5 dies). Proceed to a secondary alignment using the alignment marks created during the Silicon wet etch process. Mark the centre of any of the alignment marks, Set (0,0), compensate the offset and start exposure.

NOTE: overall die layout (left image) and detail profile (right). Resist will remain INSIDE.



DWL Energy: ___
 DWL Focus: ___

Developer: TMA 238 WA
 Development: **MANUAL DEVELOPMENT**
 Baking: @ 65 °C for 180 sec
 Cooling: until cold
 Development: 120 sec
 Rinse with DI water

Observations:

STEP 21 - Aluminum etching

Date: ___/___/___

Operator: _____

Machine: Wet bench

Pre-Treatment: Blow-dry

Material Etched: Aluminum 3000 Å

INSTRUCTIONS: Insert sample inside beaker containing Aluminum Etchant solution. Apply mechanical agitation until pattern is completely revealed. Wash with IPA and water. After the process is completed, remove the Photoresist with Acetone and clean with IPA and water once again.

Observations:

STEP 22 - Passivation: SiO₂ 3000 Å

Date: ___/___/___		Operator: _____		
Machine: Alcatel Pre-Treatment: Blow-dry Magnetron Sputtering: Yes Material deposited: Silicon Oxide (3000 Å)				
Conditions	Experimental		Aimed	
Chamber pressure before deposition		Torr	1,2x10 ⁶	Torr
Chamber pressure during deposition		Torr	2,9x10 ³	Torr
RF Power		W	140	W
φ _s		sccm	20	sccm
Rotation		rpm	4	rpm
Time		min		min
Observations: _____ _____ _____				

STEP 23 - PDMS pouring and baking

Date: ___/___/___		Operator: _____		
Machine: Hotplate Pre-Treatment: None				
PDMS preparation: Mix PDMS polymer with curing agent in a 10:1 ratio. Stir vigorously and leave it at the desiccator to remove all air bubbles.				
PDMS pouring: Spill a large amount of PDMS over a piece of Glass larger than the Si sample. Place the Si sample on top of the PDMS, facing it, and clamp both substrates.				
PDMS curing: Place both clamped substrates on the desiccator, for at least 4h. This will remove all air bubbles while starting the hardening process, effectively bonding both substrates into a single sample.				
PDMS baking: Remove the clamps from the sample and place it on top of a hotplate @ 60 °C overnight. The glass surface should be in contact with the hotplate as this will heat up (and bake) the PDMS more efficiently.				
Observations: _____ _____ _____				

STEP 24 - Structure release

Date: ___/___/___		Operator: _____		
Machine: Wet bench Pre-Treatment: None				
INSTRUCTIONS: With an X-ato, cut the excess PDMS surrounding the Si sample. Place the sample (Glass + Si) inside a container with Acetone, cover it with Parafilm, and apply Orbital agitation @ 200 rpm. Sample should detach completely after several hours. After release, the PDMS will contain all structures adhered to its surface. Clean the PDMS thoroughly with IPA and water to prevent corrosion due to the Acetone.				
Observations: _____ _____ _____				

STEP 25 - pH sensitive layer deposition

Date: ___/___/___

Operator: _____

Machine: IBD

Pre-Treatment: None

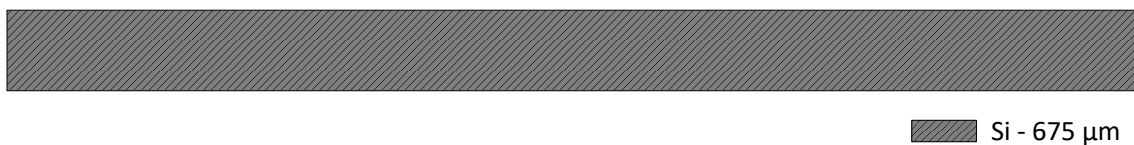
INSTRUCTIONS: (to be defined)

Observations:

Annex 6 - Process Diagram for the fabrication of Silver Microneedles

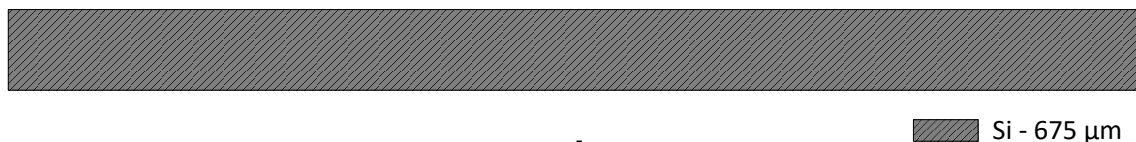
The following diagrams are purely schematic and representative. The overall dimensions are not to-scale as to allow for a better understanding of the process. The thickness of the layers is described in each legend, while the important dimensions of the profiles is depicted accordingly, and above said profiles. These diagrams are representative of the Process Runsheet for the fabrication of Silver Microneedles using a Through-Silicon-Electrodeposition process. Silicon Wafers (6 inch, {100}-oriented p-type) with no oxide barriers were used on this process.

STEP #01: Manual dicing the wafer into quarters, as both Chromium and Silicon Dioxide depositions at Alcatel are only possible with samples with the specific cut size

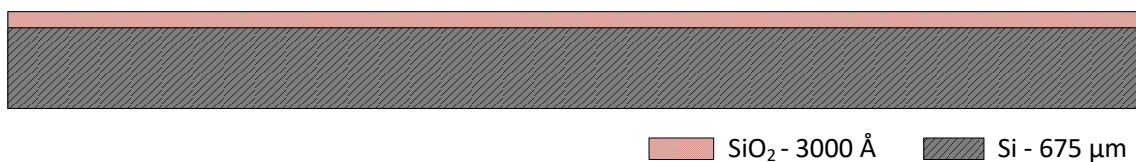


STEP #02: Silicon Dioxide deposition: SiO₂ 3000 Å

Protects the top surface from any kind of damage until it is ready to be processed. Will also act as a mask for the Silicon Wet etching process

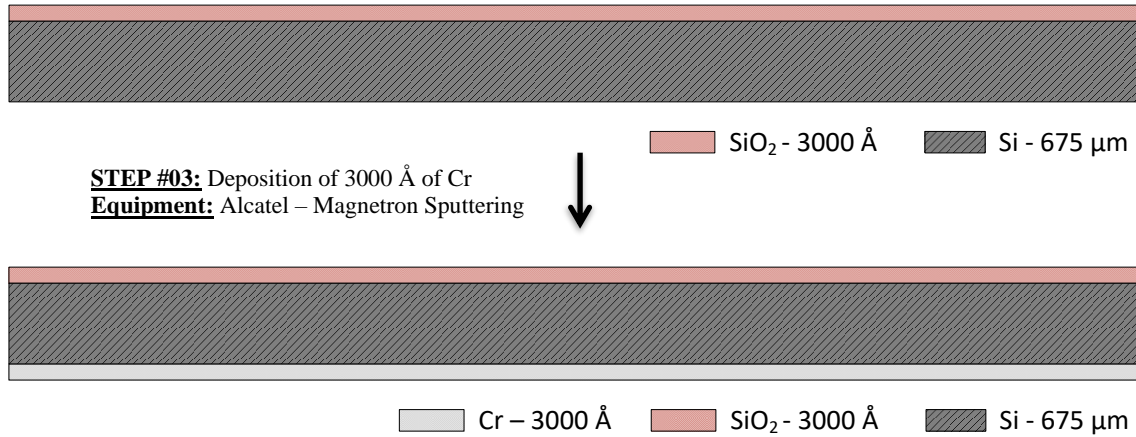


STEP #02: Deposition of 3000 Å of SiO₂
Equipment: Alcatel – Magnetron Sputtering



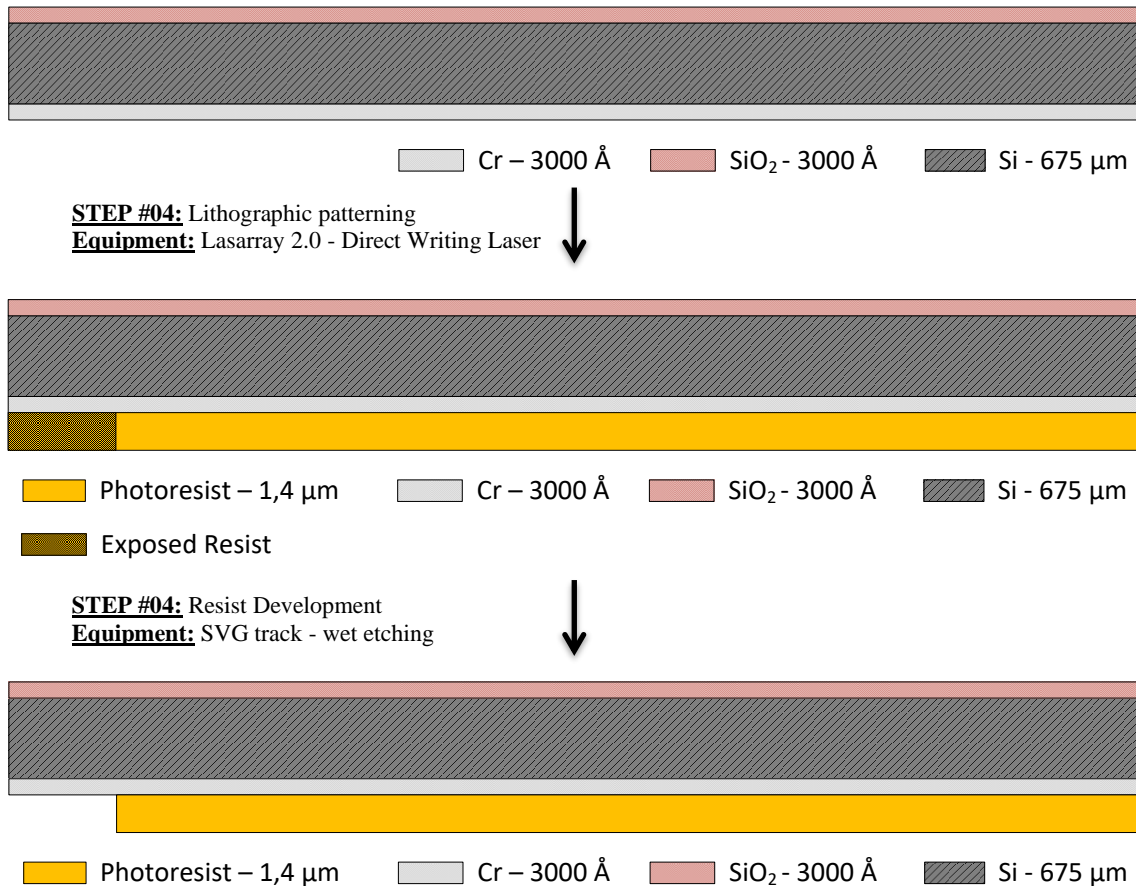
STEP 03: Chromium deposition: Cr 3000 Å (BACK SIDE)

Acts as a conductive layer to allow for the Through-Silicon-Electroplating. Chromium is one of the few metals that will withstand the KOH etching without damage.



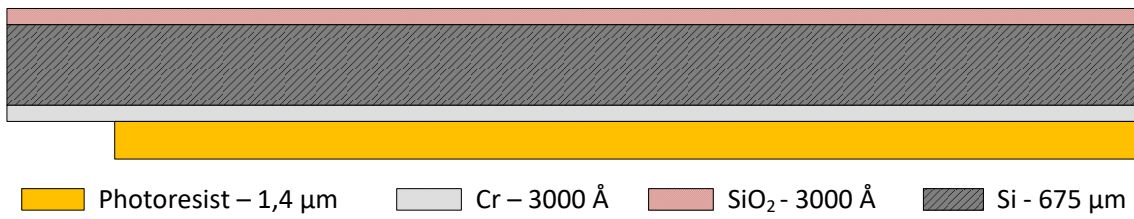
STEP 04: Lithography patterning for backside contacts (BACK SIDE)

Defines the zone where the contacts for the electrodeposition are settled. A safety margin in all 3 borders needs to be applied to prevent any current from leaking sideways.

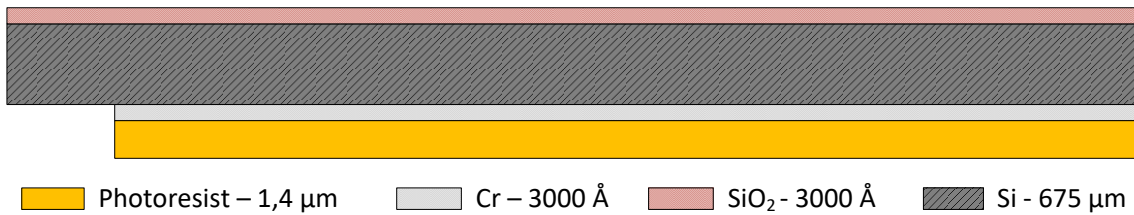


STEP 05: Chromium etching

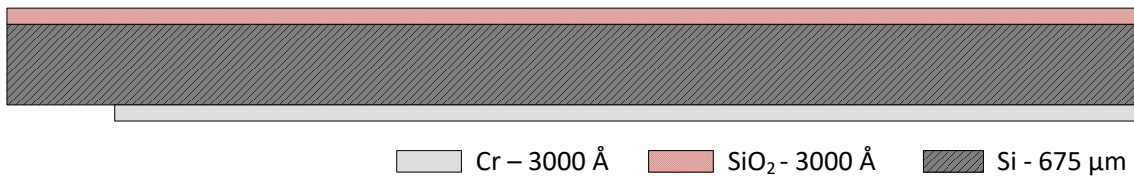
Transfers the pattern into the Chromium layer.



STEP #05: Chromium patterning
Equipment: Wet bench - wet etching

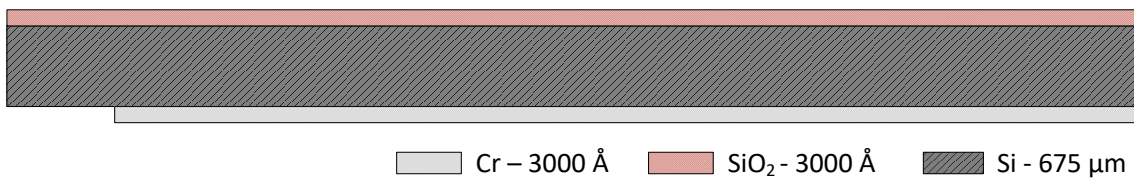


STEP #05: Resist stripping
Equipment: Wet bench - wet etching

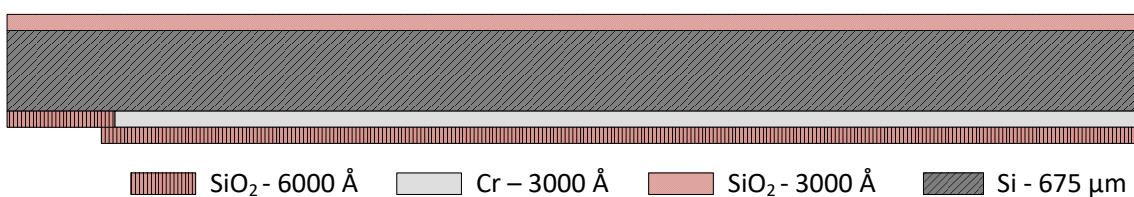


STEP 06: Silicon Nitride deposition: SiN 6000 Å (BACK SIDE)

Protects the sample back side from exposure to the KOH. Although Chromium is resistant to KOH, this step prevents any minor damage that could still occur.

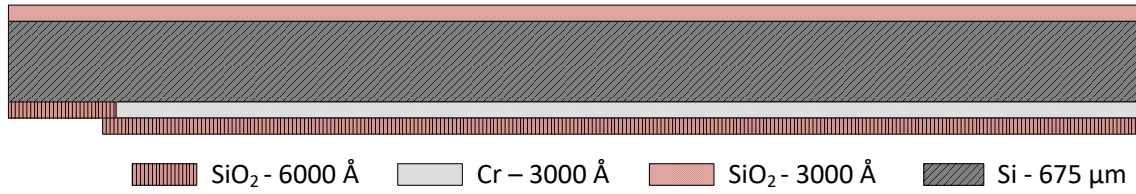


STEP #06: Deposition of 6000 Å of SiO₂
Equipment: Alcatel - Magnetron Sputtering

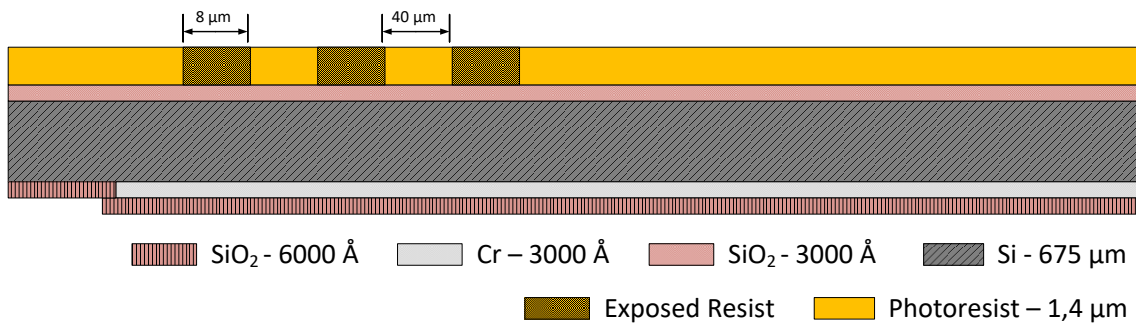


STEP 07: Lithography patterning for Silicon wet etching process

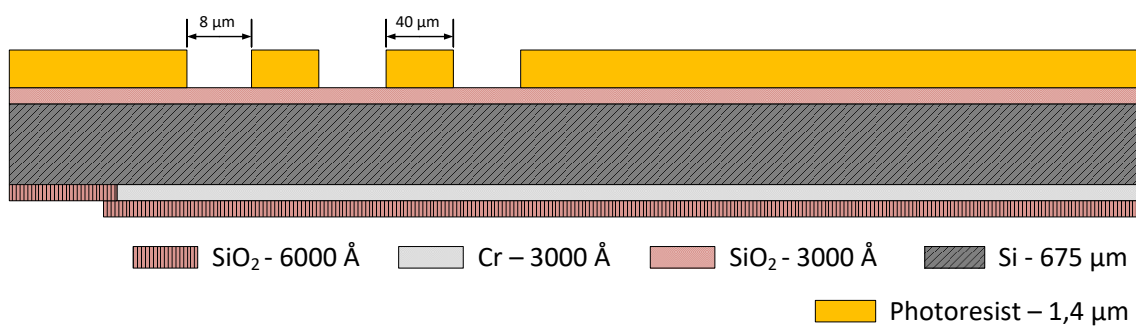
Defines the zone to be etched in the KOH process. Proper alignment with the backside Cr layer is required to ensure that a direct electrical pathway through the Si is possible.



STEP #07: Lithographic patterning
Equipment: Lasarray 2.0 - Direct Writing Laser

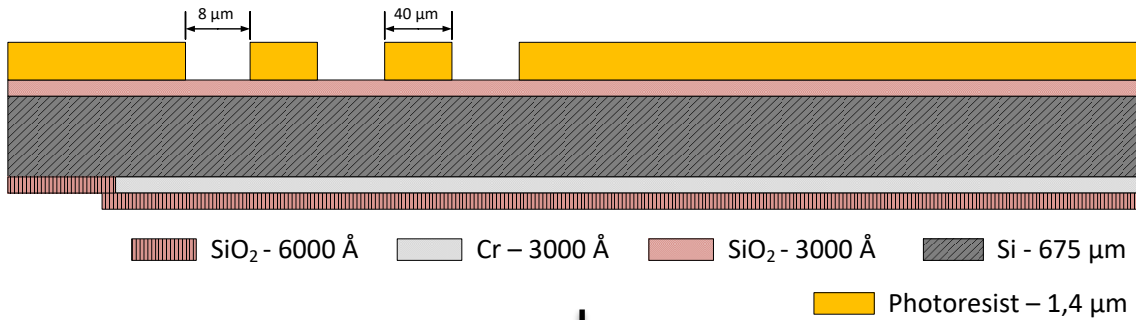


STEP #07: Resist Development
Equipment: SVG track - wet etching

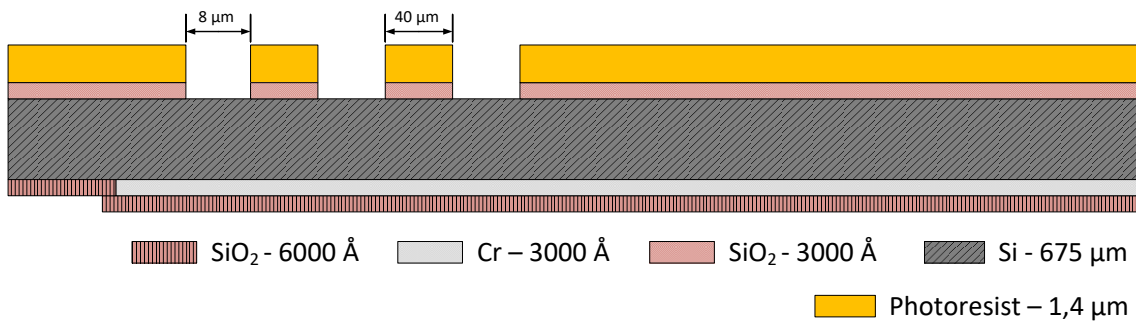


STEP 08: Vias etching - Silicon Nitride etch

Transfers the pattern into the Silicon Nitride layer, in order to allow access to the Silicon.

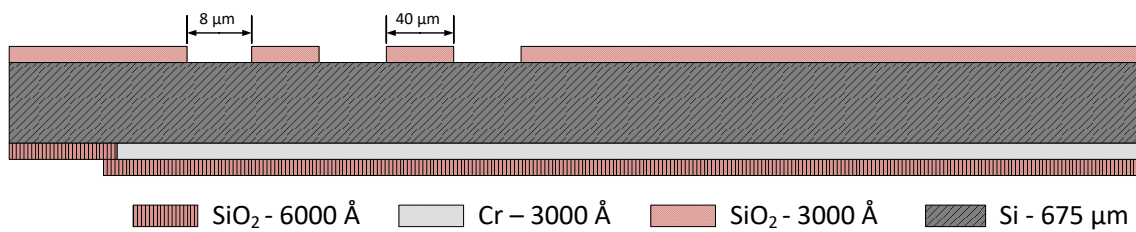


STEP #08: Silicon Dioxide patterning
Equipment: LAM - Reactive Ion Etching

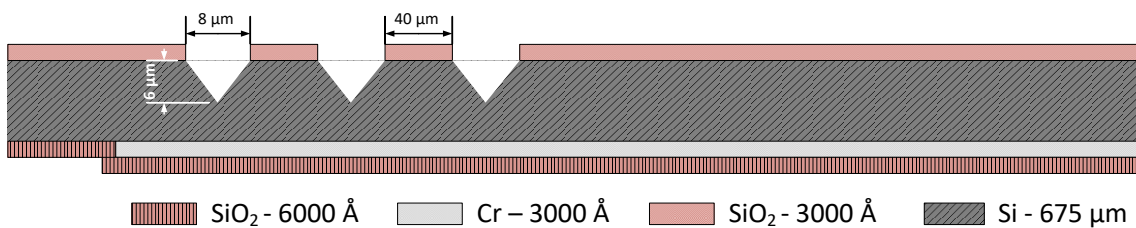


STEP 09: Silicon Wet Etching (KOH)

Patterns the Silicon wafer accordingly to the etching conditions. {100}-oriented Si wafer etching through KOH results in pyramidal structures with faces along with {111} surface.

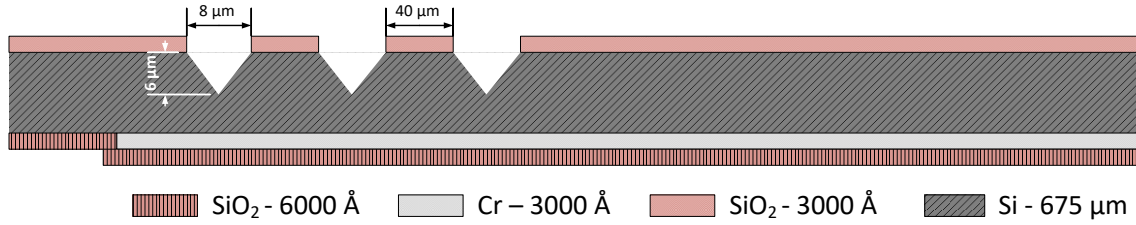


STEP #09: Silicon patterning
Equipment: Wet bench - KOH wet etching

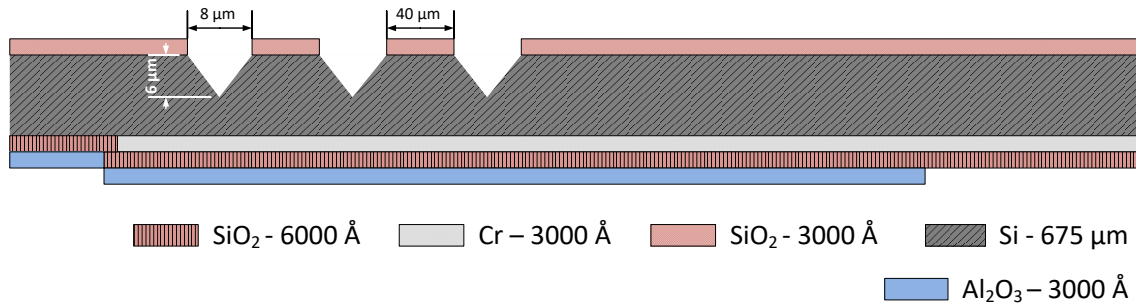


STEP 10: Alumina deposition: AlO_x 500 Å (BACK SIDE)

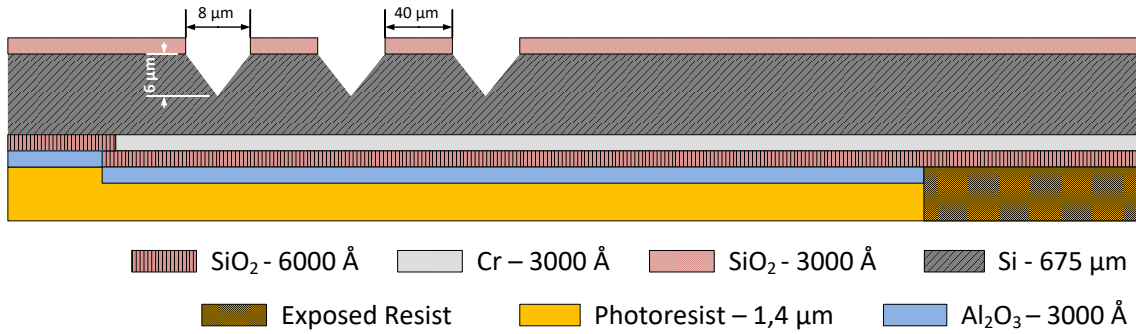
Grants a secondary electrical insulation later on the electrodeposition process and prevents any electrical current leakage to the backside, focusing it entirely in the etched pits.



STEP #10: Deposition of 3000 Å of Al_2O_3
Equipment: UHV 2 - Sputtering

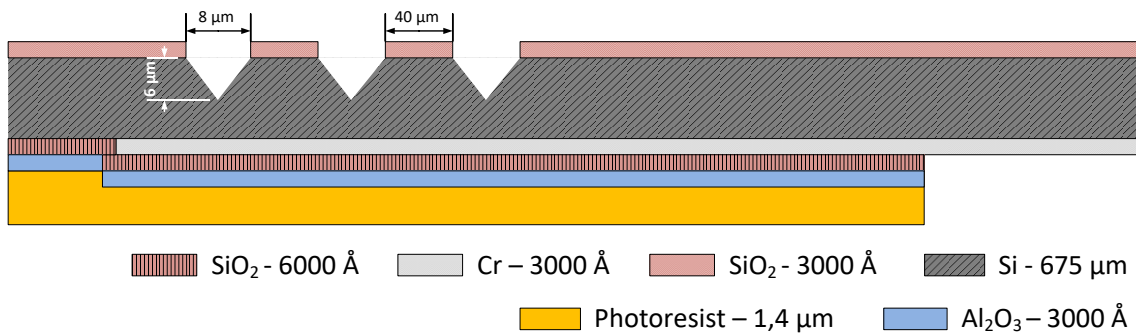


STEP 11 + 12 : Lithography patterning for backside Vias opening + Vias etching - Alumina and Silicon Nitride etch (BACK SIDE) - Allows for the electrical contact to be established during the electrodeposition step and transfers the pattern from STEP 11 into the insulator layers, allowing direct access to the Chromium layer.



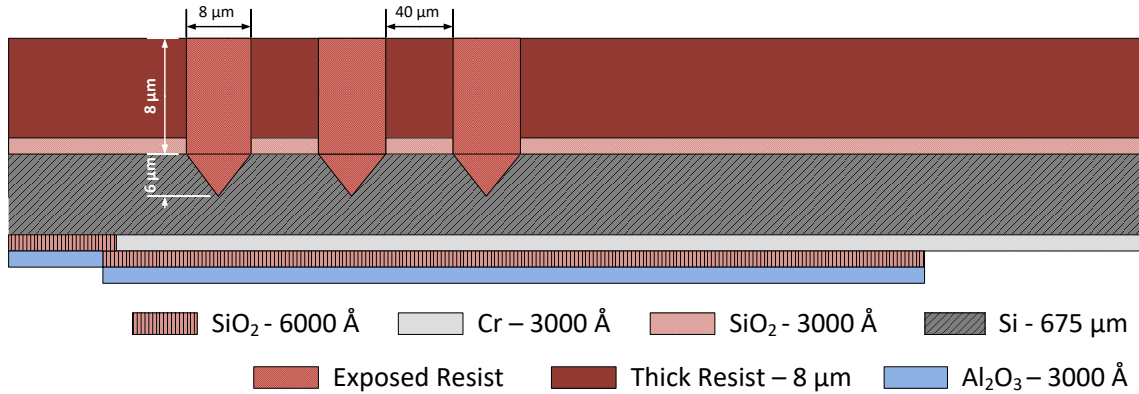
STEP #11/12: Lithographic Patterning + Vias Opening - SiO₂ patterning

Equipment: Lasaray 2.0 - Direct Writing Laser + LAM - Reactive Ion Etching

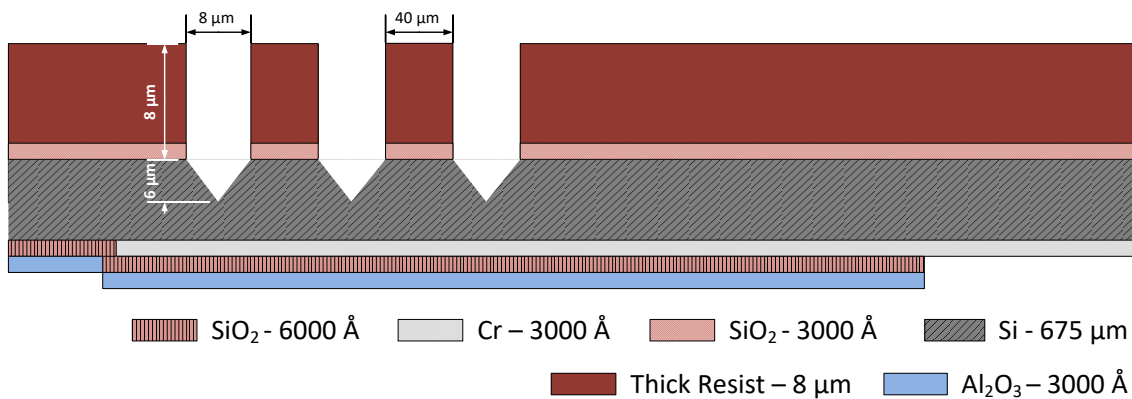


STEP 13: Lithography patterning for $\sim 5\mu\text{m}$ thick photoresist

A thicker Photoresist is used in this step to allow for a higher aspect-ratio $\mu\text{Needles}$. The patterned holes will later on be filled with Silver, thus acting as a mold.



STEP #13: Lithography patterning
Equipment: DWL

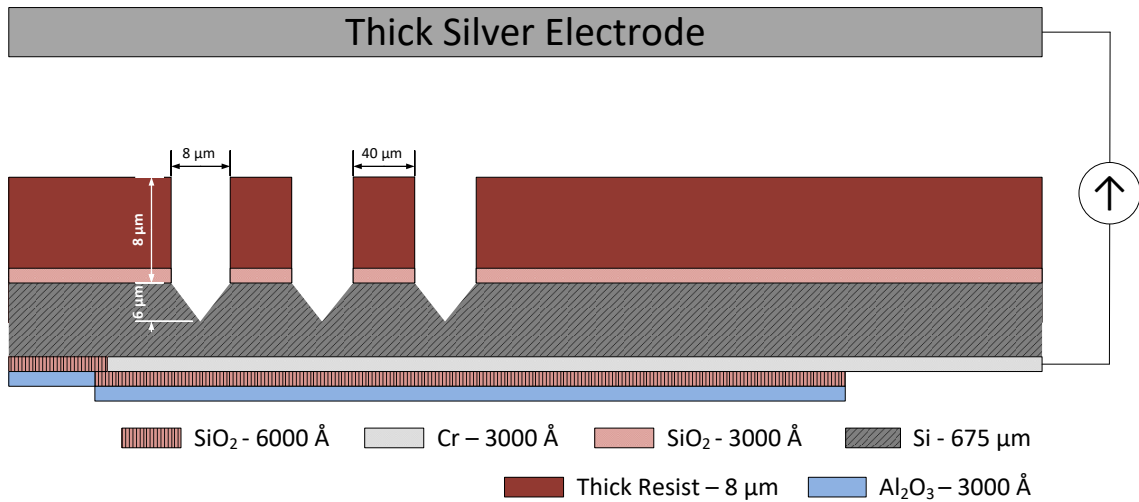


STEP 14: Sample dicing into individual dies

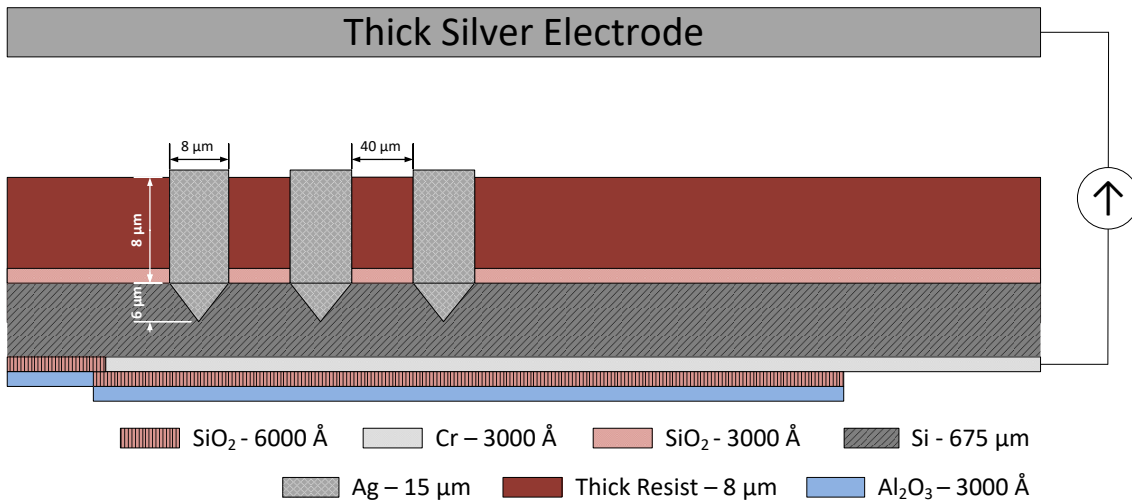
Individual dies are processed in this step forward to allow for specific electrodeposition conditions to be perfected. In a final and optimized device, such dicing could be performed only as the last step in the run sheet.

STEP 15: Silver electrodeposition: AgNO₃ electroplating solution

Electrodeposition is performed against a solid Silver electrode through the application of a constant current. The current is injected in the backside of the sample, travels through the Silicon wafer and is released at the bottom of the etched pits. The electrodeposition occurs against the walls of the pits, forming an Ag-layer that is only mildly adhered. The process continues until the patterned holes are covered.

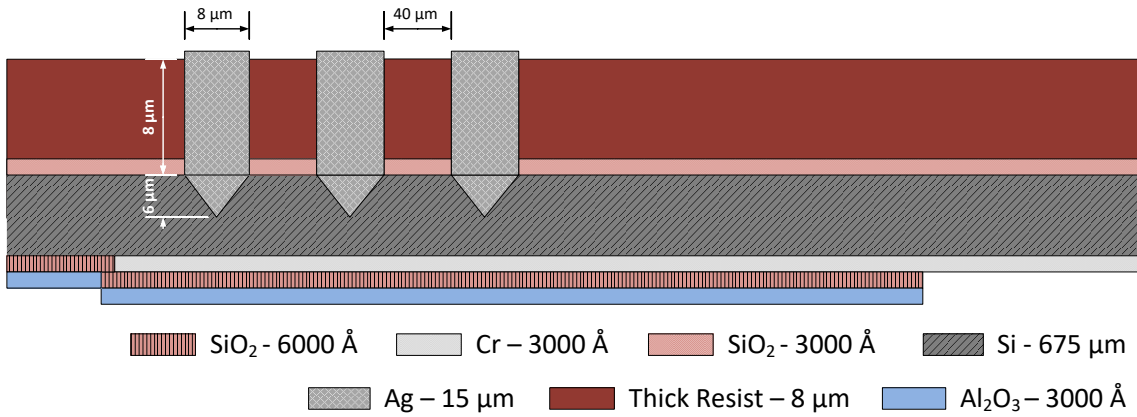


STEP #15: Silver electrodeposition
Equipment: Electrodeposition apparatus



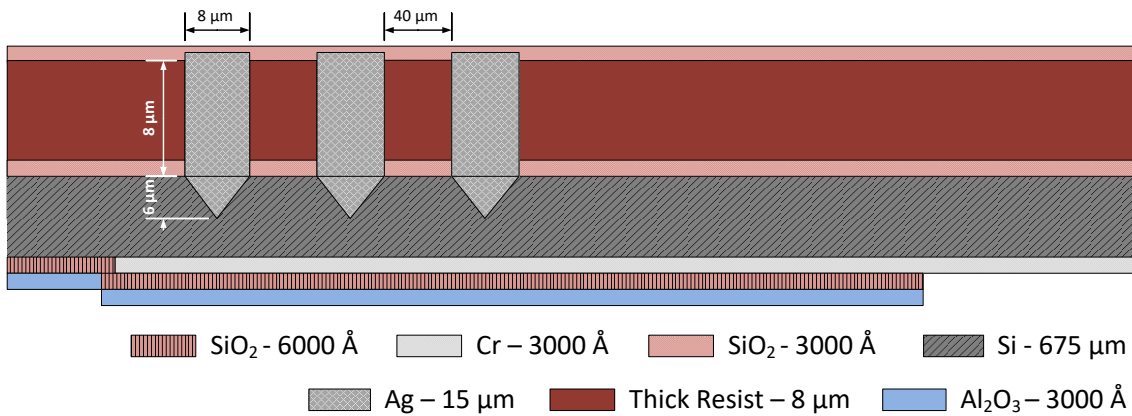
STEP 16: Passivation: SiO₂ 3000 Å

Creates a protective barrier once the device is completed that insulates the contacts.



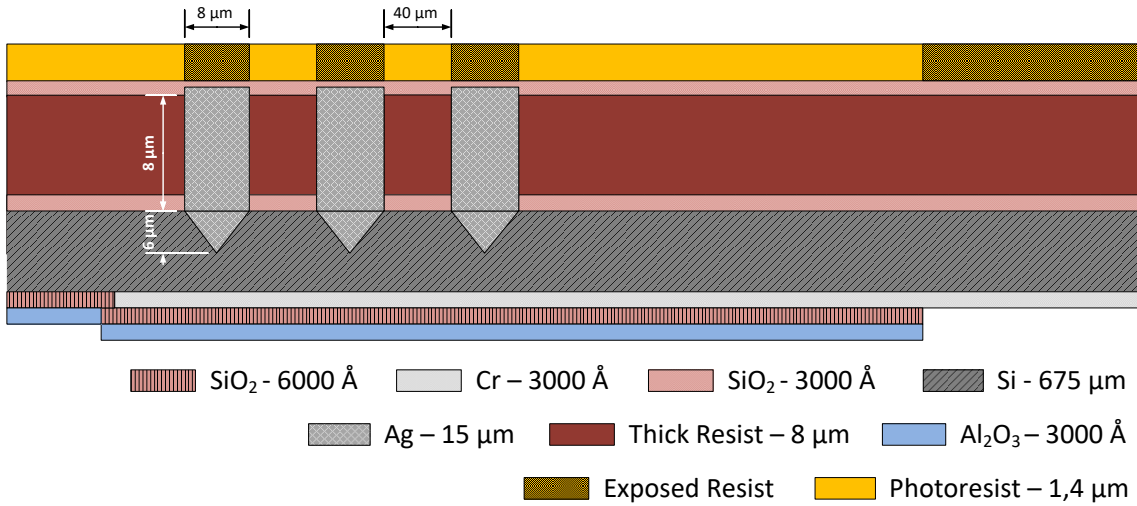
STEP #16: Passivation SiO₂

Equipment: Alcatel

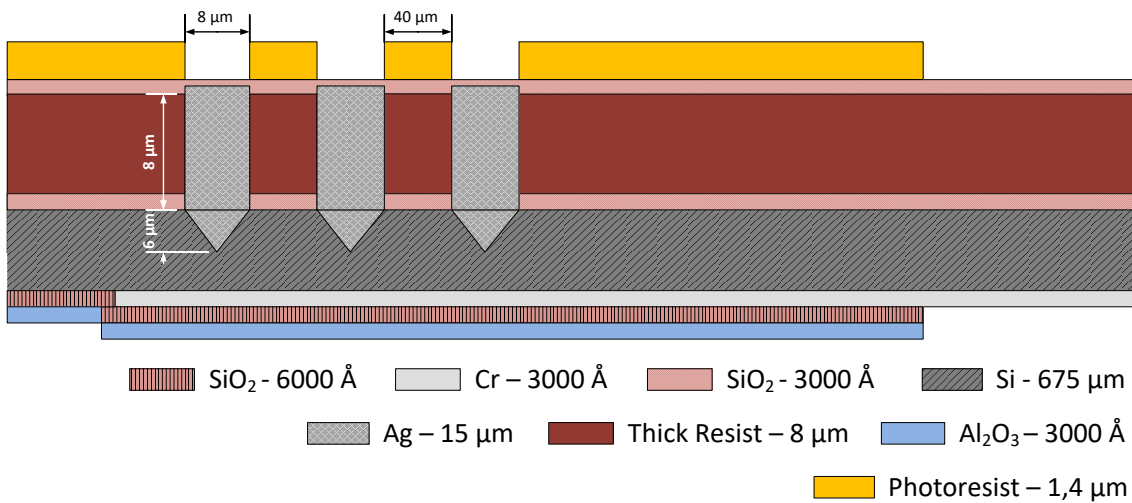


STEP 17: Lithography patterning for Vias opening

Opens Vias for the contacts to be deposited throughout the electrodeposited μ Needles. Opens an additional zone in the end of the sample for the contact Pads to be deposited.

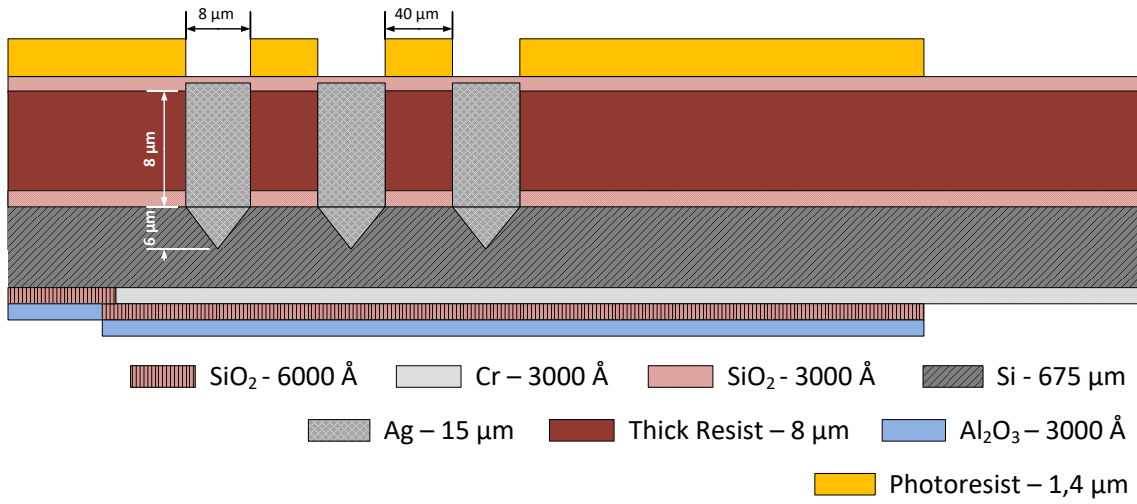


STEP #17: Lithography patterning
Equipment: DWL

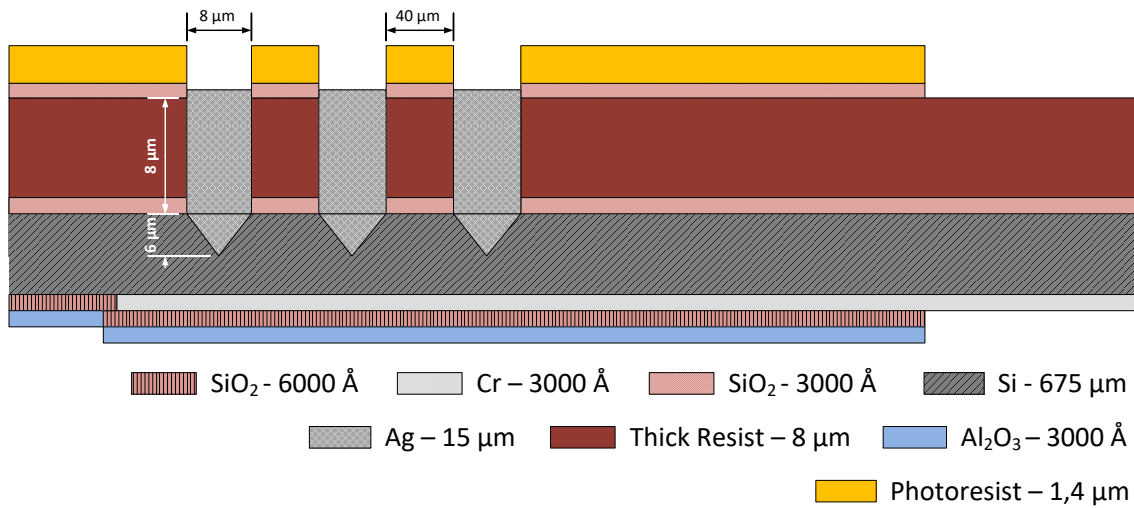


STEP 18: Vias etching - Silicon Oxide etch

Transfers the pattern to the Oxide layer.

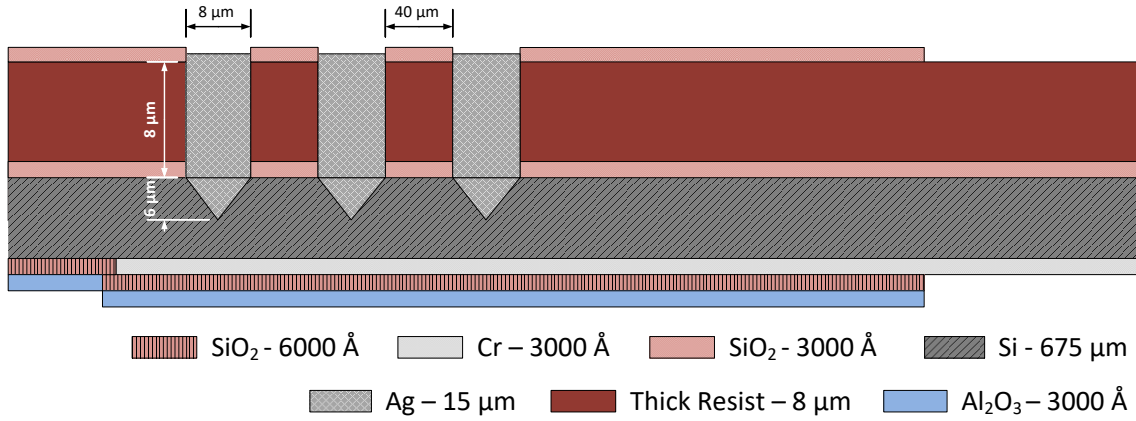


STEP #18: Vias etching
Equipment: LAM

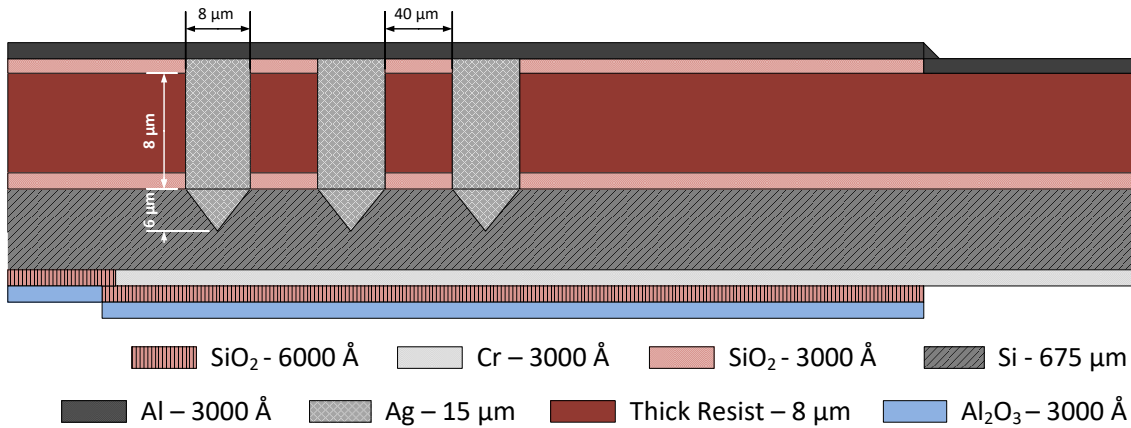


STEP 19: Contact deposition: Al 3000 Å

Deposits the desired metal to conduct the signal from the μ Needles to the Pads. If necessary, multiple μ Needles can be connected in series to increase the overall signal.

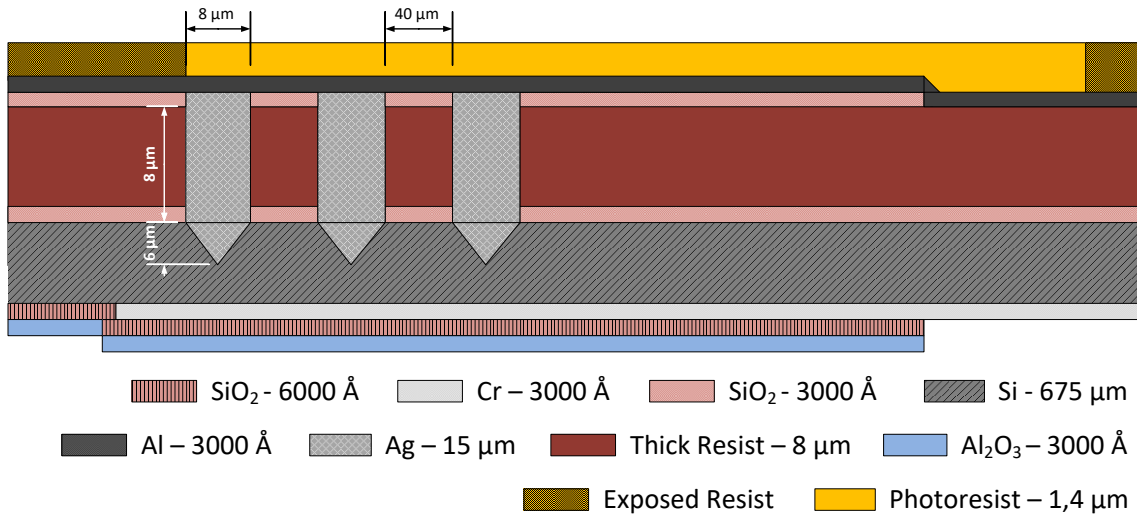


STEP #19: Contact deposition
Equipment: Nordiko 7000

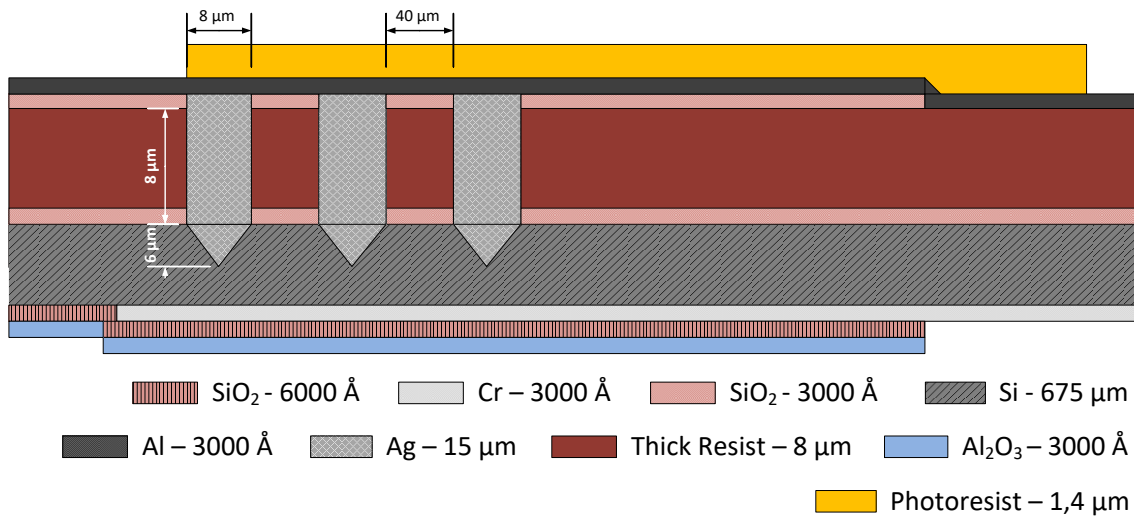


STEP 20: Lithography patterning for contact deposition

Creates the pattern for the metal lines and contact Pads to be deposited.

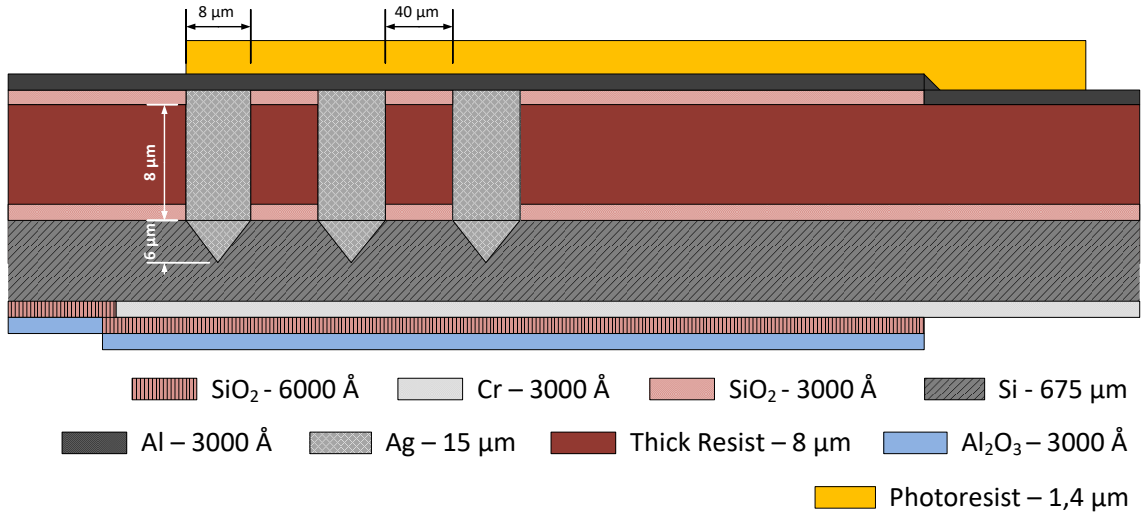


STEP #20: Lithography patterning
Equipment: DWL

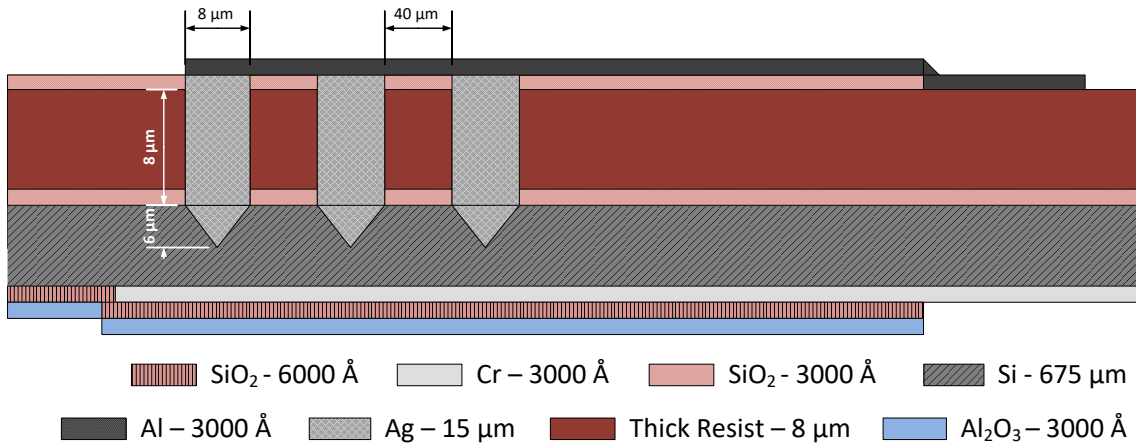


STEP 21: Aluminum Wet etching: Al 3000 Å

Transfers the pattern to the Aluminum layer through a chemical wet etch process that specifically targets Aluminum. Lift-off processes can't be used at this step as an alternative process as the underneath 5 µm-thick photoresist would be degraded as well.

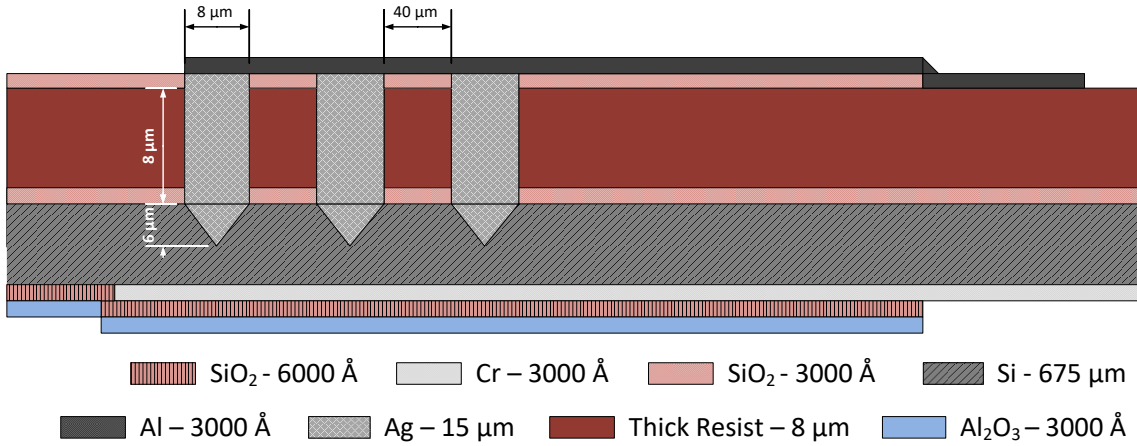


STEP #21: Aluminum Wet Etching
Equipment: Wet bench

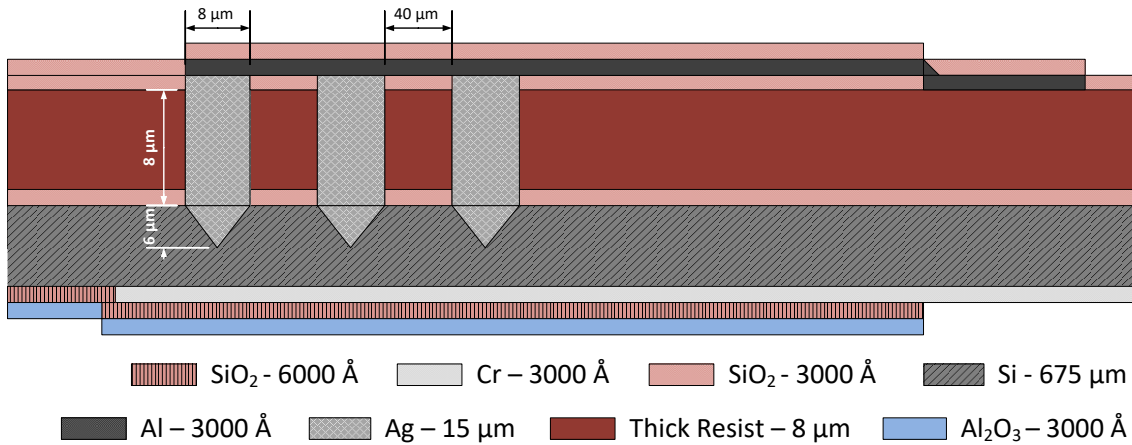


STEP 22: Passivation: SiO₂ 3000 Å

Protects the contact layers from Oxidation at the next steps.

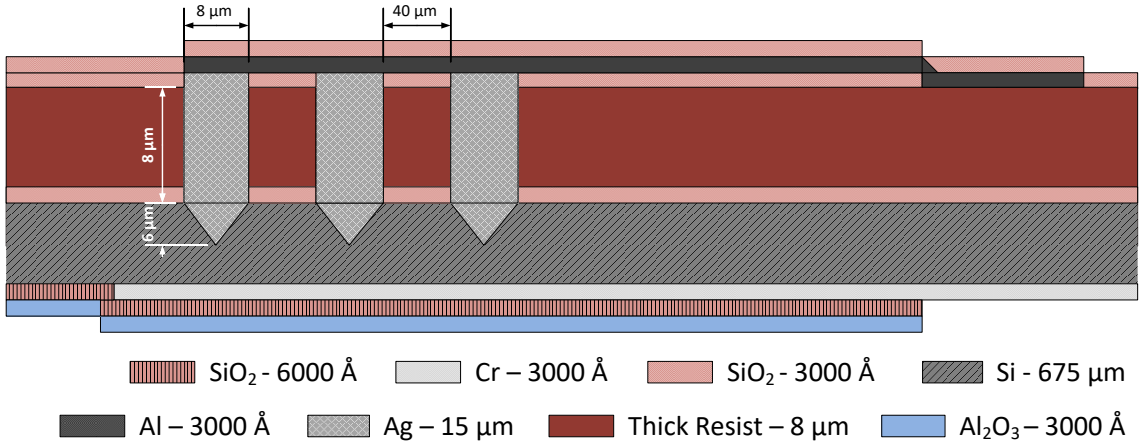


STEP #22: Passivation
Equipment: Alcatel



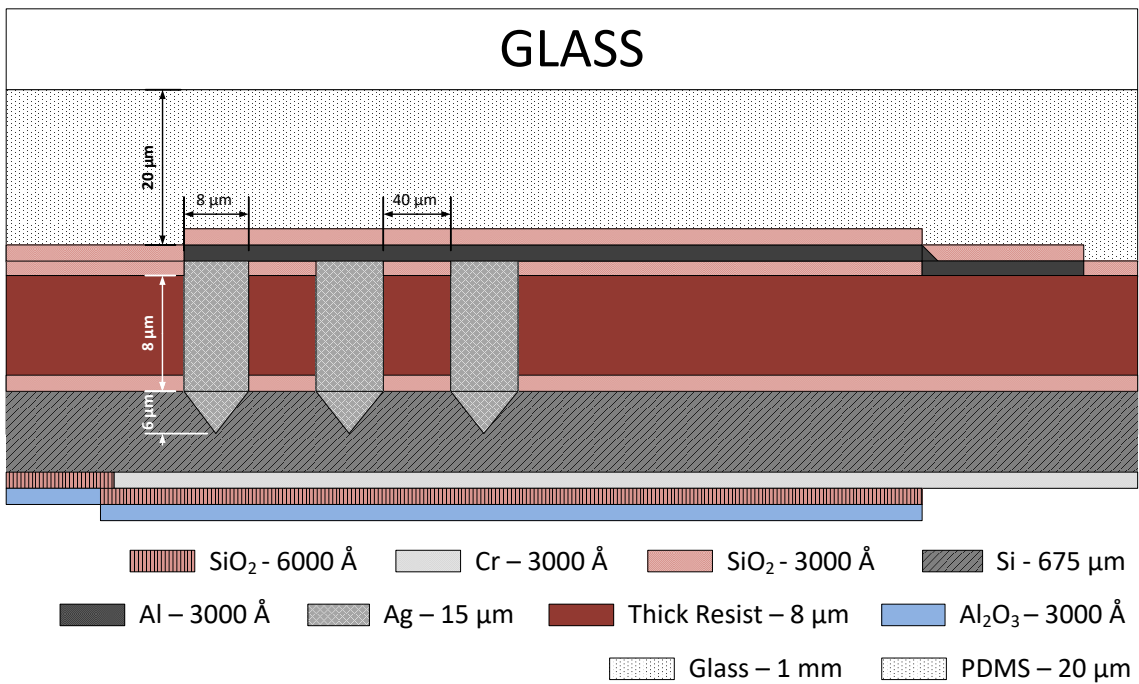
STEP 23: PDMS pouring and baking

Pouring PDMS on top of the sample, it will strongly adhere to the Oxide layer, and thus, to the rest of the structure.



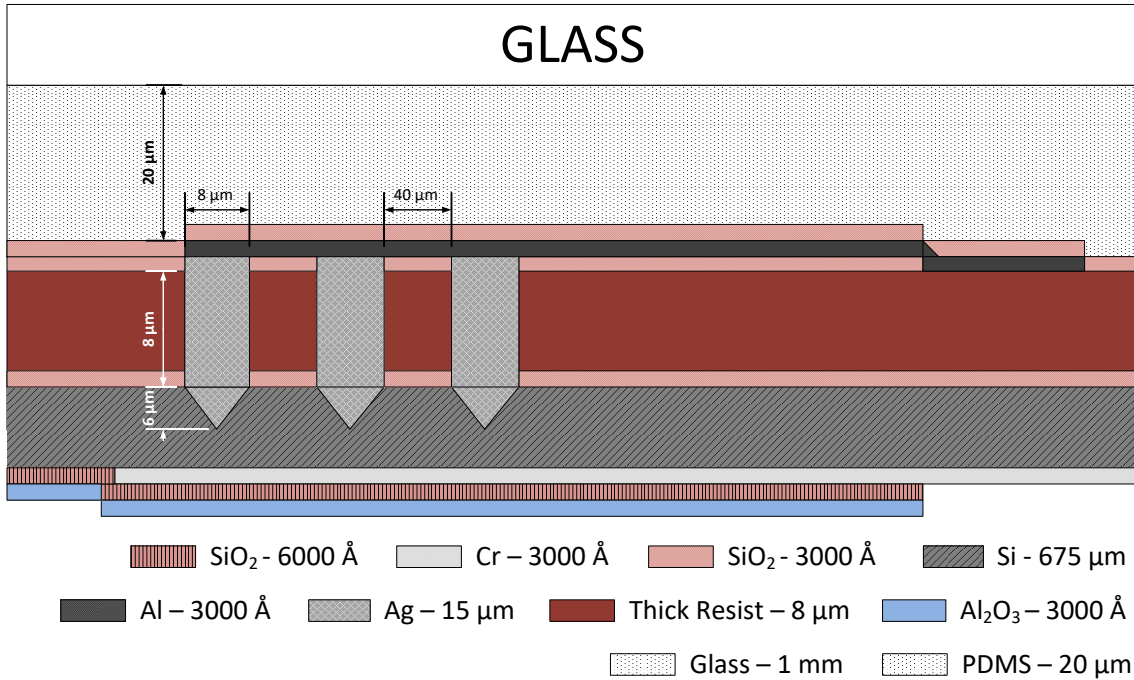
STEP #23: PDMS pouring and baking

Equipment: Hotplate



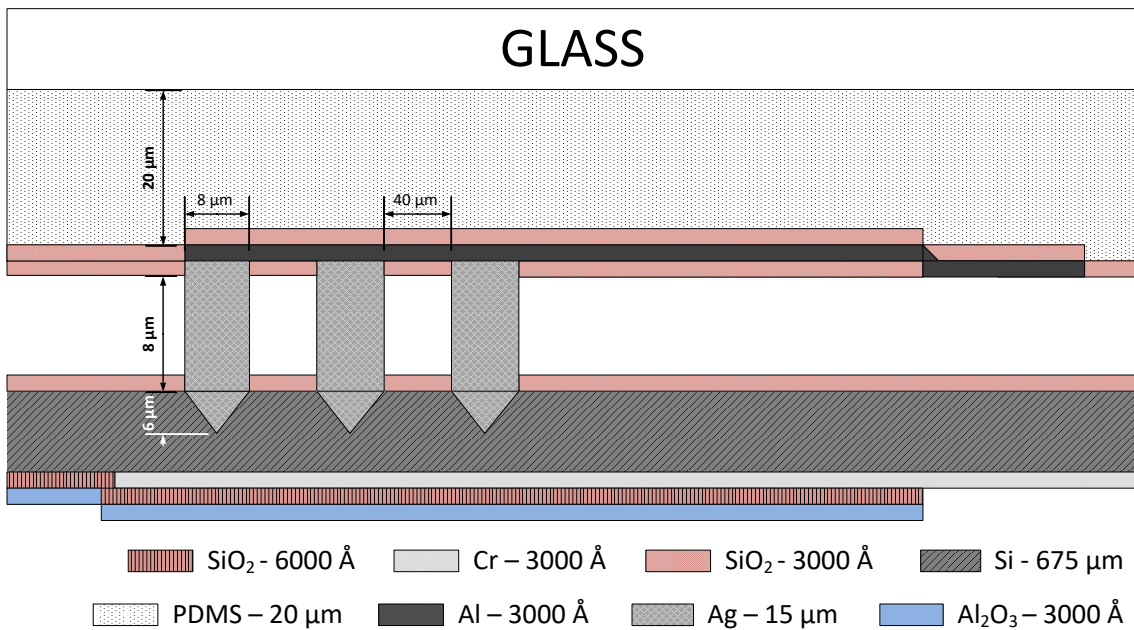
STEP 24: Structure release

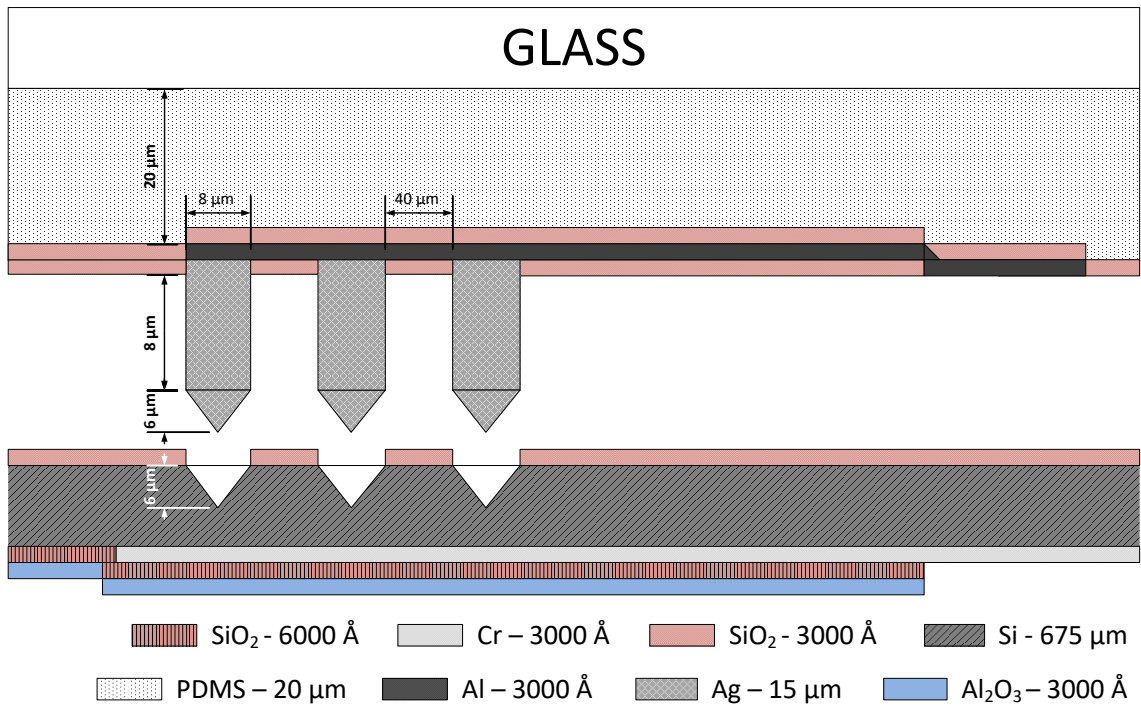
Photoresist is removed with Acetone in Ultrasounds. Careful handling of the samples is crucial at this stage. Afterwards, the two structures should be separated easily.



STEP #24: Sacrificial layer dissolution

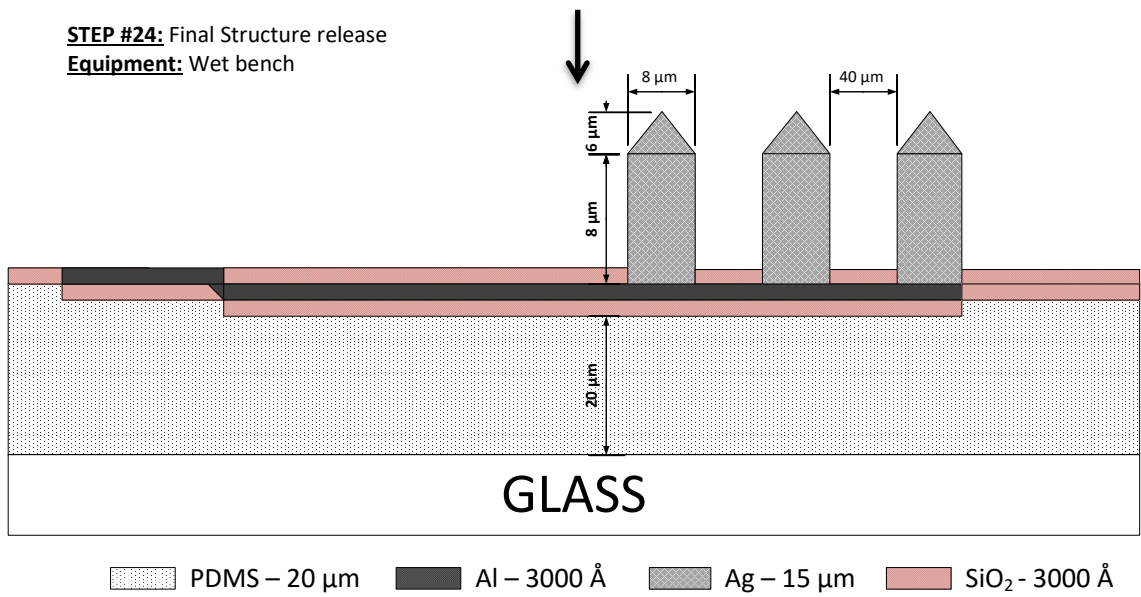
Equipment: Wet bench



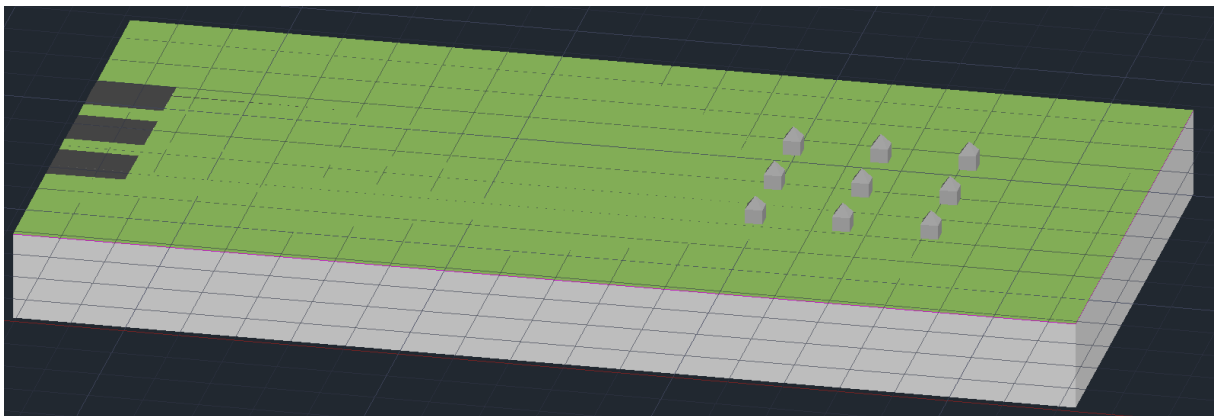
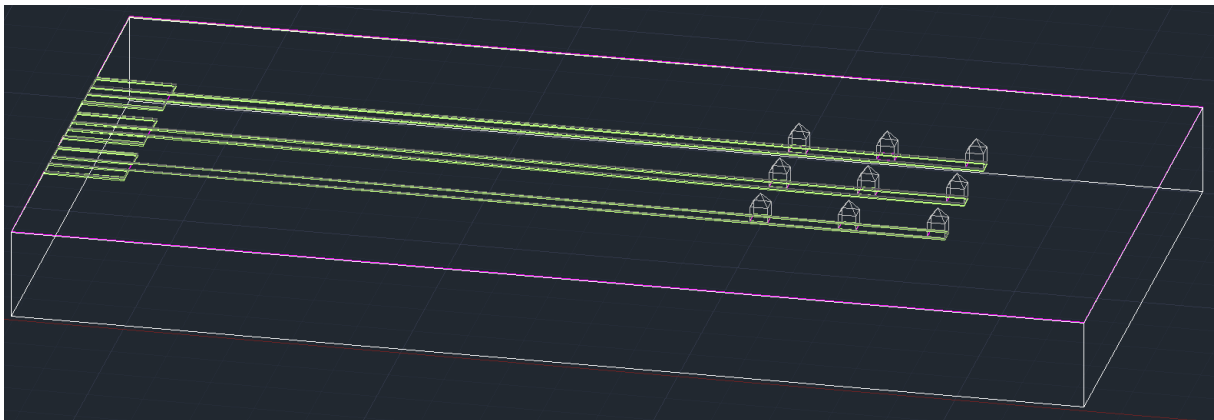


STEP #24: Final Structure release

Equipment: Wet bench



PROCESS DIAGRAM - FINAL RESULTS



This diagram is a representation of the developed system, and therefore, is not to scale. The number of Pads, Vias and Sensors is underrepresented on this diagram in order to demonstrate the concept. All structures are also exaggerated in size for the same reason.

Annex 7 - Process Runsheet for the preparation of Silver Electroplating Solutions

Solution #1 - Tollens's Reagent (Ag(NH₃)₂OH)

The described protocol will result in a dark silver oxide solution. However, with the addition of more ammonia, the silver oxide precipitate dissolves forming the Ag(NH₃)₂ complex. Glucose acts as a reducing agent, causing the precipitation of elemental silver.

STEP 01 - Silver Nitrate preparation

Date: ___/___/___	Operator: _____
<p>Reaction: $3Ag + 4HNO_3 \rightarrow 3AgNO_3 + 2H_2O + NO$ (cold + diluted)</p> <p style="margin-left: 100px;">$Ag + 2HNO_3 \rightarrow AgNO_3 + H_2O + NO_2$ (hot + concentrated)</p>	
Machine:	Wet Bench
Conditions:	<p>Insert the Silver inside a Nitric Acid bath. Heat the Nitric Acid bath to increase the reaction kinetics. Wait until all Silver is dissolved (a yellowish color will prevail, with clear white crystals formed in the bottom). Let the reaction cup to cool down and decant the excess liquid. Transfer the Silver Nitrate crystals into ceramic cups and apply 60~80 °C at an oven for several hours to evaporate the remaining liquid.</p> <p>CAUTION! Do not apply temperature over 80 °C, as the liquid (water and nitric acid) may burst and expel Silver Nitrate towards the chamber.</p> <p>CAUTION! After opening the oven door, <u>do not breath the fumes</u> as they may contain high concentration of Nitric Acid vapor. This gas is toxic and can cause respiratory problems if highly inhaled</p>
<div style="border: 1px solid gray; padding: 5px; background-color: #f0f0f0;"> <p>Nitric Acid</p> <p>Clear to yellow fuming liquid; acrid, suffocating odor. Corrosive, causes severe burns to eyes/skin/respiratory tract. Also causes: heavy exposures: lung damage. Chronic: tooth erosion, bronchitis. Strong oxidizer capable</p> <p style="text-align: center; font-size: small;">CAS No. 7697-37-2</p> </div>	<div style="text-align: center;"> </div> <p>NOTE: Use appropriated safety equipment!</p> <p>NOTE: Nitrogen Dioxide is extremely dangerous!</p> <p>Observations: _____</p> <p>_____</p> <p>_____</p>

STEP 02 - Tollens's Reagent preparation

Date: ___/___/___	Operator: _____
Machine:	Wet Bench
Conditions:	<p>On a agitation plate, insert the necessary amount of diluted ammonia into a reaction cup. The volume should be enough to engulf the area to be plated. Increase the agitation until a small vortex is observable. Afterwards, add the Silver Nitrate into a reaction cup. The quantity used in this process should be proportional to the weight of Silver to be deposited on all surfaces. After a few minutes the solution should turn dark as Silver Oxide precipitates. Continue adding small amounts of ammonia until all Silver is dissolved. Add Glucose to start the silver plating.</p>
NOTE: Use appropriated safety equipment!	
Observations: _____	

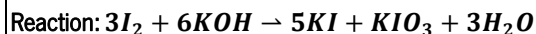
Solution #2 - Silver Iodide (AgI)

The described protocol will result in a yellow AgI solution, mostly from the presence of excess I₂ elements or precipitates. AgI solution is very aggressive towards standard 5 µm thick photoresist. After a few uses, the solution's color changes to transparent, due to the removal of excess I₂ from the solution.

STEP 01 - Potassium Iodide preparation

Date: ___/___/___

Operator: _____

**Machine:** Wet Bench

Conditions: Add KOH pellets to an Iodine solution until the color turns white. Apply temperature and agitation if needed. Filter the solution to separate the solid KIO₃ from the dissolved Potassium Iodide. Finally, evaporate the water by boiling the solution and applying 60~80°C at an oven for several hours.

Potassium Hydroxide

White or slightly yellow deliquescent pellets, rods, or lumps. Corrosive, causes severe burns to eyes/skin/respiratory tract. Toxic! May cause serious lung damage. Repeated skin contact can cause dermatitis. Reacts with water producing excessive heat.

CAS No. 1310-58-3

How to prepare 50g of Potassium Iodide!

	I ₂	KOH	KI
Molecular mass (g.mol ⁻¹)	253,808	56,11	166,0028
N° of moles (mol)	0,18	0,36	0,3
Mass/Volume (g/mL)	45,685	23,764 (85%)	50

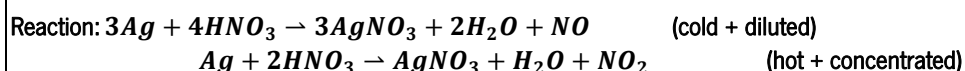
NOTE: Use appropriated safety equipment!

Observations: _____

STEP 02 - Silver Nitrate preparation

Date: ___/___/___

Operator: _____

**Machine:** Wet Bench

Conditions: Insert the Silver inside a Nitric Acid bath. Heat the Nitric Acid bath to increase the reaction kinetics. Wait until all Silver is dissolved (a yellowish color will prevail, with clear white crystals formed in the bottom). Let the reaction cup to cool down and decant the excess liquid. Transfer the Silver Nitrate crystals into ceramic cups and apply 60~80 °C at an oven for several hours to evaporate the remaining liquid.

CAUTION! Do not apply temperature over 80 °C, as the liquid (water and nitric acid) may burst and expel Silver Nitrate towards the chamber.

CAUTION! After opening the oven door, do not breath the fumes as they may contain high concentration of Nitric Acid vapor. This gas is toxic and can cause respiratory problems if highly inhaled

Nitric Acid

Clear to yellow fuming liquid; acrid, suffocating odor. Corrosive, causes severe burns to eyes/skin/respiratory tract. Also causes: heavy exposures: lung damage. Chronic: tooth erosion, bronchitis. Strong oxidizer capable



CAS No. 7697-37-2

NOTE: Use appropriated safety equipment!**NOTE: Nitrogen Dioxide is extremely dangerous!**

Observations: _____

STEP 03 - Silver Iodide preparation

Date: ___/___/___

Operator: _____



Machine: Wet Bench

Conditions: Silver Iodide precipitates with a yellow/white colour once Silver Nitrate is in contact with Potassium Iodide. Agitate the solution to assure that all molecules have reacted. Filtrate the solid Silver Iodide and evaporate any remaining dissolved Potassium Nitrate

How to prepare 0,625g of Silver Iodide!

	KI	AgNO ₃	AgI
Molecular mass (g.mol ⁻¹)	166,0028	169,87	234,77
N° of moles (mol)	2,7x10 ⁻³	2,7x10 ⁻³	2,7x10 ⁻³
Mass/Volume (g/mL)	0,442	0,452	0,625

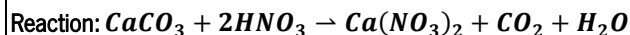
NOTE: Use appropriated safety equipment!

Observations: _____

STEP 04 - Calcium Nitrate preparation

Date: ___/___/___

Operator: _____



Machine: Wet Bench

Conditions: Prepare a 1 mol.dm³ solution of Nitric Acid. Pour the solution into a ~10x larger beaker and warm the acid to ~60 °C (Nitric Acid needs to be added in excess). Carefully and slowly add the Calcium Carbonate, allowing the effervescence to fade away. Filter the warm mixture into an evaporating basin and slowly evaporate the filtrate over a hot water bath at 60 °C. Allow the concentrated solution to cool. Filter off the crystals and place a filter paper with the crystals on a watch glass. Dry the crystals with the assistance of another piece of paper. Cover the watch glass with a piece of clean filter paper and apply 60~80 °C at an oven to evaporate the remaining solution.

How to prepare 5g of Calcium Nitrate!

	CaCO ₃	HNO ₃	Ca(NO ₃) ₂
Molecular mass (g.mol ⁻¹)	100,0869	63,01	164,088
Density (g.cm ⁻³)	-	1,51	-
N° of moles (mol)	0,03	-	0,03
Mass/Volume (g/mL)	3,05	30,5	5

Nitric Acid

Clear to yellow fuming liquid; acid, suffocating odor. Corrosive, causes severe burns to eyes/skin/respiratory tract. Also causes: heavy exposures: lung damage. Chronic: tooth erosion, bronchitis. Strong oxidizer capable



CAS No. 7697-37-2

How to prepare a 30,5 mL of 1 mol.dm³ Nitric Acid solution!

Pour 26,134 mL of water into a 250 mL beaker. Carefully add 3,916 mL of a 65% Nitric Acid solution to the water.

NOTE: Use appropriated safety equipment!

Observations: _____

STEP 05 - Preparation of AgI solution

Date: ___/___/___

Operator: _____

Machine: Wet Bench

Conditions: Add and mix the compounds.

Solution:


	Concentration	Molarity	Added
Silver Iodide	2,5 g.L ⁻¹	0,011 M	0,625 g
Potassium Iodide	200 g.L ⁻¹	1,200 M	50 g
Calcium Nitrate	20 g.L ⁻¹	0,122 M	5 g
Water	-	-	250 mL

Observations: _____

Solution #3 - Silver Nitrate (AgNO₃) in Ammonia

The described protocol will result in a clear AgNO₃ solution dissolved in NH₃ and water. With the constant use, the NH₃ and water will evaporate, thus creating a more concentrated solution. The pH values range from 11 to 12.

STEP 01 - Silver Nitrate preparation

Date: ___/___/___	Operator: _____
<p>Reaction: $3Ag + 4HNO_3 \rightarrow 3AgNO_3 + 2H_2O + NO$ (cold + diluted)</p> <p style="margin-left: 100px;">$Ag + 2HNO_3 \rightarrow AgNO_3 + H_2O + NO_2$ (hot + concentrated)</p>	
Machine:	Wet Bench
Conditions:	<p>Insert the Silver inside a Nitric Acid bath. Heat the Nitric Acid bath to increase the reaction kinetics. Wait until all Silver is dissolved (a yellowish color will prevail, with clear white crystals formed in the bottom). Let the reaction cup to cool down and decant the excess liquid. Transfer the Silver Nitrate crystals into ceramic cups and apply 60~80 °C at an oven for several hours to evaporate the remaining liquid.</p> <p>CAUTION! Do not apply temperature over 80 °C, as the liquid (water and nitric acid) may burst and expel Silver Nitrate towards the chamber.</p> <p>CAUTION! After opening the oven door, <u>do not breath the fumes</u> as they may contain high concentration of Nitric Acid vapor. This gas is toxic and can cause respiratory problems if highly inhaled</p>
<div style="border: 1px solid gray; padding: 5px; background-color: #f0f0f0;"> <p>Nitric Acid</p> <p>Clear to yellow fuming liquid; acrid, suffocating odor. Corrosive, causes severe burns to eyes/skin/respiratory tract. Also causes: heavy exposures: lung damage. Chronic: tooth erosion, bronchitis. Strong oxidizer capable</p> <p style="text-align: center; font-size: small;">CAS No. 7697-37-2</p> </div>	<div style="text-align: center;">  </div> <p>NOTE: Use appropriated safety equipment!</p> <p>NOTE: Nitrogen Dioxide is extremely dangerous!</p> <p>Observations: _____</p> <p>_____</p> <p>_____</p>

STEP 02 - Ammonia preparation

Date: ___/___/___	Operator: _____
Reaction: Simple NH ₃ dilution in water	
Machine:	Wet Bench
Conditions:	<p>Standard NH₃ solution is presented at 25% concentration with a 0,91 kg.L⁻¹ density. This represents a 13,36 M solution in the presented conditions. In order to obtain a 1 M solution of NH₃ it's required to dilute the solution into water. The value can be calculated for the final solution volume, adding directly into it. Through the dilution equation:</p> <p style="margin-left: 40px;">$C_1 \cdot V_1 = C_2 \cdot V_2$</p> <p style="margin-left: 40px;">$C_1 = 13,36 \text{ M}$ $V_1 = \text{desired measurement}$</p> <p style="margin-left: 40px;">$C_2 = 1 \text{ M}$ $V_2 = \text{final solution volume}$</p> <p>NOTE: Use appropriated safety equipment!</p> <p>Observations: _____</p> <p>_____</p> <p>_____</p>

STEP 03 - Silver Nitrite in Ammonia preparation

Date: ___/___/___

Operator: _____

Reaction: Standard dissolution of AgNO_3 in diluted NH_3 solution and H_2O

Machine: Wet Bench

Conditions: Silver Nitrate stains all organic surfaces, including human tissue, both in the pure or diluted form. Stains only appear after exposure to white light (might take several hours). Silver Nitrate volume needs to be taken into consideration in order to maintain the desired concentration. Let the solution rest for a day.

How to prepare a 0,3 M AgNO_3 in 1 M NH_3 solution!

	AgNO_3	NH_3	H_2O	Final solution
Molecular mass (g.mol^{-1})	169,87	17,03	-	-
Density (g.L^{-1})	-	910	-	-
Initial Concentration (%)	~ 100	25	-	-
Initial Concentration (M)	-	13,358	-	-
Desired concentration (M)	0,3	1	-	-
Desired volume (mL)	-	-	-	100
Required mass (g)	5,0961	-	-	-
Occupied volume (mL)	1,171	-	-	-
Required volume (mL)	-	7,486	91,342	-

NOTE: Use appropriated safety equipment!

Observations: _____

